Expérience de Hanbury Brown et Twiss dans un microscope électronique à transmission à balayage : sa physique et ses applications

Sophie Meuret

université PARIS-SACLAY

UNIVERSITÉ PARIS SUD
Comprendre le monde, construire l'avenir

NNT : 2015SACLS112

DGA

THESE DE DOCTORAT
DE
L'UNIVERSITE PARIS-SACLAY
PREPAREE A
"UNIVERSITE PARIS SUD"

ECOLE DOCTORALE N°564 PIF
Physique de l'Ile de France

Spécialité de doctorat (Physique)

Par

Sophie Meuret

Intensity Interferometry Experiments in a Scanning Transmission Electron Microscope : Physics and Applications

Thèse présentée et soutenue à Orsay le 16 Novembre 2015 :

Composition du Jury :

Mme, Robert-Philip, Isabelle	Directrice de Recherche, LPN	Présidente
Mr, Lefebvre, Pierre	Directeur de Recherche, Laboratoire Charles Coulomb	Rapporteur
Mr, Nellist, Peter	Professeur, Université d'Oxford	Rapporteur
Mr, Hohenester, Ulrich	Professeur, Université de Graz	Examinateur
Mr, Novotny, Lukas	Professeur, Université ETH	Examinateur
Mr, Kociak, Mathieu	Directeur de Recherche, LPS	Directeur de thèse
Mr, Tizei, Luiz	Chargé de recherche, LPS	Co-encadrant de thèse
Mr, Garcia de Abajo, Javier	Professeur, ICFO	Invité

Ils éclatèrent de rire. Des photons pleuvaient sur leur peau, la plupart les traversaient sans s'arrêter. Et ils se tenaient là, transparents au monde.

Kim Stanley Robinson, Mars la bleu

Abstract

Intensity interferometry experiments in a scanning transmission electron microscope : physics and applications

Quantum optics performed at the nanometer scale is an important challenge, especially for quantum emitters characterization. They can be point defects in material (few angströms) or confined structures of a few nanometers. A way to reach this scale is by using cathodoluminescence (CL) performed in a scanning transmission electron microscope (CL-STEM), which has only recently been done [1]. However, when aiming at studying the statistical properties of the light coming out of a CL experiment, which is necessary to e. g. study the quantum nature of Single Photon Emitters (SPE) emission, dedicated experiments on top of regular CL ones have to be designed. It is well known that the clear signature of SPE as measured in photoluminescence (PL) is antibunching in the $g^{(2)}(\tau)$, namely that the autocorrelation function is less than one at short delay $\tau \approx 0$. Few months before my arrival in the STEM-group of the LPS, an intensity interferometry experiment (HBT) that measures the autocorrelation function $g^{(2)}(\tau)$ of the CL signal intensity was built [2]. It demonstrated on a famous SPE, the Nitrogen vacancy (NV) defect in diamond, that CL-STEM is similar to PL when only one SPE is involved.

In this thesis we will see how CL-STEM allowed to characterize a new point defect in h-BN, showing the relevance of HBT experiments in a CL-STEM for discovering and characterizing new SPE. However, by studying the excitation of multiple SPE in CL, we discovered a new emission phenomenon, characterized by a huge bunching effect of the $g^{(2)}(\tau)$ function ($g^{(2)}_{\mathrm{CL}}(0) > 35$), in complete contradiction to PL measurements and expectations ($g^{(2)}(\tau) \approx 1$). In my thesis manuscript, this surprising effect will be experimentally investigated, theoretically explained and applied to lifetime measurement at the nanometer scale. Because quantum optics is often linked to quantum plasmonics, I will present, in conclusion, a theoretical proposal, in collaboration with J. Garcia de Abajo, about quantum plasmonics measurement in a STEM.

Remerciements

Les Remerciements... Il me faudrait écrire une deuxième thèse pour remercier proprement chaque personne qui a contribué à ce travail. Je vais tout de même essayer mais gardez en tête que ce n'est qu'une pâle représentation de tout ce que je vous dois.

Tout d'abord je souhaite remercier Pierre Lefebvre et Peter Nellist pour avoir accepté d'être rapporteurs de ce manuscrit. Il a été grandement amélioré grâce à vos remarques avant la soutenance et pendant. Je tiens aussi à remercier Isabelle Robert-Philip, Ulrich Hohenester et Lukas Novotny pour avoir accepté de faire partie de mon jury en temps qu'examinateurs. Il est commun que les examinateurs ne lisent pas la thèse mais cela n'a pas été le cas, ce qui a eu pour conséquence une discussion passionnante avec chacun d'entre vous pendant la soutenance. Le manuscrit a aussi grandement bénéficié de vos remarques et corrections.

Je souhaite ensuite remercier Dominique Chandesris, directrice du LPS pendant une très grande partie de ma thèse, et qui a soutenu l'obtention de ma bourse. Je suis aussi reconnaissante à Odile Stephan, chef d'équipe comme il y en a peu, qui m'a incluse et mise à l'aise dès mon premier jour de stage et n'a jamais arrêté depuis. Je suis convaincue que l'esprit si agréable et soudé que l'on trouve dans l'équipe STEM te doit beaucoup, et je ne parle pas de tes qualités scientifiques. On se construit avec des modèles et je suis heureuse de pouvoir compter sur le tien.

Il me faudrait au moins un chapitre sur chacun de mes directeurs de thèses, Mathieu Kociak et Luiz Tizei. Le profond respect et l'admiration que j'ai pour chacun de vous m'ont permis d'avancer toujours dans la bonne direction ayant une confiance absolue en vos conseils et critiques. Peu d'encadrants écoutent autant les élucubrations de leurs thésard(e)s et leur donnent autant de crédits ; je me suis senti apprendre à vos côtés, me transformer en quelques choses de mieux. Bref après 3 ans je suis prête à prendre mon envol vers de nouveaux horizons en gardant comme un petit padawan vos conseils pour rester du bon côté de la force. Mathieu, je te remercie tout particulièrement pour la patience avec laquelle tu m'as guidée pendant ces trois ans avec une admiration toute particulière pour la bienveillance avec laquelle tu as relu les différents modèles successifs du bunching. Luiz, tu m'as appris d'une main de maître ce que signifiait faire de la microscopie, certes sans grand succès pour ce qui est de la diffraction mais je te rassure : c'était une cause perdue d'avance. La découverte du bunching a été une passionnante aventure mais je suis sûre qu'elle se serait transformée en cauchemar sans toi. Bien sûr, je vous remercie aussi tous les deux pour cette année un peu particulière où vous avez su m'aider exactement comme il le fallait, sans trop en faire. Bref, je vous dois beaucoup.

Cette thèse a aussi bénéficié de l'aide de personnes extérieures au laboratoire. François Treussart m'a ainsi apporté un regard critique et toujours constructif sur le bunching et les différents modèles que je lui ai soumis. Ce fut un plaisir de travailler avec toi et j'espère que ce n'est que le début. Je voudrais aussi remercier Thomas Auzelle pour les nombreux échantillons de nanofils qu'il a accepté de synthétiser pendant trois ans et sans qui le chapitre 5 n'aurait pu aboutir. Un grand merci à Bruno Daudin qui le premier m'a orientée vers Mathieu et pour son enthousiasme sur tout ce qui touche de près ou de loin aux nanofils. Ainsi qu'à Bruno Gayral pour avoir pris le temps de faire avec moi ces expériences de PL résolue en temps qui ont permis de boucler la boucle. Je remercie aussi grandement Javier Garcia de Abajo qui m'a accueillie deux fois trois semaines à ICFO pour (très) patiemment me guider à travers les calculs de plasmonique quantique. Je reste admirative de la facilité avec laquelle tu arrives à expliquer au commun des mortels des choses qui te semblent pourtant si évidentes.

Cette thèse n'aurait pas été aussi chouette sans toute l'équipe STEM. Les thésards d'abords, passé et présent, Arthur Losquin et Zackaria Mahfoud qui m'ont accueillie pendant mon stage et m'ont chacun aidé à leur manière. Arthur en me faisant comprendre que les plasmons et bien c'était un peu plus compliqué que ça et Zackaria pour la patience avec laquelle tu m'as expliqué Igor. Je ne suis pas sûre Zackaria que je te remercie pour tes blagues...bon si quand même, elles me manquent trop depuis que tu es parti. Je remercie aussi Romain Bourrelier pour nos discussions de joggeurs ainsi que les expériences sur le BN, c'était un vrai travail d'équipe. Bien sûr mon jumeau de thèse, Vincent Badjeck dont la bonne humeur a été un réconfort dans les moments difficiles. Un merci aussi à Anna Tararan, arrivée juste après nous, entre autres pour m'avoir remplacée quand j'en ai eu besoin pour les TP de microscopie et à qui je n'ai pas pu rendre la pareille. Je remercie aussi bien sûr nos magiciens sans qui rien ne serait possible, Katia March pour toutes les petites attentions qui ont rendu des moments difficiles bien plus doux, Marcel Tencé sans qui le VG ne fonctionnerait plus depuis longtemps et Jean-Denis Blazit, co-bureau très patient avec mes excentricités et pour les innombrables petites pièces et améliorations que tu as pris le temps de faire lorsque je te demandais de l'aide et qui m'ont bien simplifié la vie. Ainsi que Jérome Schindfessel pour l'aide sur la cathodo et Raphael Weiss sans qui la lithographie serait à jamais restée un mystère pour moi. Je remercie aussi tous les autres permanents du groupes qui m'ont chacun aidée à leur manière, Alex Gloter, Mike Walls dont une expérience d'EDX à la dernière minutes, Alberto Zobelli, Claudie Mory et Marta De Frutos. Je remercie aussi Christian Colliex pour sa gentillesse et ses conseils avisés qui m'ont permis de mieux appréhender l'intéraction électron-matière. Un remerciement tout particulier à Laura Bocher qui m'a épaulée et écoutée pendant trois ans de la façon la plus amicale qui soit

et pour sa présence ces derniers mois (On va finir par réussir à boire ce Pomerol tu vas voir.)

J'ai aussi eu la chance d'encadrer deux stagiaires de master de grande qualité, qui ont su chacun apporter leur pierre à l'édifice. Thibault Cazimajou avec qui j'ai construit le premier modèle Monte Carlo sur le bunching et qui m'a évité bien des erreurs. Hugo Lorenco-Martins qui est arrivé juste au bon moment pour m'aider sur les premières manips de couplage et à qui je confie les rênes du bunching avec une totale confiance, je suis sûre que vous allez bien vous amuser.

Il me reste encore à remercier tout ceux qui m'ont supportée et suivie pendant cette thèse sans rien comprendre à la physique.... A mes amies de toujours, Julie et Héloïse qui m'ont toujours soutenue et sans qui je n'aurais pas pu traverser toutes les épreuves de cette dernière année. Vous êtes d'une générosité rare et je vous dois beaucoup. A Pierre aussi, dont l'amitié sans faille est une ancre dans une vie toujours changeante, à Lise pour ta présence toujours souriante et attentionnée. A Jules aussi, pour m'avoir aidée à me construire et m'avoir supportée pendant des années. Les amis de Grenoble, Hélène, Anthony, Mathieu et Thibault, toujours un plaisir de venir vous voir. On dit souvent que la famille est un trésor qui nous aide dans toutes les épreuves, ça ne pourrait être plus vrai dans mon cas. A mes parents qui m'ont tellement aidée ces dernier mois, m'ont accueillie et chouchoutée sans sourcilier et à mon frérot bien sûr qui, malgré une profonde méfiance pour la physique, m'a soutenue jusqu'au bout, je n'échangerais notre lien fraternel pour rien au monde.

Mes trois ans de thèse ont été des années très heureuses malgré les épreuves ; peu de thésards pourraient dire la même chose et c'est grâce à vous tous.

Bon allez, il est temps de faire un peu de physique !

...

Résumé

Etre capable de réaliser des expériences d'optique quantique à l'échelle du nanomètre est un des grands défit actuel de la recherche. En particulier pour la caractérisation des émetteurs de photon unique, c'est à dire des émetteurs qui n'émettent qu'un photon à la fois. Ces émetteurs aux propriétés particulières peuvent être des défauts ponctuels dans des matériaux (quelques angströms) ou des structures confinées de quelques nanomètre. Une façon de sonder la matière à cette échelle est d'utiliser leur signal de cathodoluminescence (CL) généré grâce un microscope électronique à transmission à balayage (CL-STEM) [1]. Cependant, si l'on cherche à étudier les propriétés statistiques d'émissions de la lumière émise grâce à une expérience de CL, ce qui est nécessaire pour étudier par exemple la nature quantique de ces émetteurs, une expérience dédiée doit compléter l'expérience de CL-STEM classique. Quelques mois avant mon arrivée dans le groupe STEM du LPS, une expérience d'interférence des intensités (HBT) qui mesure la fonction d'autocorrélation $g^{(2)}(\tau)$ du signal de CL a été construite [2]. Il est bien connu que la signature univoque d'un SPE en photoluminescence (PL) est le dégroupement de photon ou antibunching, c'est à dire que $g^{(2)}(0) < 1$. Ce qui signifie que la probabilité que deux photons soient détectés en même temps est plus faible qu'avec n'importe quel autre intervalle de temps τ entre les photons. Il a été récemment démontré que lorsque seulement un SPE est excité avec un système de CL-STEM, le signal émis est similaire au signal de PL [2]. La première expérience a été réalisée sur un célèbre SPE, le centre NV dans le diamant. Dans cette thèse nous montrerons comment la CL-STEM a permis de caractériser un nouveau défaut ponctuel dans le h-BN, permettant de démontrer la pertinence, pour découvrir et caractériser de nouveaux SPE, d'utiliser le signal produit par l'expérience de CL-STEM pour l'expérience HBT. Cependant, en étudiant l'excitation de multiple SPE en CL, on a découvert un nouveau phénomène d'émission, caractérisé par un grand effet de regroupement (bunching) dans la fonction $g^{(2)}(\tau)$ ($g^{(2)}(0) > 35$), en complète contradiction avec les mesures de PL ($g^{(2)}(\tau) \approx 1$). Dans mon manuscrit de thèse, cet effet surprenant a été expérimentalement étudié, théoriquement expliqué et appliqué à la mesure de temps de vie à l'échelle du nanomètre. Et parce que l'optique quantique est souvent liée à la plasmonique quantique, je présenterai pour conclure une proposition théorique en collaboration avec Javier Garcia de Abajo pour étudier la plasmonique quantique dans un microscope électronique à transmission à balayage.

L'optique quantique avec des électrons

La lumière a toujours été un outil naturel pour observer le monde. En effet, notre perception est principalement définie par la façon dont nos yeux et notre cerveau analysent la lumière qui nous entoure. Les transitions électroniques et vibrationnelles dans la matière se produisent à des énergies similaires à celle de la lumière, et donc les propriétés des matériaux peuvent dans de nombreux cas être caractérisées par des mesures optiques [3]. Depuis quelques dizaines d'années les nanosciences et les nanotechnologies ont progressé continument. Leurs succès reposent en grande partie sur les progrès en nano-fabrication, on est maintenant capable de contrôler la synthèse des matériaux à l'échelle atomique. Parmi ces nouveaux matériaux nano-structurés, certains ont des propriétés extraordinaires que l'on ne peut trouver dans les matériaux massifs, et leur étude a conduit à l'émergence de la nano-optique [4]. La nano-optique regroupe touts les phénomènes optiques se manifestant à l'échelle du nanomètre, ainsi que les techniques qui améliorent leur caractérisation ou leur manipulation. Réduire la dimension des matériaux permet la création de systèmes confinés. Par exemple, les puits quantique et les boites quantique sont des nanostructures où les électrons et les trous sont confinés dans respectivement deux et zéro dimension(s). Ce confinement change les propriétés optiques des matériaux. Par exemple, le comportement des boites quantiques est plus proche de celui des atomes que de celui d'un solide. Tout comme l'atome, elles ne peuvent émettre qu'un photon à la fois. De tels émetteurs de photon unique (SPE) rassemblent donc l'optique quantique et la physique du solide, permettant la construction de systèmes solides exploitant le caractère quantique de la lumière. Afin de caractériser ce genre de matériaux nanostructurés optiquement actifs, il est impératif de construire des expériences capables de sonder ces matériaux à l'échelle nanométrique [4]. L'une des plus célèbres et standard expérience d'optique quantique est l'expérience de Hanbury Brown et Twiss (HBT) [5]. Elle mesure la fonction d'autocorrélation en intensité du signal, appelée $g^{(2)}(\tau)$. Si $g^{(2)}(0) < 1$, un comportement appelé dégroupement, l'émetteur est un émetteur de photon unique [6, 7]. Une autre expérience est l'expérience de Hong-Ou-Mandel qui mesure l'indiscernabilité des photons émis [8, 9]. Comme expliqué précédemment, la taille de confinement est typiquement plus petite que 10 nm [10, 11], il est donc impératif de réaliser les expériences d'optique quantique à l'échelle du nanomètre. Cependant, il est difficile d'atteindre une telle limite, à cause de la diffraction de la lumière [12], sans perturber les propriétés quantiques du système. Par exemple la microscopie de déplétion par émission stimulée (STED) est très efficace pour imager les échantillons à l'échelle du nanomètre [13, 14] mais même s'il a été prouvé que le STED préserve certaine des propriétés quantiques des émetteurs [15], la nécessité d'une déplétion stimulée efficace restreint cette méthode à certains matériaux. Utiliser des électrons rapides pour observer la matière est une façon d'atteindre la résolution sous-longueur d'onde grâce à la

courte longueur d'onde des électrons [16, 17]. Une expérience de cathodoluminescence (CL) consiste à exciter un émetteur donné avec des électrons rapides et à analyser la lumière émise, permettant ainsi l'étude de ses propriétés optiques avec une résolution sous-longueur d'onde [18]. Cependant, l'interaction des électrons rapides avec la matière est un sujet large et complexe. Cette complexité apparaît à cause de l'énergie élevée des électrons incidents et de leur capacité à transférer de l'énergie aux matériaux par de multiples types d'excitations. Néanmoins, la création d'un plasmon de volume domine sur tous les autres mécanismes de pertes [19]. De plus le signal de CL dans les semiconducteurs démontre que les excitations primaires amènent ultimement à la production d'au moins une paire électron-trou (e-h) proche de l'énergie du gap qui se recombine radiativement. On peut considérer qu'en moyenne 80 % des e-h paires ayant une énergie proche de celle du gap proviennent de la décomposition d'un plasmon [20, 21]. A cause de l'énergie élevée des électrons incidents, toutes les transitions radiatives peuvent être excitées, contrairement à l'expérience de photoluminescence où l'énergie du laser restreint la partie du spectre d'émission étudiée aux transitions ayant une énergie inférieure à celle du laser. Cependant, dans les deux techniques, l'émission est dûe à la recombinaison des paires électron trou, la PL et la CL ont donc des spectres similaires [22]. Il semble donc qu'à première vue, la CL est une façon de faire de la photoluminescence à l'échelle du nanomètre. La CL réalisée dans un microscope électronique à transmission à balayage (STEM) à basse température sur un échantillon mince plutôt que dans un microscope électronique à balayage (SEM) diminue drastiquement la probabilité d'interaction par électron, permettant une meilleur résolution spatiale mais aussi d'éviter les comportements non-linéaires dû à des effets de saturation de l'émission. Au cours des dernières années, la CL-STEM a démontré sa pertinence pour les expériences de nano-optique standards [23]. Réaliser des expériences d'optique quantique dans un STEM était donc la prochaine étape logique. Cependant une des questions fondamentales associée à tel but restait sans réponse : comment l'utilisation d'électrons plutôt que de photons affecte-t-elle les états de la lumière ? Luiz Tizei et Mathieu Kociak, qui ont supervisé cette thèse au LPS, ont construit la première expérience d'HBT couplée à un système CL-STEM et ont ainsi pu mesurer la nature quantique [2] de la lumière émise par un SPE déjà bien connue, le centre "nitrogen-vacancy" (NV) du diamant [24, 25]. Ils ont ainsi prouvé que sonder un SPE avec des électrons plutôt que des photons ne change pas sa statistique, ouvrant la porte du nano-monde à l'optique quantique. Dans la première partie de cette thèse j'exposerai les expériences réalisées sur des nano-diamants en continuité de cette première expérience, mais aussi sur un nouveau SPE que nous avons pu découvrir grâce à la CL. En effet, grâce à la haute résolution spatiale de la CL il est facile de trouver des émissions localisées et donc des nouveaux émetteurs de photon unique. Cela a été le cas, avec un défaut déjà connu dans le nitrure de Bore hexagonal (h-BN) émettant à 4 eV [26]. Grâce à la CL, Romain Bourrellier, un ancien thésard du groupe, a montré

que l'émission associée à ce défaut était localisée sur des zones d'environ 80 nm. Nous avons donc construit une seconde expérience HBT fonctionnant dans l'ultra-violet, grâce à laquelle nous avons été capable de démontrer pour la première fois le caractère quantique de ce défaut (voir figure 3). L'expérience de CL-STEM est donc aussi adaptée pour découvrir et caractériser de nouveaux SPE. Pour l'instant il semble que la CL et la PL sont toujours aussi semblables. Cependant, j'ai découvert que, si on excitait plusieurs SPE en même temps, des différences entre la PL et la CL apparaissaient. En CL-STEM, à faible courant d'excitation ($I \leq 100$ pA), un large pic apparaît à délai nul ($\tau = 0$) dans la fonction d'autocorrélation du second ordre $g^{(2)}(\tau)$ ($g^{(2)}(0) > 35$) (bunching). Ce pic dont la largeur est de l'ordre de la nanoseconde dépend du courant du faisceau d'électron (voir Figure 4). Ce comportement diffère fortement de la fonction $g^{(2)}(\tau)$ obtenue en PL qui est plate lorsque de nombreux SPE sont excités en même temps [27]. J'ai mis au point deux modèles qui expliquent ce nouvel effet, appelé dans la suite l'effet de regroupement, un utilisant des simulations Monte Carlo (Figure 4) et un second analytique. Ils montrent que la désintégration de l'excitation à travers un plasmon de volume induit l'émission synchronisée de plusieurs centres et peut expliquer cet effet de regroupement dépendant du courant, démontrant l'effet des mécanismes d'excitation sur l'émission et soulignant le rôle du plasmon de volume dans les mécanismes de CL [21, 28]. A travers des expériences sur des hétérostructures de GaN technologiquement pertinentes, je montrerai que l'on peut utiliser l'effet de regroupement pour mesurer le temps de vie avec une résolution spatiale imbattable (quelques nm) et de manière très efficace (figure 5). Pour conclure cette thèse, nous irons dans un domaine que je n'ai approché que théoriquement : la plasmonique quantique. En effet, l'optique quantique est de plus en plus liée à la plasmonique quantique. Avec cette idée à l'esprit, en collaboration avec J. Garcia de Abajo, nous posons les bases théoriques nécessaires pour réaliser une expérience qui permet de sonder le caractère quantique des plasmons de surface (Figure 7).

Les outils expérimentaux

Pendant cette thèse, les expériences ont été principalement réalisées sur un STEM VG HB 501, utilisé pour faire les expériences de CL mais la perte d'énergie des électrons peut aussi être analysée (EELS), le principe est expliqué sur la figure 1. Le STEM a été utilisé dans la plupart des cas avec des électrons accélérés à 60 keV. Le courant du faisceau incident était entre 10 et 100 pA. Dans un STEM le faisceau d'électron est focalisé au niveau de l'échantillon dans une sonde, ici de 1 nm. La sonde scanne l'échantillon grâce aux lentilles de scan (SC), les images de l'échantillon sont réalisées grâce aux électrons diffusés, détectés par les détecteurs dits de fond noir (HADF) et de

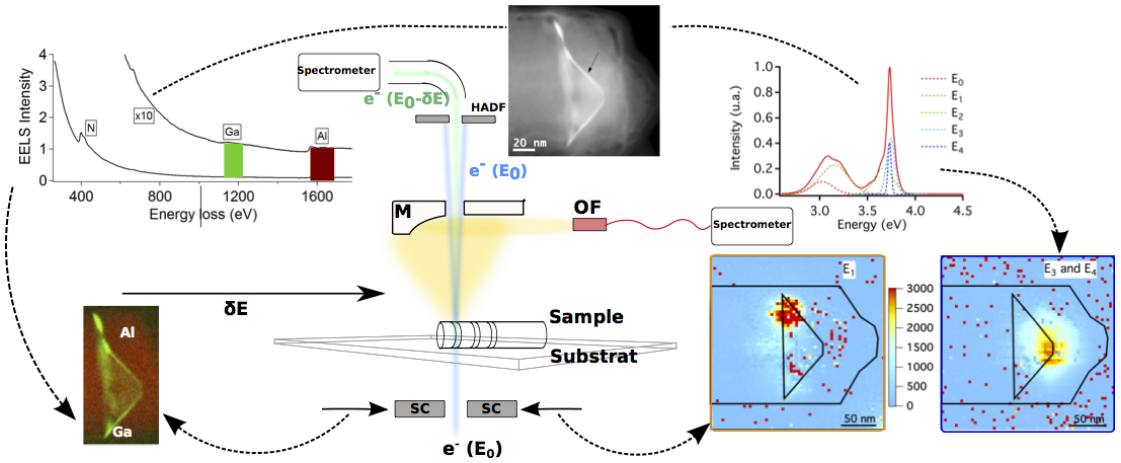

FIGURE 1: Schéma d'un STEM. Un miroir parabolique (M) avec une grande ouverture numérique a été incorporé à l'intérieur du STEM pour collecter le signal de CL de manière efficace, formant un faisceau collimaté qui est ensuite couplé à une fibre optique multi-mode (OF). Le faisceau à la sortie de la fibre est envoyé dans un spectromètre pour enregistrer le spectre d'émission. Les électrons non-diffusés sont envoyés dans un second spectromètre pour réaliser la spectroscopie des électrons par pertes d'énergie (EELS). Les électrons diffusées sont quand à eux collectés avec un détecteur de fond noir (HADF). Grâce à des lentilles de scan (SC), la sonde électronique balaye l'échantillon et à chaque pixel un spectre EELS ou CL et une image HADF sont enregistrés. On peut donc corréler les différentes émissions avec les informations structurales et chimiques de l'échantillon. Ici on illustre le principe de l'expérience en étudiant un nanofil de AlN/GaN (les images connectées par des pointillés). L'image de gauche représente la localisation du Gallium et de l'Aluminium sur le nanofil déterminé par la spectroscopie EELS. Les deux images à droite sont des images filtrées et fittées pour deux énergies d'émission différentes présentes dans le spectre de gauche. L'image en haut de la figure est l'image HADF acquise en même temps que le SPIM EELS. L'image HADF acquise en même temps que le SPIM de cathodoluminescence n'est pas représentée ici.

fond clair (BF). Les deux principales spectroscopies ont été réalisées dans le microscope utilisant l'avantage de la résolution nanométrique : la CL, qui analyse la lumière émise par l'échantillon dans la gamme du visible et l'EELS qui analyse l'énergie perdue par les électrons inélastiquement diffusés. Afin de maintenir une grande résolution spatiale et spectrale on utilise la méthode du spectre image. Le faisceau d'électrons scanne l'échantillon, et pour chaque pixel un spectre d'émission (CL) ou un spectre EELS est enregistré. Pour les mesures d'EELS, les électrons inélastiquement diffusés sont dispersés en énergie grâce à un prisme magnétique et détectés par un scintillateur. Un spectre EELS peut être divisé en trois parties : un pic intense, appelé le "zero-loss" pic (ZLP) qui contient les électrons qui n'ont pas interagi avec l'échantillon de manière suffisamment significative pour être mesurés, suivi par la partie dite de faible pertes (entre 0.5 et 100 eV) et la région des pertes de cœur (entre 100 eV et plusieurs keV). Le pic "zero-loss" permet d'évaluer la proportion d'électrons qui n'ont pas interagi avec l'échantillon, ce qui permet d'estimer l'épaisseur de l'échantillon [20].

Les électrons incidents créent un champ électromagnétique qui agit à nouveau sur

l'électron, qui perd alors de l'énergie. Cette interaction sera donc visible sur le spectre EELS dans la région des faibles pertes. Ces champs électromagnétiques sont principalement les modes de plasmons de surface et de volume de la particule. Cartographier les plasmons de surface grâce aux électrons, avec EELS [29–31] ou la CL [32, 33] est très efficace et a été le point d'entrée de la microscopie électronique dans la nano-optique. L'EELS est maintenant une technique largement utilisée pour étudier les plasmons de surfaces [34, 35]. A haute énergie, dans la région des pertes de cœur du spectre EELS, des informations importantes sur la structure chimique, cristallographique ou électronique peuvent être obtenues. L'analyse du signal EEL dans la région des pertes de cœur est une technique très répandue qui permet d'obtenir des informations sur une unique colonne atomique (Figure 1). Bien que la diffusion des porteurs soit souvent de plusieurs dizaines de nanomètres, en réalisant les expériences de CL dans un STEM, on peut améliorer drastiquement la localisation de l'émission. En effet, en extrayant pour une certaine énergie le maximum de l'intensité d'émission, on peut mesurer la localisation des porteurs (Figure 1) et aussi très facilement identifier des défauts ponctuels dans les matériaux (Figure 3). Cependant, dans cette thèse, afin d'aller au delà de la simple image spectrale, dans la plupart des cas le système de CL a été couplé à une expérience d'interférence des intensités (HBT) pour enregistrer la fonction d'autocorrélation $g^{(2)}_{CL}(\tau)$ du signal de CL. Afin de réaliser des expériences d'interférence des intensités, nous avons utilisé un système très connu en optique, mais qui est encore très récent en CL [2], inspiré par l'expérience de Hanbury Brown et Twiss (HBT) [5]. Le principe est expliqué dans la figure 2. Cette expérience permet de mesurer la probabilité que deux photons émis par l'échantillon soient séparés par un certain retard τ. En normalisant par le signal non-corrélé, elle permet de remonter à la fonction d'autocorrélation du signal appelée dans la suite $g^{(2)}(\tau)$. La forme de la fonction $g^{(2)}(\tau)$ permet de distinguer les trois comportements statistiques de la lumière, le comportement et la particularité de chacun étant expliqués dans la troisième partie de ce résumé et représentés Figure 2

Afin de mesurer la $g^{(2)}_{CL}(\tau)$ du signal CL la fibre optique récoltant le signal de CL (figure 1) est connectée à l'expérience HBT au lieu du spectromètre. Pendant ma thèse, deux expériences HBT ont été construites, une dans le visible utilisant des photodiodes à avalanche τ–SPAD et une avec des détecteurs PMT (tube photomultiplicateur), détectant dans l'UV. Un des avantages principal de la CL provient de la haute énergie des électrons incidents, qui permet d'exciter aussi facilement dans l'UV et dans le visible, alors que dans les expériences de PL, il est nécessaire d'utiliser un laser hautement énergétique pour exciter les émissions UV, ce qui augmente drastiquement les problèmes d'aberrations et de collections. Afin d'étudier le couplage des plasmons avec des émetteurs et aussi de réaliser des expériences corrélées CL/PL, la méthode

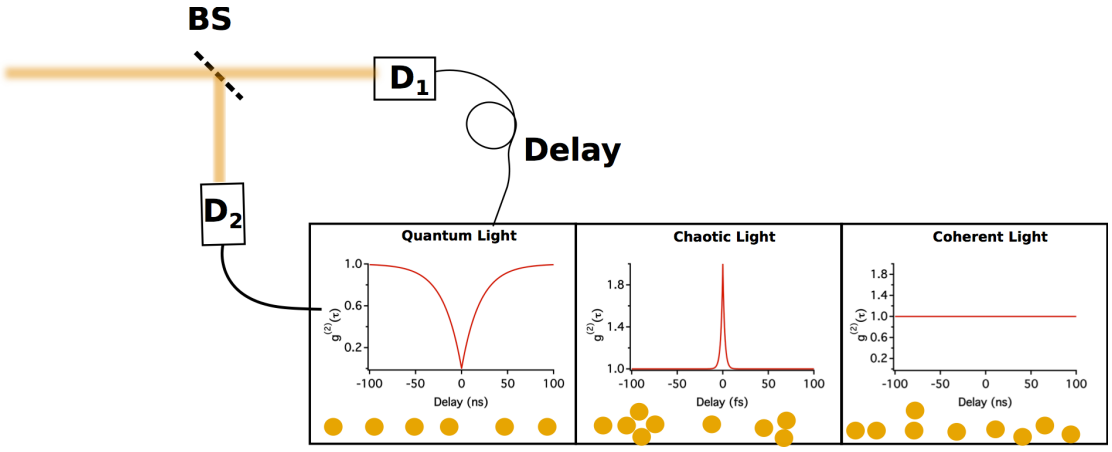

FIGURE 2: Schéma de l'expérience d'Hanbury Brown et Twiss (HBT) permettant la mesure de la fonction d'autocorrélation $g^{(2)}(\tau)$. La lumière émise est divisée par une lame séparatrice (BS). Le photon arrivant sur le premier détecteur (D1) amorce une horloge qui s'arrêtera quand un second photon sera détecté par le second détecteur (D2). Les différents retards enregistrés entre les photons sont alors répartis sur un histogramme. Cette courbe normalisée par le signal non-corrélé est la fonction $g^{(2)}(\tau)$ de la lumière émise. Sur la figure le $g^{(2)}(\tau)$ des trois sortes de lumière que l'on peut obtenir sont représentées.

de lithographie par faisceau électronique a été utilisée. La difficulté réside ici dans la finesse (15 nm) des membranes de Si3N4 où les structures ont besoin d'être dessinées. En effet, les membranes doivent être les plus fines possibles afin que les électrons incidents interagissent le moins possible avec elles. Pendant cette thèse le processus de fabrication a été amélioré pour assurer une meilleure efficacité et des structures de moins de 100 nm ont pu être réalisées. Afin de dessiner des particules métalliques en face de diamants, les méthodes de réalignement ont aussi été investiguées.

HBT dans un STEM : Caractérisation de SPE

Comme expliqué précédemment, l'expérience d'interférence des intensités permet de mesurer la fonction $g^{(2)}(\tau)$ qui donne des informations sur la statistique d'émission de la lumière. Il existe trois sortes principales de comportements statistiques [36]. Il y a tout d'abord la lumière dite cohérente, comme le laser, elle correspond à une distribution aléatoire de photons avec un $g^{(2)}(\tau) = 1$ pour tout retard τ, c'est une statistique poissonienne. La deuxième sorte est reliée à une statistique dite super-poissonienne, c'est par exemple la lumière classique ou chaotique. Une statistique super-poissonienne se traduit par une corrélation entre les photons proches les uns des autres c'est à dire que $g^{(2)}(\tau) > 1$ à faible τ. Un tel comportement est souvent appelé un comportement de regroupement. Cependant, le temps de corrélation de la lumière chaotique est de l'ordre des femto secondes et donc la fonction $g^{(2)}(\tau)$ enregistrée expérimentalement est

plate et égale à 1 (résolution > 100 ps). Le dernier comportement rencontré est lié à une statistique dite sub-poissonienne, c'est à dire super cohérente, le principal exemple étant la lumière générée par les émetteurs de photon unique. Comme les SPE ne peuvent émettre qu'un photon à la fois, il y a une probabilité nulle d'avoir deux photons en même temps sur les deux détecteurs, et donc on observe un creux à délai nul dans la fonction $g^{(2)}(0) < 1$. La présence du creux, appelée comportement d'anti-regroupement, est caractéristique de l'émission de photon unique. La première expérience d'HBT sur des émetteurs de photon unique faite avec un STEM, a été réalisé par Luiz Tizei et Mathieu Kociak [2] sur des centres NV dans le diamant. Cette expérience prouve que l'excitation par des électrons ne change pas la statistique d'émission des SPE et qu'il est possible de mesurer deux fonctions de $g^{(2)}(\tau)$ différentes entre deux points de la même particule séparés par une distance inférieur à 200 nm. De plus, le temps de vie mesuré pour le centre NV est similaire à celui mesuré en PL (20 ns), alors que dans les expériences d'électroluminescence le temps de vie mesuré est de l'ordre de 100 ns [37]. Si l'on ajoute à cela que, spectralement, la PL et la CL sont similaires, tout semble montrer que la PL et la CL ont des mécanismes d'excitations comparables. J'ai appliqué cette technique à l'étude d'un défaut dans le h-BN moins connu que le centre NV du diamant. En effet, grâce à la haute résolution spatiale du system CL-STEM, Romain Bourrelier a été capable de caractériser un défaut déjà répertorié du h-BN [26], comme produisant une émission très localisée à 4.1 eV, souvent signe d'un émetteur de photon unique. A cause de l'émission dans l'UV et le besoin de sélectionner un défaut individuel la même étude serait difficile à réaliser en PL. Comme montré sur la figure 3, nous avons fait une expérience d'HBT sur ce système et trouvé un comportement d'anti-regroupement [38]. On remarque sur la figure 3-c la présence d'une autre émission à la même énergie, appelée dans la suite "large bande" (lignes bleues sur la figure 3-c). Nous pouvons voir que cette émission est présente tout autour du défaut ponctuel sur la figure 3-b. Ce signal secondaire rend difficile toute mesure en PL-HBT car, contrairement à la CL-HBT, on ne peut pas sélectionner spatialement le défaut, et donc on ne peut pas limiter l'influence de la large bande sur la mesure de la fonction $g^{(2)}(\tau)$. Cet exemple nous permettra de discuter l'influence du faisceau d'électrons sur l'émission des défauts et d'exposer la méthode de soustraction du fond dans les expériences de HBT-CL [2].

HBT dans un STEM : L'effet de Bunching

De façon surprenante, alors que les expériences de CL et de PL des défauts uniques produisent des comportements spectraux et temporels similaires, une des plus importantes découverte de cette thèse est la mise en évidence d'une différence entre les propriétés d'émissions d'un ensemble N d'émetteurs de photon unique ($N > 1$), lorsqu'ils sont

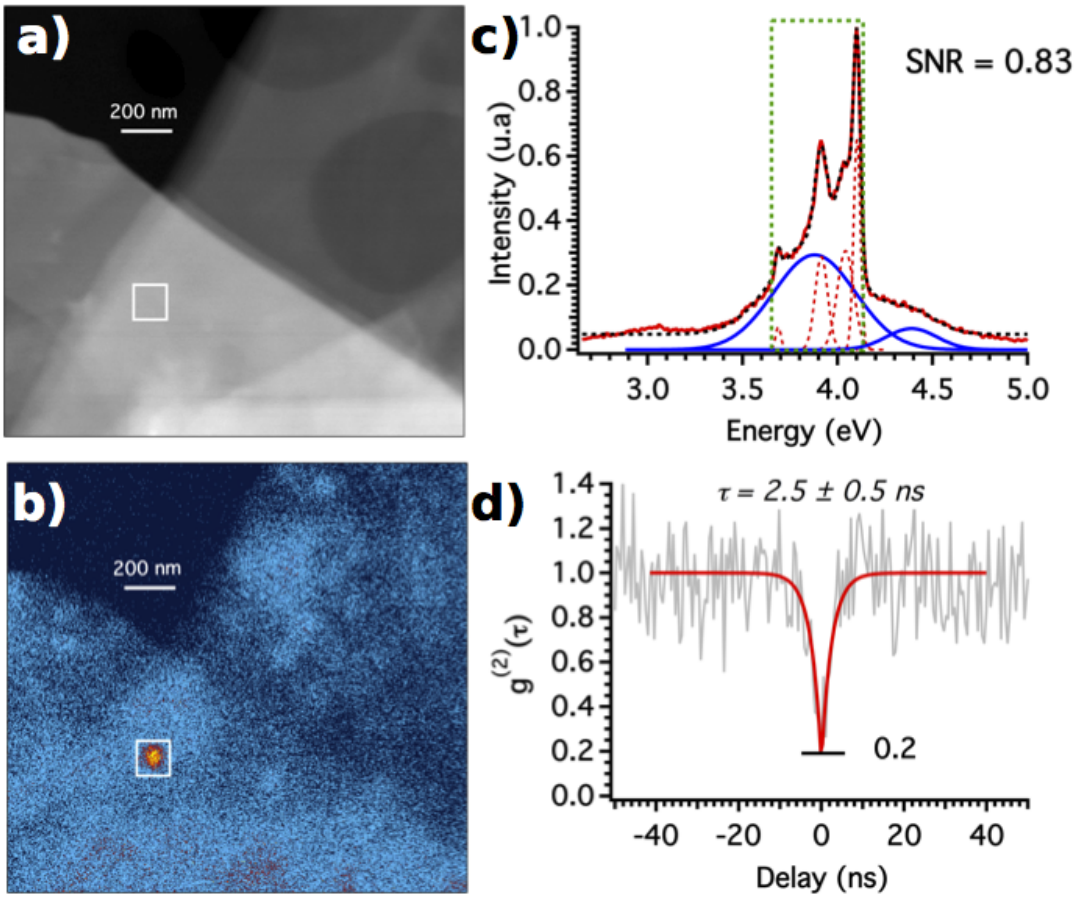

FIGURE 3: Image HADF d'une couche de h-BN a) prise en même temps que l'image du nombre de comptes enregistré sur les détecteurs à chaque pixel montré en b). Le spectre d'émission pris lorsque l'on excite dans le carré blanc est représenté en c). Le rapport signal sur bruit (SNR) représente la part dans l'intensité totale d'émission due au défaut (lignes en pointillées) comparé à l'émission de la large bande (lignes bleues). En d) on peut voir la fonction $g^{(2)}(\tau)$ enregistrée pendant que le faisceau d'électron scanne le carré blanc. Le bruit de fond a été soustrait en prenant le SNR de c).

excités par des photons ou par des électrons. Dans les expériences de PL, on peut montrer que $g^{(2)}(0) = 1 - 1/N$ avec N le nombre d'émetteurs excitables dans l'échantillon [36]. Cela signifie que dans les expériences de PL le $g^{(2)}(\tau)$ est indépendant du courant d'excitation et que $g^{(2)}(0)$ est toujours inférieur à 1. Cependant, si on effectue la même expérience en CL, le résultat obtenu est très différent. Sur la figure 4 on peut voir le résultat de l'excitation par le faisceau d'électrons d'une centaine des défauts dans l'h-BN décrit dans la partie précédente. Le $g^{(2)}(\tau)$ montre un important comportement de regroupement avec $g^{(2)}(0) > 35$ et un temps caractéristique de l'ordre de la nanoseconde [27]. De plus, ce comportement, en complète opposition avec les résultats de PL, dépend du courant d'excitation. En effet, lorsque le courant décroit le phénomène de regroupement augmente ($g^{(2)}(0)$ augmente). Cela signifie que plus les électrons incidents sont loin les uns des autres plus l'effet de regroupement est important, on en conclut donc que cet effet est provoqué par chaque électron

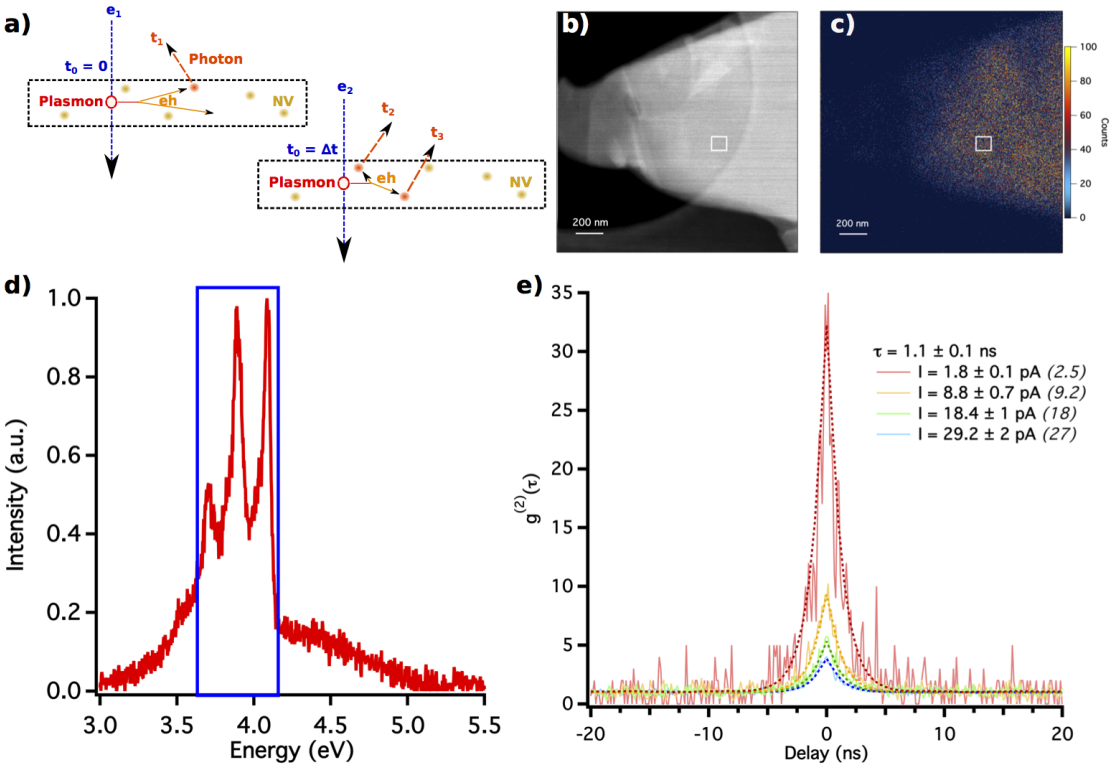

FIGURE 4: Etude de $N > 100$ défauts dans le h-BN. a) Schéma d'une chaine possible d'événements allant de l'interaction de l'électron avec l'émission de photons. b) Image d'une couche de h-BN ; c) Image CL filtrée, montrant la distribution dans l'échantillon ; d) Spectre du défaut. Le carré bleu représente le filtre utilisé dans l'expérience HBT (300-340 nm). On reconnait la "zéro phonon line" ainsi que les deux répliques de phonons à plus basse énergie ; e) Mesure du $g^{(2)}(\tau)$ pour différents courants I. Entre parenthèse, les valeurs de courant retrouvées dans les simulations Monte Carlo avec un temps de vie $\tau = 1.1$ ns.

Ce phénomène (effet de regroupement) peut être expliqué par la particularité des mécanismes de désexcitation mis en jeu lors de l'interaction électron-matière. Comme expliqué dans la section I, dans une expérience de CL, les paires électron-trou qui se recombinent radiativement proviennent de la désexcitation d'un plasmon de volume. Dans les semi-conducteurs ou les isolants, a cause de la haute énergie des plasmons de volume (15-20 eV) leur décroissance peut produire plus d'une paire électron-trou [21, 28]. Le débat est toujours ouvert sur le nombre exact mais il semblerait qu'un plasmon produit entre 1 et 10 e-h paires suivant le matériau (autour de 3 pour le diamant). Ainsi, un électron peut exciter simultanément plus qu'un centre. Il y a donc une forte probabilité que chacun de ces centres émette un photon approximativement en même temps. Donc, un électron incident peut créer un paquet de photons. Si les électrons sont loin les uns des autres, le détecteur HBT recevra des paquets de photons parfaitement séparés et distribués de façon aléatoire dans le temps (statistique poissonienne du faisceau d'électrons) mais, si le courant augmente, les électrons incidents seront plus proches les uns des autres et les paquets de photons se mélangeront jusqu'à ce que l'effet ne soit plus visible. Pour

valider cette explication heuristique j'ai construit deux modèles théoriques. Le premier utilise la méthode de Monte Carlo et simule la fonction $g^{(2)}(\tau)$ d'une particule avec un grand nombre de centres ($N > 10$). Le second, analytique, décrit la fonction $g^{(2)}(\tau)$ pour des particules minces ($L < 30$ nm) avec un faible nombre d'émetteurs ($N < 5$). Dans le premier modèle, le nombre de centres est plus grand que 5, ce qui signifie que l'on peut négliger la saturation des centres. Les simulations réalisées montrent que l'amplitude du regroupement dépend principalement du courant, de l'épaisseur de l'échantillon et du temps de vie de l'émetteur. Les deux premières quantités peuvent être mesurées expérimentalement et le temps de vie s'obtient par un simple fit exponentiel de la fonction $g^{(2)}(\tau)$. La figure 4-e montre les résultats pour une couche de BN contenant un grand nombre de centres. On peut voir que les courants expérimentaux et ceux retrouvés pour les simulations Monte Carlo sont proches. Dans mon manuscrit, j'explique en détail ce modèle, ainsi que l'influence sur le regroupement des différents paramètres et du choix du mécanisme de décroissance du plasmon de volume. Pour compléter ces simulations, j'ai construit un modèle phénoménologique prenant en compte la saturation des centres, ce qui signifie que si les centres sont déjà dans un état excité ils ne peuvent pas être excités une seconde fois avant d'avoir retrouvé leur état fondamental. Certaines approximations ont été faites pour simplifier les calculs. La principale étant de limiter le nombre maximum de plasmons par électron, ce qui signifie donc de limiter l'épaisseur de l'échantillon. Le modèle devient moins précis si l'épaisseur est supérieure au libre parcours moyen de l'électron dans le matériau. On peut montrer que, dans le cas d'un échantillon mince, la fonction $g^{(2)}(\tau)$ peut s'écrire:

$$g^{(2)}(\tau) = \frac{I_0}{I.P_{el}^1}\left(1-\frac{1}{N}\right)e^{-\tau/\tau_e} + \left(1-\frac{1}{N}e^{-\tau/\tau_e}\right) \quad (1)$$

I_0 est le courant d'électron requis pour avoir un électron par temps de vie. La première partie de la somme dans l'équation 1 décrit la corrélation produite par l'excitation des électrons qui se traduit par l'effet de regroupement. La deuxième partie, identique à l'expression du $g^{(2)}(\tau)$ en PL, décrit le comportement statistique des centres et se traduit par le comportement d'anti-regroupement. On peut clairement voir que lorsque le courant I augmente la partie qui induit un regroupement devient négligeable, la fonction $g^{(2)}(\tau)$ devient alors similaire à celle attendu en PL. Grâce à l'effet de regroupement, on comprend maintenant mieux les mécanismes de désexcitation produisant les paires électron-trou en CL. Cet effet doit être pris en compte quand on réalise des expériences d'HBT ainsi que pour la soustraction du fond. On remarque que la valeur de $g^{(2)}(0)$ est indépendante de la longueur d'onde d'excitation (réglable en choisissant le matériau), il est donc possible d'utiliser de tels signaux pour construire des sources pour les mesures

de fluorescence à deux photons [39], où l'amplitude de l'effet dépend linéairement de $g^{(2)}(0)$. Mais surtout nous allons voir dans la suite comment la mesure de la fonction $g^{(2)}(\tau)$ de CL peut aussi être utilisée pour mesurer le temps de vie des émetteurs à l'échelle du nanomètre.

Mesure du temps de vie

Même s'il a été observé et théorisé en premier sur les émetteurs de photons uniques, l'effet de regroupement apparaît dans la fonction $g^{(2)}(\tau)$ de n'importe quel émetteur. En effet, un puits quantique, par exemple, sera excité plusieurs fois par un seul électron, ce qui se traduira par l'émission d'un paquet de photons dont la largeur temporelle sera reliée à son temps de vie. Comme nous l'avons expliqué dans la section précédente, en fittant la fonction $g^{(2)}(\tau)$ expérimentale par une courbe exponentielle, on retrouve le temps de vie de l'émetteur. Donc, en combinant cette mesure et la grande résolution spatiale de la CL-STEM on est capable de mesurer le temps de vie à l'échelle du nanomètre sans avoir recours à un canon à électron pulsé. Atteindre la résolution du nanomètre pour la mesure du temps de vie est particulièrement important pour des matériaux nanostructurés. Par exemple les hetérostructures III-N comme AlN/GaN sont intéressantes à cause de leur capacité à émettre même à température ambiante et leur possible application en optoélectronique [40, 41] ou pour la fabrication les diodes électroluminescentes [42]. La figure 5 montre un exemple de mesures de temps de vie sur un nanofil AlN/GaN synthétisé par épitaxie par jet moléculaire. Les puits quantiques sont séparés les uns des autres par 15 nm. A cause des différences d'épaisseur entre les puits, la longueur d'onde d'émission ainsi que le temps de vie varient d'un puits quantique à l'autre. Comme attendu, les puits quantiques avec une plus haute énergie d'émission ont des temps de vie plus court [43]. Ce premier résultat montre comment la caractérisation complète des propriétés optiques peut être réalisée distinctement pour chaque objet confiné d'une même structure. La caractérisation est, de plus, rapide (environ une heure par nanofil), permettant la mesure d'une dizaine de nanofils en un jour, dont le SPIM de CL et l'image ADF (80 puits quantique au total). Un si large ensemble est idéal pour l'acquisition de données pertinentes statistiquement pour l'échantillon étudié (en considérant les variations entre les nanofils d'un même échantillon).

Grâce aux simulations Monte Carlo nous savons que nous mesurons le temps de vie de l'état excité de l'émetteur. Mais ce temps de vie est il similaire à celui mesuré usuellement en μ–PL ? La figure 6 montre une comparaison statistique du temps de vie de différents nanofils mesurés en PL et en CL. Pour cette expérience, un échantillon avec un unique puits quantique par nanofil a été utilisé, car il est impossible en PL de distinguer deux

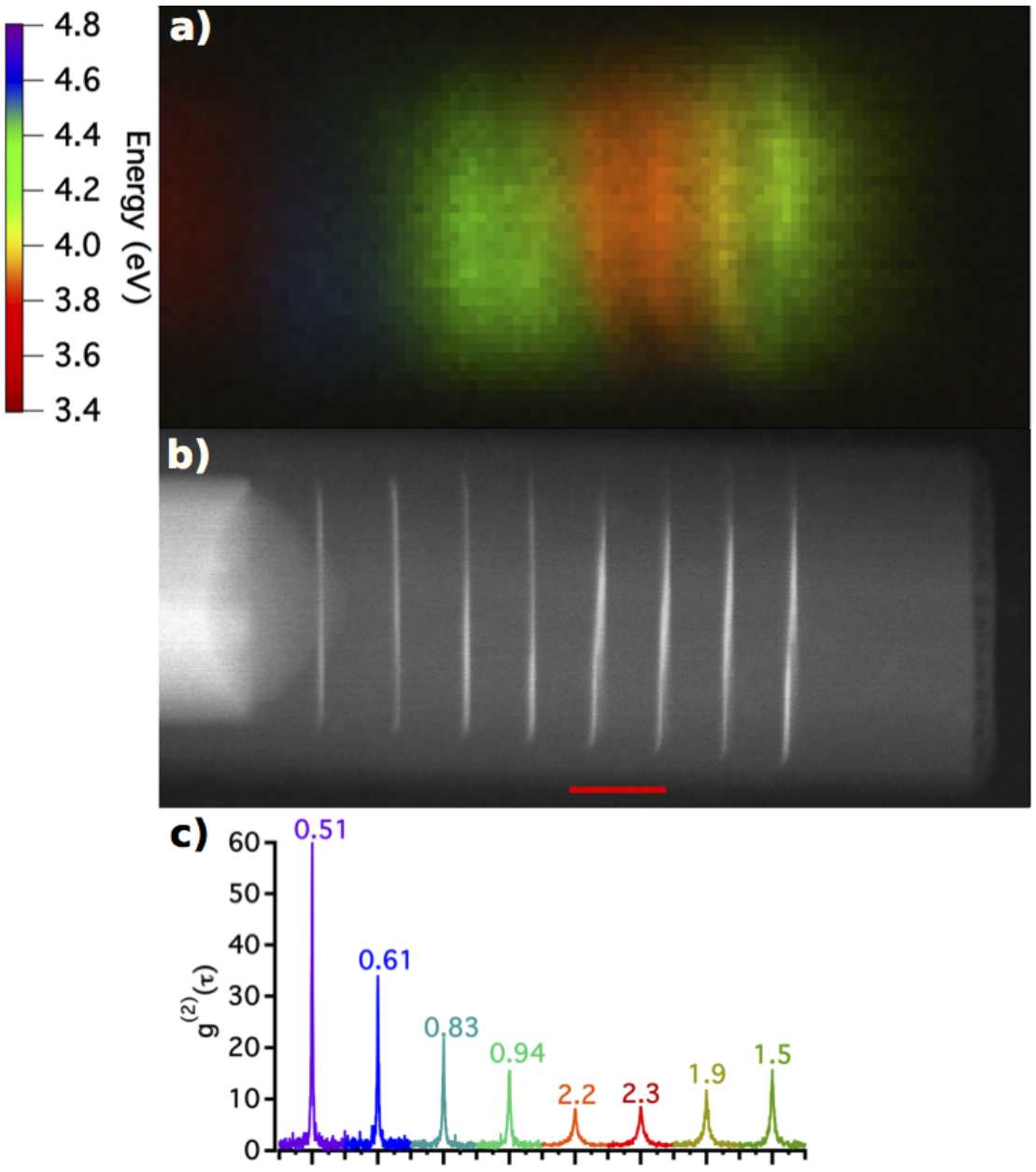

FIGURE 5: Etude typique d'un nanofil d'AlN/GaN. a- compression du spectre image dans la direction de l'énergie, avec une couleur appliquée pour chaque canal d'énergie. b- Image fond noire haute résolution (HADF) du nanofil étudié. Il a été pris après les mesures de CL dans un Ultra-STEM Nions à 200 keV. La barre d'échelle est de 20 nm. c- $g^{(2)}(\tau)$ de 8 puits quantiques mesurés séparément. Les fonctions $g^{(2)}_{CL}(\tau)$ sont représentées alignées avec les puits quantiques de l'image HADF (b) où ils ont été mesurés. Les nombres sur le haut des courbe sont les temps de vie (ns) retrouvés en utilisant un fit exponentiel pour chaque fonction $g^{(2)}_{CL}(\tau)$.

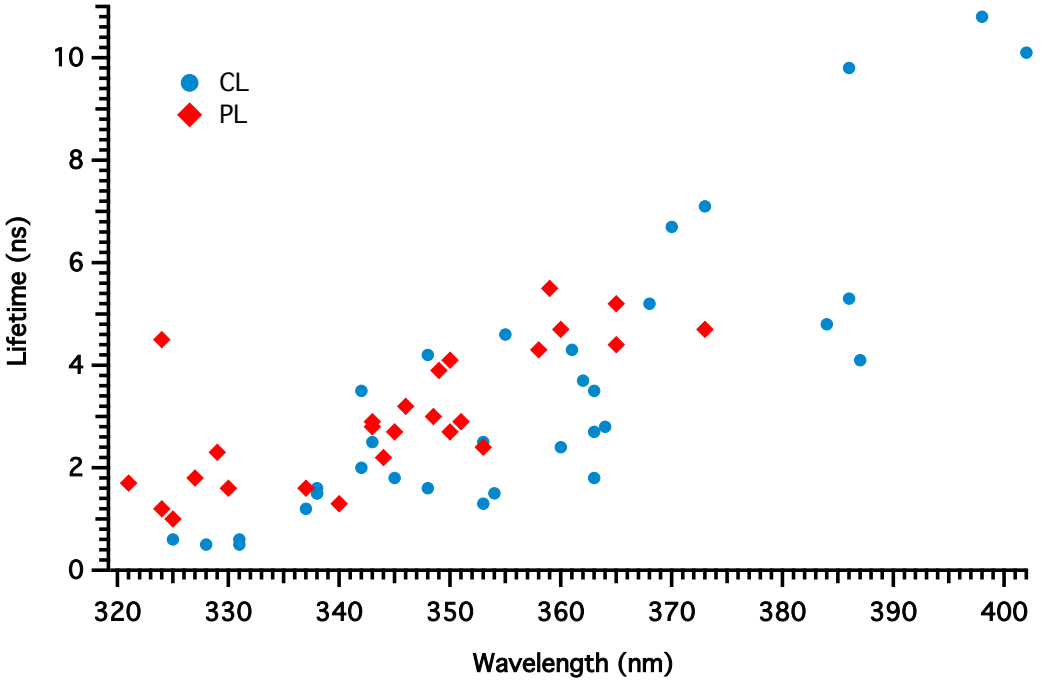

FIGURE 6: Mesures du temps de vie en CL et PL de nanofils de GaN/AlN avec une insertion par nanofil, sur le même échantillon mais sur différent fils. On peut voir que la distribution des temps de vie est similaire. Les mesures de CL permettent d'étudier les insertions avec de grandes longueurs d'onde parce qu'il est possible de séparer spatialement le signal des insertions et le signal du GaN de volume.

signaux venant de différents puits quantiques dans le même nanofil. Les temps de vie associés à des émissions au dessus de 360 nm (3.4 eV) sont difficilement mesurables en μ–PL à cause de la superposition de signal avec l'émission du GaN de volume provenant du pied du nanofil (émission sur la figure 2-b à 3.5 eV). La figure 6 montre que les distributions de temps de vie en PL et en CL sont similaires. Comme attendu, le temps de vie augmente pour une augmentation de la longueur d'émission. Ceci montre la pertinence d'utiliser la CL pour caractériser les propriétés optique des nanostructures. Cette résolution sous-longueur corrélée aux images structurelles (HADF) est essentielle pour comprendre ces matériaux, particulièrement les systèmes utilisant les nitrures. J'applique aussi cette méthode à l'étude de défauts localisés dans la matrice d'AlN et à l'effet Stark quantique confiné visible dans les puits quantiques épais.

Vers la plasmonique quantique dans un STEM

Tout au long de cette introduction nous avons montré qu'en utilisant un système de CL très efficace couplé à une expérience HBT, les premières expériences d'optique quantique dans un STEM ont été réalisées. Comme expliqué dans la section 2, les électrons rapides

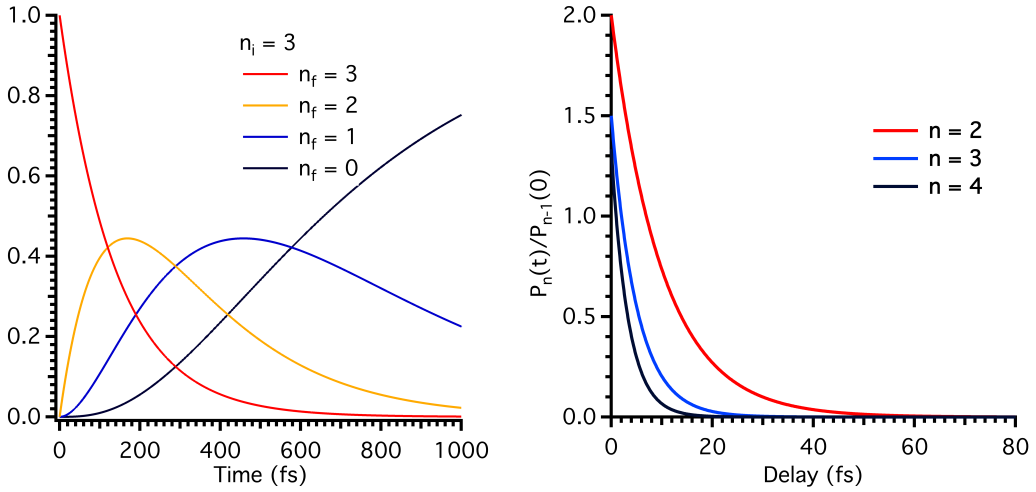

FIGURE 7: A $t = 0$ l'électron interagit avec l'échantillon et laisse le système dans l'état $|n_i\rangle\langle n_i|$. La figure de gauche représente $(\frac{\rho_{n_f\ n_f}(t)}{\rho_{n_i\ n_i}(0)})$, pour $n_f \leq n_i = 3$. La figure de droite représente $\frac{\rho_{n\ n}(t)}{\rho_{n-1\ n-1}(0)}$, qui est la probabilité d'avoir l'état $|n\rangle\langle n|$ si l'échantillon interagit avec l'échantillon à un retard Δt et si l'on sait que le système était dans l'état $|n-1\rangle\langle n-1|$ à $t = 0$. Le système évolue dans le temps à cause de la dissipation du plasmon, donnant une superposition d'état même si l'état à $t = 0$ est connu

d'un STEM sont extrêmement efficaces pour sonder les propriétés des plasmons de surface (SP) de nanostructures. La prochaine étape envisagée est donc la mesure dans un STEM des phénomènes reliés à la plasmonique quantique. Ce chapitre décrit une proposition théorique développée en collaboration avec Javier Garcia de Abajo pour mesurer le comportement bosonique des plasmons de surfaces dans un STEM, et spécialement l'effet de la dissipation sur leur propriété. Grâce à l'EELS, il est possible de détecter si un électron créait un plasmon dans le système. On peut donc calculer la probabilité pour un électron de créer un plasmon dans une nanoparticule s'il existe déjà un plasmon dans le système. En effet, si les plasmons ont une statistique bosonique alors la probabilité de créer un plasmon sera $(n+1)P_1$, mais si leur comportement est classique, la probabilité sera de P_1, avec P_1 la probabilité qu'un plasmon soit créé si il n'y a pas déjà un plasmon dans la particule. Dans ma thèse, le calcul est expliqué en détail ainsi que les possibles expériences permettant la mesure de ce phénomène.

Perspective : Couplage entre des émetteurs et des plasmons

Dans cette thèse les particularités de l'excitation par des électrons ont été mises en évidence. Elle induit l'émission de paquet de photons visible à faible courant sur la fonction d'autocorrélation $g^{(2)}(\tau)$. En effet, ce comportement se caractérise par un important effet de regroupement dans la courbe d'autocorrélation $g^{(2)}_{CL}(0) > 35$. On a montré que cet effet peut être utilisé pour mesurer le temps de vie de systèmes à l'échelle

du nanomètre, ce qui permet de caractériser complètement les propriétés optiques de matériaux nanostructurés comme les nanofils GaN/AlN. En effet il peut être appliqué à tous les nano-systèmes optiquement actifs étudiables dans un STEM. Un de ces systèmes est, par exemple, un système couplant un plasmon et un émetteur de photon unique. Ce genre de système hybride est un sujet important de l'optique et plasmonique quantique [44, 45], où la grande résolution spatiale de la CL pour les émetteurs [46] et la spectroscopie EELS pour les plasmons de surface permettent d'utiliser la complémentarité de ces deux outils pour mener des études complètes du couplage émetteur/plasmon avec une résolution sous-longueur d'onde. De plus il est bien connu que le couplage entre les émetteurs et les plasmons réduit le temps de vie des émetteurs [47, 48]. On peut donc imaginer comme prochaine étude utilisant l'effet de regroupement, l'étude du couplage entre les plasmons et les émetteurs à l'échelle du nanomètre en utilisant la mesure du temps de vie. Dans cette visée, des simulations ont été réalisées sur le couplage avec le module Matlab MNPBEM qui simule les expériences d'EELS et de CL [49, 50]. Puis nous verrons les premières étapes vers le couplage entre des émetteurs et des nanoparticules métalliques. En particulier deux expériences ont été réalisées. La première consiste à mesurer le temps de vie sur le même diamant avant et après la déposition d'une couche d'or. Comme attendu, la déposition d'une couche d'or diminue le temps de vie des émetteurs de quelques nanosecondes. La seconde expérience consiste à réaliser la mesure du temps de vie sur le même diamant avant et après avoir dessiné un nano-triangle d'or juste à côté. Cependant, le rapport signal sur bruit devra être amélioré avant d'aboutir à une solide conclusion. Afin d'avoir de meilleurs résultats, un émetteur plus brillant doit être trouvé. Cependant ces premières expériences valident la pertinence d'utiliser la mesure de temps de vie pour étudier le couplage à l'échelle du nanomètre.

...

Contents

Introduction

Light has always been a natural tool to observe the world. Indeed, our perception is mainly defined by the way our eyes and brain analyze the light that surrounds us. Electronic and vibrational transitions in matter may arise at energy similar to that of the light, and therefore properties of materials can in many cases be characterized by light measurements [3]. For a few decades, nanosciences and nanotechnologies have emerged and are progressing continuously. Their success lies in great parts in the improvement of nano-fabrication and synthesis, giving the possibility to monitor material synthesis down to the atomic layer. **Among them, some have extraordinary properties not found in the bulk, and their study led to the emergence of nano-optics** [4]. It regroups all the optical phenomena arising at the nanometer scale, as well as the techniques that improve their characterization or manipulation.

Reducing the scale of material creates confined systems. For example, quantum wells and quantum dots are nanostructures whereas electrons and holes are confined in respectively two and zero dimension(s). This confinement changes the optical properties of light: for example, quantum dots act more like atoms than solids, and they may emit only one photon at a time, emphasizing the quantum character of light. Such single photon emitters (SPE) bring quantum optics to solid state physics, seeking to design devices exploiting the quantum character of light [36]. **To characterize this kind of optically active nanostructured materials it was mandatory to design experiments working at the nanometer scale** [4]

On the other hand, one of the most famous and basic experiment of quantum optics is the Hanbury Brown and Twiss (HBT) experiment [5]. It measures the intensity time autocorrelation function of a signal, called $g^{(2)}(\tau)$. If $g^{(2)}(0) < 1$, a behavior called anti-bunching, the emitter is an SPE [6, 7].

Doing quantum optics at the nanometer scale makes sense due to the size of the observed systems. Indeed, confinement sizes are typically smaller than 10 nm [10, 11]. However, it is difficult to reach such limit, because of light diffraction [12], or without perturbing the quantum properties of the system. **Using fast electrons to observe matter is**

a way to reach sub-wavelength resolution thanks to the short wavelength of electrons [17, 51]. Cathodoluminescence (CL) consists in exciting a given emitter with fast electrons and analyzing the emitted light. The existence of a CL signal in semiconductors proves that primary excitations lead ultimately to the production of at least one e-h pair close to the energy gap which recombines radiatively. We can consider that typically 80% of gap energy e-h pairs originate from plasmon decay [20, 21]. Due to the high energy of the incoming electrons all the radiative transitions can be excited, contrary to photoluminescence where the energy of the laser can select only part of the emission spectrum. However, in both techniques, the emission is driven by electron-hole pair recombinations and therefore **PL and CL spectra are similar [22]**. We can say that CL, at first glance, is a way to do photoluminescence at the nanometer scale. CL performed in a cooled scanning transmission electron microscope (STEM), rather than in a scanning electron microscope (SEM), decreases drastically the probability of interaction per electron, leading to a better spatial resolution but also to the avoidance of non-linear optical behavior due to saturation of the emission. It is therefore a perfect tool for classical nano-optics [23].

Performing quantum optics in a CL-STEM was the logical next step. **One of the fundamental questions associated with such a goal was: how does using electrons instead of light affect the light states?** Luiz Tizei and Mathieu Kociak, who have been supervising this PhD work at the LPS, built the first HBT experiment coupled to a CL-STEM system. They measured the quantum nature [2] of the light emitted by an already well known SPE, the "nitrogen vacancy" (NV) defect in diamond [24, 25]. They proved that exciting a single SPE with electrons doesn't change its statistics (with respect to what was known in PL experiments), bringing quantum optics to the nanometer scale. My thesis consisted in continuing this work on this unique experiment of intensity interferometry coupled to a scanning transmission electron microscope. The main results and implications of this work will be exposed in the 6 following chapters.

Chapter 1: CL in an STEM: from Nano-optics to Quantum-Optics

In this first chapter, a brief reminder will be done of the knowledge necessary to apprehend quantum-optics in solids and the motivation to performing nano-optics at the nanometer scale. Then the advantages and drawbacks of using fast electrons to probe matter will be exposed, especially for the two main techniques used: cathodoluminescence and electron energy loss spectroscopy. Finally I will do an overview of the main results in CL-STEM and expose the principal materials studied during this thesis for example the NV center in diamond or III-N heterostructures.

Chapter 2: Experimental Tools

In this second chapter I will describe the different experiments used to obtain the results exposed in chapters 3, 4 and 5. Two main spectroscopies have been performed in an STEM taking advantage of the nanometer resolution: CL, that analyze sample light emission in the visible range and EELS that retrieves information from the energy lost by the inelastically scattered electrons. The starting point of nano-optics in an electron microscope was to map the surface plasmon modes thanks to EELS [29–31] or CL [32, 33], and EELS is now a widely used technique to study surface plasmons [34, 35]. On the other hand, by performing CL in an STEM, we can improve drastically the spatial localization of the emission, making it a very efficient tool to study semi-conductor materials at the nanometer scale. However, to go beyond spectral imaging, in most cases the CL system was coupled to an interferometry experiment (HBT) to record the auto-correlation function $g^{(2)}_{\mathrm{CL}}(\tau)$ of the CL signal. Two set-ups have been built and will be described in detail in this chapter, one in the visible range and another one in the UV range.

Chapter 3: SPE characterization

In this chapter, after a brief reminder of the theory behind the HBT experiment in photoluminescence, I will expose the results obtained on single photon emitters (SPE). Two SPE have been studied : *NV* center in diamond in continuity with the results already obtained by L. Tizei and M. Kociak [2] and a new SPE discovered thanks to CL. Indeed, due to the high spatial resolution of CL, it is easy to find localized emissions and therefore potential single photon emitters. It was the case with an already known defect of h-BN emitting at 4 eV [26]. Thanks to CL-STEM, Romain Bourrellier, a former PhD in the group, found that the associated emission intensity spatial distribution was spanning an area of less than 80 nm. We thus designed a second HBT experiment working in the UV range and we were able to demonstrate the SPE character of this defect for the first time. It shows that CL-STEM is therefore also suited to discover and characterize new SPEs. At the end of this chapter, one could say that PL and CL have never been so close.

Chapter 4: Photon Bunching in CL

However, in chapter 4, I will show that PL and CL are fundamentally different. Indeed, I discovered that if we excite multiple SPE at the same time some differences arises between PL and CL. At low incoming electron currents (I $\leq$ 100 pA), the second

order auto-correlation function $g^{(2)}(\tau)$ of the CL signal intensity $I(t)$ displays a large nanosecond-range peak at zero delay ($g^{(2)}(0) > 35$) (bunching), which depends on the incoming electron current. This behavior strongly departs from the PL $g^{(2)}(\tau)$ function which is flat when multiple independent SPE are excited [27]. I will describe two models built to explain this new effect, called hereafter the bunching effect, one based on Monte Carlo simulations and a second one analytical. They show that decay through bulk plasmons induces a synchronized emission of several emitters and can account for this current intensity dependent bunching effect, revealing a true difference with PL and emphasizing the forgotten role of bulk plasmon in CL mechanisms [21, 28].

Chapter 5: Lifetime Measurement

In this chapter, we expand the HBT-CL experiment to other systems than SPE. Indeed even if it has been at first observed and theorized for SPEs, the bunching effect will also be present for any emitter. Indeed, an emitter, like a quantum well, will be excited multiple times by a single electron and will emit a bunch of photons on a time window close to its radiative lifetime. As it will be proved in chapter 4, by simply fitting the experimental curve of the $g^{(2)}(\tau)$ function by an exponential we can retrieve the lifetime of the emitter. Thus we can combine this effect with the high spatial resolution of CL-STEM to measure lifetimes at the nanometer scale without a pulsed electron gun. Reaching the nanometer scale for lifetime measurement is particularly important for nanostructured material. For example III-nitride heterostructures like AlN/GaN are of great interest for their emission at room temperature and their application in optoelectronics [40, 41] and more generally GaN structures are interesting for light emitting diode device [42]. We will compare our result to the lifetime obtained in time resolved μ-PL and show that the quantities are similar. Therefore this new technique allowed to reach sub-wavelength resolution for lifetime measurements, bringing CL to the level of a comprehensive tool for nano-optics measurement. This sub-wavelength resolution correlated to structural images (HADF) is essential to understand nanostructured materials, especially nitride based devices. I will also apply this method to study localized defects in AlN matrix and the Quantum Confined Stark Effect on thin quantum wells.

Chapter 6: Quantum non-linearities in EELS

In the last three chapters we have seen that thanks to a very efficient CL system coupled to an HBT experiment, the first step towards quantum-optics in STEM has been taken. As mentioned before, the fast electrons of an STEM are extremely efficient to probe surface plasmons (SP) properties of nano-structures. Therefore the next logical step

will be quantum plasmonic measurements in STEM. This chapter describes a theoretical proposal developed in collaboration with Javier Garcia de Abajo to directly measure the bosonic behavior of surface plasmons in an STEM, and especially the effect of damping on their properties. Thanks to EELS, it is possible to detect if an electron creates a plasmon in the system. We can therefore calculate the probability for an electron to create a plasmon on a nano-particle if there are already n plasmons in the system. If plasmons have a bosonic statistic then the probability will be $(n+1)P_1$, but if they are completely classical, the probability will be P_1, with P_1 the probability that a plasmon is created when there is no plasmon on the particle. In the manuscript, the calculation will be explained in details as well as the experimental possibilities for such single plasmon detection.

⋆ ⋆ ⋆

Chapter 1

CL in an STEM: from Nano-optics to Quantum-Optics

> We have come a long way, we have a long way to go. In between we are somewhere
>
> *Kim Stanley Robinson*

1.1 Quantum Optics at the Nanometer Scale

Matter and light have always been intimately connected. Matter, depending on its properties, absorbs and reflects light at different energies. Therefore, using light to understand and characterize matter is natural. For decades, different techniques have been used to study light emission of solids, each having their advantages and drawbacks. In this thesis I used a scanning transmission electron microscope (STEM) to study the optical emission of matter when excited with fast electrons, through the use of cathodoluminescence (CL) spectroscopy, allowing to reach sub-wavelength resolution. More particularly my goal was to study the statistics of CL emission, the main objective behind it being to study quantum optical properties at the relevant scale ($\approx$ 1 nm). In this chapter I will first introduce my motivations, then I will explain the advantages and drawbacks of using fast electrons and finally I will expose the main results already obtained before this thesis with CL in an STEM.

1.1.1 Luminescence in Solids: from optics to nano-optics

Solid: band structure and optical properties

Solids, because of atoms strong proximity, have their outer orbitals overlapping and interacting strongly. Due to this interaction, valence electrons are usually delocalized, creating a continuum of energy instead of discrete levels found in atoms. We call valence band the last band filled with electrons, and conduction band the first empty band in semi-conductors. The smallest difference of energy separating these two bands is called the gap energy E_g. In addition to broad bands, it is possible, due to impurities or defects in the crystal periodicity, to find discrete levels in the gap of the material. If a level is close to the conduction band it is called a donor level E_d, if it is close to the valence band it is called an acceptor level E_a (see figure 1.1).

An excitation of energy $\hbar\omega \gg E_g$ will lead to the transition of electrons from the valence band to an empty band leaving an empty state in the valence band. The pseudo-particle composed of a hole in the valence band and of an excited electron in an empty band is called an "electron-hole" pair (eh pair). If the two entities are connected by coulombic interaction, a bound eh, called an exciton, is formed. Once excited, there are different possibilities for a solid to retrieve its equilibrium state through the recombination of the eh pairs, two of them being by the emission of light (photons) or by the coupling with the vibrational modes of the crystal (phonons). The optical properties will depend on the energy absorbed from the incident beam, the transfer of that energy to the emission center and the conversion efficiency of this energy into photons, compared to phonons for example. The way the solid is excited may also influence the luminescence. Different forms of excitation exist, for example: photoluminescence (PL) for light excitation [4], cathodoluminescence (CL) [18] for electron excitation, and electroluminescence (EL) if the excitation energy comes from the injection of electrons and holes from electrical contacts [52]. PL and CL create in most cases free electron-hole pairs. In the case of photoluminescence, we can tune the excitation wavelength to excite at the absorption energy of the luminescence, it is called a resonant excitation. One of the main advantages, in the case of emitters like two levels systems, is to increase the coherence of the emitted photons [53]. However in most cases $\hbar\omega \gg E_g$. In cathodoluminescence, the energy transfer mechanism imposes non-resonant excitation. The differences and similarities between CL and PL will be investigated in details in this thesis.

There are two kinds of transition in solids, intrinsic and extrinsic.

Intrinsic emission comes from the intrinsic properties of the material. For example, it can be the transition at the gap energy, characterized by the excitonic gap state. This

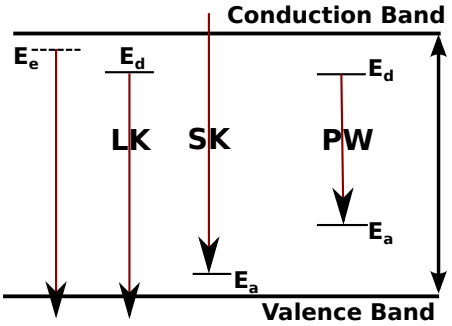

FIGURE 1.1: Different radiative transitions for energy relaxation after a non-resonant excitation. E_e represents the excitonic level, E_d the donor level and E_a the acceptor level. The Lamb-Kick (LK) model, the Schön-Klasen (SK) model and the Peer-Williams (PW) model are represented.

state is due to the coulombic interaction of the eh pair that brings the two energy levels closer together than the gap energy E_g. It is the exciton state of the material and it is close to E_g. For example hexagonal Boron Nitride (h-BN) is well known for its intense exciton luminescence at 5.8 eV [54, 55]. In quantum well, excitonic states also exist but are not quite visible at nitrogen temperature. In the following we will therefore omit exciton in quantum well and talk more generally of the density of state and its changes due to confinement.

Extrinsic emission, on the other hand, comes from impurities in the material, such as the Nitrogen Vacancy (NV) defects in diamond [56]. Different extrinsic transitions are possible: the Lambe-Klick model which corresponds to a donor free-hole transition [57], the Schön-Klasen model which corresponds to the recombination of a free electron and an acceptor level [58] and Peer-Williams model which corresponds to the donor-acceptor transition [59]. Figure 1.1 summarizes the different transitions.

The relaxation of excitation via phonons is particularly important in the case of impurities excitation. Indeed, phonons are quasi-particles associated with the vibration of the crystal lattice. These vibrations can be seen as a superposition of harmonic oscillators. The transition from one vibrational level to the next correspond to an exact amount of energy $\hbar\omega$ linked to the emission or absorption of one phonon. The emission of a phonon from a vibrational energy level of the conduction band (v') to one of the valence band (v) is ruled by the Franck-Condon principle [60], that evaluates the intensity of vibronic transition ($v' \rightarrow v$). It states that the probability of transition from one vibrational level to another increases if the two vibrational wave functions overlap significantly. The principle is reproduced in figure 1.2. Therefore an impurity emission is likely to have several secondary transitions in addition to the transition without phonon ($v = 0 \rightarrow v' = 0$), the so called "Zero-phonon line" (ZPL). This is the case, for example, for the NV center in nanodiamond that will be explained in details in section 1.3.

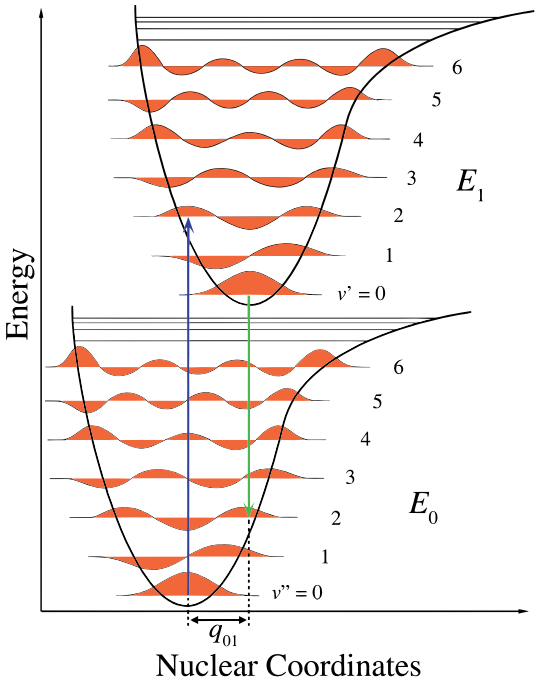

FIGURE 1.2: Franck-Condon principle energy diagram. Since electronic transitions are very fast compared to nuclear motions, transition between vibrational levels are favored when they correspond to a minimal change in the nuclear coordinates. The potential wells are shown favoring transitions between $v = 0$ and $v = 2$. From [61]

Optical Properties of Nanostructures: Nano-Optics

Thanks to the improvement in nano-fabrication and growth technologies that allows designing materials down to the atomic layer, we can drastically change the properties of materials compared to their bulk form. It is possible to confine charge carriers (eh pairs) into 1, 2 or 3 dimensions. In fact, quantum physics predicts a discretization of the energy if the spatial dimension is less than the De Broglie wavelength $\lambda_B = \frac{2\pi\hbar}{\sqrt{2m_e^* k_B T}}$, where m_e^* is the effective mass of the electron, k_B the Boltzmann constant and T the temperature. If there is confinement in 0, 1, 2 or 3 dimensions of space the density of states $\rho(E)$ will not be the same, for example :

- If there is no confinement (bulk material) : $\rho(E) = \sqrt{E - E_g}$
- If there is confinement in 1 dimension (quantum well) : $\rho(E) = \sum_i H(E - E_i)$
- If there is confinement in 3 dimensions (quantum dot) : $\rho(E) = \sum_i \delta(E - E_i)$

With H the Heaviside step function and δ the Dirac delta function. In this thesis we study mainly quantum wells and quantum dots. Quantum wells have well defined transition energies E_i, and therefore well defined peaks of emission, but with a continuous density of states, which means that a large number of carriers can recombine at the

same energy. Energies E_i are determined by the dimension of the quantum well and the materials used. Thanks to nano-fabrication we can design nano-structured materials with the right absorption and emission properties. We can cite for example light emitting diodes (LED) [42] that use GaN nano-structured materials and revolutionized the world of lighting. To study such confined structures it is essential to probe them at the nanometer scale, to understand the correlation between structure and emission, and therefore improve material design.

In the case of quantum dots, the density of states is a sum of discrete states, at well defined energies. Their density of states is similar to the one of atoms. Thus quantum dots might be considered in first approximation as a two level system. Other solid systems acting like atoms are donor-acceptor impurities, for example the already mentioned NV centers in diamond. As for atoms, it is impossible to have two electron-hole pairs on the same level at the same time. Therefore, this kind of systems emits only one photon at a time. For this reason, they are called single photon emitters (SPE). With SPE, it becomes possible to study the quantum character of light in solid systems at room temperature. This is the beginning of quantum optics in solids at room temperature. But before going into quantum optics in solids and especially at the nanometer scale, an introduction of the basics of quantum optics is needed.

1.1.2 Quantum-Optics

It is well known that physics is acting differently at the atomic and macroscopic levels, which are ruled respectively by quantum and classical physics. Quantum physics is very difficult to apprehend due to the scale at which it appears and its sensitivity to perturbation. Founders of quantum physics have imagined about 100 years ago a series of experiments [62–64] that would prove its existence and test its strangest properties like particle entanglement and state superposition [65]. Photons, particles associated with the electromagnetic field, interact weakly with their environment because of their absence of charge and mass, and therefore they are ideal candidates to probe quantum physics. Quantum optics encompasses all the optical phenomena that can only be explained with quantum physics. Quantum optics was mainly studied for a long time with cold atom as single photon source. Indeed, S. Haroche was rewarded with the Nobel prize in physics in 2012 *"for ground-breaking experimental methods that enable measuring and manipulation of individual quantum systems"*, where he used trapped photons in cavities to study state superposition and entanglement [66, 67]. These experiments were performed at the same time on ions by D. Wineland who was also rewarded with the Nobel prize in physics [68]. Another example in the field of quantum optics, is the

experimental demonstration of the violation of Bell's inequality [64] that was demonstrated by A. Aspect et al [69–71] proving that there are no hidden variables in quantum physics, inspired by the EPR paradox [72].

Proving quantum physics rightness justifies all by itself these different experiments. However, manipulating single particles and using quantum physics also open the way to possible applications, for example in quantum computing [73, 74] and quantum cryptography [75]. We can for example mention the Linear Optical Quantum Computation (LOQC) approach that relies only on the use of single photon sources and linear optical elements [76]. Single atoms, as SPE, are difficult to integrate in electronic devices in perspective applications. It is thus imperative to find a way to master solid single photon emitters like point defects in bulk materials or quantum dots presented before. However, solid single photon sources are not trivial to use and not systematically obtained. For example, it is mandatory to make sure that only one point defect is probed at a time or that quantum dots are designed well enough to be single photon sources at the temperature of the experiment. One of the basic experiments of quantum optics permitting to characterize without a doubt the single photon source nature is the Hanbury Brown and Twiss (HBT) experiment [5, 77].

It is an interferometry experiment that measures the intensity autocorrelation function $g^{(2)}(\tau)$ ($g^{(2)}(\tau) = < I(t)I(t+\tau) > / < I(t) >^2$), i.e the probability that one photon is detected at time t_0 and that a second one is measured at time $t_0 + \tau$. If there is only one photon at a time emitted by the sample, the probability to measure two photons at the same time is zero ($g^{(2)}(0) = 0$). We will see in chapter 3 the different forms of $g^{(2)}(\tau)$ depending on the statistics of the emitted light and especially that $g^{(2)}(0) < 1$ is only possible for quantum states of light, therefore characterizing without any doubt the SPE character of the emitter [36].

Another experiment worth mentioning, even if it will not be used in this thesis, is the Hung Ou Mandel experiment that allowed to test the indistinguishability of photons [8, 36]. Two photons are sent at the same time on a beam splitter. If the two photons are indistinguishable they will always go on the same side of the beam splitter. Whereas if there are not, they will have a 50% probability to each side.

With these two experiments we are able to fully characterize single photon sources. For more than a decade now, quantum dots have been demonstrated to be single photon emitters [6, 7, 9], as points defects like NV centers in diamond [78, 79]. Solid SPE are even used to build quantum cryptographic devices for example with quantum dots [80] or diamond [81]. However, even if it does not seems essential in order to design single

photon sources, the fact that we are not able to optically investigate all these nano-structures at the nanometer scale makes it harder to improve design and discover new SPEs, for example new point defects in materials.

It was therefore imperative to bring nano-optics to quantum optics. In the next section different possibilities to do nano-optics will be presented, as well as their potential to perform quantum optics.

1.1.3 Different Techniques used in Nano-Optics

SNOM

A popular technique to probe samples at the nanometer scale is the scanning near field optical microscopy (SNOM) [82, 83]. Mainly two kinds of SNOM exist. The first one uses a small aperture of diameter d that is put very close to the sample. Therefore the maximum resolution Δx is not limited by the Rayleigh criterium ($\Delta x > 0.61\lambda/nsin\theta$) and therefore by λ, but by the aperture diameter d. However due to the low light throughput and limitation of the size of d the resolution can hardly go below 50 nm, which is already a huge step towards nano-optics. To go further, a second kind of SNOM was developed, called the apertureless SNOM [84]. In this case, the sample is excited by a laser and a sharp probe, usually metallic, enhances locally the near-field by transforming non-propagating modes into propagating modes able to couple with the far-field. One can retrieve the local signal by distinguishing between the enhanced signal and the rest of the emitted light coming from the sample. This technique allowed to reach resolutions of about 20 nm [85, 86]. However it takes a huge scattering effect to obtain a good signal to background ratio, that depends mainly on the dielectric constant of the sample, electromagnetic properties of the probe and the sample preparation that needs to be perfectly flat to avoid distance effects [87]. The difficulties to understand the signal recorded render very difficult the study of complex optically active heterostructures and non flat samples like nanowires.

STED

In 2014, Stephen Hell received the nobel prize in chemistry "*for the development of super-resolved fluorescence microscopy*", the stimulated emission depletion (STED) [13, 88] that allows to reach with far field optical spectroscopy less than 10 nm resolution [89, 90]. The principle is in fact simple, the sample is excited with a laser beam synchronized with a donut-shape laser beam [14], the second one depletes emitters fluorescence everywhere but at the center of the donut. The emission comes only from this region. The resolution

depends on the intensity and the quality of the donut-shape, but no physical effect limits the resolution, making it a very promising techniques for imaging samples at the nanometer scale. It is a non-destructive microscopy with very simple data analysis. It is therefore very well suited for biological imaging and in vivo experiment [91].

However these two techniques have been rarely used for quantum measurements. One can note the study of spin conservation of the NV center in diamond with STED [15] and the conservation of SPE characteristic of diamond with SNOM [92]. We can add that the emission mechanisms for these two microscopies are far from photoluminescence mechanism because of stimulated depletion for STED and enhancement scattering for SNOM.

Cathodoluminescence in that sense seems to be a very well suited technique to perform nano-optics and even quantum nano-optics. In this thesis CL in an STEM is chosen to do quantum optics at the nanometer scale. The two main advantages being the proximity with PL and the acquisition at the same time of structural and morphological information with an atomic resolution (see chapter 2). HADF images give for example chemical and thickness contrasts with a nanometer resolution (see for example figures 1.5-a and 1.7). In the next section, I will explain in details the electron-matter interaction and describe briefly the two main spectroscopies used in this thesis, electron energy loss spectroscopy (EELS) and cathodoluminescence (CL).

1.2 Using Fast Electrons to Probe Matter

1.2.1 Electron-Matter Interaction

Interaction of fast electrons with matter is a broad and complex topic. This complexity arises from the electron high energy and its large interaction cross section with various scattering mechanisms, leading to energy transfer into different material excitations. Inelastic collisions at high energy, compared to optical excitation, for example, give rise to secondary electron (SE) essential for imaging in a scanning electron microscope (SEM). Some of those interactions generate Auger electrons (AE) or X-ray radiation which can be used to retrieve chemical information. In semiconductors, inelastic scattering mainly gives rise to hot carriers like high energy electron-hole pairs (HE e-h) [16] and bulk plasmons [19, 29]. HE e-h and plasmons are intimately connected, one being able to transform into the other [20].

However, in a scanning transmission electron microscope (STEM), thanks to the high energy of the incoming electrons and small sample thickness, the interaction with the

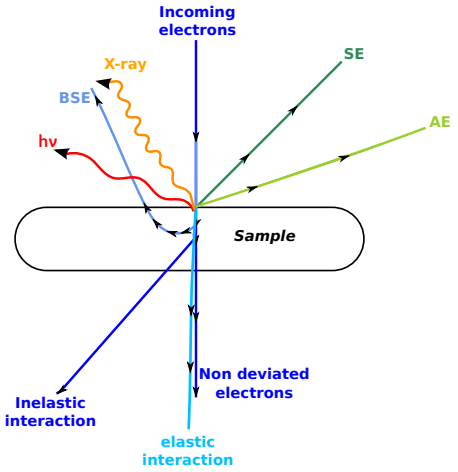

FIGURE 1.3: Different interactions between an electron and a sample. AE : Auger electrons, BSE : Backscattered electrons

sample is reduced to its minimum. We can define the interaction pear as the volume where incoming electrons are spread into the material due to collisions and diffusion. In the case of a thick sample most of the electrons are not transmitted. In an STEM the thinness of the samples (less than 200 nm) and incoming electron energy (typically more than 60 keV) reduce drastically the interaction pear as well as the backscattered electrons, leading to an improved spatial resolution. Nevertheless, the question of radiation damage is still important. Three main effects have to be taken into account. The first one, called knock-on, is due to the elastic interaction between the incoming electron and the sample. At high incoming electron energy, the energy transmitted to the material can lead to atomic displacements. This effect increases with incoming electron energy, however below 100 keV the effect can be neglected in some cases [93]. The second one is heating due to inelastic scattering, collisions between incoming electron and atoms leading to a certain amount of energy transfer that will eventually transform into heat. It can be evacuated pretty easily, even for bad conduction material and therefore can be neglected if the sample is thin with incoming electron energy above 40 keV and an excitation current less than 100 pA [93], which is the case in a typical STEM. This is different from the SEM situation. The last effect is atomic displacement due to inelastic scattering, called radiolysis, which can be reduced by cooling the sample [93]. Therefore by using a cooled sample stage in an STEM with incoming electron energy between 40 and 100 keV we reduce significantly damages produced by electrons and the number of interactions between the electron beam and the sample, allowing for the study of single excitation processes.

I have used two kind of STEM spectroscopies: cathodoluminescence and electron energy loss spectroscopy (EELS). I will present the principle of EELS and CL in the following.

As it is the main spectroscopy used during this thesis, CL will be discussed with more details in section 1.3.

1.2.2 Electron-Energy Loss Spectroscopy: EELS

In a transmission electron microscope, it might be worth analyzing the transmitted electrons, as the energy losses of transmitted electrons provide numerous informations about the sample. An EELS spectrum, like the one shown in figure 4.18, is traditionally separated in two regions, the valence region (or low-loss) and the core loss region. The limits between the two can be arbitrary put at 50 eV. The core loss region corresponds to energy losses larger than 50 eV. In this case, losses are due to interaction of the electron with the core electrons, giving insight in chemical composition, the crystallographic environment and the valence of atoms. In this thesis, core-loss EELS spectroscopy has been performed only a few times and will therefore not be explained in detail but complementary information can be found in [94].

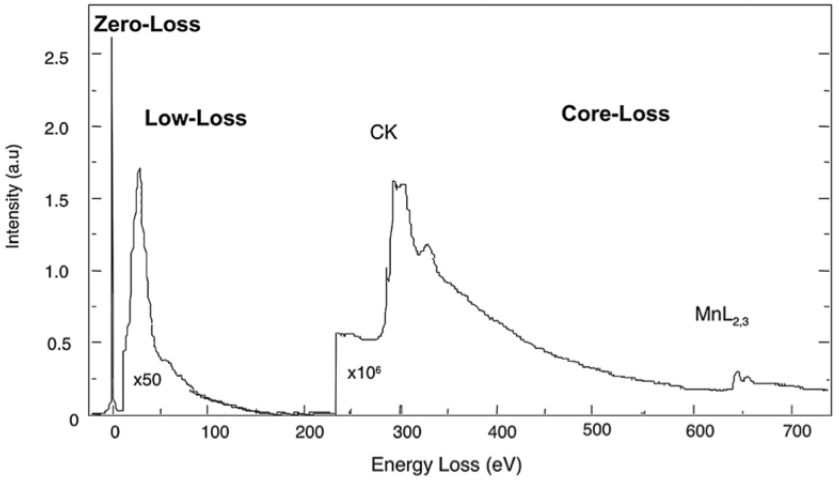

FIGURE 1.4: Typical EELS spectrum (carbon nanotube filled with manganese). The signal of the low-loss region is much more intense than the core loss part, showing that the major part of interactions between electron and matter are valence losses which means surface and bulk plasmons. From [95]

The incoming electrons can create an electromagnetic field inside a metallic nanostructure that acts back on the electron, inducing losses below 50 eV. These electromagnetic fields are mainly due to the bulk and the surface plasmon modes of the metallic nanostructure. Bulk and surface plasmons are connected to the optical properties of the material [29, 96]. Losses due to the bulk plasmons are directly connected to the dielectric function ϵ of the material [97]. One can show [29] that $\Gamma_{\text{bulk}}^{\text{NR}}$, the probability for an electron to lose energy $\hbar\omega$ through bulk plasmon in the non-retarded approximation, is given by equation 1.1 with L the sample thickness, q_c a cutoff wave vector and

respectively e and ν the charge and the speed of the incoming electron.

$$\Gamma_{\text{bulk}}^{\text{NR}} = \frac{2e^2 L}{\pi\hbar\nu^2}\Im\left[\frac{-1}{\epsilon}\right]\ln\left(\frac{q_c\nu}{\omega}\right) \tag{1.1}$$

The surface plasmon modes appear at the interface between a dielectric medium (1) $\Re[\epsilon_1] > 0$ and a metal (2) $\Re[\epsilon_2] < 0$. They are collective modes of conduction electrons and can be seen as oscillations of the electromagnetic field at the surface of the metallic nanostructure. They have been first observed in EELS by Watanabe in 1956 [98]. However, at that time, the energy resolution of EELS spectra did not allow to detect losses of less than 3 eV [99, 100]. Data processing techniques like the deconvolution methods [101] allowed to reach smaller energy losses [30, 31] and now the new generation of monochromated electron microscopes improves the nominal resolution from 100 meV to 10 meV allowing plasmon detection of energy less than 150 meV [102].

The surface plasmon modes are intimately connected to the shape and size of the metallic nanostructure, and are characterized by charge distribution at defined energies. The electromagnetic local density of state (EMLDOS) describes in terms of modes the spatial and spectral variation of the electromagnetic field. In the following we will overview the key theoretical points in the quasi-static (QS) approximation that connect an EELS spectrum to the EMLDOS. A much thorough description can be found elsewhere [95, 103, 104].

Surface plasmons modes are solutions of the Maxwell equations. However in the QS approximation we only need the Poisson equation (equation 1.2) and the boundary conditions (equation 1.3) to describe them :

$$\nabla.\epsilon\left(\vec{r},\omega\right)\nabla\phi\left(\vec{r},\omega\right) = 0 \tag{1.2}$$

$$\vec{D}_1.\vec{n} = \vec{D}_2.\vec{n} \tag{1.3}$$

It can be shown [105] that equation 1.2 and 1.3 can be arranged as a self consistent equation for the surface charges. The solution of this equation is a set $\{i\}$ of charge distribution eigenvectors $\sigma_i(\vec{r})$ associated with eigenvalues Λ_i defined in equation 4.5. Thanks to this mode, we can also find the eigen-potential $\phi_i(\vec{r})$ and eigen-electric fields $\vec{E}_i(\vec{r})$.

$$\Lambda\left(\omega_i\right) = \frac{1+\epsilon\left(\omega_i\right)}{1-\epsilon\left(\omega_i\right)} = \Lambda_i \tag{1.4}$$

We can define the vectorial EMLDOS along an arbitrary $\vec{z}$ direction as in equation 1.5.

$$\rho_z(\vec{r},\omega) = \frac{1}{2\pi^2\omega}\sum_i \Im\left(f_i(\omega)\right)|\vec{E}_i(\vec{r})|^2 \quad (1.5)$$

$$f_i(\omega) = \frac{\lambda_i+1}{\lambda_i-\lambda(\omega)} \quad (1.6)$$

One can show [106, 107] that the loss probability in EELS can be writen in terms of modes as in equation 1.7, where $\tilde{\phi}_i(\vec{R}_\perp,\omega/\nu)$ is the Fourier transform along the path direction $\vec{z}$ at point $\vec{R}_\perp$, the point coordinate in the plane ($\vec{x}$,$\vec{y}$) perpendicular to $\vec{z}$, and at point $q_z=\omega/\nu$ in the reciprocal space. It can be transformed in the QS approximation to equation 1.8.

$$\Gamma_{EELS}(\vec{R}_\perp,\omega) = \frac{e^2}{\pi\hbar\nu^2}\sum_i \Im\left(f_i(\omega)\right)|\tilde{\phi}_i(\vec{R}_\perp,\frac{\omega}{\nu}^2)| \quad (1.7)$$

$$\Gamma_{EELS}(\vec{R}_\perp,\omega) = \frac{e^2}{\pi\hbar\omega^2}\sum_i \Im\left(f_i(\omega)\right)|\tilde{E}_i^z(\vec{R}_\perp,\frac{\omega}{\nu}^2)| \quad (1.8)$$

One can see in equation 1.8 that EELS is close to the projection along the direction of the incoming electron (z) of the EMLDOS (z-EMLDOS) (equation 1.5) in the QS approximation, within a Fourier transform along the z axis and an ω factor. This Fourier transform will lead to non-trivial differences between the two quantities. However, eigenvalues, eigen-modes and hot-spots positions will be similar. Even in the retarded regime the relation between EELS and EMLDOS still holds, although a modal decomposition cannot be easily found. We can therefore in first approximation say that EELS is representative of the z-EMLDOS. This means that by acquiring, in each point of the nanostructure, an EELS spectrum we can map the z-EMLDOS at certain energies. An example is shown in figure 1.5 for silver lithographic nano triangles. The first mapping of nano particles was done simultaneously by Nelayah et al [30] on nano-prisms and Bosman et al [31] on rods and spheres. Moreover, relative to optical measurements, Losquin et al [108] proved recently that EELS is linked to optical extinction. In chapter 6, I will present a theoretical idea, developed in collaboration with J. Garcia de Abajo, using EELS spectroscopy to realize quantum plasmonics measurement.

1.2.3 Cathodoluminescence Spectroscopy

Cathodoluminescence signal of metallic materials and of semiconductors originate from two different kinds of excitations. In metallic particles the CL signal is due to the coupling of plasmons modes with the far-field (see section 1.3.1). In semiconductors, decay mechanisms are far more complicated. Since one of the main contributions of

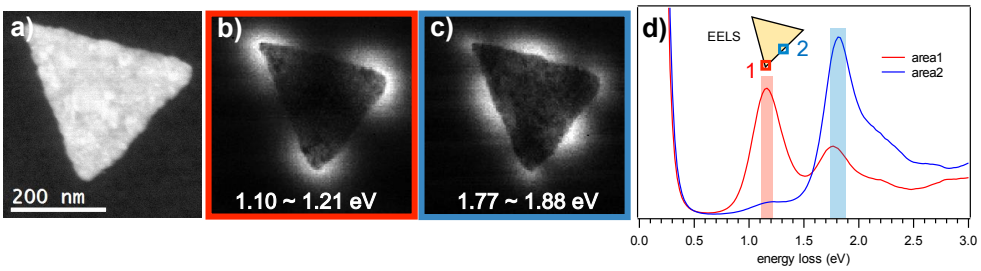

FIGURE 1.5: Example of surface plasmon mapping in EELS for the two first modes (dipolar and quadrupolar modes). The experiment and analysis were performed by Naohiko Kawasaki at the LPS [109] on lithographic silver nano-triangles I designed and fabricated (see chapter 2). a) HADF image, the nano triangle is 360 nm long, b) and c) respectively the dipolar and quadrupolar modes (after deconvolution) of the EELS spectrum. d) Spectra after deconvolution taken respectively at a corner (point 1 of the insert) and on the side (point 2 of the insert).

this thesis will be to explain some differences between PL and CL (see chapter 4), understanding decay mechanisms in semi-conductors is essential.

The existence of a CL signal in semi-conductors proves that primary excitations created upon electron irradiation lead ultimately to the production of at least one e-h close to the energy gap which recombines radiatively [110]. CL detects radiations due to transitions between the conduction and valence bands and also levels lying in the gap of the material. It implies a lot of different signals and, therefore, contrary to X-ray radiation, no general emission rule can be applied to characterize the emission energy. Due to the high energy of incoming electrons all the radiative transitions can be excited, contrary to photoluminescence where tuning the energy of the laser helps to monitor the emission spectrum. However, in both techniques, the excitation is driven by electron-hole pair recombination at energy minima in the material, and therefore PL and CL spectra are similar [22]. We can say that CL, at first glance, is a way to do photoluminescence at the nanometer scale. However we will see that the way electron hole pairs are created can change the emission statistics dramatically (see chapter 4).

A large set of theories have been elaborated to understand the chain of events leading from the electron-matter interaction down to e-h creation. Shockley was the first to propose a model [111] focusing on the role of phonon energy loss. This model was later modified mostly by Klein, to include bulk plasmons as intermediate states [112, 113]. Another model used to understand the process leading from high energy e-h (HE eh) to e-h was proposed by Rossbroeck [114–116]. Most of these works concerned thick samples, in which multiple plasmons are created along with numerous HE e-h per incident electron. Therefore, their concern was not the effect of a single primary excitation, mainly because at this time it was difficult to access it experimentally. However, isolating the

effect of one primary excitation is necessary to understand the creation of electron hole pairs.

Electron energy loss spectroscopy (EELS) shows that the creation of plasmon dominates over other loss mechanisms, including HE e-h creation [19]. Moreover, HE e-h themselves can decay into plasmons. Therefore, typically 80% of e-h pairs originate from plasmon decays [21]. Based on simple arguments about energy and momentum conservation, Rothwarf theorized that these plasmons decay into 1 or powers of 3 e-h pairs depending on the ratio between the bulk plasmon energy and material energy bandgap [21]. However, despite being a long disputed issue [28, 117, 118], the decay of one bulk plasmon into multiple e-h instead of one has not yet been observed experimentally because it is difficult to isolate the effect of a single bulk plasmon. Thanks to the radiative recombination of e-h, luminescence techniques, such as CL, are well adapted to probe surface and bulk plasmon dynamics. However, emission spectra are only sensitive to the average effect of material excitation giving no information on emission dynamics. Thus, to isolate the decay of a unique bulk plasmon, some experimental development has to be done. We will show in chapter 4 the impact of decay mechanism on emission dynamics.

1.3 CL-STEM: From Nano-Optics to Quantum Optics

1.3.1 CL-STEM: Nano-Optics

As mentioned in section 1.1.3, CL in an STEM can be used to perform nano-optics. The advantages and drawbacks of such technique on the different emitters we can encounter in the nano-world - quantum wells, quantum dots, material impurities and plasmons - will be explained in details in this section.

Confined Structures: Quantum Wells and Quantum Dots

In this thesis, only quantum wells grown by molecular beam epitaxy (MBE) [119, 120] have been studied even if metalorganic chemical vapor deposition MOCVD is also a common technique [121] for III-N semiconductors growth. MBE is simple in its principle: on a substrate the atomic layers are built one by one by chemical flux in a high vacuum chamber. By controlling these fluxes of elements, we can control the design at the atomic layers. In this thesis only nanowires of AlN/GaN have been used. Common parameters for the growth can be found here [122]. One of the main advantages of nanowires compared to thin films is the reduction of defects in the AlN matrix, even if we will characterize in chapter 5 AlN matrix defects emitting around 3 eV.

As explained in section 1.1.1, quantum wells are optically active structures that confine carriers in 2 dimensions. For example, bulk gallium nitride (GaN) has an energy gap of 3.4 eV, whereas bulk aluminum nitride (AlN) has a gap of 6 eV. Thus, a few atomic layers of GaN inside a matrix of AlN (see Figure 1.7-a) lead to confinement of carriers in the GaN layers (In GaN $\lambda_B \approx 17$ nm at room temperature see section 1.1.1). This leads to a discretization of energy in the confined dimension. It can be schematically represented as a potential well where carriers diffuse before decaying radiatively. Due to the small size of such structures (a few atomic layers), and to the dependence of optical properties with the structural and chemical composition of the QW, CL is the perfect tool to investigate it. CL has been used for over a decade for III-V heterostructures [1, 123, 124]. Using electrons instead of light increases the spatial resolution below the hot carrier diffusion l_d, allowing its observation.

AlN/GaN nanowires have been used especially for the lifetime measurement presented in chapter 5. Nanowires have been grown at INAC in the team of B. Daudin by molecular beam epitaxy. I will introduce the main characteristics of this nano-structured material but more thorough descriptions can be found in [43, 125]. AlN and GaN are III-N materials, which means that each metal atom is surrounded by 4 nitrogen (N) atoms. In certain conditions, GaN has the ability to grow naturally in column without the need of a patterned substrate. To design AlN/GaN heterostructures, the growth begins always by a base of GaN to form the nanowire before growing AlN. Then a thin GaN layer is grown to form the quantum well. Contrary to CL, we will see in chapter 5 that the presence of a GaN base can be a problem in PL experiments if the emission of the quantum well is close to the bulk emission because it will be difficult to distinguish one from the other. Due to the growth conditions used here the crystal structure is always wurtzite (WZ) (see figure 1.6), the growth direction being [0001] or [000$\bar{1}$]. However, in III-N materials, the unit cell is not perfect and the ratio a/c is different from the ideal case ($a/c = 1.633$). This distortion is one of the reasons why AlN/GaN nanowires have a piezoelectric polarization that leads to a strong internal electric field [126]. Due to the absence of a center of symmetry in the WZ structure the direction [0001] and [000$\bar{1}$] are not equivalent. As shown in figure 1.6, [0001] is called the metal polar direction and [000$\bar{1}$] the N-polar direction. In order to illustrate particularities of the STEM-CL and to introduce III-N properties relevant for chapter 5, we will exemplify typical effects in STEM-CL in the case of III-N structures which are dominated by a strong electric field [43, 127].

Incoming electrons create high energy electron hole pairs that can diffuse towards the quantum wells. In CL, it is easy to measure this diffusion because it corresponds to the maximum length between the electron probe and the quantum well such that light emission from the quantum well is still observed. In figure 1.7-c, one can see that the emission

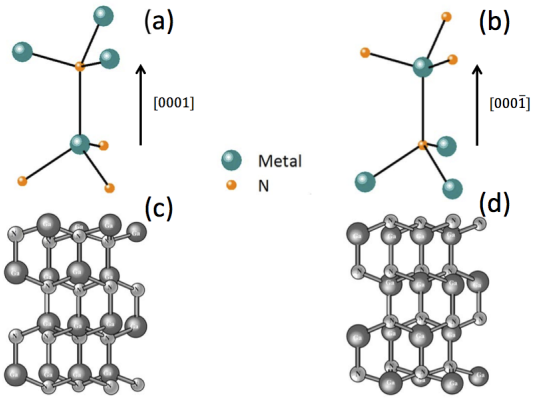

FIGURE 1.6: a) Metal-polar and b) N-polar directions in the III-N wurtzite (WZ) cell. c) and d) respectively Ga-polar and N-polar stick-and-ball representations of WZ GaN. From [125]

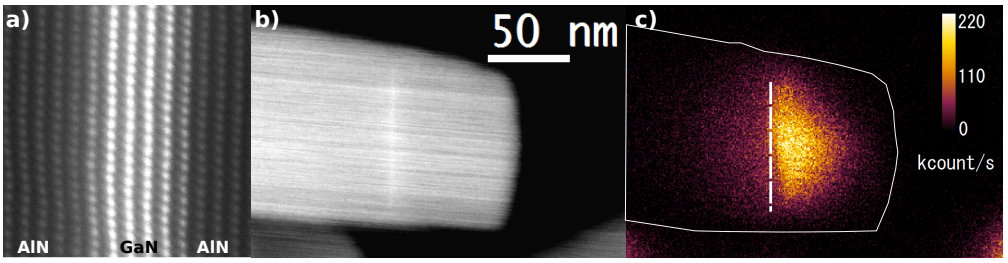

FIGURE 1.7: a) Atomic resolved HADF of a quantum well, Gallium atoms are brighter than Aluminum atoms. One can see that the GaN quantum well is only a few atomic layers thick. c) Emission intensity for the different excitation probe localization, the HADF image taken at the same time is represented in b). The quantum well is noted in c) with a white dashed line. From [122],

intensity of the quantum well depends on the localization of the excitation probe along the nanowire [122]. Indeed, in figure 1.7 the diffusion length and the emission intensity are not the same on either side of the quantum well. It seems that the carrier diffusion is much more effective on the right side of the quantum well. This can be explained [122] by hole mobility. Indeed, the internal electric field in AlN/GaN structure is strong in the growth direction, which means the direction perpendicular to the quantum well. The direction of the electric field depends of the polarity of the material. It can be shown by convergent beam electron diffraction (CBED) [128] that the polarization is N. It means that holes will drift toward the quantum well on the right while they will drift away from the quantum well on the left. Cathodoluminescence highlights carrier diffusion mechanisms thanks to sub-wavelength resolution.

In III-N heterostructures, the internal electric field is very strong, and particularly in AlN/GaN thin films [129, 130] or nanowires [1, 127, 131]. It is responsible for the Quantum Confined Stark Effect (QCSE) [132, 133]. The internal electric field induces a band distortion that modifies the transition energy and separates the envelope functions of the hole and of the electron, implying a reduction of the emission rate [134] (see figure

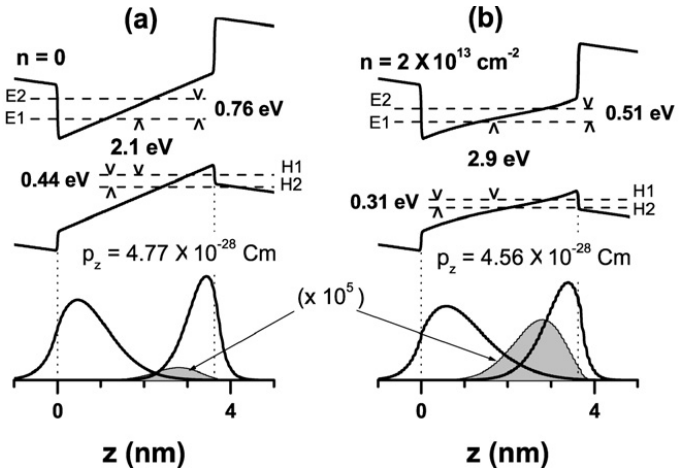

FIGURE 1.8: a) Calculated properties of a 14 monolayers-wide GaN/AlN QW under weak excitation, i.e. with no electron-hole pairs present (n = 0). b) Result of a self-consistent solution of Schrödinger and Poisson equations for $n = 2.10^{13}$ cm^{-2} . The first two electrons (E1 and E2) and holes (H1 and H2) levels are displayed, with mention of the various relevant intersubband energies. The envelope functions for the E1 and H1 states are represented in the lower part of the figure, together with their product, shown by gray areas. The values of the e-h dipole moment p_z in these two extreme situations are displayed, too. From [43]

1.8) and an increase in the lifetime [43]. The thicker the QW the stronger the effect, however, the QCSE will diminish if the density of carriers (eh pair) in the quantum well increases [135] because these carriers will screen the internal electric field. If one performs PL, the charge carrier density will depend on the intensity of the laser beam. Indeed, it has been proven that increasing the beam current decreases the lifetime of the emitter [127]. With electrons, such a screening effect can be seen, either by increasing the intensity of the incoming electron current [110, 136] or by changing the distance between the excitation point and the quantum well. Indeed, if incoming electrons are far from the quantum well, only few carriers will reach it, in comparison to the situation where the beam is close to the QW. This effect needs to be taken into account when comparing PL and CL signal of AlN/GaN nanowires, and it is difficult to evaluate to which laser beam intensity the used electronic excitation condition corresponds.

A second type of confined structure studied in CL-STEM is the quantum dot (QD). QDs are nano-structured materials where carriers are confined in the 3 directions, leading to discrete energy levels. Due to this particular form they are sometimes called artificial atoms. However the size (tens of nanometers) and the solid structure of the QD lead to a strong dependence of the optical properties of the QD on the surrounding material [137, 138]. One of the main drawbacks of quantum dots is competition between the radiative decay and non-radiative Auger recombination [139]. The challenge to study this kind of structures at the nanometer scale is important and a study has been made, by

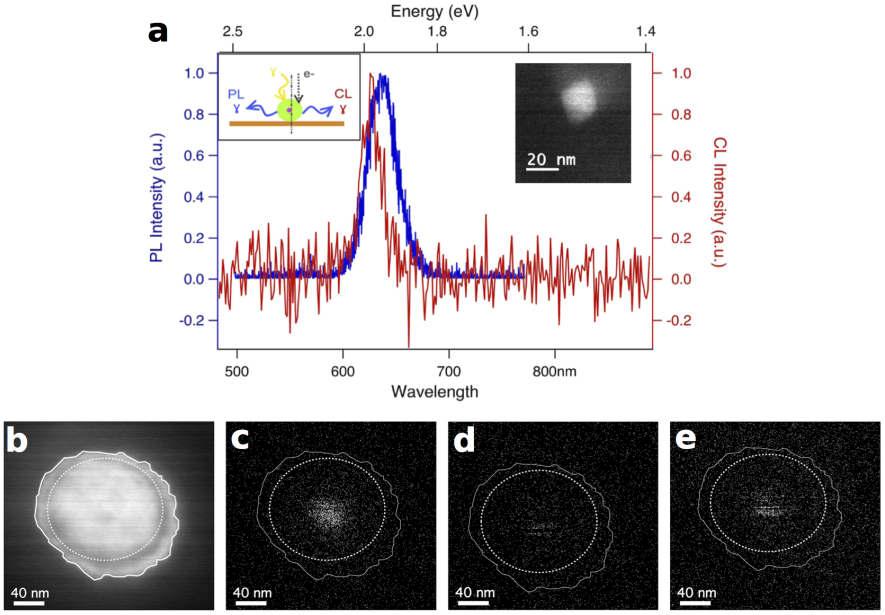

FIGURE 1.9: a) Comparison between PL and CL spectra of individual CdSe/CdS QDs. CL and PL spectra of the same QD. The integration time is 1 min for PL and 50 ms for CL. The energy shift can be explained by a temperature difference between the measurements. (Inset, left) Scheme of the nano CL/PL experiment. (inset, right) HADF image of the QD studied. From [22] b)-e) CL studied of a CdSe/CdS surrounded by silica and gold. b) HADF image of the QD c-e) respectively filtered images of the CL emission during b) the first exposure to the electron beam, d) just after 30s of exposure) three scans later than d).

Z. Mahfoud a former PhD student at the LPS, where he proved that CL and PL signals are similar [22] (see figure 1.9-a). However in studying their quantum statistics we didn't find, for now, quantum dots resisting long enough (more than 5 minutes of exposure) to the electron beam. An example of luminescence decrease due to electron beam exposure is presented in figure 1.9-b-e on colloidal CdSe/CdS quantum dot surrounded by gold grown at the ESPCI (école Supérieure de Physique et de Chimie Industrielles) in the team of Dubertret [140].

Point Defects in Materials

A point defect in a material acts optically also as an atom, for example a vacancy in the material matrix or atom substitution. Due to the sub-wavelength resolution of CL, point defects are a relevant field of application. However, the displacement of atoms and charges accumulation on such fragile structures are difficult to avoid. An example of the effect of an electron on a fragile point defect emitting at 520 nm in the h-BN is shown on figure 1.10. However, even if the photo-stability of this defect is not good enough to perform quantum optics, one can notice the benefits of studying these point defects with electrons. In this example, the diffusion length is of the order of 100 nm

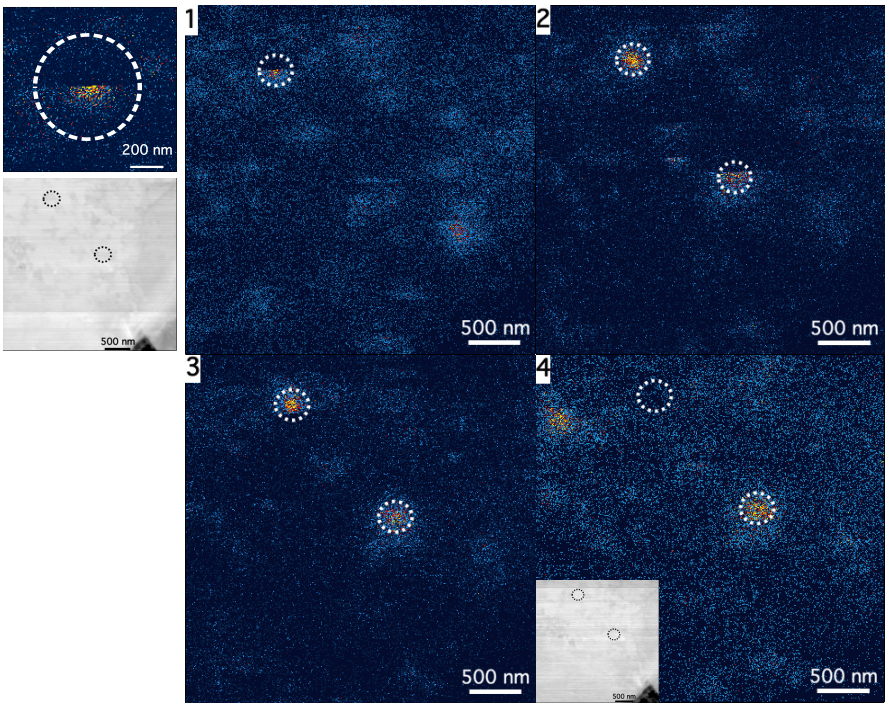

FIGURE 1.10: Electron beam damage on h-BN Impurities. 1-4) Four emission maps of four consecutive scans with the electron beam of the same area. Two point defects are identified (white dashed circles). We can see the apparition and disappearance of the first one and the appearance of the second one. The appearance of the first defect during the scan is magnified on the top left of the image.

and the proximity between point defects makes it difficult to isolate a single one with PL. To perform quantum optics with electrons we need to find stable point defects. NVs in diamond are one example. We will also present in chapter 3 another type of defect that we found in h-BN.

One of the most famous point defects is the "nitrogen-vacancy" NV complex defect in diamond. It is made up of a vacancy near a nitrogen atom in the carbon matrix of diamond (see Figure 1.11). It has been extensively used during this thesis as a test emitter to understand the effect of electrons on the excitation of quantum emitters, as presented in chapters 3 and 4. There are two forms of the NV defects, the charged NV^- with a zero phonon line (ZPL) at 1.9 eV and the neutral NV^0 with a ZPL at 2.16 eV [141]. As explained in section 1.1.1 and in figure 1.2, the zero phonon lines is accompanied by a vibronic band at lower energy in emission. Figure 1.11-b shows an emission spectrum of the NV^0, the zero phonon line at 2.16 eV and the three first phonon replicas at respectively 2.11 eV, 2.07 eV and 2.01 eV. NV^- is the most commonly used in PL experiment, mainly because of its spin properties. Indeed, the extra electron forms with the vacancy a spin S = 1 making a good candidate for spin manipulation [142, 143]. However in CL it is almost impossible to observe NV^- signature. Even for nano-diamonds containing a high concentration of NVs, only NV^0 emission has been

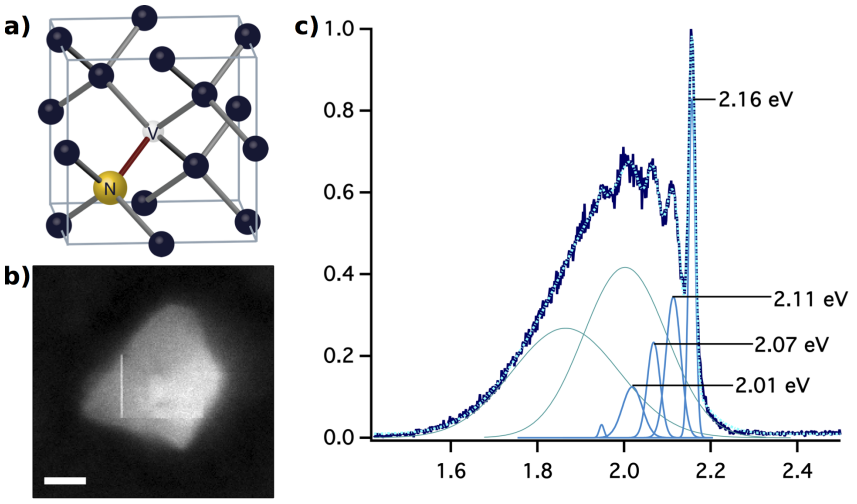

FIGURE 1.11: a) Crystallographic representation of the Nitrogen Vacancy (NV) center in the diamond matrix. Dark atoms are carbons. The yellow one (N) is the nitrogen atoms near the vacancy (V). Credit : Peter Allen from [147]. b) HADF image of a nano-diamond with a high concentration of NV^0 defects. c) Spectrum of the NV^0 emission from on the nano-diamond presented in b).

observed during this thesis (see chapter 4). Apart from rare studies [144], it is worth noting that this has been the case for almost all known studies on NV centers by CL [145, 146].

Plasmons

We have seen in section 1.2.2, that surface plasmons can be excited by fast electrons. Some of the surface plasmon modes can couple to the far field, which means that they can decay by emitting light. These are called bright modes. They have been studied for a decade now with CL in SEM [33, 148, 149] and they were first observed in a CL-TEM by Yamomoto et al [123]. A more recent study in an STEM done by A. Losquin, a former PhD student at LPS, [108], proved that while EELS is close to the optical extinction CL is close to optical scattering. Some of the results of this study are reproduced on figure 1.12. The coupling between surface plasmons and far-field is weak, therefore performing CL on plasmons demands high electron currents.

1.3.2 Quantum-Optics with Fast Electrons

In the previous section, we have shown the pertinence of CL to study confined structures, impurities and plasmons, mainly because of sub-wavelength resolution and the similarity between CL and PL (see figure 1.9). This last point is the main advantage of CL-STEM compared to SNOM or STED spectroscopies and what makes it a perfect candidate to

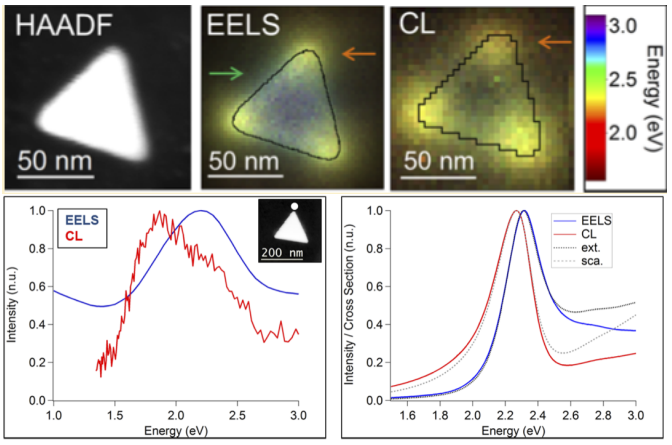

FIGURE 1.12: Top, combined HAADF imaging (left), EELS (middle), and CL (right) spatially resolved data sets. It shows that EELS data exhibit both dipolar and higher order modes (dipolar mode around 1.9 eV and higher mode around 2.4 eV), whereas the CL data exhibit mainly the dipolar mode. At the bottom on the left, measured EELS (blue) and CL (red) spectra taken at the tip of a 140 nm edge long gold prism lying on a carbon foil. Inset: HAADF image of the nanotriangle. The white disk indicates the electron beam position. On the right, calculated extinction (black dotted line) and scattering spectra (gray dotted line) superimposed to calculated EELS (blue) and CL (red) tip spectra for a single small nanoprism of 50 nm edge length, 50 nm thickness surrounded by vacuum. In the case of the optical cross sections, the light propagation direction is chosen perpendicular to the prism, and the polarization is parallel to one of the edges. From [108].

perform quantum optics at the nanometer scale. However the question remains: how using electrons instead of light will affect the light states?

The first experiment of quantum optics in an STEM was realized by Luiz Tizei and Mathieu Kociak on the NV center of a nano-diamond [2]. They coupled an HBT interferometer to a CL system experiment (see section 1.1.2) and proved that, when excited by fast electrons, the NV centers keep their quantum statistics ($g^{(2)}(0) < 1$). The main results are reproduced in figure 1.13. One can see that the dip at zero delay $g^{(2)}(0)$ changes from one point of excitation to another separated only by 150 nm. What this variation could mean for the nano-diamond studied will be discussed in chapter 3. However, it proves two things : first, that fast electrons do not change the statistics of a single SPE; and second that STEM-CL allows probing quantum optics properties with sub-wavelength resolutions.

This experiment marks the beginning of quantum optics in STEM and the possibility to fully characterize SPE at the nanometer scale combining HADF images, cathodoluminescence signal and HBT experiment on the same nano-particle and the same experiment. In this thesis, I used this new experiment to study further SPE characterization with CL-STEM, with the discovery and characterization of a new SPEs in h-BN (see chapter 3).

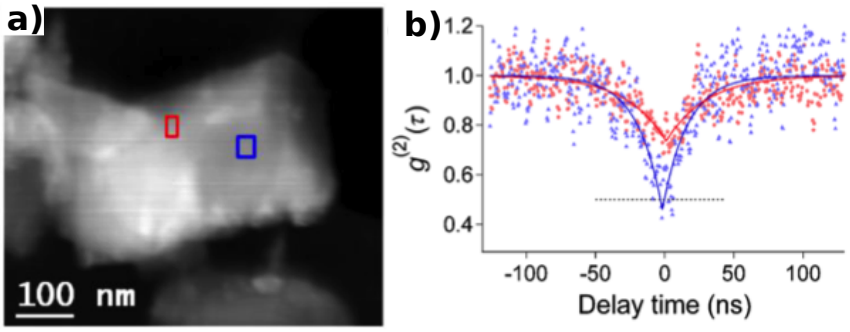

FIGURE 1.13: b) $g^{(2)}(\tau)$ function of the CL signal for two different excitation areas noted by the red and blue squares on the HADF image in a). From [2]

Chapter 2

Experimental Tools

> He had learned in recent days, though, that rather than drown in uncertainty it was best to surf right over the top of it
>
> *Terry Pratchett*

2.1 Scanning Transmission Electron Microscope

Before going through the main results of this thesis, it is essential to understand the main experimental tools I have used or developed. Especially, I will concentrate on the advantages and drawbacks of using a scanning transmission electron microscope (STEM) to perform cathodoluminescence and intensity interferometry experiments. In this first section I will describe the basic principle of an STEM, the acquisition of electronic images as well as the utility of spectrum imaging to perform spectroscopy in an STEM.

2.1.1 Optics and Images

In this thesis, experiments have been mainly realized on an STEM VG HB 501, with a sample cooled with liquid nitrogen to a temperature of about 150 K. The cooling system improves the vacuum in the microscope column by one order of magnitude and suppresses contamination issues. It also improves the cathodoluminescence signal intensity of most emitters and increases their resistivity to the electron beam as explained in chapter 1. The operation system of an STEM can be divided in three main parts, the electron gun, magnetic lenses that drive the electron beam onto the sample and the detection system after the sample (see figure 2.1).

The electron gun

The incoming electron beam is produced and accelerated in the electron gun. There are three kinds of electron sources, thermionic sources, Schottky cathode and the cold field electron gun (C-FEG). One of the main characteristic of the electrons source is its brightness, defined as the minimum size of an electron beam for a given electron current and beam convergence. The brightness of a thermionic source is much smaller ($< 10^4$ A sr^{-1}cm^{-2}) as is its spectral resolution (2 eV compare to ≈ 300 meV) compared to the other two. The Schottky cathode and the C-FEG are sometimes called "point sources cathode". In these two cases electrons are extracted from a very small point source that ensures a higher brightness ($5*10^8$ A sr^{-1}cm^{-2} for the Schottky and $2*10^9$ A sr^{-1}cm^{-2} for the C-FEG). The principle is explained in the insert of figure 2.1. Electrons are extracted from the cathode with an electric potential (V_1) of a few kV and accelerated further with an electric potential (V_0) between 60 and 100 kV called the electron microscope high tension (EHT). The STEM VG has a cold-field emission gun. The cathode is, in that case, at room temperature. The extraction is achieved by tunneling effect due to electric field induced by the first anode. The vacuum needed in the electron gun is therefore high ($<\approx 10^{-8}$ Pa). For the Schottky source, the cathode, a tungsten tip, is heated to 1800 K before extracting electrons thanks to the electric field. There is therefore no need for a tunneling effect to extract the electron from the cathode. The vacuum in the electron gun can therefore be smaller ($<\approx 10^{-6}$ Pa). However, as mentioned before, the Schottky emission source have a smaller brightness (for more details see chapter 4 of [17]).

Magnetic Lenses

To focus and position the electron beam emitted from the electron gun onto the sample, magnetic lenses are used as shown in figure 2.1. We can distinguish three kinds of magnetic lenses: the condenser lenses, the scanning coils and the objective lens. The condenser lenses collect the beam at the exit of the electron gun. In our microscope if the two condenser lenses (C1 and C2) are turned on, the system collects most of the electrons coming out of the gun and therefore the current of the beam is higher when only one condenser lens is on (C2). A factor of 6 in the current value is expected between the two configurations. In the first configuration (C1 and C2), the current is high but the brightness is lower due to geometrical aberrations which means that the probe is bigger, and therefore we will have a degradation of the spatial resolution. The objective lens focuses the beam on the sample. Thanks to the scanning coils the focus point can be moved on the sample, probing different parts of the sample. The smaller the probe, the higher the spatial resolution achievable. In state of the art microscopes, a few other optical elements to correct aberrations of higher orders are inserted into the column,

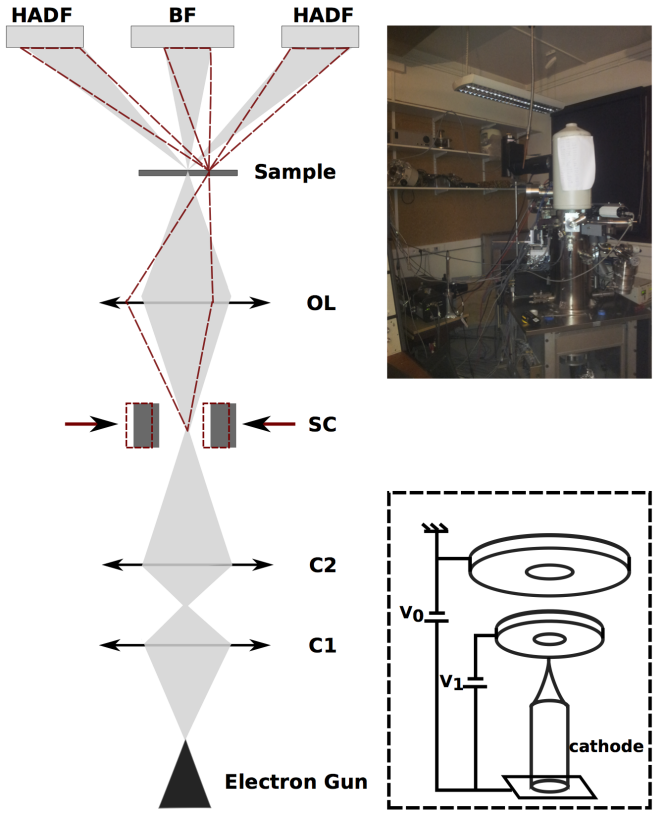

FIGURE 2.1: Sketch of an STEM VG HB 501. The electron gun at the bottom produces an electron beam at an energy between 40 and 100 keV. The sketch of the field emission (inside the electron gun) is shown at the bottom on the right. Magnetic lenses along the column are represented by horizontal arrows, C1 and C2 being the two condenser lenses and OL the objective lens. The beam is focused thanks to these three lenses on the sample in a probe of about 1 nm, the transmitted electrons are collected on the High Angular Dark Field (HADF) and Bright Field (BF) detectors. Thanks to the scanning coils (SC) the sample is scanned with the probe and a HADF and BF signals are recorded at each point. HADF and BF images are obtained after reconstruction of the image with the contrast in each points. Top right of the image, picture of the STEM VG HB 501. The white cylinder is a Deware for liquid nitrogen to cool down the microscope at 100 K.

allowing the formation of sub-angstrom probes [150]. But in our case, we can reach a resolution of the order of 1 nm which is sufficient in most cathodoluminescence studies.

Detection System

In a transmission electron microscope, the electron beam is transmitted through the sample. Each electron interacts elastically or inelastically with the sample. Two detectors collect transmitted electrons, the high angular dark field detector (HADF) and the bright field detector (BF). The HADF collects scattered electrons at high angle. As the scattering cross section at high angle is proportional to the atomic number of the atoms

and the thickness of the sample, heavier elements or thicker parts of the sample will scatter a higher number of electrons on the HADF. The BF on the other hand is on the optical axis, it collects small angle scattered electrons. Contrary to the HADF contrast, the BF is sensitive to diffraction effects. To realize an image, the probe is scanned on the sample thanks to the scanning coils. At each point of the scan, a number of electrons is recorded by the HADF and BF detectors. The HADF and BF images are reconstructed a posteriori by plotting respectively the number of electrons for each pixel of each detector. Since electrons interact weakly with the sample, the background will appear dark on the HADF image and white on the BF image, hence the respective names of dark and bright fields. Figure 2.2 shows the HADF and BF images of a GaN/AlN multiple QWs nanowire. The gallium (Ga) having a higher atomic number than aluminum (Al), GaN appears brighter on the HADF image and vice versa on the BF image.

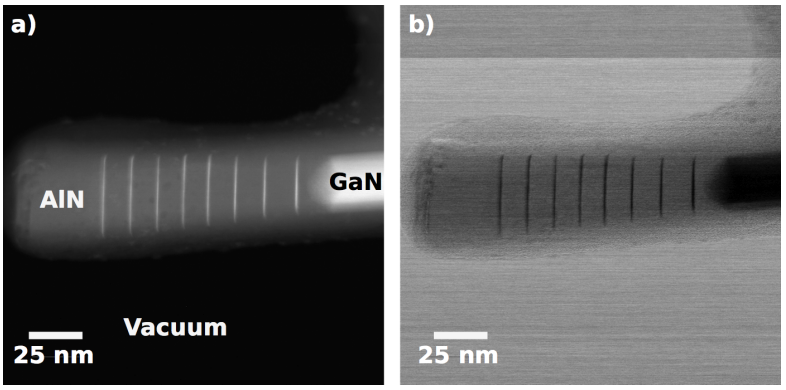

FIGURE 2.2: HADF a) and BF b) images of a GaN/AlN nanowire. The gallium appears brighter on the HADF image because it has a higher atomic number than the aluminum.

2.1.2 Spectroscopies in STEM

As explained in chapter 1, two main STEM spectroscopies have been used. First, electron energy loss spectroscopy (EELS) that retrieves information from the energy lost by inelastically scattered electrons. Second, cathodoluminescence (CL), that analyzes light emitted in the visible range by the sample. In order to maintain a high spatial and spectral resolution we used the method of spectrum imaging. The electron beam scans the sample, and for each pixel an EELS spectrum or an emission spectrum is recorded. We obtain a data cube in 3 dimensions called a spectrum image (SPIM): to each pixel (x,y) of the image, a spectrum is associated. It is represented in figure 2.3-a. At the same time an HADF image is recorded allowing the association of each spectrum with an HADF contrast 2.3-d.

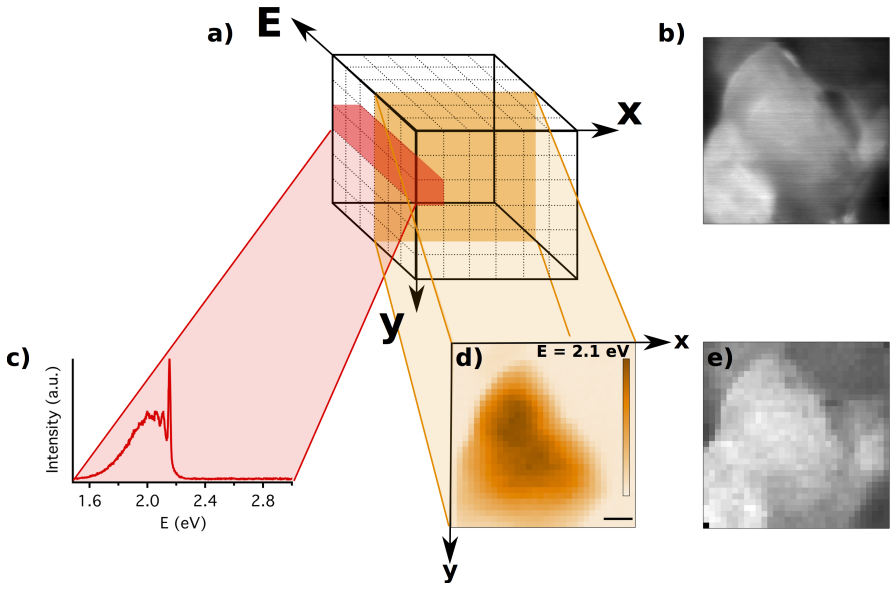

FIGURE 2.3: a) Schematic representation of a spectrum image (SPIM). In each pixel of the scan (x,y) on the sample a spectrum of EELS or CL is acquired, the data set is a cube in three dimensions (x,y,E). For example, in the case of a diamond (high resolution HADF image in b)) we can extract c) an emission spectrum corresponding to the excitation from a pixel at the center of the (x,y) area or d) a filtered imaging where for a fixed value of E (here E = 2.1 eV) we plot the emission intensity at each pixel. An HADF image e) is acquired at the same time as the SPIM. The black scale bar in d) is 70 nm.

For EELS measurements, the inelastically scattered electrons have to be collected and dispersed in energy. Due to aberration issues in the spectrometer, we collect only the inelastically scattered electrons at small angles in regards to the optical axis. The beam is dispersed in energy by a magnetic prism which is detected by a scintillator coupled to a CCD as shown in figure 2.6.

For CL measurements, photons emitted by the sample are collected thanks to a parabolic mirror with a high numerical aperture (NA = 0.6) incorporated inside the STEM. Figure 2.4 shows a picture of the CL system outside the microscope. Only the mirror is in vacuum, three verniers allow controlling the position of the mirror optimizing the collection of the CL signal. This is a critical point, because the focal point of the system is small ($\approx \mu 300m$) and requires fine positioning.

The parabolic mirror gives a parallel beam which is focused into the optical fiber (OF) by an optical lens. The OF brings the signal to an imaging spectrometer. The grating inside the spectrometer can be changed as a function of the energy range of interest. After the spectrometer the signal is collected by a Princeton EMCCD (electron multiplying charge coupled device). The energy sampling is determined by the grating and the 1600 horizontal channels of the CCD. The collection efficiency is improved by the use of a bundle of 19 fibers of 200 μm of diameter. On the mirror side, the fibers are arranged

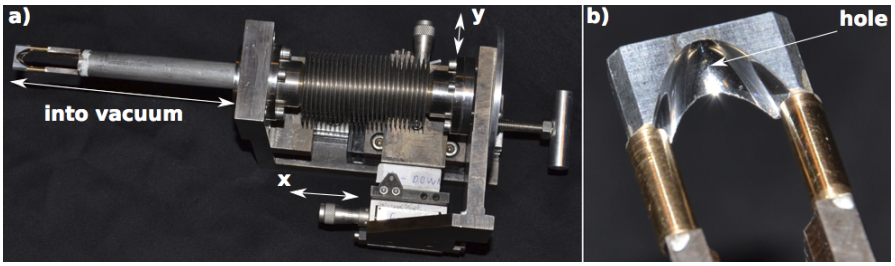

FIGURE 2.4: a) Picture of the entire CL system, the part inside the microscope is indicated with a double arrow as well as moving axes (x,y) (z direction is hidden). b) Magnification of the parabolic mirror, the hole of 500 μm is indicated. This hole allows the incoming electrons to go through.

in circle, while on the side close to the spectrometer, they are aligned vertically. In this configuration, the area of collection is much higher than 200 μm but on the other side the spectral resolution is the same as for a single 200 μm fiber. By simply summing vertically the pixel of the EMCCD camera, we retrieve the signal from the 19 fibers. The principle is explained in figure 2.5

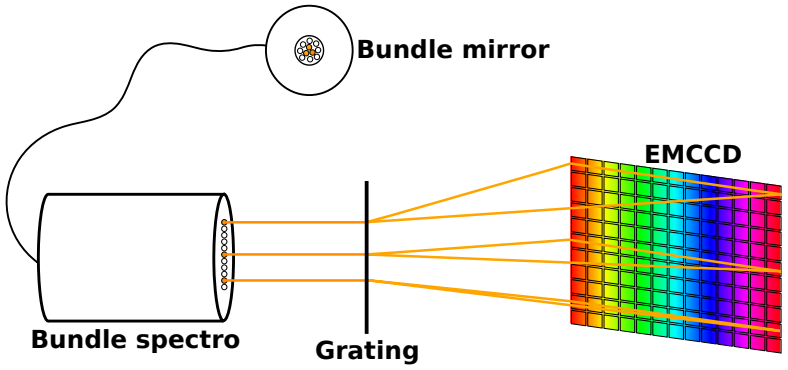

FIGURE 2.5: Schematic representation of the bundle. The signal is collected by the bundle end close to the mirror and travels to the bundle end close to the spectrometer. The light coming from each fiber is then dispersed horizontally by the grating inside the spectrometer and detected by the CCD. By summing vertically the pixels of the CCD we retrieved for each energy the total signal collected by the fibers.

In cathodoluminescence experiments the spatial resolution is limited, in principle, by the diffusion length l_d of carriers. Indeed, different (x,y) pixels of a SPIM are the places of excitation but emission can come from anywhere inside a circular area of radius l_d around the pixel. However, in this circular area, the probability of excitation of the emitter will increase if we excite closer to the emitter. This means that if we come near it, the intensity of emission will increase. From a SPIM we can extract an intensity emission map at a given energy as represented in figure 2.2-c. By identifying on the map the maximum of emission intensity, we can identify with a resolution larger than l_d the localization of the center of emission. If two emissions are energetically overlapping, in order to identify more clearly the emission center of each of them, we can go further by

fitting the emission spectrum at each (x,y) pixel. We then retrieve filtered and fitted intensity emission maps as shown in figure 2.6.

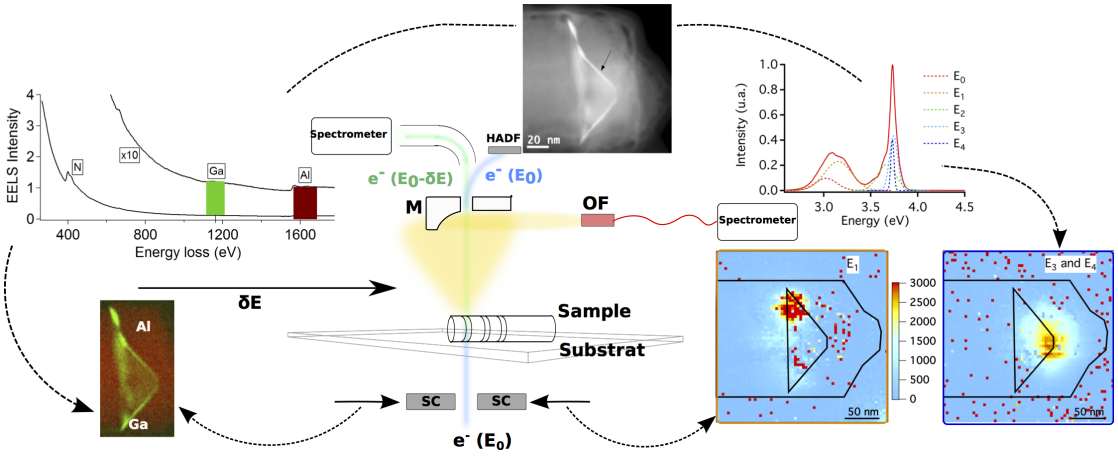

FIGURE 2.6: Principle of an STEM and associated signals. A parabolic mirror (M) with a high numerical aperture collects the CL signal efficiently, forming a collimated beam which is then coupled to a multimode optical fiber (OF). The fiber output beam is sent to an imaging spectrograph to record the emission spectrum. The non-scattered electrons are sent to another imaging spectrograph to perform electron energy loss spectroscopy (EELS). The scattered electrons are collected with an High Angular Dark Field detector (HADF). Thanks to the scanning coils (SC), the electron probe can be scanned, and at each pixel an EELS or CL spectrum and an HADF signal can be recorded. We can then correlate the different emission, structural and chemical information of the same particle. We illustrate this principle by the study of a AlN/GaN nanowire (image connected by dashed lines). The image on the left represents the localization of gallium and aluminum on the nanowire determined by EELS spectroscopy. The two images on the right are filtered and fitted images of the emission for two different energies represented in the spectrum on the left. The image on the top is the HADF image acquired at the same time that EELS spectrum. The HADF image acquired at the same time as the cathodoluminescence spectrum is not represented here.

2.2 Hanbury Brown and Twiss Experiment

2.2.1 HBT-PL

As explained in chapter 1, in this thesis we want to measure the intensity autocorrelation function ($g^{(2)}(\tau)$) of the CL signal. The $g^{(2)}(\tau)$ is the probability to observe the emission of two photons separated by a given delay τ. If the emitted photons are not correlated we have $g^{(2)}(\tau) = 1$, as it will be explained in details in chapter 3. However if we simply record the arrival time of each photon on a single detector, photons separated by less than the dead time T_D of the detector will not be detected ($T_D \approx 70$ ns for silicon avalanche photodiode (SPAD), used here for the visible range experiments). Therefore the $g^{(2)}(\tau)$ will have a time resolution $\Delta t = T_D$. In order to improve the time resolution, the $g^{(2)}(\tau)$ is recorded with an intensity interferometry experiment usually called HBT

experiment after the names of the inventors Hanbury-Brown and Twiss. The principle is simple and explained in figure 2.7. The emitted photons are sent onto a beam splitter. Thus, each photon will go either on detector D_1 or D_2. When a photon arrives on D_1, it starts a clock that will stop when a second photon arrives on D_2. The delay between the two photons will be recorded and, as it involves two detectors, this delay can be much smaller than T_D. All the recorded delays are then arranged on a histogram with a certain time sampling Δt fixed by the Time-Correlated Single Photon Counting (TCSPC) system. Depending on the time range of the correlation we want to measure, Δt can be adjusted to improve the signal to noise ratio from 4 ps to 512 ps.

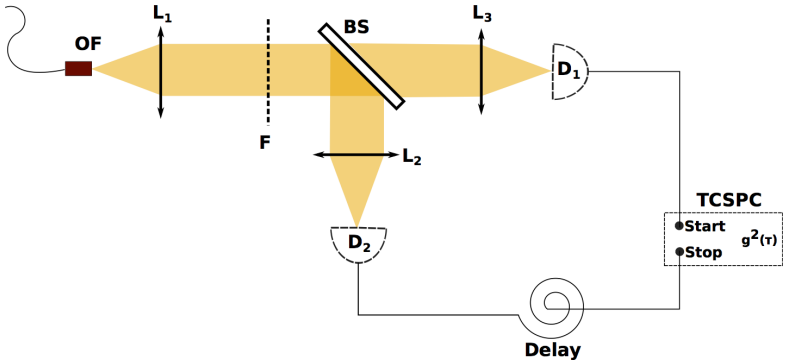

FIGURE 2.7: Light comes out of the optical fiber (OF) which is placed in the focal point of L_1. The parallel beam arrives on the beam splitter (BS) and is either transmitted to D_1 or reflected to D_2. The two detectors are put respectively at the focal point of L_3 and L_2. In order to obtain a spot of 200 μm with a fiber of 200 μm the focal lengths of L_1,L_2 and L_3 have to be equal. A filter (F) can be add before the beam splitter to select the right emission.

The delay between a photon arriving first on D_2 and another arriving later on D_1 can be seen as the symmetric of the delay recorded if the first photon has hit D_1 first. However, in this configuration the TCSPC can record delays only from the second case. Moreover, the main results are often around $\tau = 0$. It is therefore useful, to avoid artifacts, to record the two kinds of delays to make sure that we have a symmetrical $g^{(2)}(\tau)$. A delay of about 120 ns is thus introduced between D_2 and the TCSPC system, which corresponds to a cable of 23 m. In this configuration, if two photons arrive at the same time on a different detector, the signal coming from D_1 will arrive, at the TCSPC 120 ns before the signal coming from D_2. It will thus induce an artificial delay of 120 ns between the two photons, an offset in time Δ_{off} is therefore added to the histogram. We can measure precisely this offset by sending the same signal in the two channels (the two cables are for example plugged on the same detector). A histogram with only events at $\tau = 0 + \Delta_{off}$ will be recorded.

2.2.2 HBT-STEM

In our case, to record the autocorrelation function, we inject the CL signal collected by the optical fiber into an HBT experiment. This means that the optical fiber goes either into the spectrometer or into the HBT experiment. Two HBT experiments have been used, the first one in the visible range was built before I arrived. We developed a second one in the UV range during my thesis. Pictures of the two experiments are shown in figure 2.8.

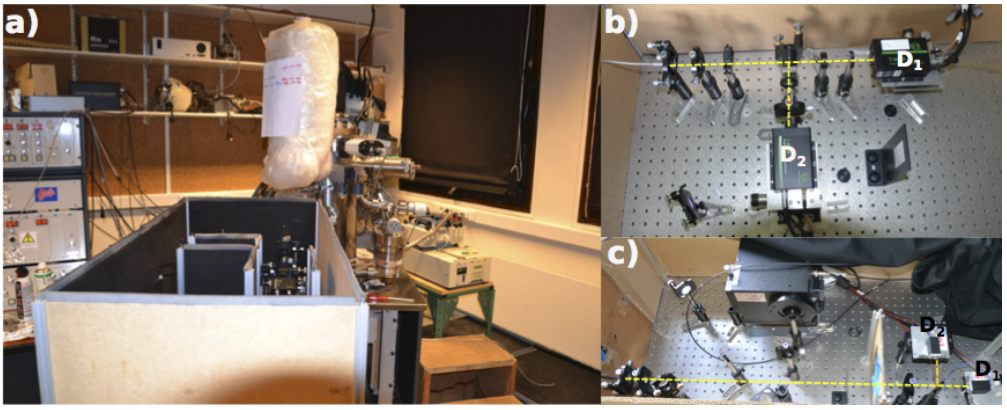

FIGURE 2.8: a) Picture of the STEM with the HBT experiment in front. b-c) HBT in the visible and UV range respectively, the light path is represented by a yellow dashed line and the two detectors are noted on each experiment D_1 and D_2.

HBT in the Visible Range

This experiment used two silicon avalanche photodiode detectors τ-SPAD from Picoquant. The dead time is less than 70 ns and the quantum efficiency at 600 nm is around 60 %. Their detection efficiency are above 50 % for wavelengths between 550 and 850 nm as shown in figure 2.9. The sensor of the τ-SPAD is a square with 200 μm sides. Therefore, if one wants to match numerical apertures and beam sizes, an optical fiber with a diameter of 200 μm or less is needed to be used as well as lenses with identical focal lengths (L_1, L_2 and L_3 of figure 2.7). Collecting the CL signal on a 200 μm fiber instead of the bundle used for CL spectrum imaging makes the adjustment rather difficult. In order to simplify the alignment, Jean-Denis Blazit, an engineer working in the team, designed a new connection system to plug the optical fiber into the CL system. It allows a more precise adjustment of the position of the optical fiber relative to the mirror. To improve the collection efficiency, we also used a coated optical fiber to increase the transmission in the range of 350-700 nm, limiting its use to this range. The lenses we used also have a special coating to improve the transmission and thus cannot be used for wavelength below 450 nm.

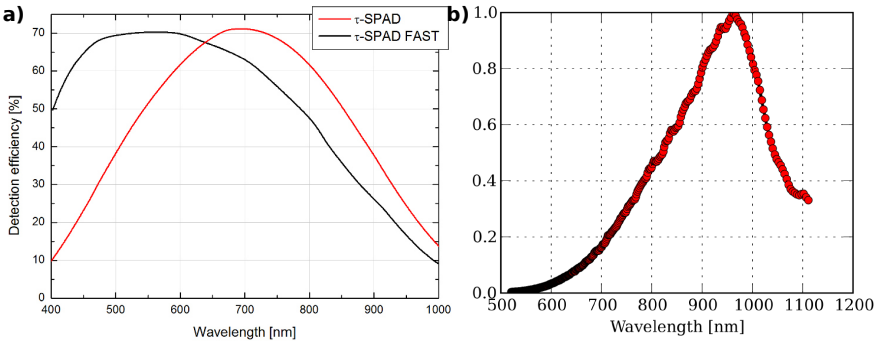

FIGURE 2.9: a) Detection efficiency of the picoquant τ-SPAD for wavelength between 400 and 1000 nm from the datasheet. b) Emission wavelength of photons produced by the τ-SPAD during the avalanche process, from [151]

When a SPAD detects a photon, an avalanche reaction occurs. Therefore, for one incoming photon, multiple electrons are created, producing the electrical pulse to be detected. It is a very efficient way to amplify the signal, allowing sensitivity to single incoming photons. However, one of the drawbacks is that these detectors emit an afterglow in the near infra-red. Photons which go backwards to the other detector, and therefore are detected as incoming photons, resulting in a crosstalk phenomenon [152]. This will be visible in the $g^{(2)}(\tau)$ function by two peaks $g^{(2)}(\tau) > 1$ at $\tau \approx \pm$ 10 ns, as shown in figure 2.10. This delay corresponds to the time of photon emission in the τ-SPAD and not the time for the photons to go from one detector to the other which is negligible. The emission spectrum of the SPAD is shown in figure 2.9. To avoid this spurious signal we added a low-pass filters (< 750 nm) in front of each detector. As they are single photon detectors, they are very sensitive to light, a count rate larger than 10^9 counts/s can damage the detector as well as an exposition bigger than 10 minutes for a count rate above 10^6 counts/s.

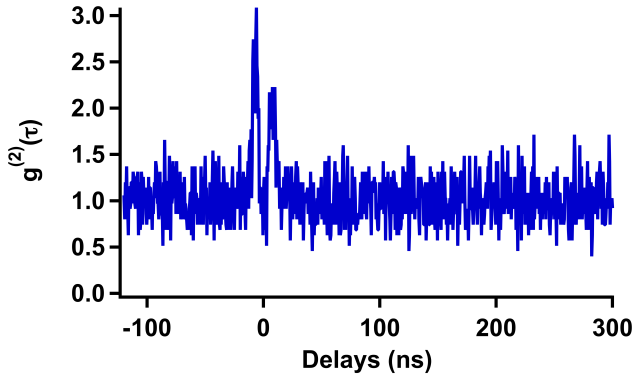

FIGURE 2.10: Crosstalk phenomenon. $g^{(2)}(\tau)$ measured with the HBT-visible experiment on a nanodiamond. Without the two low pass filters, two peaks are visible at $\tau = \pm$ 7 ns.

HBT in the UV Range

For the experiment in the UV range, we used Hamamatsu photomultiplier tube (PMT) H10682-210 with a quantum efficiency larger than to 50 % between 320 and 470 nm (figure 2.11-a). The definition of the electric pulse of the PMT is worse than that of the τ-SPADS, adding noise to the $g^{(2)}(\tau)$ function. However, the dark count is much lower, by a factor of approximately 10. One of the main advantages is that the circular sensor has a diameter of 6 mm, facilitating the alignment. We used an optical fiber of 600 μm and UV lenses that work with a reflectance of less than 1 % between 250 and 400 nm. Therefore, in this configuration, the experiment is working only between 320 and 400 nm. To avoid degradation of the detector, the beam is defocused to obtain on the sensor a spot about the size of the sensitive area (6 mm). To preserve the particular low dark counts rate of the PMTs, the sensitive area should not be exposed to ambient even when off. A special blanker was designed to avoid any exposure to normal light intensity. Turned on, as for the τ-SPAD, the rate of 10^9 counts/s should not be exceeded. Due to the easy alignment in the case of PMT, we used a single lens placed before the beam splitter instead of the two individual ones (L_2 and L_3) represented in figure 2.7, thus working in a confocal configuration.

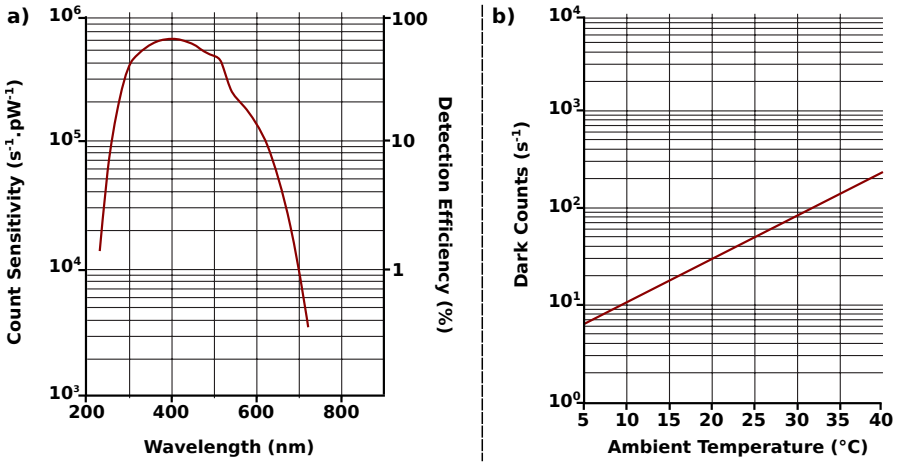

FIGURE 2.11: a) Detection efficiency as a function of the wavelength, with a maximum efficiency of 60 % at 400 nm. b) Dark counts as a function of the temperature, at 20 ^oC (temperature of the experimental room) the dark counts is of 30 counts/s (200 counts/s for the SPAD).

The two HBT experiments are complementary. They allow for the study of CL signal on two main spectral regions, 320-400 nm with the UV-HBT experiment and 550-700 nm with the visible-HBT experiment. We used a TCSPC system that requires a NIM (Nuclear Instrumentation Module) signal. The τ-SPAD delivers it as well as a TTL (Transistor-Transistor logic) signal but the PMT delivers only a TTL signal. In the case of PMT we had to convert the TTL pulses to NIM pulses before the TCSPC. The

NIM signal must also be between −400 mV and −700 mV to avoid detection problems or deterioration of the correlator. We used an attenuator of 20 dB on each channel for the visible-HBT experiment and an attenuator of 20 and 10 dB on the channel with and without delay for the PMT experiment.

The signal of one of the two detectors is also sent to an electronic card that records the number of counts in a given time window. We thus have a synchronization of the HADF contrast taken at each pixel and the number of photons recorded on the detector during the time of exposition of the pixel. It allows the acquisition of emission maps at the same speed as the HADF images, simplifying the localization of regions of interest, as in the example shown in figure 2.12.

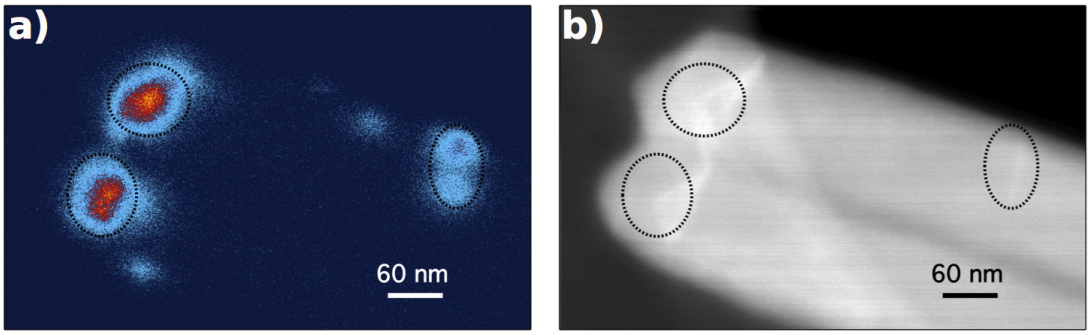

FIGURE 2.12: a) Counts recorded by one of the two photon count detectors during the excitation of the (x,y) pixels. This image is acquired at the same time that the HADF image b). These 512 x 512 two images were acquired with a dwell time of 128 ps per pixel, or a total acquisition time of about 30 s.

2.3 Lithography

2.3.1 Principle

Electron beam lithography is a very efficient way to design plasmonic structures at the nanometer scale. During this thesis, I continued the work started by Zackaria Mahfoud, a former PhD in the team, to design plasmonic patterns with electron beam lithography. First of all, I will explain the principle and the specificities of electron beam lithography on TEM grids. Then I will explain the realignment process in order to couple plasmonic structures with emitters.

For STEM experiments, the substrate employed needs to be almost transparent to electrons, and therefore really thin.Thus, we cannot rely on bulk lithography. For example, in our case, the grids used are Si_3N_4 substrates with 9 windows of 100 μm x 100 μm of 15 nm thickness produced by Ted Pella (see figure 2.13). Electron beam lithography

implies multiple steps, therefore breaking one or two windows during the process is common. It is thus important to print, if it is possible, the same design on more than one window to increase the chances of success. Figure 2.13 summarizes the different steps to perform lithography on a TEM grid:

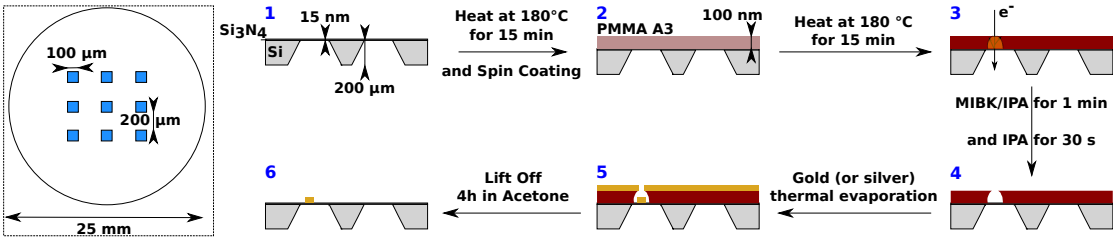

FIGURE 2.13: Lithography Principle. Dashed square on the left, schematic representation of a Si_3N_4 TEM grid, the 9 windows of 15 nm thick are represented in blue. 1/ to 6/ schematic representation of the different steps to perform electron beam lithography.

1. First a resin of PMMA is spin coated on the grid. I noticed that heating the sample at 180 ^oC during 15 minutes before the deposition increases the uniformity of the PMMA layer. To design structures with a thickness between 30 and 50 nm, a layer of about 100 nm of PMMA is needed. A spin coating at 4000 rotations/min during 30 s with a PMMA A3 type is optimum. The PMMA is characterized by the length of the polymer molecules. The smaller the polymer, the better the resolution of the design.

2. After the deposition, the PMMA is heated at 180 ^oC for 15 minutes and put in a scanning electron microscope (SEM). Here we used a ZEISS SEM-FEG Supra55vp at EHT = 30 kV. The design of the plasmonic structure is done thanks to Designcad and the control of the writing mastered by the software NPGS. The electron beam writes the structure on the grid. The main parameter is the time of exposure at each scanned point. In our case the exposure time must be significant because of the very thin substrate that diminishes the interaction between the electron beam and the sample. Therefore, it requires a relatively long time of integration. However the thinness of the substrate also improves dramatically the resolution, because very few secondary electrons are produced. This means that the interaction volume is smaller and the area of interaction is limited to the diameter of the probe (around 10 nm in this SEM).

3. Once the pattern is written, we remove the irradiated PMMA in a solution of Methylisobutylcetone and Isopropanol (MIBK/IPA) (1 minutes of soaking)

4. A layer of the chosen metal is then deposited thanks to Joule evaporation deposition. If gold is deposited, a Titanium layer of 5 nm is added before gold to improve the adherence of the metal on the substrate.

5. The last step is to remove the remaining PMMA. To avoid breaking windows during this step, we simply put the grid in acetone for 4 hours and the PMMA will dissolve slowly.

An example of the final result is shown in figure 2.14. In this case the plasmonic pattern was gold nano-triangles of sizes going from 50 to 600 nm as shown in figure 2.14-b. A second pattern was designed all around the structures to avoid charging problems. Indeed, on Si_3N_4, the electron beam induces, due to secondary electrons or Auger electrons, charges on the substrate that have difficulties to disperse. They will thus interact with the electron beam provoking a blurring of the image. This design resolved the problem by evacuating the charges away from the area under study.

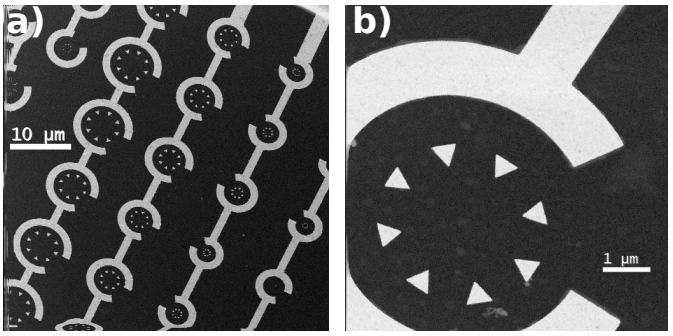

FIGURE 2.14: HADF images of a lithographic pattern. a) High magnification of the pattern, the plasmonic structures of interest are gold triangles drawn inside the gold circles as shown on b).

2.3.2 Realignment Process

In order to study the coupling between plasmons and emitters, I mastered a new manufacturing process. First I lithographed on each window an alignment pattern shown in figure 2.15-a. I then deposited emitters, for example nanodiamonds. I located their position regarding the alignment pattern as shown in figure 2.15-b and c (up). I drew the plasmonic structure after realignment thanks to the first pattern, with NPGS. The result is shown in figure 2.15-b and c (bottom) where we designed plasmonic antennas of 400 nm in front of nano-diamonds.

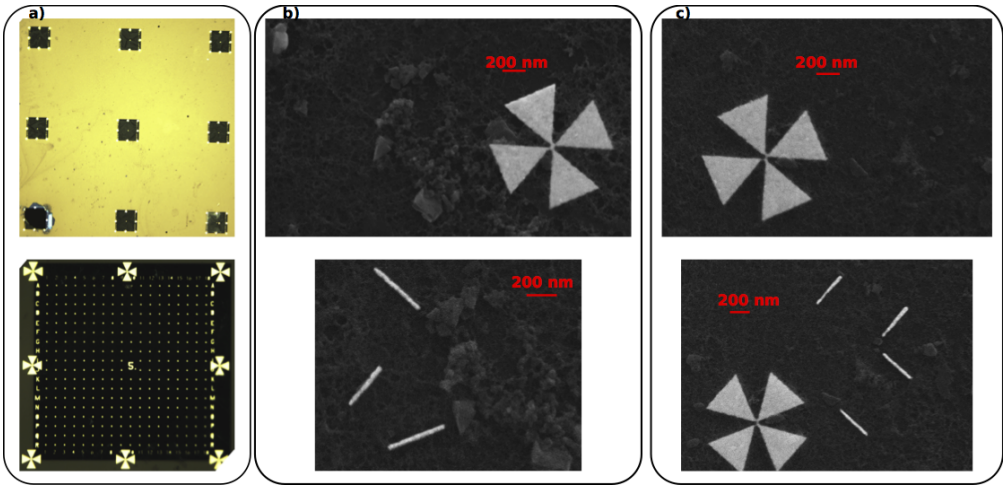

FIGURE 2.15: Results of lithographic design in front of nano-diamonds. a) Optical microscopic image of the nine windows after designing the alignment pattern. Bottom: the central window is magnified (the number is different for each window). b) and c) 2 examples of antenna drawn in front of nano-diamonds. SEM images after nano-diamond deposition on the grid and at the bottom after drawing plasmonic antennas in front of the structure.

Chapter 3

Intensity Interferometry Experiment: SPE Characterization

> Nothing travels faster than the speed of light, with the possible exception of bad news, which obeys its own special laws.
>
> *Douglas Adam*

3.1 The Hanbury Brown and Twiss Experiment

To fully characterize an emission it is imperative to study also the temporal properties of the light in addition to its spectral information. Temporal fluctuations of the light intensity can be characterized by interferometry experiments, which measure the second order intensity correlation function $g^{(2)}(\tau)$, that is the interference of the beam with itself. To do this, one uses the Hanbury Brown and Twiss experiment already presented in chapter 2. In this first section we will introduce the $g^{(2)}(\tau)$ function and what we expected for the three main kinds of light we can encounter: Poissonian light, chaotic light and Fock states of light. A more detailed description can be found elsewhere [36, 153].

3.1.1 Statistics of Emission

The Second Order Correlation Function : $g^{(2)}(\tau)$

A light beam with stationary statistical properties has a constant average intensity value with fluctuations around it. We can therefore define a cycle average intensity. If we want to study the temporal fluctuations, we can perform on the cycle average intensity a two-time measurement at a fixed delay τ. We can define the auto-correlation intensity function $G^{(2)}(\tau)$ as in equation 3.1, but it is convenient to work with its normalized form called the second-order correlation function $g^{(2)}(\tau)$ reproduced in equation 3.2.

$$G^{(2)}(\tau) = \langle I(t)I(t+\tau)\rangle \tag{3.1}$$

$$g^{(2)}(\tau) = \frac{\langle I(t)I(t+\tau)\rangle}{\langle I(t)\rangle^2} \tag{3.2}$$

As we consider a stationary statistical emission, the $g^{(2)}(\tau)$ function is symmetrical $g^{(2)}(\tau) = g^{(2)}(-\tau)$. If we consider first the problem from a classical point of view, we can deduce some general behavior. Thanks to Cauchy's Inequality the measurements of the intensity at two times t_1 and t_2 follows:

$$2I(t_1)I(t_2) \leq I(t_1)^2 + I(t_2)^2 \tag{3.3}$$

For a number N of measurements equation 3.3 becomes:

$$\left\{\frac{I(t_1) + I(t_2) + ... + I(t_N)}{N}\right\}^2 \leq \frac{I(t_1)^2 + I(t_2)^2 + ... + I(t_N)^2}{N} \tag{3.4}$$

In practice, N is large, we can write that in average : $\langle I(t)\rangle^2 \leq \left\langle I(t)^2\right\rangle$, which means that $1 \leq g^{(2)}(0)$. Therefore in the classical limit the $g^{(2)}$ at zero delay has a lower limit, but no upper limit is defined. We can also deduce from equation 3.3 the inequality that follows:

$$\{I(t_1)I(t_1+\tau)+...+I(t_N)I(t_N+\tau)\}^2 \leq \left\{I(t_1)^2+...+I(t_N)^2\right\}\left\{I(t_1+\tau)^2+...+I(t_N+\tau)^2\right\} \quad (3.5)$$

Same as equation 3.4, N going to ∞, equation 3.5 becomes $\langle I(t)I(t+\tau)\rangle \leq \left\langle I(t)^2\right\rangle$, which implies that $g^{(2)}(\tau) \leq g^{(2)}(0)$.

Therefore in the limit of classical physics, $g^2(\tau)$ will respect two principles:

- $1 \leq g^{(2)}(0)$
- $g^{(2)}(\tau) \leq g^{(2)}(0)$

The second point gives a lower limit for $g^{(2)}(0)$ but no upper limit. But in fact, it is difficult to find a light with a $g^{(2)}(0) >> 2$. One can define a coherence time τ_c of the light beam, which defines the time-scale where intensity fluctuations are visible. It means that the intensity fluctuation at time t and $t+\tau$ will be completely uncorrelated with each other if $\tau \gg \tau_c$. We can define the intensity at time t as $I(t) = \langle I\rangle + \Delta I(t)$ with $\Delta I(t)$ the fluctuation at t from the mean value. Therefore $\langle \Delta I(t)\rangle = 0$ and we can deduce that:

$$\begin{aligned}
\langle I(t)I(t+\tau)\rangle_{\tau\gg\tau_c} &= \langle(\langle I\rangle + \Delta I(t))\,(\langle I\rangle + \Delta I(t+\tau))\rangle \\
&= \langle I\rangle^2 + \langle I\rangle\langle \Delta I(t)\rangle + \langle I\rangle\langle \Delta I(t+\tau)\rangle \\
&\quad + \langle \Delta I(t)\Delta I(t+\tau)\rangle \\
&= \langle I\rangle^2 \\
g^{(2)}(\tau \gg \tau_c) &= 1
\end{aligned} \quad (3.6)$$

One can notice that a perfect coherent light ($\tau_c = 0$) will have $\langle \Delta I(t)\rangle = 0\ \forall t$ and will therefore have $g^{(2)}(\tau) = 1\ \forall\tau$. We can show that this corresponds to a source with **Poissonian statistics of photon emission**. The most common example of Poissonian light is the monochromatic laser beam. All less coherent light will have $g^{(2)}(0) > 1$. This behavior is called bunching. **The two most common non-coherent sources are the chaotic light and the thermal light**. As an example, the $g^{(2)}(\tau)$ of a chaotic light will be presented in what follows.

Chaotic Light

Chaotic light is for example the light of a single spectral line of a discharge lamp. It will have intensity fluctuations on a time scale determined by τ_c. A discharge lamp works thanks to the emission from atoms at a given energy, corresponding to an electronic transition. Each atom of the discharge lamp will emit at the same energy $\hbar\omega_0$, but the phase of the electric field radiated by each atom will be different. The phase ϕ_i of the electric field E_i associated with each atom i will stay constant until a collision with another atom. Collisions are stochastic events and could be considered instantaneous, allowing us to disregard changes during collisions. In a first approximation, the collision will only induce a change in the phase of the electric field emitted by the two atoms but no change of the emission energy $\hbar\omega_0$. The lamp is constituted of a large number N of atoms, the total electric field amplitude at a given time t will be

$$\begin{aligned} E(t) &= E_1(t) + ... + E_N(t) \\ &= E_0 exp(-i\omega_0 t)\{exp(i\phi_1(t)) + ... + exp(i\phi_N(t))\} \end{aligned} \tag{3.7}$$

The intensity of the total electric $\bar{I}(t)$ field can be written as:

$$\bar{I}(t) = \frac{1}{2}\epsilon_0 c|E(t)|^2 \tag{3.8}$$

As collisions are stochastic events, the intensity average over time taken on a period much larger than τ_c, $\left\langle \bar{I}(t) \right\rangle$, will be given by:

$$\begin{aligned} \left\langle \bar{I}(t) \right\rangle &= \frac{1}{2}\epsilon_0 c E_0^2 \left\langle |exp(i\phi_1(t)) + ... + exp(i\phi_N(t))|^2 \right\rangle \\ &= \frac{1}{2}\epsilon_0 c E_0^2 N \end{aligned} \tag{3.9}$$

And

$$\begin{aligned}\left\langle \bar{I}(t)^2 \right\rangle &= \frac{1}{4}\epsilon_0 c E_0^4 \left\langle |exp(i\phi_1(t)) + ... + exp(i\phi_N(t))|^4 \right\rangle \\ &= \frac{1}{4}\epsilon_0 c E_0^4 \left(\sum_i \left\langle |exp(i\phi_i(t))|^4 \right\rangle + \sum_{i\neq j} \left\langle |2exp\left[i(\phi_i(t)+\phi_j(t))\right]|^2 \right\rangle \right) \\ &= \frac{1}{4}\epsilon_0 c E_0^4 \left(N + 2N(N-1)\right) \qquad (3.10)\end{aligned}$$

$$\frac{\left\langle \bar{I}(t)^2 \right\rangle}{\left\langle \bar{I}(t) \right\rangle^2} = \left(2 - \frac{1}{N}\right) \qquad (3.11)$$

Equations 3.9 and 3.10 are the results respectively for $\left\langle \bar{I}(t) \right\rangle$ and $\left\langle \bar{I}(t)^2 \right\rangle$ after taking into account that $\langle |exp\left[i(\phi_i(t)+\phi_j(t))\right]| \rangle = 0$ for $i \neq j$. We can consider that in a discharge lamp $N \to \infty$ therefore equation 3.11 becomes $g^{(2)}(0) = 2$. In fact one can show that $g^{(2)}(0) = 1 + exp\left(-2|\tau|/\tau_c\right)$, where τ_c can be related to the time between two collisions. τ_c is of the order of femtoseconds, which means that in experimental measurement where temporal resolution Δt is of the order of hundreds of picoseconds ($\Delta t \gg \tau_c$), the $g^{(2)}(\tau)$ of a chaotic light will appear flat and equal to 1.

From a classical point of view the most coherent light is the Poissonian light and is taken as a reference ($g^{(2)}(\tau) = 1 \ \forall\tau$). All other classical light will have a $g^{(2)}(0) > 1$, like the chaotic light where $g^{(2)}(0) = 2$. But in fact there is more coherent light than Poissonian light. However, only a quantum treatment reveals this possibility. Such light states are called quantum states of light. Among those, one can mention Fock states (number states), produced by single photons emitters, and squeezed states [153]. In this thesis, only Fock states have been used and therefore the next development concerns only single photon emitter.

Quantum Theory of the $g^{(2)}(\tau)$ Calculation

In quantum theory, the electromagnetic field is quantized. To treat the problem, we need to take into account the probability that photons are detected by the first or the second detector of the experiment. The HBT experiment is explained in detail in chapter 2, but the principle is reminded in figure 3.1.

We defined the $g^{(2)}(\tau)$ function by the average number of photons n_1 and n_2 detected with a certain delay τ on detectors D_1 and D_2, respectively:

$$g^{(2)}(\tau) = \frac{\langle n_1(t) n_2(t+\tau) \rangle}{\langle n_1(t) \rangle \langle n_2(t) \rangle} \qquad (3.12)$$

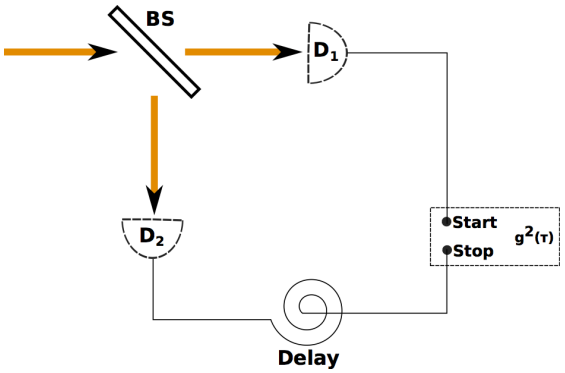

FIGURE 3.1: Principle of the HBT measurement. Light is coming from the left on a beam splitter (BS) and goes either to the detector D_1 or D_2. Detection of a photon in D_1 will start a clock that will be stop in D_2. All the events recorded are plot on a histogram giving after normalization the $g^{(2)}(\tau)$ function.

We define a_i^+ and a_i as respectively the creation and annihilation operators associated with the i^{th} detector:

$$g^{(2)}(\tau) = \frac{\langle a_1^+(t)a_2^+(t+\tau)a_2(t+\tau)a_1(t)\rangle}{\langle a_1^+(t)a_1(t)\rangle \langle a_2^+(t+\tau)a_2(t+\tau)\rangle} \tag{3.13}$$

We have seen that correlation appears at short delays. One can focus on the calculation of the $g^{(2)}(0)$ only, simplifying the calculation and allowing one to see difference with the classical calculation clearly. $g^{(2)}(0)$ can be written as:

$$g^{(2)}(0) = \frac{\langle a_1^+ a_2^+ a_2 a_1\rangle}{\langle a_1^+ a_1\rangle \langle a_2^+ a_2\rangle} \tag{3.14}$$

$$g^{(2)}(0) = \frac{(n-1)}{n} = 1 - \frac{1}{n} \tag{3.15}$$

Where n is the average number of photon emitted in average at the same time. The path from equation 3.14 to equation 3.15 can be found in chapter 8 of [36]. With equation 3.15, we see clearly that $g^{(2)}(0) < 1$ which is in complete contradiction with classical theory. This means that if emission is composed at any time by a well defined number of photons, it cannot be described classically. Moreover, single photon emitters that emit only one photon at a time will have an average number of photons $n = 1$ and therefore $g^{(2)}(0) = 0$. The coherence time τ_c of the system will be defined by the lifetime of the emitter τ_e and for long delay ($\tau \gg \tau_e$) $g^{(2)}(\tau) = 1$. Therefore $g^{(2)}(\tau)$ will have a dip at zero delay called the anti-bunching behavior and characteristic of single photon emitter. One can note that if we have N SPE in the system the average number of photons emitted by the sample will be $n = N$. Thus equation 3.15 for N single photon emitters becomes equation 3.16. Figure 3.2 shows the $g^{(2)}(\tau)$ function expected depending of the

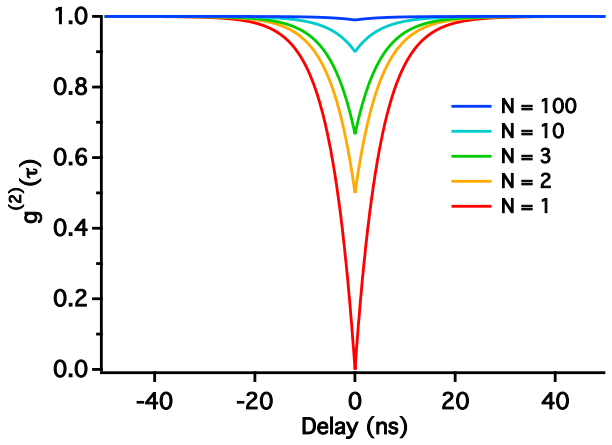

FIGURE 3.2: Theoretical $g^{(2)}(\tau)$ function (see equation 3.15) for a number N of SPE excited with a laser beam.

number N of SPE in the system.

$$g^{(2)}(0) = 1 - \frac{1}{N} \tag{3.16}$$

One can add that for a single photon emitter the probability to detect a photon at time $t = \tau$ when one has already been detected at time $t = 0$ is ruled by the population of the excited state. In the case of single photon emitters the radiative decay of an excited state is most of the case driven by an exponential law. We will therefore have :

$$g^{(2)}(0) = 1 - \frac{1}{N} exp(-(r + |\tau|)/\tau_e) \tag{3.17}$$

With τ_e the total lifetime of the excited state and r the pumping rate, which goes to zero for low laser power (below the saturation limit). It means that in the case of single photon emitters, excited at low beam currents, one can retrieve the lifetime by simply fitting the $g^{(2)}(\tau)$ function with an exponential.

3.1.2 PL Experiment

As mentioned in chapter 1, measuring the $g^{(2)}(\tau)$ function with a photoluminescence experiment has been extensively performed particularly for single photon source characterization [6, 77, 154]. In this section, I will introduce, in the case of PL measurement, the problem of background subtraction, experimental normalization and coherence losses.

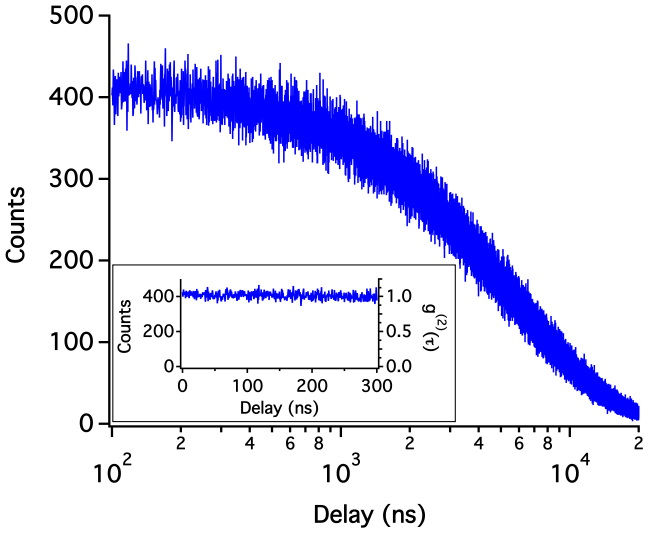

FIGURE 3.3: HBT histogram of the signal coming from a laser. The insert at the bottom is a magnification of the curve at small delay. The right axis is the value of $g^{(2)}(\tau)$ associated after normalization of the curve. The time sampling is 512 ps.

Normalization

The HBT experiment does not give directly the $g^{(2)}(\tau)$ function. After correction of the zero delay as explained in chapter 2, the HBT histogram of a laser beam looks like the one in figure 3.3. Contrary to the discussion of the latter section, we can see that the curve is not flat at very long delay due to an experimental artifact. Each time a photon arrives on detector D_1 (see figure 3.1), it starts a clock that will be stopped when a photon arrives on detector D_2. This means that, in order to record an event on D_2 at very long times, all photons, except the one hitting D_2, have to hit D_1. The probability to go either on D_1 or D_2 for each photon being 50/50, the chances of such an event are rare. This effect will become stronger as the number of counts per second (c/s) becomes higher. Therefore the histogram at long delay has to be discarded and the c/s kept sufficiently low (less than 5.10^5 c/s) to have a flat curve for small delay, but larger than τ_c.

As explained in the latter section, the $g^{(2)}(\tau)$ function is normalized to one for uncorrelated events. This means that for a Poissonian source $g^{(2)}(\tau) = 1$ for every τ. In a Poissonian emission, photons are randomly distributed in time, therefore N_{tot} the number of events recorded during a time T for delays between τ and $\tau + \Delta t$ is equal to $TN_1N_2\Delta t$. With N_1 and N_2 the number of counts per second recorded on the two detectors. To obtain the $g^{(2)}(\tau)$ function we divide the experimental curve by N_{tot}. For example, in the case of figure 3.3, $N_1 = 1.5 * 10^5$ c/s, $N_2 = 9.2 * 10^4$ c/s, T = 50 s and

Δt = 512 ps therefore N_{tot} = 400, 38 and the $g^{(2)}(\tau)$ function obtained after normalization is presented in figure 3.3. One can see that we have $g^{(2)}(\tau)$ = 1 for every τ, in the limit of small delay (< 300 ns) as explained before.

However, even if this is the most rigorous method to perform normalization, it is not always possible to have a constant c/s on each detector. An HBT measurement can last more than 10 minutes. For example, in our case, the electron beam current often decreases during the time of integration, or the emitter gets bleached under the incoming electron beam. In all these cases, N_1 and N_2 are not easy to evaluate and we use an imperfect but common method to normalize the signal by considering that for $\tau \gg \tau_c$, $g^{(2)}(\tau)$ = 1. Therefore we divide the $g^{(2)}$ function by the average number of counts at delay larger than τ_c ($\approx$ 300-400 ns).

Background Subtraction

In an experiment there is always a background intensity coming from emitters in the vicinity of the SPE. One way to take this intensity into account is to use the Poissonian background subtraction. Let us consider a Poissonian background B and a signal S coming from the SPE. The total signal is therefore S+B and we can consider that the two signals are not correlated. Therefore the $g^{(2)}(\tau)$ function is given by [155]:

$$\begin{aligned} g^{(2)}_{tot}(\tau) &= \frac{\langle (S(t)+B(t))\,(S(t+\tau)+B(t+\tau))\rangle}{\langle S(t)+B(t)\rangle^2} \\ &= \frac{\langle S(t)S(t+\tau)\rangle}{\langle S(t)+B(t)\rangle^2} + \frac{\langle B(t)B(t+\tau)\rangle}{\langle S(t)+B(t)\rangle^2} \\ &= \frac{\langle S(t)S(t+\tau)\rangle}{\langle S(t)+B(t)\rangle^2} + \frac{\langle B(t)B(t+\tau)\rangle}{\langle B(t)\rangle^2}\frac{\langle B(t)\rangle^2}{\langle S(t)+B(t)\rangle^2} \end{aligned} \tag{3.18}$$

B being a Poissonian noise, $g^{(2)}_B(\tau)$ = 1. If we define the signal to background ratio as $\rho = \frac{\langle S(t)\rangle}{\langle S(t)+B(t)\rangle}$ we can rewrite equation 3.18 as:

$$
\begin{aligned}
g^{(2)}_{tot}(\tau) &= \frac{\langle S(t)S(t+\tau)\rangle}{\langle S(t)+B(t)\rangle^2} + 1 - \rho^2 \\
&= \frac{\langle S(t)S(t+\tau)\rangle}{\langle S(t)\rangle^2}\frac{\langle S(t)\rangle^2}{\langle S(t)+B(t)\rangle^2} + 1 - \rho^2 \\
&= g^{(2)}_S(\tau)\rho^2 + 1 - \rho^2
\end{aligned} \tag{3.19}
$$

$$
\Rightarrow g^{(2)}_S(\tau) = \frac{g^{(2)}_{tot}(\tau) - (1-\rho^2)}{\rho^2} \tag{3.20}
$$

Equation 3.20 means that if we measure the signal to background ratio ρ you can retrieve the $g^{(2)}_S(\tau)$ of a single emitter.

Correlation Loss

Losses due to the different elements of the optical system have to be considered. There are three main sources of losses. First, losses in the collection system where only a fraction of the light emitted by the sample is collected. Second, losses due to the different optical components. And third, losses due to the non-perfect quantum efficiency of the detection process. All these losses select random photons from the original flux. The distribution obtained by random sampling of a chain of photons is more random than the previous distribution (chapter 5 of [36]). This means that measurement degrades the coherence of the flux of photons and at small integration time T the distribution appears completely random.

Thus SPE anti-bunching measurements will be particularly sensitive to losses because each loss phenomenon will bring the emission close to a Poissonian emission. Therefore efficiency of the system is primordial but it shows also the importance of long integration times to have a meaningful $g^{(2)}(\tau)$. This time will increase if the number of counts per second decreases.

3.2 HBT-CL on Diamond

In chapter 1 we introduced the NV center in diamond as a famous SPE. This point defect has been extensively studied thanks to photoluminescence [56, 78] and was therefore used as a test sample for anti-bunching measurement in an STEM.

3.2.1 Nanodiamonds in CL-STEM

Nano-diamonds are particularly well adapted to CL-STEM measurements because of their small thickness (less than 200 nm) and the ease of deposition on carbon grid. However it is common to find other point defects than NV centers [124, 141]. In CL, the presence of other defects can be a bigger problem than in PL experiment, because in CL, we excite at high energy and therefore all the different kinds of point defects present can be excited. For now, we cannot spectrally select the defect of interest by changing the excitation energy as in PL. The most commonly encountered in our case is the H3 center that emits around 530 nm while the NV^0 emits at 570 nm (see figure 3.4-a). Figure 3.4 shows a group of nano-diamonds where the two kinds of centers are present. In this case, each emitting nano-diamond has either one or the other type of defect. We can see the overlap of two signals. However thanks to the technique of spectral image (SPIM) explained in detail in chapter 2 and the spatial resolution of STEM, we can distinguish one nanodiamond from the others.

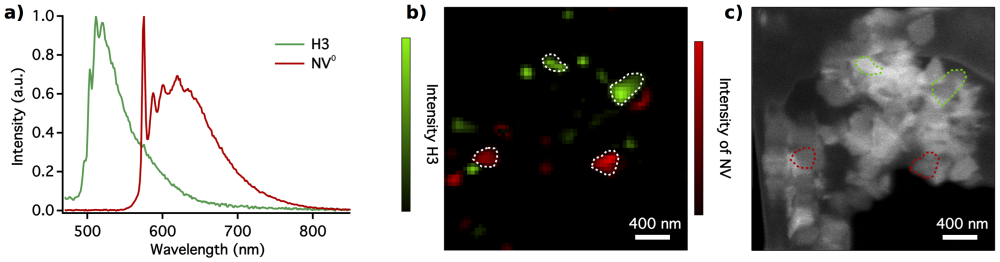

FIGURE 3.4: Example of two different kinds of color centers present in nanodiamonds. a) Normalized spectrum of H3 emission and NV^0 emission. b) Superposition of H3 and NV filtered maps extracted from a SPIM respectively at 515 ± 25 nm and 610 ± 40 nm. Some of the contrast of emitted diamonds are reproduced on the HADF image taken after the SPIM thanks to the HADF image acquired during the SPIM but not represented here.

However it is also possible to have both kinds of centers on the same nano-diamond, in figure 3.5 both centers are only separated by 50 nm. In figure 3.5-c) it is obvious that even with a spectral selection using an optical filter for the NV^0 defect (570-720 nm) part of the signal is coming from the tail of the H3 emission. The SPIM without special data treatment allowed us to distinguish the two centers, but H3 signal needs to be subtracted for $g^{(2)}(\tau)$ measurement as it will be explained in section 3.21.

The First HBT-CL Experiment

The first experiment of HBT-CL has been performed by L. Tizei and M. Kociak on an NV^0 center [2]. Results are reminded in figure 3.6. The normalization has been done

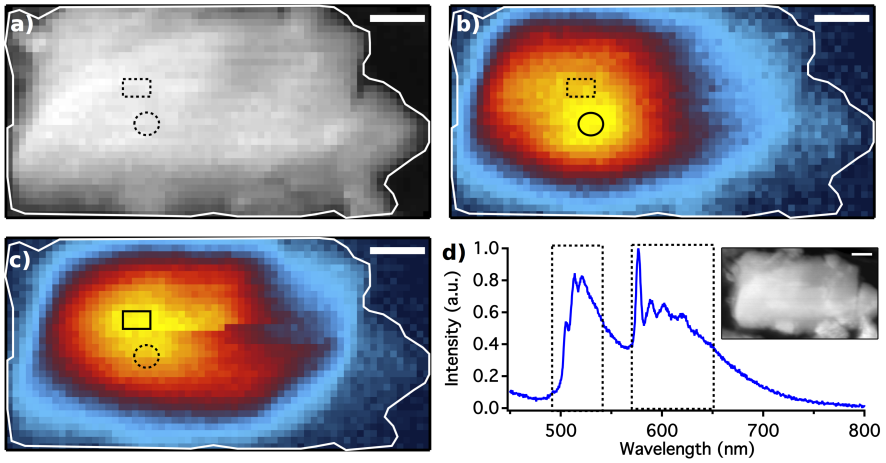

FIGURE 3.5: Spatial separation of NV^0 and H3. a) HADF image taken simultaneously with the SPIM from which filtered images of b) and c) are extracted. The white scale bar is 50 nm. b) Filtered image extracted from the SPIM at 610 ± 40 nm it corresponds to the NV^0 center and of the right dashed square in the spectrum. c) Filtered image at 515 ± 25 nm it corresponds to the H3 center and of the left dashed square in the spectrum d). Spectrum in d) is the sum of 70 pixels of the SPIM taken around the two color centers. The insert is an HADF image of the nano-diamond taken after the SPIM.

thanks to the value at large delay and a filter has been used to select the NV^0 emission (570-720 nm). Two $g^{(2)}(\tau)$ functions have been measured on the same nano-diamond separated by less than 150 nm. This proved the existence of SP emission in STEM. The fact that the $g^{(2)}(\tau)$ function changes between the two points, means that we can resolve $g^{(2)}$ with a resolution of at least 150 nm. The red area (see figure 3.6) has a $g^{(2)}(0) < 0.5$ proving that we excited close to an NV^0. Whereas in the excitation from the blue area we detected an SPE behavior since $g^{(2)}(0) < 1$ but the signal can come from multiple centers or a center and another defect. Unfortunately, no SPIM or spectrum was measured for this first experiment that would allow us to conclude on the second hypothesis. But this first experiment proved the possibility to do quantum optics with an STEM and showed the similarities between CL and PL experiment.

In addition, we have seen in the last section that for SPE the lifetime of the emitter can be measured by fitting the $g^{(2)}(\tau)$ curve with an exponential (equation 3.16). In the case presented here, the lifetime retrieved is $\tau_e = 18 \pm 4$ ns, which is compatible with lifetime measurements in PL [156]. This is in contrast with HBT experiments performed in electroluminescence (EL) where they find a lifetime close to 100 ns [37] unveiling that excitation mechanism is drastically different between EL and PL. Here it seems that excitation in CL and PL are close enough to give the same lifetime and the same emission spectrum.

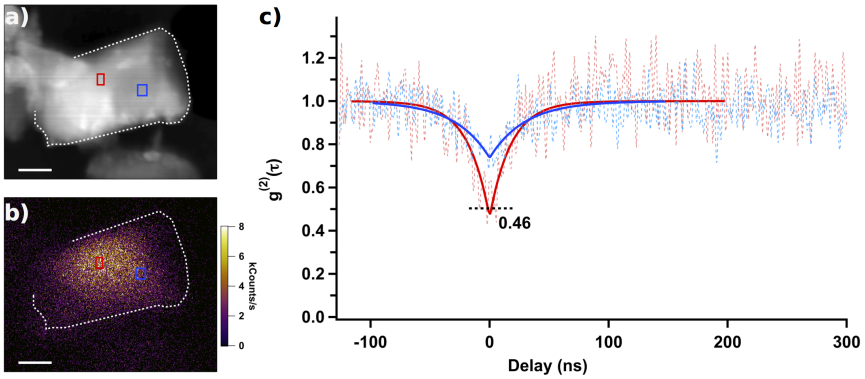

FIGURE 3.6: a) HADF image. b) Filtered images (570-720 nm) c) $g^{(2)}(\tau)$ function of the CL signal for two different excitations area noted by the red and blue squares on the HADF image in a). From [2]

The last point that needs to be discussed on this first experiment is the effect of saturation. Both NV^- [79, 154] and NV^0 [157] can be modeled as a three level system. The dark state in NV^- as been extensively studied and is responsible for a bunching behavior at small delay when the saturation is reached, as shown in figure 3.7. In the case of NV^0, nothing as significant occurs, however one can observe an important reduction of the lifetime when the saturation is reached. Indeed, the decay rate of the excited level is the sum of the pumping rate and of the spontaneous emission rate. Therefore, if there is pumping (i.e. saturation) the lifetime will be shorter. In our case, the lifetime measured is closed to the one expected without saturation, which seems to proves that even if we excite with fast electrons we are far from the saturation limit.

This first experiment shows that CL excitation is very similar to PL excitation in the case of the emission from single SPE: the anti-bunching behavior is retrieved, the lifetime is close to PL measurement and the saturation limit is not reached at standard excitation currents I = 100 pA (1.6 electron per ns). In order to go further on HBT-CL measurement, we applied on the next section the background subtraction technique to CL measurement, using the spatial resolution as a tool.

3.2.2 Background Subtraction in HBT-CL Experiment

We have seen above that the H3 emission tail acts as a background to the NV^0 signal in the spectral window collected for the $g^{(2)}(\tau)$ measurements (570-720 nm). Such background impacts the $g^{(2)}(\tau)$ measurement. In particular, it limits the anti-bunching at zero delay for single photon emitters. However, within certain limits, if the background

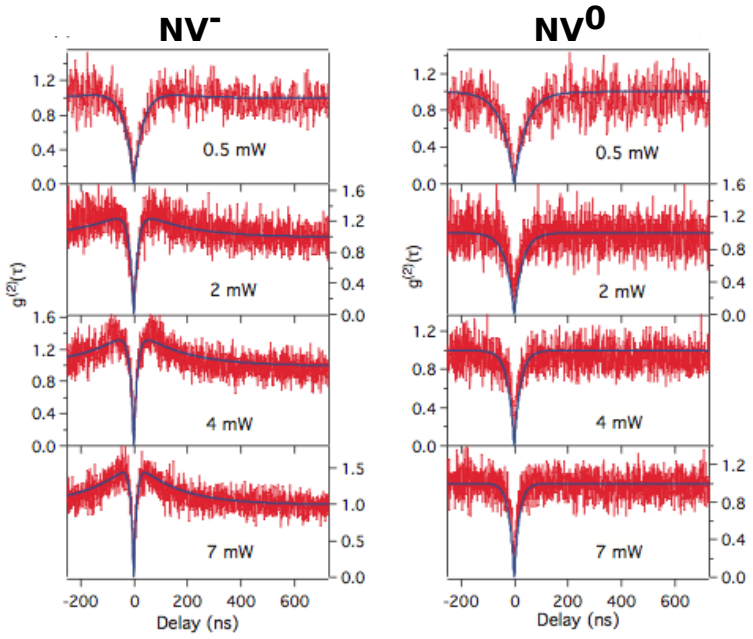

FIGURE 3.7: The left and right column are the autocorrelation function measurements for respectively NV^- and NV^0 at different currents. All measurements are realized under the same experimental conditions and at room temperature. From [158].

can be properly quantified, its effect can be subtracted from the $g^{(2)}(\tau)$ curves as explained in section 3.1.2. Results from this section are published in [159]. We define the signal to background ratio (SBR) as:

$$SBR = \frac{I_{NV^0}}{I_{NV^0} + I_{H3}} \tag{3.21}$$

where I_{NV^0} and I_{H3} are the integrated intensities on the spectral window used for $g^{(2)}(\tau)$ measurement (dashed line in figure 3.8-a), of respectively the NV^0 and the H3 signals. The H3 emission background tail has been modeled by an exponential curve (see figure 3.8). To ensure the reproducibility of the fit, we have measured it on seven nano-particles containing only H3 emission. Although not supported by any theoretical statement, figure 3.8-b demonstrates that the exponential fit is a good model for H3 emission background. Despite the fact that background removal techniques are not widely applied in CL, they are widespread and mature in EELS where they are used routinely to treat spectral images often relying on *ad hoc* background functions [20].

With this information we estimated the contribution of H3 emission to the total detected intensity of the emission spectrum taken on the same area as the HBT measurement (figure 3.8). Considering the fit parameters obtained from an interpolation of the H3

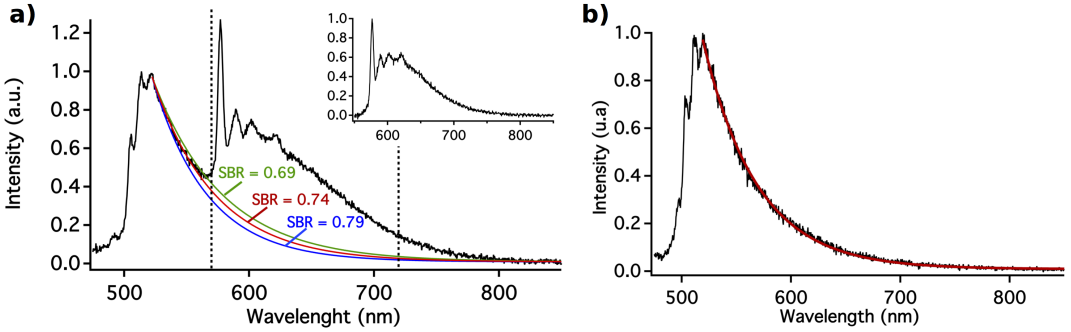

FIGURE 3.8: a) H3 and NV^0 signals from the nanodiamond shown in figure 3.5 (inset shows the NV^0 signal after background subtraction). The dotted lines indicate the wavelength range, 570-720 nm, defined by filters and used for the HBT experiments. The different colored curves show the fit to the background (red) and the range of confidence of the fit (blue and green). The signal to background ratio (SBR) is 0.74 for this spectrum, with a one sigma confidence interval between 0.69 and 0.78. b) H3 signal from a different diamond nanoparticle used to validate the exponential model used for the background subtraction

signal (with the decay between 520 and 550 nm and the flat region above 750 nm), we have estimated the contribution of the H3 emission to be 26% of the total intensity $I_{NV^0} + I_{H3}$, thus an SBR = 0.74. Considering the error on the fit coefficients of the H3 emission tail, this contribution is between 21% (SBR = 0.79) and 31% (SBR = 0.69), validating this fitting procedure as a good tool to estimate the background for this particular system.

The $g^{(2)}(\tau)$ was measured in a single diamond nano-particle of size 370 nm x 180 nm (see figure 3.9). During the acquisition, the electron beam was kept scanning a region 42 nm x 48 nm wide (rectangle in Fig. 4). The total acquisition time was 260 s. The background subtracted experimental data is shown in gray in 3.9. To measure the depth of the anti-bunching dip we have fit the curve with an exponential model (equation 3.17). A fit by this function of the non processed data results in $g^{(2)}(0) = 0.9$ (which is shown in black in figure 3.9). For this curve $\tau_e = 34 \pm 4$ ns, which is consistent with PL measurements in nano-diamond [156]. However, the emission spectrum of figure 3.8-a shows that in the wavelength integration window used for the intensity correlation measurement we have a non-negligible contribution of H3 color centers emission. Using the exponential model described previously we have estimated this H3 emission background to represent 26 ± 5 % of the total intensity.

A flat $g^{(2)}(\tau)$ is taken in the nano-diamond where only the H3 center emits. Therefore we can subtract its contribution from the measurement as a Poissonian signal (see equation 3.20). This subtraction, along with the confidence limits, is shown in figure 3.9 (red, green, and blue curves, respectively). The background subtracted data fit gives $g^{(2)}(0) = 0.81$. The confidence interval of this fit to the treated data is represented by the blue and

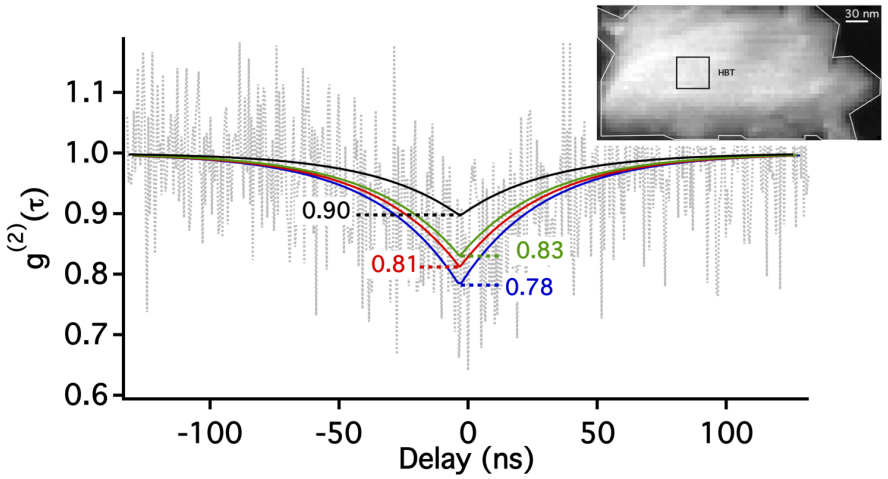

FIGURE 3.9: Second order correlation function $g^{(2)}(\tau)$ measurement. The black curve corresponds to the fit of the non-processed $g^{(2)}(\tau)$ (data not shown) by the exponential function (equation 3.17) leading to a zero delay anti-bunching dip $g^{(2)}(0) = 0.90$. The red curve is a fit to the background subtracted data inferred from the spectrum image of figure 3.8, and shown as a dotted gray curve, having a zero delay dip $g^{(2)}(0) = 0.81$. The green and blue curves show the confidence interval.

green curves in figure 3.9, which results in $g^{(2)}(0) = 0.78$ and $g^{(2)}(0) = 0.83$, respectively (calculated based on the uncertainty on the H3 background fit). If we refer to equation 3.16 we deduce the number of centers excited from the value of $g^{(2)}(0)$, however as it will be explained in chapter 4, another effect needs to be taken into account when more than one single emitter are present. This effect can change drastically the value of the dip.

The H3 signal subtraction has been applied to other nano-diamonds, a second example is presented in figure 3.10. In this case we are able to distinguish two NV centers only separated by 150 nm. On the filtered image we can see that the two emissions are well separated, the H3 signal being probably localized close to the first center (blue area on the HADF image). However the signal was too weak to allow us to perform a spectrum image of the nano-diamond limiting the localization of the different signals.

3.3 SPE in h-BN

3.3.1 Boron Nitride optical properties

Light in the UV range has the strong advantage to propagate through air without significant attenuation. Moreover, UV devices have important technological interest for example in microbial sterilization of surgery tools. UV sources have been therefore investigated over the past decades. And in this particular case, CL has a real advantage

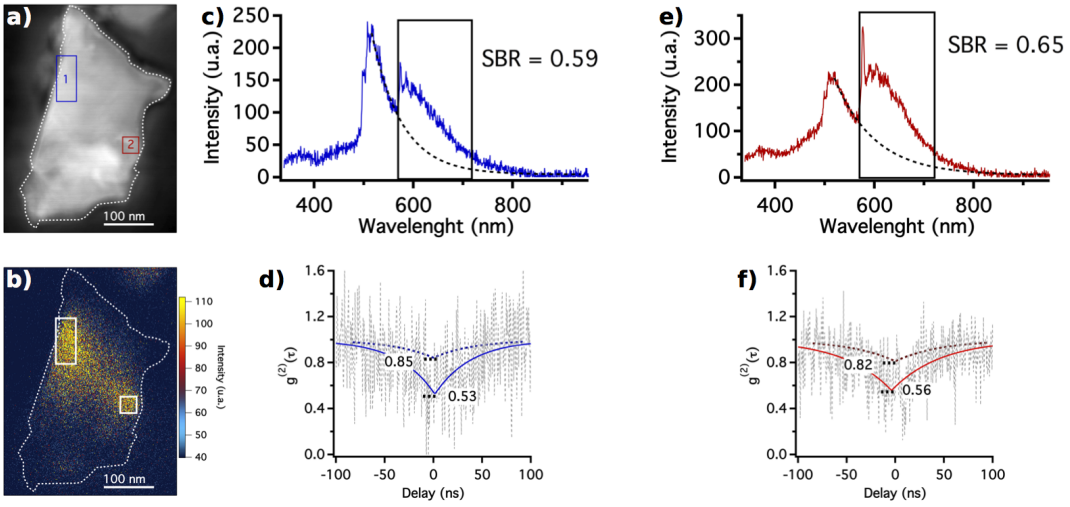

FIGURE 3.10: Second order correlation function $g^{(2)}(\tau)$ measurement on a single nanodiamond. The blue and red squares on the HADF image a) represent the two areas where HBT measurements have been performed, shown respectively in d) and f). The value before and after H3 signal subtraction taking the SBR of the two emissions spectra c) and e) is shown. The filtered images (570-720 nm) in b) give insight into the spectral distributions of the two centers.

because it allows easy excitation in the UV range due to the high energy of incoming electrons. III-N nano-structured materials, like those presented in chapter 1, focused most of the attention for a long time. However, the low efficiency of AlN LEDs due to multiple defects in the AlN matrix [160, 161] forced new research. Hexagonal boron nitride (h-BN) is an attracting alternative to III-N materials. It is a layered material with sp^2 hybridation like graphene. h-BN is especially known for its strong luminescence peak at 5.75 eV [54] due to a Frenkel type exciton [162, 163]. But, obtaining an h-BN crystal with a single emission peak demands a high quality crystal without defects. For most cases the emission spectrum is constituted of a series of sharp peaks localized between 5.3-5.9 eV close to the main exciton, as shown in figure 3.11. Romain Bourrellier, a former PhD student of the team showed, thanks to the CL-STEM system, that those sharp peaks were related to local changes in the layer stacking order [164].

In addition to these multiple sharp peaks close to the exciton signature, an emission broad band (3.2-4.5 eV) can appear but its nature is for now unknown. h-BN is a material that can accommodate several defects (triangular defects [165], grain boundaries [166], stacking faults [167], reconstructed edges [168]). Among them, one defect, usually attributed to the presence of oxygen [169] appears with a zero phonon line around 4.1 eV [26, 170] and phonon replicas at 3.73 and 3.91 eV. These three peaks are superimposed to the broad band signal as shown in figure 3.12. Romain Bourrellier has shown that the localization of the intensity associated to each peak is the same, and localized over 80 nm. This is similar to the NV^0 center in diamond where the zero phonon line at 2.16

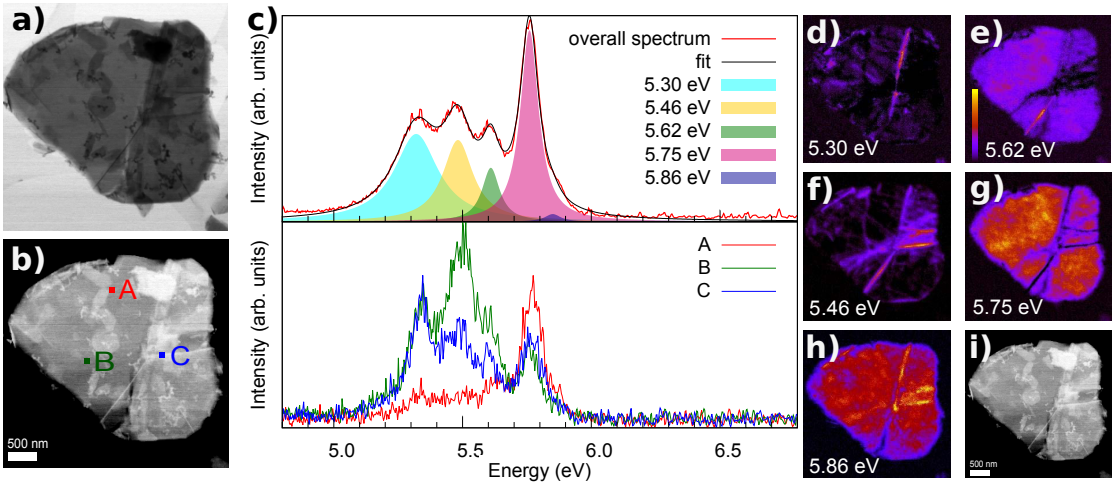

FIGURE 3.11: Figure from [164]. a) Bright field and b) dark field images of an individual BN flake. c) Overall emission spectrum of the flake and individual spectra taken at specific probe positions indicated in panel b). d-h) Emission maps for each individual emission peak. Intensity is normalized independently within each individual map.

eV is followed by multiple phonon replicas the first two being at 2.11 eV and 2.07 eV [124, 141]. The localization of the signal is a clue to the nature of the emission, however only an HBT experiment can prove the quantum nature of the emission.

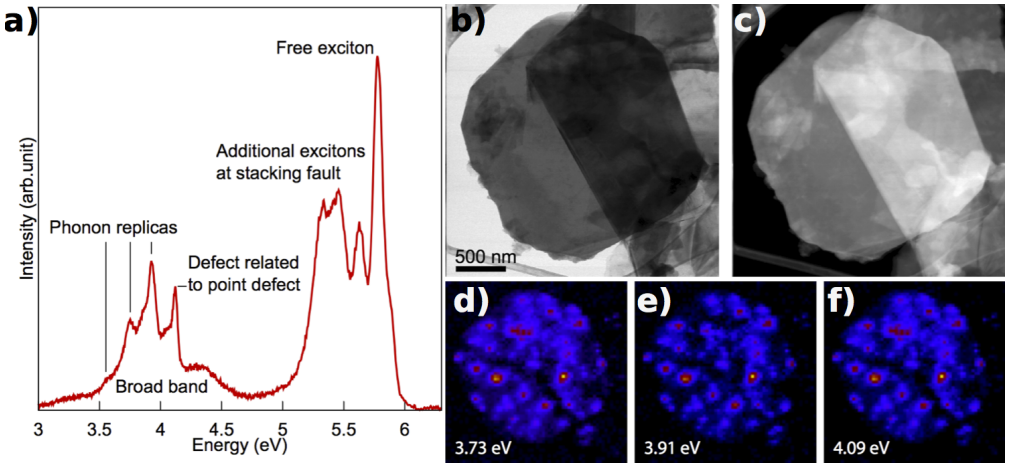

FIGURE 3.12: From [171]. a) Spectrum of an h-BN flake where all kinds of signal presented appear. b)-c) respectively the ADF and BF image of an h-BN flake. d)-f) filtered images of the SPIM taken on the h-BN flake of b) at the three energy peaks.

3.3.2 HBT-CL on h-BN

In order to perform the HBT experiment we used the second HBT system described in chapter 2 working in the near-UV range, with a band pass filter set at 300-340 nm. The time sampling of the HBT experiment was Δt = 0.512 ps. Figure 3.13 shows the

anti-bunching behavior of the defect emission, proving its quantum character for the first time. One can add that in this particular case, CL in an STEM was an asset. Indeed, it allowed to chracterize the localization of the defect (≈ 80 nm) and to perform HBT measurement on single point defect very easily. In this case, PL measurements would not permit to select one single defect as shown in figure 3.12. In this first experiment the defect emitting at 10^5 c/s, yields a $g^{(2)}(\tau)$ with a high signal to noise ratio in only 40 s. However, after about 20 seconds of recording, the dip at zero delay began to decrease while the count rate on each detector increased. The spectrum shown in figure 3.13 has been recorded after the 40 s of beam exposure. One can see the strong presence of the broad band added to the point defect signal. A second $g^{(2)}(\tau)$ function was acquired after the spectrum measurement at the same place and the dip at zero delay was no longer visible. The lifetime retrieved from the first of the $g^{(2)}(\tau)$ functions gives $\tau = 2.5 \pm 0.1$ ns in perfect agreement with PL measurements [170].

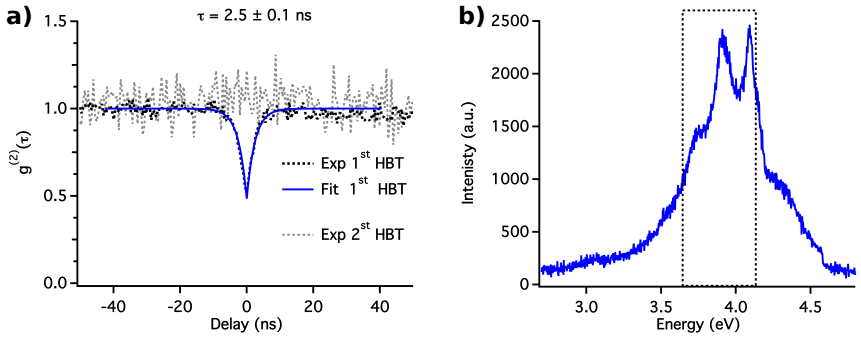

FIGURE 3.13: a) $g^{(2)}(\tau)$ function of the first and second measurements. The first one was recorded during 40 s and the second was taken after the spectrum shown in b).

To better understand this first experiment, a second one has been performed on another of these point defects. This time, the $g^{(2)}(\tau)$ was acquired in only 6 s. Then a first spectrum was recorded. The defect was then exposed during 150 s to the electron beam. After that, a second spectrum and a $g^{(2)}(\tau)$ were acquired. The results are shown in figure 3.14. One can see the increase of the broad band between the two measurements (Figures 3.14 c) and e)), decreasing the signal to background ratio respectively SBR = 0.83 and SBR = 0.72. This increase of the broad band emission leads to a reduction of the dip at zero delay, going from $g^{(2)}(0) = 0.43$ to $g^{(2)}(0) = 0.58$, respectively. By applying the background subtraction technique presented on section 3.21 we retrieve $g^{(2)}(0) = 0.2$ in the two measurements. The value of 0.2 is not zero but considering the time sampling of 0.512 ps and the lifetime of the emitter (2.5 ns), it is certainly the best we could reach. This experiment seems to prove that the broad band signal is increasing under exposure to the electron beam (see figure 3.14) and is responsible for the reduction of the dip at zero delay in the first experiment, and that the defect behavior stays unchanged. One can add that, as we can see in figure 3.14-b, the broad

band signal is present everywhere around the point defect.Therefore, in a PL experiment, the excitation of an area of more than 400 nm around the point defect would lead to a low SBR rendering any HBT measurement difficult. Here the spatial resolution allowed us to select only the area of interest.

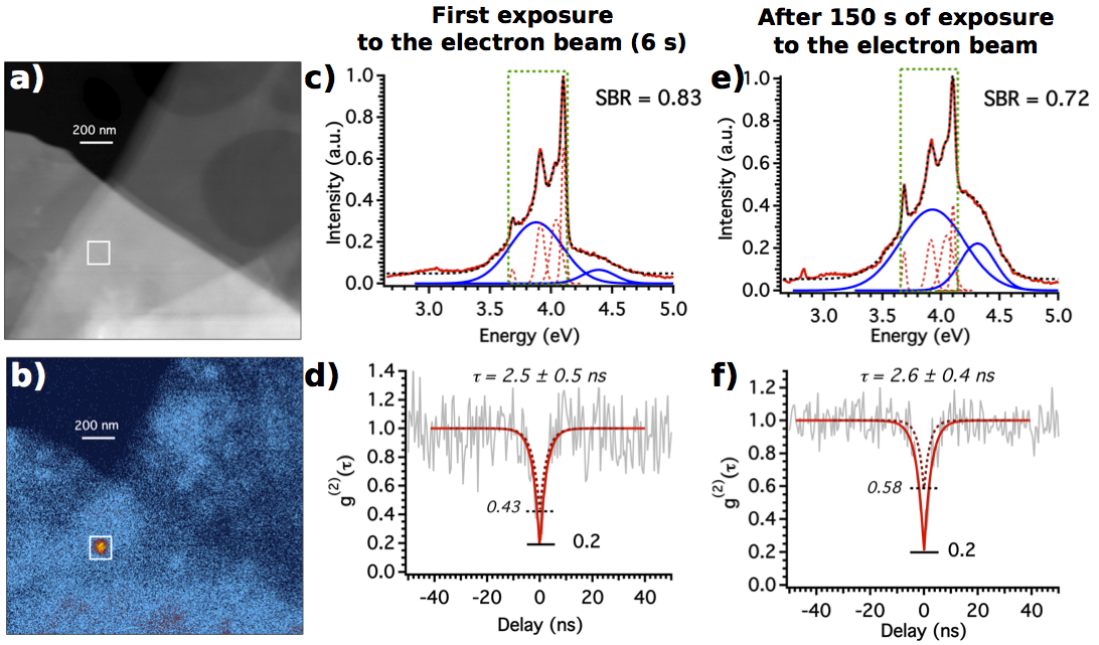

FIGURE 3.14: a) ADF image of the h-BN flake under study. b) filtered image (300-320 nm) of the emission synchronized with ADF in a). The localization of the point defect is clearly visible (highlighted by the white square) as the presence of the broad band everywhere in the flake. c) spectrum taken just after the recording of the $g^{(2)}(\tau)$ function of d). After about 150s of electron beam exposure (the probe was scanning the white area in a) a second spectrum was taken e) then the second $g^{(2)}(\tau)$ function f).

However the question remains of why the electron beam has such an influence on the broad band emission. Being unable to characterize its nature we couldn't answer this question. In the literature, as it was already mentioned, this defect is associated with the presence of oxygen [26, 170]. This is indicated by the high concentration of defects present in h-BN heated at two hundreds degrees in an oxygen environment whereas after reduction of the same h-BN flake the defect emission is missing. Nevertheless, we were not able to corroborate this statement by EELS measurements. Indeed the point defect in CL is visible only on very thick h-BN flakes, certainly due to the small probability of interaction of the electron beam with thin layers, whereas EELS measurements are only possible on thin h-BN flakes. We couldn't find, for now, the right sample that would exhibit the two signals at the same time.

In conclusion, we exposed in this chapter the feasibility of HBT experiments in an STEM for SPE. Thanks to the complete set of information at our disposal: HADF images,

spectrum images and HBT measurements, we are able to perform a full characterization of the emission, its localization and its quantum characteristics. In the case of h-BN, we have seen that the CL-STEM is an appropriate tool for studies in the UV emission range, the defect localization and spatial filtering in regards to the broad band signal appearing at the same energy. However in this case the electron beam changes the emission properties of the h-BN defect increasing the broad band signal. In the two examples, NV and h-BN defects, the similarity between CL and PL is strong. However, we will see in the next chapter that despite these similarities in the case of fast electrons excitation of multiple SPE, the $g^{(2)}(\tau)$ function takes an unexpected form.

Chapter 4

Intensity Interferometry Experiment: Photon Bunching in Cathodoluminescence

- Just believe everything I tell you, and it will all be very, very simple.
- Ah, well, I'm not sure I believe that

Douglas Adam

4.1 Observation of the Bunching Effect

In the lastest chapter we have seen that if only one SPE is excited by the electron beam we retrieve the anti-bunching behavior characterized by a dip at zero delay (τ = 0) of the autocorrelation function ($g^{(2)}(0) < 1$). As explained in details in chapter 3, this proves that the electron beam doesn't change the statistics of single photon emitters, at least for point defects in materials. In this chapter we will see the consequences on the autocorrelation function ($g^{(2)}(\tau)$) of the excitation of several SPE at a time with an electron beam. As the autocorrelation function obtained in PL and CL experiment will be different in this chapter, from now on we will distinguish between the two by noting respectively $g^{(2)}_{\mathrm{PL}}(\tau)$ and $g^{(2)}_{\mathrm{CL}}(\tau)$. The differences with PL experiment will be explained thanks to two models, one using the Monte Carlo method to simulate the $g^{(2)}_{\mathrm{CL}}(\tau)$ of a particle with a high number of centers ($N > 10$) and a second one, analytical, for thin particles ($L < 30$ nm) with a few number of centers. The main results of this chapter are published in [27].

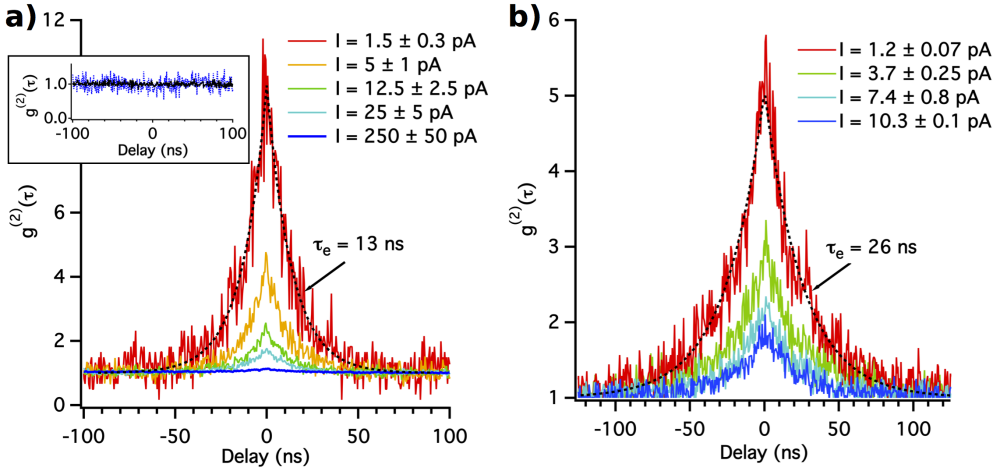

FIGURE 4.1: $g^{(2)}_{\mathrm{CL}}(\tau)$ measurement for two different NDs. For intensities I ranging from 1.2 to 200 pA. Discussion on the measurement of I is done in section 4.2.2. Each measurement lasted between 5 and 20 mn. The characteristic time τ_e was retrieved using an exponential fit to the bunching curves. τ_e measured for the cure at lower current is indicated in each figure, the fit performed on each $g^{(2)}_{\mathrm{CL}}(\tau)$ function gives respectively for a) and b) 13 ± 1 and 26 ± 1 ns. Inset : PL $g^{(2)}_{\mathrm{PL}}(\tau)$ measurements performed at two different laser excitation powers on another ND from the same batch.

4.1.1 Observation on Nano-Diamond and h-BN

If we excite N SPEs in a PL experiment, as explained in chapter 3, $g^{(2)}_{\mathrm{PL}}(0) = 1 - 1/N$. This means that at high N value, $g^{(2)}_{\mathrm{PL}}(0) \approx 1$ and the experimental curve seems flat. Moreover below the saturation limit, $g^{(2)}_{\mathrm{PL}}(\tau)$ doesn't depend on the current.

To investigate the differences between CL and PL statistics, we measured the $g^{(2)}_{\mathrm{CL}}(\tau)$ from several diamond nanocrystals [172] (nanodiamond (ND) with a mean size $\approx$ 100 nm) each containing a large number, $N \approx 900$, of NV centers [173] using the same setup as in chapter 3. The $g^{(2)}_{\mathrm{CL}}(\tau)$ function is inferred from the normalization of the time-delay histogram to 1 at long time delays, the justification for the normalization will be explained below. Figure 4.1 displays a representative experimental data set for two different NDs. One can note that a bunching $g^{(2)}_{\mathrm{CL}}(\tau) > 1$ peak is observed at all intensities for the studied NDs and the $g^{(2)}_{\mathrm{CL}}(\tau)$ value increases upon a decrease of the electron beam current. In sharp contrast, a $g^{(2)}_{\mathrm{PL}}(\tau)$ taken well below the saturation power in a confocal geometry results in a flat $g^{(2)}_{\mathrm{PL}}(\tau) \approx 1$ (inset of Figure 4.1), as expected. $g^{(2)}_{\mathrm{CL}}(\tau) \approx 1$ is also retrieved at high excitation current (typically 200 pA, see figure 4.1-a). The appearance of a bunching peak will later be called the "bunching effect".

The characteristic time τ_e, extracted from an exponential fit $g^{(2)}_{\mathrm{CL}}(\tau) = 1 + g_e exp(-|\tau|/\tau_e)$, is similar for all the $g^{(2)}_{\mathrm{CL}}(\tau)$ measured on the same nanodiamond and lie between 10 and 30 ns in all the nearly 100 investigated NDs (respectively 13 ± 1 and 26 ± 1 ns in

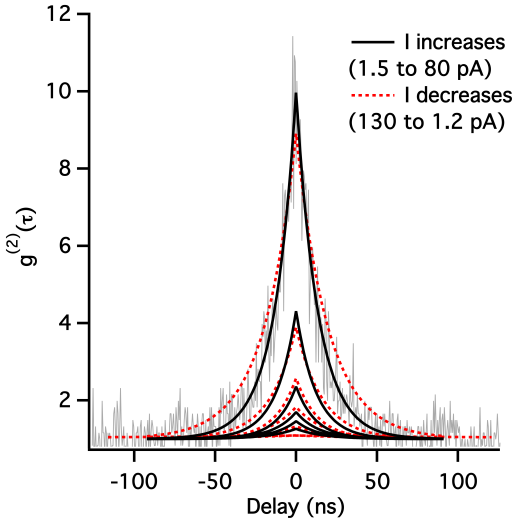

FIGURE 4.2: Reversibility of the bunching effect. On the same nanodiamond the current was first increased (black curves) until complete disappearance of the bunching effect ($g^{(2)}_{\mathrm{CL}}(\tau) \approx 1$) then decreased again until 1.2 pA (red dashed curves). τ_e deduced from the second series (red curves) was larger than from the first series.

figure 4.1), which is compatible with the NV^0 center excitation lifetime in NDs [156]. As shown in figure 4.2, the bunching effect with similar peak intensity value can be retrieved by diminishing the electron excitation current again, indicating that the latter effect is reversible. However, in the case of figure 4.2, the current was first increased until complete disappearance of the bunching effect ($g^{(2)}_{\mathrm{CL}}(\tau) \approx 1$) then decreased again until 1.2 pA. One can note that the τ_e found for the second series of measurements (decrease of the current down to 1.2 pA) is higher, $\tau_e = 13 \pm 1$ ns for the first series and $\tau_e = 18 \pm 2$ ns for the second series. This difference will be explained in section 4.2.3.

The same kind of experiment was performed on the h-BN defect shown to be an SPE in chapter 3. The HBT set-up used for the measurement of defects in h-BN is different from the one used for the nanodiamond (see chapter 2 for details); in particular we used a band pass filter set at 300-340 nm. This proves that, whatever the set-up, the bunching effect is present. The time resolution of the HBT experiment was 128 ps and each measurement lasted between 10 and 60 s. Results are shown in figure 4.3. For this point defect, τ_e measured for different defects lies between 1 and 3 ns, which is also compatible with known lifetime values of the defect [26]. One can note that in the case of h-BN $g^{(2)}(0) \geq 50$ at low current.

For all these experiments, the normalization was done by normalizing the time-delay histogram to 1 at long time delays. As explained in chapter 3, this is not the most rigorous way to proceed. However, due to the long lasting time of exposure, some of the defect centers stop emitting and thus the count rate in each detector is not constant.

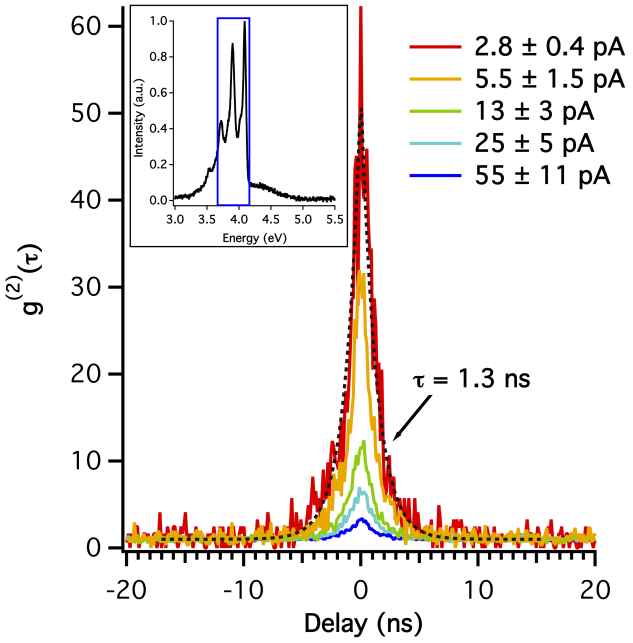

FIGURE 4.3: $g^{(2)}_{\mathrm{CL}}(\tau)$ measurement on h-BN. For intensities I ranging from 2.8 to 55 pA. Each measurement lasted between 10 and 60 seconds. The characteristic time τ_e was retrieved using an exponential fit of the bunching curves with a value $\tau_e = 1.2 \pm 0.1$ ns. τ_e measured for the curve at lower current is indicated on the figure. **Inset** emission spectrum measured at the location of the HBT-CL measurement.

Without a precise recording of the count rate on each detector during the experiment, the normalization by the method explained in chapter 3 is not precise. However in order to make sure that there is no hidden effect due to the normalization, we checked the order of magnitude. The result is shown in figure 4.4, with the c/s of each detectors N = 5000 c/s, the time sampling Δ = 512 ps and the total integration time T = 2600 s. After normalization we found at long delay $g^{(2)}_{\mathrm{CL}}(\tau)$ = 0.93, which seems right given the approximation. In what follows, we have therefore normalized using the long time delay value.

In conclusion, in sharp contrast with what can be observed under laser excitation, the $g^{(2)}_{CL}(\tau)$ can be:

- A huge bunching at zero delay $g^{(2)}_{\mathrm{CL}}(0) >> 1$
- The lower the current, the higher the bunching peak amplitude
- A characteristic correlation time τ_e similar to the lifetime of the emitter.

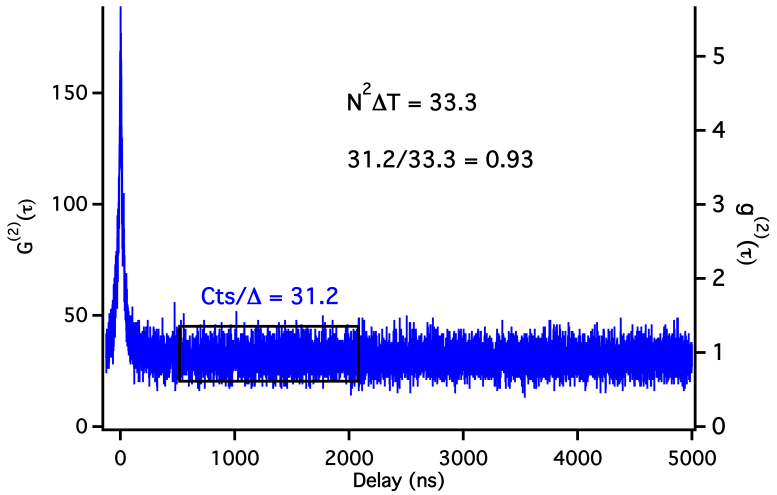

FIGURE 4.4: Normalization of a $g^{(2)}_{\mathrm{CL}}(\tau)$ with bunching using the method exposed in chapter 3. In this case the number of counts per second N of each detector was equal to $5000c/s$, the time resolution Δ = 512 ps and the total integration time T = 2600 s. The left and right axes are respectively the values of the $g^{(2)}(\tau)$ before and after normalization.

4.1.2 Heuristic Model

Photon bunching is well known in PL. However, zero-delay bunching appears at the pico or femtosecond time scales for thermal light [174], amplified spontaneous sources [175], and semiconductor microcavities in the strong coupling regime [176]; it has been also observed at the nanosecond time scale in specific cases (quantum dots in cavities [177] or coupled to plasmons [178], superradiant emitters in cavities [179]). Bunching is also observed in single-emitter fluorescence (organic dyes in particular) due to intersystem crossing from the excited state to metastable states, and in fluorescence correlation spectroscopy due to the fluctuations of the number of emitters in the excitation volume. However, these photon bunchings take place at nonzero time delays [180]. Nanosecond timescale bunching was also observed due to amplitude fluctuations of a semiconductor nanolaser [181]. A transition of a system from an incoherent state to a coherent state like a Bose-Einstein condensate or a lasing state can also produce bunching of light. Nonetheless, the transition to a coherent state is accompanied by a drastic change on the spectral emission [176, 182–184] which is not the case here as shown in figure 4.5. Contrary to PL, as discussed in chapter 3, in our case $g^{(2)}(0) \geq 2$ at low excitation current amplitudes. Therefore, the observed effect has to stem from another cause. In summary, all previous reports of photon bunching depart from our observations, which therefore require a different interpretation.

Synchronizing the emission from multiple emitters may lead to bunching. Synchronized emission can happen when two or more centers are excited at the same

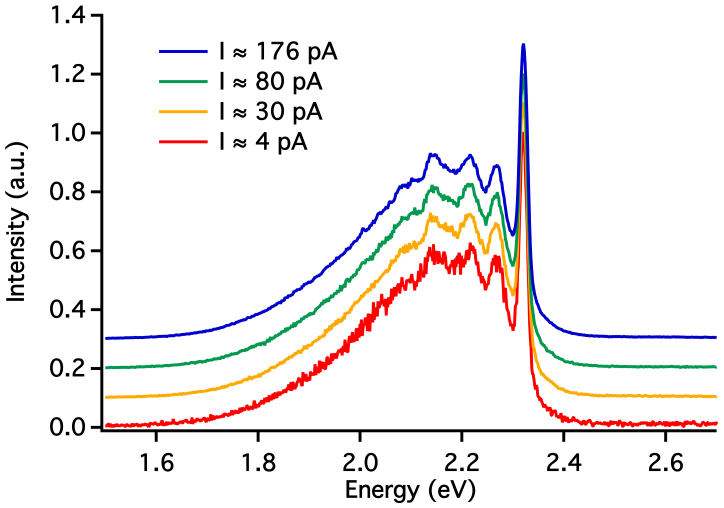

FIGURE 4.5: NV^0 spectrum emission from current laying between 4 and 176 pA. A vertical offset was added to increase the visibility. Despite the bunching behavior observed at low current no spectrum variation is visible.

time. It is worth noting that even for current values corresponding to less than 1 incoming electron per excited-state lifetime (typically $I < 24$ pA for NVs), the bunching effect is present. This clearly indicates that the photon correlations are not related to incoming electron correlations, but **are the result of a single electron excitation mechanism**.

In the case of a photon exciting a semiconductor, the excitation energy is only slightly larger than that of the emission. A single e-h pair is created, exciting at most one center. In contrast, an electron creates bulk plasmons of high energy ($E_p \approx 30$ eV in diamond) [20]. From this, there are two possibilities to explain the bunching. One is the creation of multiple e-h pairs originating from the same plasmon decay, an event made possible by the high energy of the plasmon compared to the gap energy ($E_g \approx 5$ eV). The second is the creation of multiple e-h pairs that may stem from two different plasmons. Whatever the mechanism, all these e-h pairs may excite several centers at once. If at least 2 centers are excited by the recombinations of e-h pairs coming from the same single electron, there is a high probability that at least two photons will be emitted in a given time window. Therefore, each electron produces a packet of photons. If the electrons are sufficiently separated in time, the HBT interferometer will receive well-separated packets of photons, leading to bunching. As the incoming electron current increases, packets of photons produced by different electrons will arrive closer and closer in time until they become indistinguishable. Thus, increasing I will blur the bunching effect. As the electron arrival time statistics are Poissonian, at high I, we have $g^{(2)}_{\mathrm{CL}}(\tau) \approx g^{(2)}_{\mathrm{PL}}(\tau)$. The time scale of a packet of photons produced by one electron is approximatively the

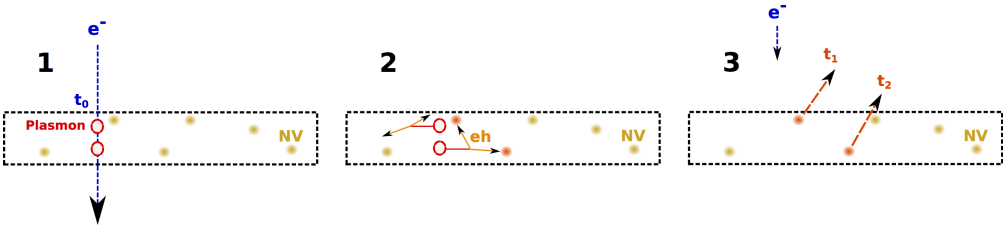

FIGURE 4.6: Example of a possible chain of events from the excitation by an electron beam (blue line) of a nano-diamond (dashed square) to the emission of photons. 1- The electron e^- interacts with the sample at time t_0 and plasmons (red circle) are created. 2- They decay into e-h pairs (orange arrow) and each created e-h pair can excite an NV center (yellow point). 3- Each excited NV center emits a photon (orange dashed arrow) at times t_1 and t_2, respectively, before a second electron arrives.

lifetime of the emitters; thus, the width of the bunching peak is related to the emitter lifetime. Figure 4.6 summarizes the bunching mechanism.

4.2 Monte Carlo Model

4.2.1 Description

Based on this analysis, we developed a Monte Carlo method to calculate the photon emission probability as a function of time for emitters excited by electrons. We then retrieved the $g^{(2)}_{\mathrm{CL}}(\tau)$ function by calculating the delay between emitted photons. In this method the number of centers available for the electron hole pairs is considered constant which means that we didn't consider saturation effects. This model is therefore valid if there is a large number of centers available ($N \geq 10$). Because the exact number of e-h pair created per plasmon and the mechanism of e-h pairs production vary in the literature [21, 28], we evaluated several models in which we changed the plasmon decay mechanism, with either exactly m_{eh} e-h pairs produced per plasmon or a Poissonian distribution of e-h pairs with mean value m_{eh}.

In all cases, as represented in figure 4.6, we define a chain of events made up of:

1. The creation of n_{pl} plasmons by an electron with probability $P_{\mathrm{el}}(n_{\mathrm{pl}})$[20]
2. Decay of plasmons into either a constant number m_{eh} of eh pair or a number defined by a Poissonian distribution with mean value m_{eh}.
3. The excitation of centers by the e-h pairs happening a few picoseconds later with probability P_{int}

4. The radiative relaxation, at time t_{rad} for a center (lifetime τ_e) excited at time t_0, with probability P_{rad}

The first three steps take place simultaneously compared to the lifetime of the emitter. In order to simulate $g^{(2)}(\tau)$ we need to generate an ensemble of CL photon emission times $\{t_{\rm rad}\}$ consecutive to the interaction of $N_{\rm e}$ electrons with the sample at times $\{t_{0,i}\}$, with $i = 1, \ldots, N_{\rm e}$.

At low electron current intensity, the **time distribution of the incoming electrons** follows a Poissonian statistics, so that the probability of having an electron interacting with the nanodiamond during the interval $\Delta t_{0,i} \equiv t_{0,i+1} - t_{0,i}$ is given by $\Delta t_i/\Delta t_{\rm m} \exp(-\Delta t_i/\Delta t_{\rm m})$, where $\Delta t_{\rm m}$ is the mean interval of time between two consecutive electrons in the beam, which is considered constant for a given value of I. Then $\{t_{0,i}\}$ are generated from random numbers $\{r_i^{(1)} \in [0,1]\}$ according to $t_{0,i+1} = t_{0,i} + \Delta t_i$, with $\Delta t_i = -\ln(1 - r_i^{(1)}) \times \Delta t_m$, where we took $\Delta t_{\rm m}({\rm ps}) = 1600/I({\rm pA})$.

The probability for one electron to create $n_{\rm pl}$ plasmons also follows the Poisson law given by:

$$P_{\rm el}(n_{\rm pl}) = \frac{1}{n_{\rm pl}!}\left(\frac{L}{\lambda_e}\right)^{n_{\rm pl}} e^{-L/\lambda_{\rm e}} \tag{4.1}$$

where L/λ_e is the ratio of the thickness crossed by the electron (L) to its mean free path (λ_e) for plasmon excitation. We calculate $P_{\rm el}(n_{\rm pl})$ for $n_{\rm pl} = 0$ to $n_{\rm pl} = 150$, and generate $N_{\rm e}$ random numbers $\{r_i^{(2)}\}$. We then consider the probability for one electron to create a maximal number of $n_{\rm pl}^{\rm max}$ plasmons: $P_{\rm el}^{\rm s}(n_{\rm pl}^{\rm max}) = \sum_{n_{\rm pl}=0}^{n_{\rm pl}=n_{\rm pl}^{\rm max}} P_{\rm el}(n_{\rm pl})$. The upper bound number $n_{{\rm pl},i}^{\rm max}$ of plasmons created by the $i^{\rm th}$ electron is inferred from the inequalities $P_{\rm el}^{\rm s}(n_{{\rm pl},i} - 1) < r_i^{(2)} < P_{\rm el}^{\rm s}(n_{{\rm pl},i})$, with the additional conditions that $P_{\rm el}^{\rm s}(-1) = 0$ and $P_{\rm el}^{\rm s}(151) = 1$.

Now that the number of plasmons created by each electron is known, we need to determine **how many electron hole pairs (e-h) ($N_{eh,j}$) per plasmon (j) are created**. We consider two models: in the first one a constant number $m_{\rm eh}$ of e-h is created per plasmon, whereas in the second one this number follows a Poisson distribution $P_{\rm eh}(n_{\rm eh})$ with $m_{\rm eh}$ as the expectation value:

$$P_{\rm eh}(n_{\rm eh}) = \frac{m_{\rm eh}^{n_{\rm eh}}}{n_{\rm eh}!} e^{-m_{\rm eh}} \tag{4.2}$$

In the first model $N_{eh,j} = n_{\rm eh}\, n_{{\rm pl},j}$, where $n_{\rm eh}$ is constant, while in the second model, we generate $N_{\rm pl,tot}$ random numbers $r_j^{(3)}$ between 0 and 1, with $j = 1, \ldots, N_{\rm pl,tot}$. Then we assign for each plasmon a number of e-h created following the same approach as in the second step (creation of plasmons).

Then we consider the e-h interaction with centers. Each e-h can interact with one center with the probability $P_{\text{int}}(\rho, l_d, \sigma)$ deduced from the Beer-Lambert law with l_d the diffusion length, ρ the defect density considering the material as homogeneous, and σ the absorption cross section described by:

$$P_{\text{int}} = \left(1 - e^{-l_d \sigma \rho}\right) \tag{4.3}$$

We then generate $N_{\text{eh,tot}}$ random numbers $\{r_k^{(4)}\}$, where $N_{\text{eh,tot}}$ is the total number of e-h created. If $r_k^{(4)} < P_{\text{int}}$ the k^{th} electron-hole pair recombination put the center into its excited state. All the e-h created by plasmons coming from the same electron i are considered to interact (or not) almost instantaneously with the NV center. Therefore, in the model, the centers are excited at the time of interaction $t_{0,i}$ of the incoming electron. We also consider that centers have a unity quantum efficiency, so that they always decay by emitting one photon.

The probability $P_{\text{rad}}(t_{\text{rad},i})$ for a center to decay by **emitting one photon** at time $t_{\text{rad},i}$ if it is excited at $t_{0,i}$, is described by:

$$P_{\text{rad}}(t_{\text{rad}}) = \frac{1}{\tau_{\text{e}}} e^{-(t_{\text{e}} - t_0)/\tau_{\text{e}}} \tag{4.4}$$

For the i^{th} electron, we generate $N^i_{\text{e,tot}}$ random numbers $\{r_l^{(5)}\}$, where $N^i_{\text{e,tot}}$ is the total number of centers excited by this electron. The time $t^i_{\text{rad},l}$ of emission of the photon emitted by the l^{th} center excited by the i^{th} electron is given by: $t^i_{\text{rad},l} = t_{0,i} - \ln(1 - r_l^{(5)}) \times \tau_{\text{e}}$.

Finally, to obtain the time-intensity correlation function $g^{(2)}(\tau)$ function, we calculate the delays between each photon and all the others. For a given time resolution $\delta\tau$, $g^{(2)}(\tau)$ corresponds to the histogram of the delays $c(\tau)$, normalized to the value corresponding to a Poissonian source: $g^{(2)}(\tau) = c(\tau) / \left[(N_{\text{ph,tot}})^2 \, \delta\tau \, T_{\text{max}}\right]$, where $N_{\text{ph,tot}}$ is the total number of emitted photons and T_{max} is the duration of the coincidence counting experiment, i.e. the time of detection of the last photon [24].

Whatever the parameters, the simulations exhibit a bunching profile converging to 1 at large delays and with $g^{(2)}(0)$ decreasing when I is increasing, proving that multiple excitations by a single electron are indeed responsible for the bunching effect. An example corresponding to the realistic excitation of a nanodiamond is shown in figure 4.7 for an excitation at 100 keV with $L/\lambda_e = 1.8$, $l_d = 50$ nm [124], $\sigma = 95$ nm^2 [185], $\rho = 6.10^{-4}$ nm^{-3} [172] and $\tau_e = 10$ ns, the current I lies between 1 pA and 200 pA. The number of eh pairs per plasmon has been taken with a Poissonian distribution with a mean value $m_{eh} = 1$.

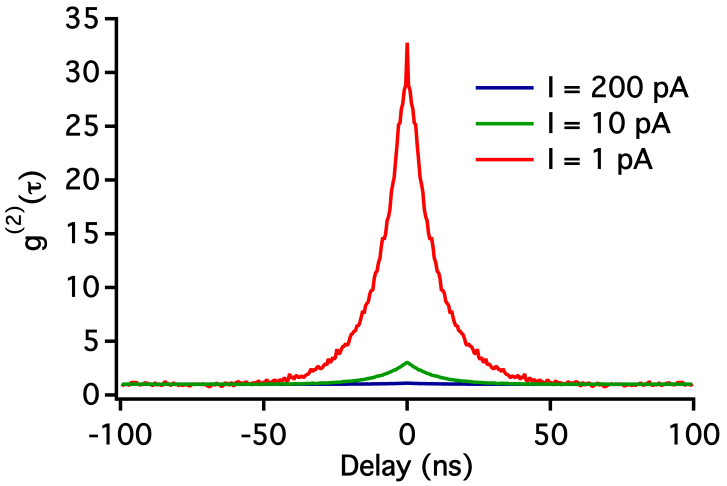

FIGURE 4.7: Monte Carlo simulation of the $g^{(2)}(\tau)$ function for three values of the current I : 1, 10 and 200 pA. The other parameters are L/λ_e = 1.8, l_d = 50 nm, σ = 95 nm^2, ρ = $6 * 10^{-4}$ nm^{-3} and τ_e = 10 ns. The bunching behavior as a function of I is retrieved.

In the next section, we are going to discuss the main results of the simulation and the role of the different parameters. Then we will compare simulated and experimental $g^{(2)}(\tau)$.

4.2.2 Discussion

As shown in figure 4.7 the Monte Carlo simulation reproduces the bunching effect and its dependence on current. For now, the number of parameters is huge: I, L/λ_e, l_d, σ, ρ and τ_e. But we will see that we can either ignore or measure all these parameters.

Simulations show the negligible influence of the value of P_{int} over several orders of magnitude, on the value of $g^{(2)}_{\mathrm{CL}}(0)$ (see figure 4.8), and therefore that the precise values of the parameters ρ, σ, and l_d are not needed. This fact leads to two remarks. First, we don't need to know precisely the material parameters. And second, in the range of large N, the fact that we excite a single photon emitter is not relevant. **Therefore all these results would be true also for super-Poissonian emission of quantum wells or bulk materials excited by an electron, corresponding to N tending to infinity.** Of course for small values of N, the quantum character of SPE needs to be taken into account as it will be the case for the analytical model explained in section 4.3.

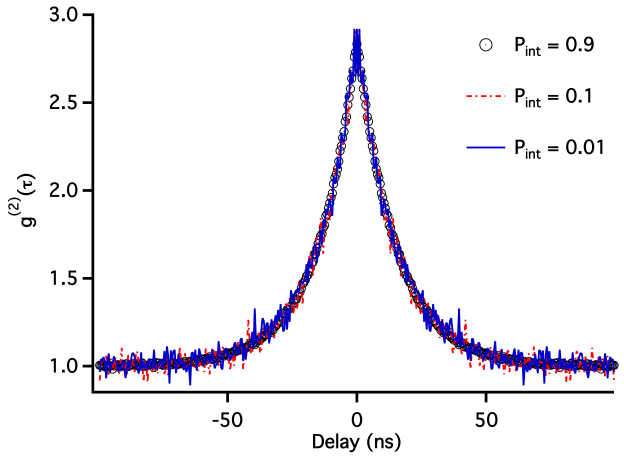

FIGURE 4.8: Effect of changing P_{int} over two orders of magnitude. For the simulation all the other parameters were kept constant : L/λ_e = 1.2, I = 5 pA, τ = 15 ns. No change of the $g^{(2)}(\tau)$ curve is detectable.

Measurement of τ_e

We have reduced the number of parameters from 6 to 3: I, L/λ_e and τ_e. Simulations show that the curves can be fitted with an exponential curve, the decay parameter of which is precisely equal to τ_e. Figure 4.9-a shows Monte Carlo simulations with every parameters fixed except the numbers of incoming electrons, which means different signal to noise ratios (SNR). Figure 4.9-b shows the distribution of lifetimes retrieved after an exponential fit for these four cases of SNR. Each time, 300 identical Monte Carlo simulations have been done. The accuracy of the lifetime measurement will be discussed in details in chapter 5. Nevertheless, we have a very simple way to measure the free parameter τ_e by simply fitting with an exponential the experimental $g^{(2)}_{\mathrm{CL}}(\tau)$. By measuring the $g^{(2)}_{\mathrm{CL}}(\tau)$ function we thus also have a way to measure the lifetime of emitters with potentially very high spatial resolution. We will develop this application on chapter 5 for different kinds of emitters.

Measurement of L/λ_e

The ratio L/λ_e is measurable thanks to energy electron loss spectroscopy (EELS). Using EELS, we can measure the energy lost by the electron after passing through the sample at the position where the bunching curves have been acquired. Comparing the fraction of electrons crossing the sample with no loss to the fraction of electrons transferring their energy to plasmons, it can be shown [20] that the ratio of the area under the zero-loss peak I_{zl} to the area of the total EELS spectrum I_{tot} is given by:

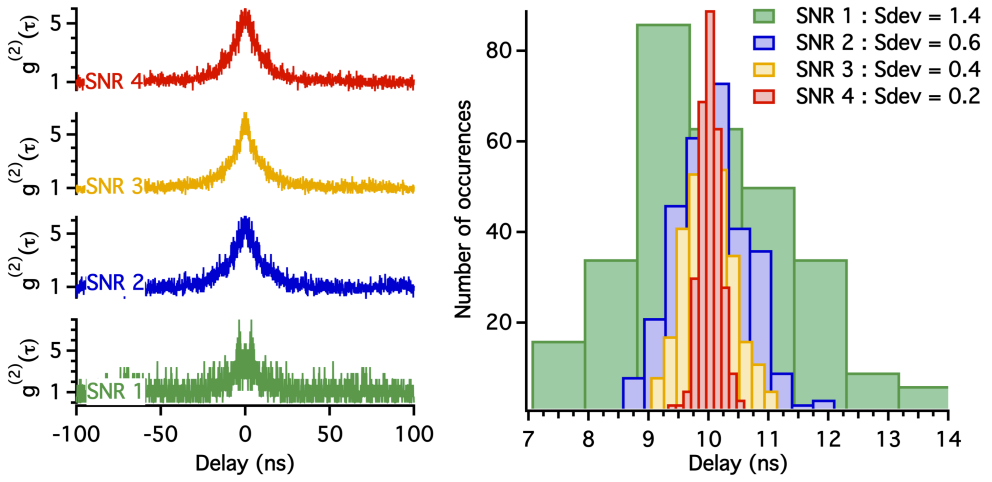

FIGURE 4.9: Influence of the signal to noise ratio (SNR) on lifetime measurement a) Monte Carlo simulation for : from bottom to top 1000, 5000, 10000 and 50000 incoming electrons. The high tension was 100 keV, P_{int} = 0.8, L/λ_e = 0.95, I = 5 pA. The lifetime was fixed to τ_e^{MC} = 10 ns and the histogram temporal resolution was 100 ps. b) Monte Carlo simulations for the 4 possibilities presented in a) were iterated 300 times, we represent the histogram distribution of lifetimes retrieved after a fit. The standard deviation (Sdev) is indicated.

$$\frac{I_{\mathrm{zl}}}{I_{\mathrm{tot}}} = e^{-L/\lambda_{\mathrm{e}}}, \tag{4.5}$$

where λ_{e} is the mean free path of the electron in the material. Using the EELS toolbox of DigitalMicrograph$^{\mathrm{TM}}$ (Gatan Inc., Pleasanton, CA, USA) software we can infer the value of L/λ_e, which is needed for computing the correlation curves. For example, in the case exemplified in figure 4.10 L/λ_e = 1.2. This measurement can be considered in most cases (relatively small thickness, without diffraction effect) very effective. Nevertheless, in the case of the nanodiamonds under study, possibly due to diffraction issues, the L/λ_e measured at 60 keV is different from the value at 100 keV by more or less 20 %. Therefore the measurement of the $g^{(2)}(\tau)$ have to be done at 100 keV if a comparison with Monte Carlo simulations is needed.

The $g^{(2)}(0)$ values depend greatly on this parameter as shown in figure 4.11. This could be explained by the fact that if we increase the thickness we increase the probability of interaction between the electron and the sample. It has therefore an effect similar to the increase of the current I. The measurement of the thickness is therefore essential for a good comparison with experiments. We can consider that the measurement by EELS gives L/λ_e with an error of 10 % [20].

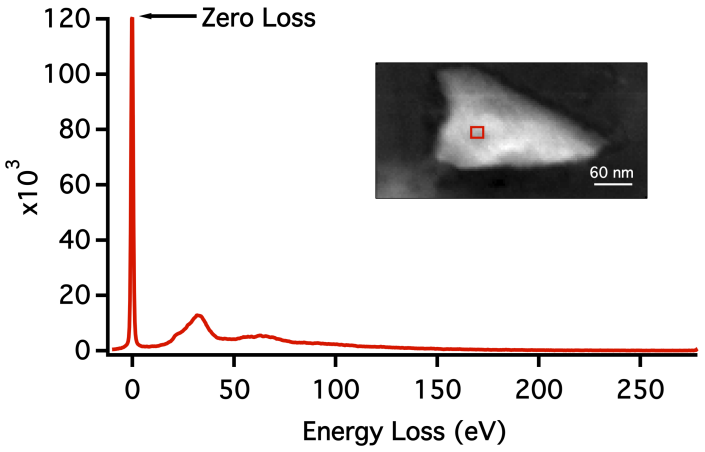

FIGURE 4.10: Electron energy loss spectrum recorded at 100 keV, for the nanodiamond shown in the main text. **Insert**: HAADF image with the red square indicating the restricted area scanned during EELS and HBT measurements.

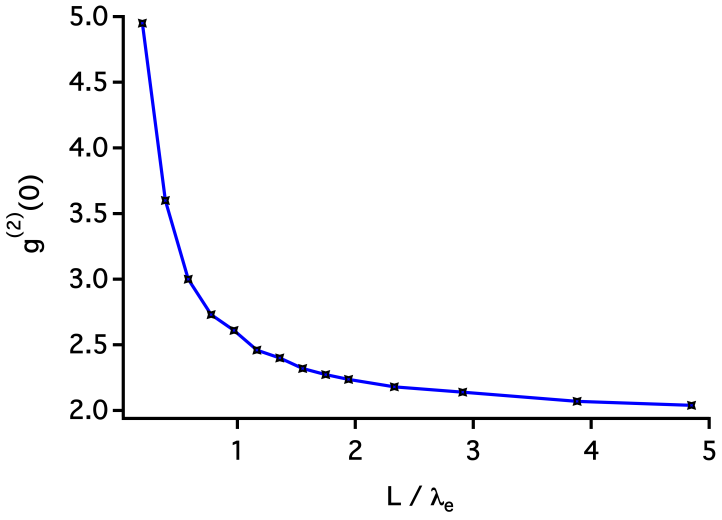

FIGURE 4.11: $g^{(2)}_{\mathrm{CL}}(0)$ As a function of L/λ_e. For these Monte Carlo simulations, I = 5 pA, τ_e = 26 ns, P_{int} = 0.7 and the number of eh pairs per plasmon follows a Poisson distribution with 2 as the expectation value.

Measurement of I

Out of all parameters, the current I remains unknown. In our case, the current is measured during the experiment on the real objective aperture (I_{ROA}) and a ratio with the real current is found later by comparing the current I_{ROA} in nA measured in a vacuum and the current found on the EELS collector I_{VSM} in pA. The principle is represented in figure 4.12. The ratio I_{VSM}/I_{ROA} is theoretically constant for fixed experimental conditions. However the shape of the gun tip is not constant during experiments (see chapter 2) and therefore the ratio may change from one measurement to the other. For

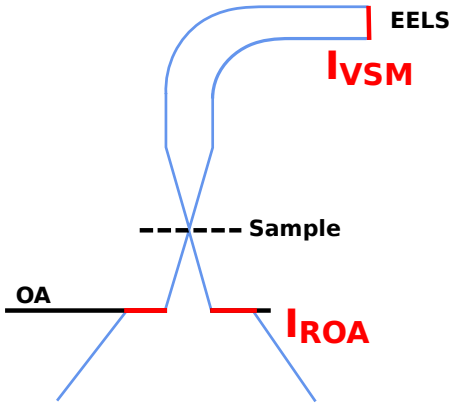

FIGURE 4.12: The electron beam (blue line) is focussed on the sample, the angle of convergence is reduced thanks to the objective aperture (OA). The current I_{ROA} is measured on the OA (horizontal red line) after the sample the electron beam is deviated through the EELS detectors where the current I_{VSM} can be measured.

example, in usual experimental conditions for HBT-CL experiment (EHT = 60 keV, C2 only, objective aperture = 100 μm, see chapter 2) the ratio can fluctuate between 2 and 3. Moreover the current I_{VSM} is very small and the uncertainty for small value of the current can be large. Therefore the measured values of the current will be $I = I_{ROA} \pm \Delta/2$ where $\Delta = 3I_{ROA} - 2I_{ROA}$ (see figure 4.1 and 4.3).

4.2.3 Comparison with Experiments

The Case of NV^0 Centers in Nano-Diamond

We first compare Monte Carlo simulation with measurements in nanodiamonds. Getting a sufficient signal to noise ratio on the $g^{(2)}_{\mathrm{CL}}(\tau)$ measurement to allow for an accurate comparison requires a long integration time (up to 20 minutes). This means, first, that the nano-diamond needs to be able to resist the electron beam exposure for such an exposure time and that the current needs to stay constant.

The first point is not crucial, since the number of centers in the nanodiamond is high. Even if half of the centers stop emitting during the experiment, the counts per seconds on each detector will be lower and therefore the time of integration to have meaningfull SNR will increase. It will not change the amplitude of $g^{(2)}_{\mathrm{CL}}(\tau)$ but what can change is the average NV^0 lifetime measured, since the lifetime of NV^0 centers in nanodiamond lies between 10 and 30 ns. It is most probably what happens on the nanodiamond shown in figure 4.2, where the lifetime increases between the first series of measurements and the second one. At the end of the first series the current was high ($I \approx 300$ pA) and it destroyed some of the centers, most probably the centers with the shorter lifetime that have a more efficient radiative recombination, shifting the mean lifetime value by 2 ns.

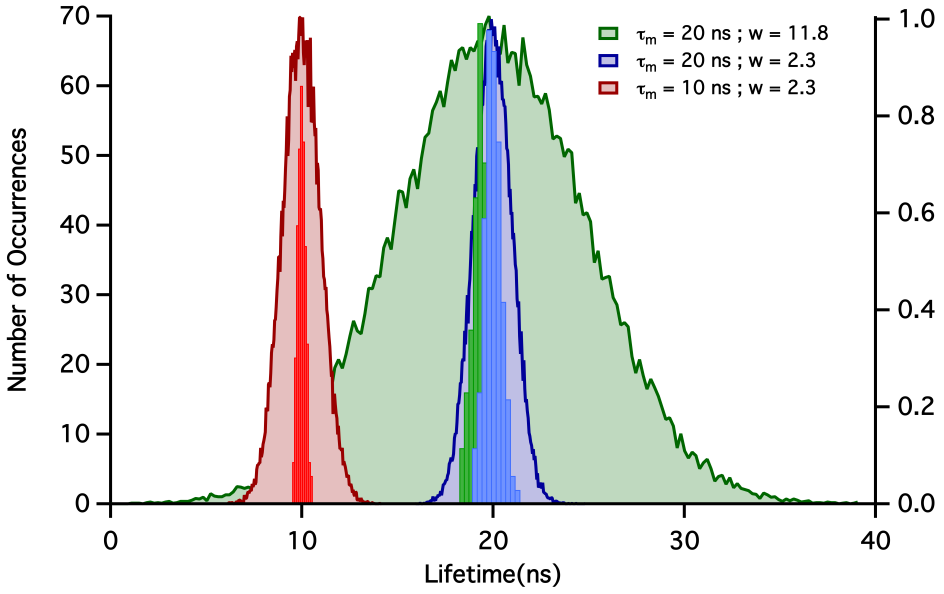

FIGURE 4.13: Bar plots represent the number of occurrences of the fitted lifetime for the 300 iterations of Monte Carlo simulations for the three different configurations of lifetime distributions. The lifetime distributions are plotted with solid lines and normalized to one. The other parameters for the Monte Carlo simulation are kept fixed : P_{int} = 0.8, L/λ_e = 0.97, I = 5 pA, and we take a Poissonian distribution for the eh pairs created per plasmon with m_{eh} = 1. The histogram bin size was 100 ps.

In figure 4.13 we show the distribution of lifetimes retrieved after an exponential fit for 300 Monte Carlo simulations with the same parameters (P_{int} = 0.8, L/λ_e = 0.97, I = 5 pA). We used a Gaussian distribution for the emitter lifetimes centered around a average lifetime τ_m for different full widths at half maximum w. We retrieve the mean value for w = 2.3 ns and almost the mean value for w = 11.8 (19 ns instead of 20 ns).

The stability of the current is a critical point and because the microscope used in this thesis is old, the current is often unstable on a timescale smaller than 5 minutes. Therefore, despite the hundreds of nanodiamonds studied during this thesis, the condition necessary to accurately compare the different models was only met once. But the other measurements, even if less accurate, show that the Monte Carlo model reproduces qualitatively the experimental data.

In order to compare the accuracy of the different models (Poissonian or not) we proceeded as follows. First, τ_e was determined by fitting an exponential to an experimental $g^{(2)}_{\mathrm{CL}}(\tau)$ at a given I. τ_e was then kept fixed for the curves acquired for other values of I. L/λ_e was directly measured from EELS data. The current was then determined as the only free parameter (For P_{int}, we took ρ from [173], $\sigma \approx 95$ nm^2 [185], and $l_d \approx 50$ nm for NDs [124] in order to remain realistic) by comparing a series of simulations to experimental curves. The accuracy of the different models can thus be inferred from

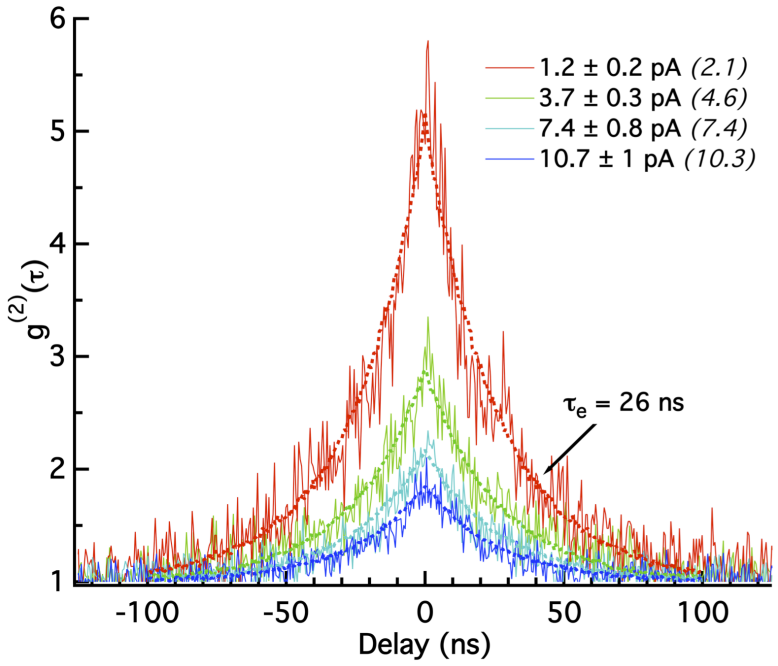

FIGURE 4.14: $g^{(2)}_{\mathrm{CL}}(\tau)$ measurement (continuous lines) for intensities I ranging from 1.2 to 11 pA for an individual, 60 nm thick ND. Each measurement lasted 5-20 min. The data were fitted with the Monte Carlo simulations explained in the text (dashed lines). The lifetime τ_e was retrieved using an exponential fit of the bunching curves, leading to τ_e = 26 ns. All the parameters of the Monte Carlo simulation were kept fixed except the current, which was changed until a good agreement between the experiment and the simulation was found. The resulting fitted currents are written in parenthesis next to the measured experimental values.

the comparison between the fitted and simulated results. In figure 4.14 the experiments and associated simulations are shown. The presented model, that seems to work best, is the one with a Poissonian distribution for the plasmon decay into eh pairs with a mean value m_{eh} = 1. However, we compared the experiment with the different models.

Taking into account [21, 28] we present results with m_{eh} = 1 or m_{eh} = 3, but we obtained similar conclusions for other m_{eh} values. As shown in figure 4.15, all the simulations reproduce the bunching effect, again confirming that multiple excitations by a single electron are responsible for the effect. Models in which the number of e-h pairs per plasmon is constant underestimate the bunching effect in nanodiamonds. Models assuming a Poissonian distribution for the plasmon decay seem to work better, highlighting the complexity of plasmon decay in the materials, but without giving any reason or insight into it. This may be due to stochastic phonon-e-h interaction, or to the creation of Auger and secondary electrons for example. Further studies, unfortunately outside the scope of this thesis, would be needed to clarify the exact plasmon decay mechanisms.

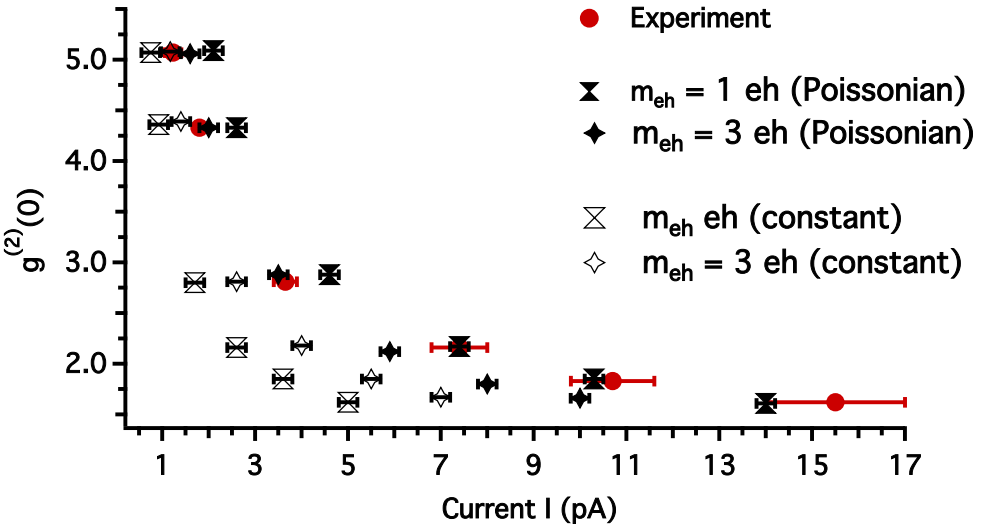

FIGURE 4.15: Comparison between the different Monte Carlo models for NV^0. $g^{(2)}_{\mathrm{CL}}(\tau)$ calculated from Monte Carlo simulations within the two different models for the decay mechanism compared to experimental data points extracted from figure 4.14. For all the simulations, all parameters are fixed except the current. Error bars in the simulations are generated by introducing a ±1 ns error in the estimate of τ_e and a very conservative ±10% error on L/λ_e. The bunching effect is qualitatively reproduced by both models.

The Case of Defects in h-BN

To make sure that the model is also valid for other kinds of defects we also compared the simulations with experimental $g^{(2)}_{\mathrm{CL}}(\tau)$ of the h-BN defect presented in chapter 3 and discussed at the beginning of the chapter. The huge bunching effect (up to $g^{(2)}(0) \gg 50$ in figure 4.3, here up to 35) seen on the h-BN compared to the one on NV centers in diamond ($g^{(2)}(0) \gg 5$) is mainly due to the lifetime of the emitter. Indeed, the bunches will have the same quantity of photons but on a smaller time range and therefore $g^{(2)}(0)$ is higher. Here we measured a lifetime of 1.2 ± 0.1 ns. This huge bunching effect allowed us to record $g^{(2)}_{\mathrm{CL}}(\tau)$ functions with a high signal to noise ratio in less than a minute.This avoids the problems described for the nanodiamond. However, another problem has been encountered, the excitation of the point defects seems difficult on thin h-BN flakes, as shown in figure 4.16-b where the signal is coming from the thicker part of the flake (whiter part of the flake in the HADF image in figure 4.16-a). Therefore the challenge was to find an area thick enough to have a CL signal but thin enough to allow for the measurement of the L/λ_e with EELS. In figure 4.16, the thickness was measured to be $L \approx 160$ nm in the region of the $g^{(2)}(\tau)$ measurement giving a $L/\lambda_e = 2.1$.

This time, the comparison of the different models presented in figure 4.17 shows that models where the number of e-h pairs per plasmon is constant seem to work better than the ones assuming a Poissonian distribution : the latter overestimates the bunching

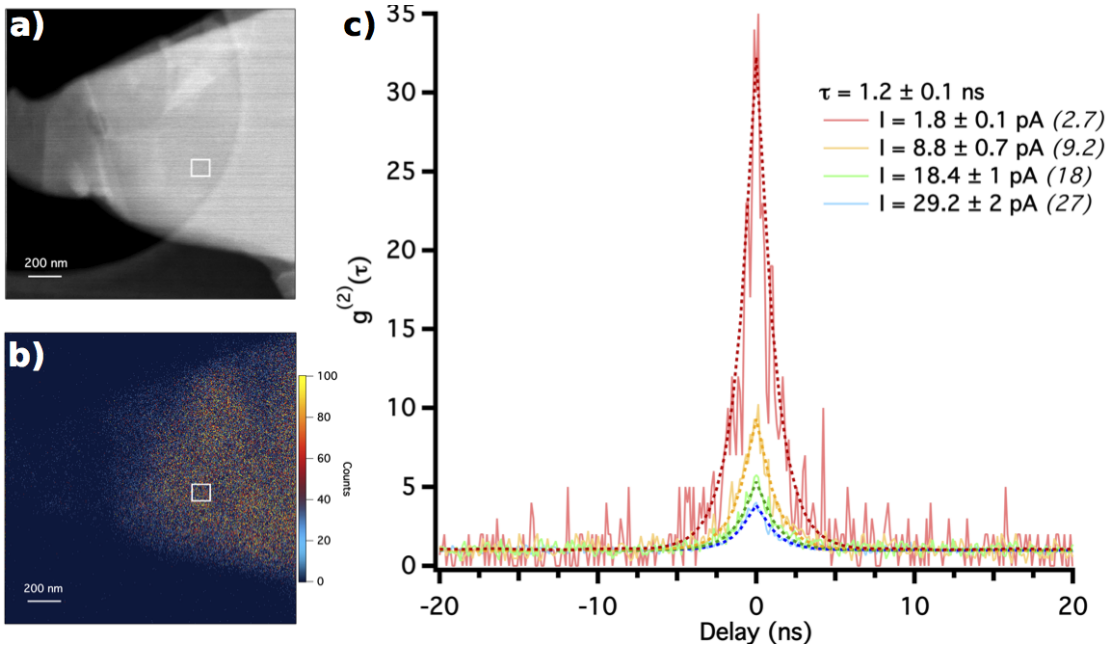

FIGURE 4.16: Comparison between Monte Carlo simulations and experiments on h-BN. a). Image of a hBN flake; b). A CL map filtered on a range 300-340 nm. c) $g^{(2)}(\tau)$ measurements versus incoming electron current I, performed on the h-BN flake represented in a). In parenthesis, current values of the Monte Carlo simulation with a lifetime of τ_e = 1.2 ns.

effect in this material. This seems to highlight that the transformation of electron hole pairs is more efficient in h-BN because the number of e-h pair created seems to depend less on the non-radiative processes. Maybe because the lifetime is smaller, the non-radiative processes like Auger electron occurs less frequently due to a very efficient radiative recombination. But a study of the Auger electrons for these two materials have to be carried out to corroborate this theory.

These two examples show that regardless of the Monte Carlo model used and regardless of the material, the simulations exhibit a bunching profile converging to 1 at large delays that qualitatively reproduce the experimental curves. This proves that multiple excitations by a single electron are indeed responsible for the bunching effect.

4.3 Analytical Model

4.3.1 Description

Finally, we turn to the low N regime, in which anti-bunching [2] and bunching compete, i.e. for a small number of centers $N \leq 5$. We modeled phenomenologically the behavior of the $g^{(2)}_{\mathrm{CL}}(\tau)$ function in the case of weak interaction. It is the case in diamond for

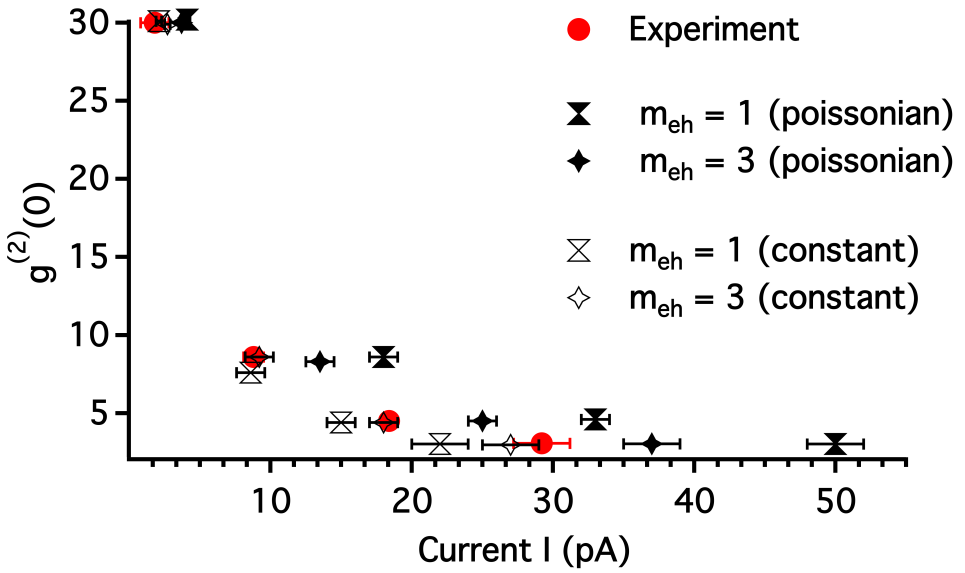

FIGURE 4.17: Comparison between the different models of Monte Carlo for h-BN. $g^{(2)}_{\mathrm{CL}}(\tau)$ calculated from Monte Carlo simulations within the two different models for the decay mechanism compared to experimental data points extracted from figure 4.16. For all the simulations, all parameters are fixed except the current. Error bars in the simulations are generated by introducing a ± 0.1 ns error in the estimate of τ_e and a very conservative ± 10% error on L/λ_e. The bunching effect is qualitatively reproduced by both models.

a thickness $L \approx 30$ nm, smaller than the electron mean free path $\lambda_e = 50$ nm. In that case, we can consider that the electron creates zero or one plasmon. This is the main approximation of this calculation. We also tried to do the calculation for 2 plasmons but the number of possibilities increased drastically and, in the end, other approximations have to be made rending the calculation less accurate. We also consider the simplified situation where the plasmon decays in only 2 electron-hole pairs.

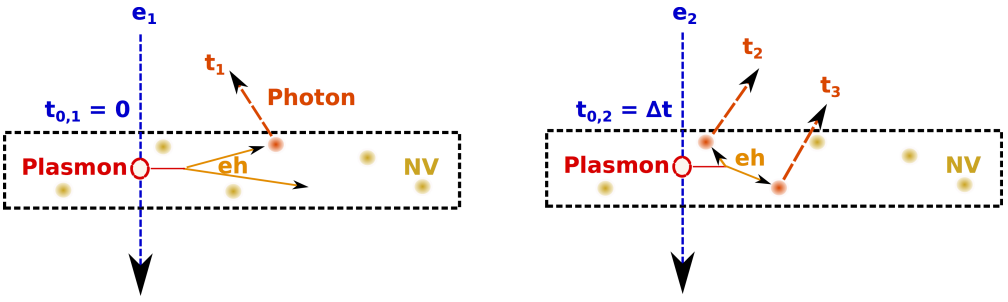

FIGURE 4.18: One of the possible chains of events from the interaction of incoming electrons e_1 and e_2 with the sample, at respectively $t_{0,1} = 0$ and $t_{0,2} = \Delta t$, to the emission of photons, at respectively t_1 and (t_2, t_3).

The second order correlation function $g^{(2)}(\tau)$ can be inferred from the probability $P(\tau)$ of detecting two photons separated by a delay τ. To calculate $P(\tau)$ we consider two

electrons e_1 and e_2 interacting with the nanodiamond one after the other. Table 4.1 shows all events leading to the emission of at least 2 photons. Events #1 and #2, #4 and #5, #6 and #7 are symmetric in time, so that they all have similar probabilities and only one of them needs to be calculated.

Chain of events #	electron e_1 creates plasmon pl_1	electron e_2 creates plasmon pl_2	Number of (e-h) pairs generated from pl_1	Number of (e-h) pairs generated from pl_2	Number of emitted photons after (e-h)→ NV excitation
1	Yes	No	2	0	2
2	No	Yes	0	2	2
3	Yes	Yes	1	1	2
4	Yes	Yes	2	1	3
5	Yes	Yes	1	2	3
6	Yes	Yes	2	0	2
7	Yes	Yes	0	2	2
8	Yes	Yes	2	2	4

TABLE 4.1: All possible events leading to the emission of at least 2 photons. The event presented in Figure 4.18 is event #5

$P(\tau)$ results from the combination of (i) the probability of creating one plasmon per electron given by the equation 4.1 of section 4.2.1, (ii) the probability of interaction of the plasmons with centers (equation 4.3), and (iii) the radiative probability of two photon emission at times separated by the delay τ (equation 4.4).

The plasmon creation probabilities for each relevant chain of events (# 1, #3, #4, #6 and #8) are summarized in Table 4.2.

To calculate the probability P_I that the e-h pairs, created consecutively by the two electrons, interact with centers, we consider an extended expression of the probability P_{int} defined in equation 4.3 taking into account the number N_{ex} of centers already in the excited state:

$$P_{int}(N_{ex}) = \left(1 - e^{-l_d \sigma \frac{N-N_{ex}}{V_{ND}}}\right) \approx \left(l_d \sigma \frac{N - N_{ex}}{V_{ND}}\right) = C(N - N_{ex}) \tag{4.6}$$

where V_{ND} is the nanodiamond interaction volume, and C is a constant for given values of L, σ, l_d and V_{ND}. In our case $V_{ND}/(l_d\sigma) \approx 15$ and $C \approx 0.06$. The approximation in equation (A.1) corresponds to the case $N \lesssim 5$ leading to $N - N_{ex} \ll V_{ND}/(l_d\sigma)$. Of course,

Chain of event #	Symbol	Probability of plasmon creation for Table 4.1 events
1	$P_{\text{el}}^{(1)}$	$P_{\text{el}}^{1} \times (1 - P_{\text{el}}^{1})$
3	$P_{\text{el}}^{(3)}$	$(P_{\text{el}}^{1})^2$
4	$P_{\text{el}}^{(4)}$	$(P_{\text{el}}^{1})^2$
6	$P_{\text{el}}^{(6)}$	$(P_{\text{el}}^{1})^2$
8	$P_{\text{el}}^{(8)}$	$(P_{\text{el}}^{1})^2$

TABLE 4.2: Probabilities of plasmon creations corresponding to the chains of events of Table 4.1

the smaller C, the better the approximation. In the case of diamond, the large interaction cross section σ limits the validity of the model to a small number of NV centers. For events #3, #4 and #8 the number of SPE already in the excited state will depend on the arrival time $t_{0,2} = \Delta t$ of the second electron. P_{I} expressions are summarized in Table 4.3, the different possibilities for events #3, #4 and #6 are noted with index Letters. P_{I} values are calculated in the case of a diamond of $L \approx 30$ nm and $N = 5$. We considered events for which the emission of more than 2 photons can be neglected, so that only the chains of events #1, #3 and #6 are considered in the following. The complete model taking into account events #4 and #8 has been calculated, the principle is the same as for events #1, #3 and #6 but for the sake of simplicity these two events are described in appendix A. The influence of these two events will be discussed in section 4.3.2.

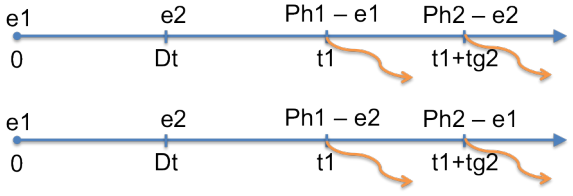

FIGURE 4.19: Time line of emission for event #3. The first photon (Ph_1) is either coming from the center excited by e_1 (Ph_1-e_1) or by the center excited by e_2 (Ph_1-e_2).

The **probability P_{rad} that a photon is emitted at** t_1 if the color center was excited at t_0 is given by equation 4.4, $P_{\text{rad}}(t_1, t_0) = \frac{1}{\tau_{\text{e}}} e^{-(t_1 - t_0)/\tau_{\text{e}}}$. In the chains of events #1, #3 and #6 the two photons are emitted at t_1 and $t_1 + \tau$. The radiative probability P_{rad}^{i} of the chain of events #i, is the product of two exponentials, corresponding to the decay of the two excited centers. Depending on whether the two centers are excited by the

Chain of events #	P_{I}	
1	$P_{\mathrm{int}}(0)P_{\mathrm{int}}(1)$	0.061
3a	$P_{\mathrm{int}}(0)(1-P_{\mathrm{int}}(1)) \times P_{\mathrm{int}}(1)(1-P_{\mathrm{int}}(2))$	0.039
3b	$P_{\mathrm{int}}(0)(1-P_{\mathrm{int}}(1)) \times P_{\mathrm{int}}(0)(1-P_{\mathrm{int}}(1))$	0.044
4a	$P_{\mathrm{int}}(0)P_{\mathrm{int}}(1) \times P_{\mathrm{int}}(2)(1-P_{\mathrm{int}}(3))$	0.009
4b	$P_{\mathrm{int}}(0)P_{\mathrm{int}}(1) \times P_{\mathrm{int}}(1)(1-P_{\mathrm{int}}(2))$	0.011
4c	$P_{\mathrm{int}}(0)P_{\mathrm{int}}(1) \times P_{\mathrm{int}}(0)(1-P_{\mathrm{int}}(1))$	0.012
6	$P_{\mathrm{int}}(0)P_{\mathrm{int}}(1)(1-P_{\mathrm{int}}(2))^2$	0.042
8a	$P_{\mathrm{int}}(0)P_{\mathrm{int}}(1) \times P_{\mathrm{int}}(2)P_{\mathrm{int}}(3)$	0.001
8b,c	...	≤ 0.005

TABLE 4.3: Probability P_{I} that the e-h pairs interact with color centers. For example, in the case of event #3, one of the two eh created by the first electron will interact with a color center with the probability $P_{\mathrm{int}}(0)$. Then one of the two eh of the second electron will interact with a color center with a probability $P_{\mathrm{int}}(1)$, if the color center excited by the first electron is still in the excited state at that time, and with the probability $P_{\mathrm{int}}(0)$ if it has retrieved its fundamental state. This leads to the probabilities 3a and 3b depending on the case.

same electron (events #1 and #6) or by two different electrons (# event 3), P^{i}_{rad} will be different:

- Chain of events #3. One photon is emitted following excitation by e_1 and one photon is emitted after e_2 excitation. Two emission configurations are possible: (Ph_1,Ph_2)-(e_1,e_2) in which the photon emitted first (Ph_1) comes from e_1 (see Figure 4.19-a), and (Ph_1,Ph_2)-(e_2,e_1) in which Ph_1 comes from e_2 (see Figure 4.19-b). Due to color center saturation the two configurations sketched in Figure 4.19 give different interaction probabilities (see Table 4.3), but they give the same radiative probability:
$$P^{(3)}_{\mathrm{rad}} = \frac{1}{\tau_{\mathrm{e}}} e^{-\frac{t_1}{\tau_{\mathrm{e}}}} \times \frac{1}{\tau_{\mathrm{e}}} e^{-\frac{t_1+\tau-\Delta t}{\tau_{\mathrm{e}}}} = \frac{1}{\tau_{\mathrm{e}}^2} e^{-\frac{2t_1+\tau-\Delta t}{\tau_{\mathrm{e}}}} \tag{4.7}$$
- Chains of events #1 and #6, in which two photons result from e_1 excitation. Ph_2 is emitted at the same time as Ph_1, so that the radiative probability is:
$$P^{(1),(6)}_{\mathrm{rad}} = \frac{1}{\tau_{\mathrm{e}}} e^{-\frac{t_1}{\tau_{\mathrm{e}}}} \times \frac{1}{\tau_{\mathrm{e}}} e^{-\frac{t_1+\tau}{\tau_{\mathrm{e}}}} = \frac{1}{\tau_{\mathrm{e}}^2} e^{-\frac{2t_1+\tau}{\tau_{\mathrm{e}}}} \tag{4.8}$$

In a Hanbury Brown and Twiss (HBT) setup using single photon counting modules with detection deadtimes, the detection of two consecutive photons Ph_1 and Ph_2 separated by a delay τ requires that Ph_1 is detected by the detector A linked to the correlator START

input, while Ph_2 is detected by the detector B, located on the other port of the 50/50 beamsplitter, and connected to the correlator STOP input. This situation happens with a probability of 1/4 for two emitted photons arriving on the HBT setup. We consider the probabilities $P^{(i)}(\Delta t, t, \tau)$ for each event $\#i$. Each of these probabilities depends on the arrival time Δt of electron e_2, on the time of emission t_1 of the first photon Ph_1 and on the delay τ between the two detected photons. $P(\tau)$ results from the sum of $P^{(i)}(\Delta t, t, \tau)$ over all possible values of Δt and t_1, as displayed in Table (4.4).

$P^{(3)}(\tau)$	(Ph_1,Ph_2)-(e_1,e_2) + (Ph_1,Ph_2)-(e_2,e_1)	$\frac{1}{4}P_{\text{el}}^{(3)}\left\{P_{\text{I}}^{(3a)}\int_0^{+\infty}dt_1\left(\int_0^{t_1}P_{\text{rad}}^{(3)}d\Delta t\right)+P_{\text{I}}^{(3b)}\int_0^{+\infty}dt_1\left(\int_{t_1}^{t_1+\tau}P_{\text{rad}}^{(3)}d\Delta t\right)\right\}$ + $\frac{1}{4}P_{\text{el}}^{(3)}P_{\text{I}}^{(3a)}\int_0^{+\infty}dt_1\left(\int_0^{t_1}P_{\text{rad}}^{(3)}d\Delta t\right)$ $=\frac{1}{4}P_{\text{el}}^{(3)}P_{\text{I}}^{(3a)}e^{-\tau/\tau_e}+\frac{1}{4}P_{\text{el}}^{(3)}P_{\text{I}}^{(3b)}\left(1-e^{-\tau/\tau_e}\right)$
$P^{(1),(6)}(\tau)$	(Ph_1,Ph_2)-(e_1,e_2)	$\frac{1}{4}P_{\text{el}}^{(1),(6)}P_{\text{I}}^{(1),(6)}\left(\int_0^{+\infty}dt_1\int_0^{t_1}P_{\text{rad}}^{(1),(6)}d\Delta t\right)$ $=\frac{1}{8}P_{\text{el}}^{(1),(6)}P_{\text{I}}^{(1),(6)}e^{-\tau/\tau_e}$

TABLE 4.4: Probabilities of detecting two photons separated by the delay τ, for the three chains of events considered (#1, 3 and 6).

The total probability $P^{\text{tot}}(\tau)$ results from a sum including $P^{(1)}$ and $P^{(6)}$ which are due to the same electron and are therefore considered as correlated events, and $P^{(3)}$ for the chain of events #3 due to two different electrons corresponding to uncorrelated events.

The probability of detecting two photons from a single electron excitation is independent from the electron beam current (disregarding saturation effects). On the other hand, the probability that the two photons come from different electrons (e.g. chain of events #3) increases with the number of electrons interacting with the sample. We define I_0

the incoming electron current such as one electron arrives on the sample during a color center lifetime τ_e.

The probability for e_2 to be responsible for a photon emitted at t_1, depends on the number of electrons arriving between $t_1 - \tau_e$ and t_1. Therefore in the expression of $P^{tot}(\tau)$, we weight the chains of events where the two emitted photons come from different electrons by the ratio I/I_0. This dependence in current was inspired by the experimental observation that $g^{(2)}(0)$ varies like $1/I$.

$$P^{tot}(\tau) = 2\left(P^{(1)}(\tau) + P^{(6)}(\tau)\right) + \frac{I}{I_0}P^{(3)}(\tau) \tag{4.9}$$

The multiplication by 2 accounts for the chain of events where two color centers are excited by e_2 ($P^{(2)}$ and $P^{(7)}$), which happens with the same probabilities as $P^{(1),(6)}$ corresponding to excitation by e_1.

Finally, we infer $g^{(2)}(\tau)$ from the normalization of $P^{tot}(\tau)$ by its value at infinite delay:

$$g^{(2)}(\tau) = \frac{P^{tot}(\tau)}{P^{norm}} \tag{4.10}$$

where $P^{norm} = \frac{1}{4}\frac{I}{I_0}\left(P^1_{el}P_{int}(0) * (1 - P_{int}(1))\right)^2$.

If $P_{int} \ll 1$ then we can consider that $1 - P_{int} \approx 1$, which is the case in nano-diamond for N = 2 ($P_{int} = 0.1$), but becomes increasingly less valid as N increases. In the case of weak interaction we can simplify $P^{(i)}(\tau)$ for $i = 1, 6$ and 3:

$$\begin{aligned}
P^{(1)}(\tau) &= \frac{1}{8}P^1_{el}(1 - P^1_{el})P_{int}(0)P_{int}(1)e^{-\tau/\tau_e} \\
P^{(6)}(\tau) &= \frac{1}{8}(P^1_{el})^2P_{int}(0)P_{int}(1)e^{-\tau/\tau_e} \\
P^{(3)}(\tau) &= (P^1_{el})^2\left(\frac{1}{4}P_{int}(0)P_{int}(1)e^{\tau/\tau_e} + \frac{1}{4}P_{int}(0)^2\left(1 - e^{-\tau/\tau_e}\right)\right).
\end{aligned}$$

In the case of $N \lesssim 5$, we can consider the simplified equation (A.1) for $P_{int}(N_{ex})$, so that we finally get:

$$\begin{aligned}
g^{(2)}(\tau) &\approx \frac{(N-1)e^{-\tau/\tau_e} + \frac{I}{I_0}P^1_{el}\left(N - e^{-\tau/\tau_e}\right)}{\frac{I}{I_0}P^1_{el}N} \\
&\approx \frac{I_0}{I * P^1_{el}}\left(1 - \frac{1}{N}\right)exp\left(-\frac{\tau}{\tau_e}\right) + \left(1 - \frac{1}{N}exp\left(-\frac{\tau}{\tau_e}\right)\right)
\end{aligned} \tag{4.11}$$

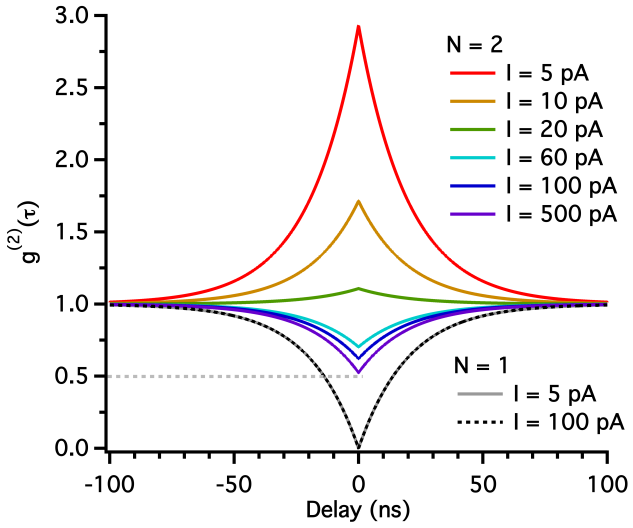

FIGURE 4.20: Simulation for a ND with L = 30 nm and τ_e = 20 ns. For N = 1 the $g^{(2)}_{\mathrm{CL}}(\tau)$ is independent of the probe current. For $N > 1$ (here N = 2) the expected anti-bunching behavior is retrieved at high current but not at low current.

The first term in equation 4.11 represents correlations due to individual electron excitations and is thus responsible for the bunching effect. The second term, identical to the $g^{(2)}_{\mathrm{PL}}(\tau)$ expression, represents the correlation due to the sample emission and is responsible for the anti-bunching behavior for single photon emitters. We can clearly see that when the current increases, the bunching part is blurred, leading to a $g^{(2)}_{\mathrm{CL}}(\tau)$ function similar to that for PL [45]. We also note that the expression formally diverges at zero current. However, at such a value, the bunch of photons is emitted with an infinite delay, preventing such a diverging limit from being reached experimentally. Also, equation 4.11 indicates the possibility of getting large $g^{(2)}_{\mathrm{CL}}(0)$ for short lifetimes, as clearly demonstrated for defect centers in h-BN (figure 4.3).

4.3.2 Discussion

The $g^{(2)}_{\mathrm{CL}}(\tau)$ for N = 1 and N = 2 are shown in figure 4.20 for different currents. An individual NV center in a nanodiamond can only be excited by one e-h pair at a time, leading to anti-bunching with $g^{(2)}_{\mathrm{CL}}(0) = 0$ for all currents. If more than one center is present, bunching effects will appear superimposed on the anti-bunching behavior. For N = 2, a transition from bunching to anti-bunching is expected upon increasing I. This shows that the law $g^{(2)}(0) = 1 - 1/N$ is difficult to observe in CL-STEM. The transition between the bunching and anti-bunching is also difficult to observe experimentally, as the necessary integration time to obtain a meaningful $g^{(2)}(\tau)$ (typically 5 min) is large enough to induce radiation damages for a small number of defect centers.

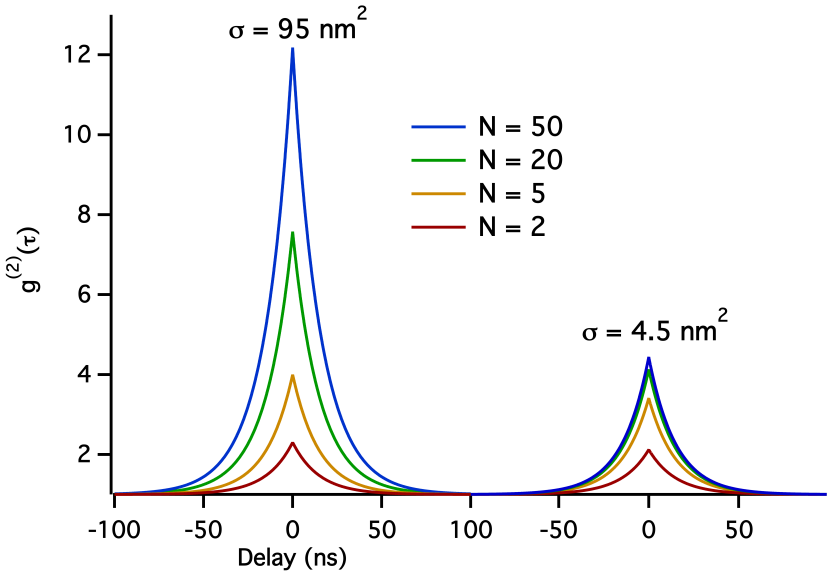

FIGURE 4.21: $g^{(2)}_{\mathrm{CL}}(\tau)$ as a function of N for two different values (σ = 95 nm^2 and σ = 4.5 nm^2) with the model taking into account events #4 et #8. This corresponds respectively to $C \approx 0.06$ and $C \approx 0.03$ (equation A.1). Here, τ_e = 15 ns and $L/\lambda_e = 0.6$.

Contrary to the model based on Monte Carlo, this time the bunching effect is dependent on the number N of centers as shown in figure 4.21. For this simulation we used the model taking into account events #4 et #8. We can see that the value of $g^{(2)}(0)$ increases with the number of centers. However in the weak interaction regime (interaction cross section is low σ = 4.5 nm^2, i.e $C \approx 0.01$), for a given current I, the $g^{(2)}(0)$ value saturates for high number of centers. Due to the saturation of centers the variation as a function of the number of centers is expected. However, the model being complete, we would expect no changes as a function of the cross section σ, as in the Monte Carlo simulation (see figure 4.8). Likewise for the saturation of the $g^{(2)}(0)$ value at high N. The limit of validity of the analytical model even in its complete form seems to be the weak interaction $C < 0.01$ (equation A.1).

As no experimental check of this model could have been done, only comparison with Monte Carlo simulations can be performed. In figure 4.22 we compare the Monte Carlo model with the 2 analytical models: first the model taking into account all the events ((figure 4.22-a)) and second the model with only the events #1, #3 and #6 (figure 4.22-b). For high values of σ ($C \approx 0.06$) the first model seems to work better but if $\sigma < 4.5$ nm^2 ($C < 0.01$) the two models seem equivalent. The difference with Monte Carlo simulations can be explained by the fact that we consider that no more than one plasmon is created even if in reality for L = 30 nm in the case of diamond at 100 keV (λ_e = 50 nm) the probability to have two plasmons ($P_{\mathrm{e}}(2)$ = 0.09) is about 1/3 of the probability to have one ($P_{\mathrm{e}}(1)$ = 0.3). Therefore in the analytical model the probability

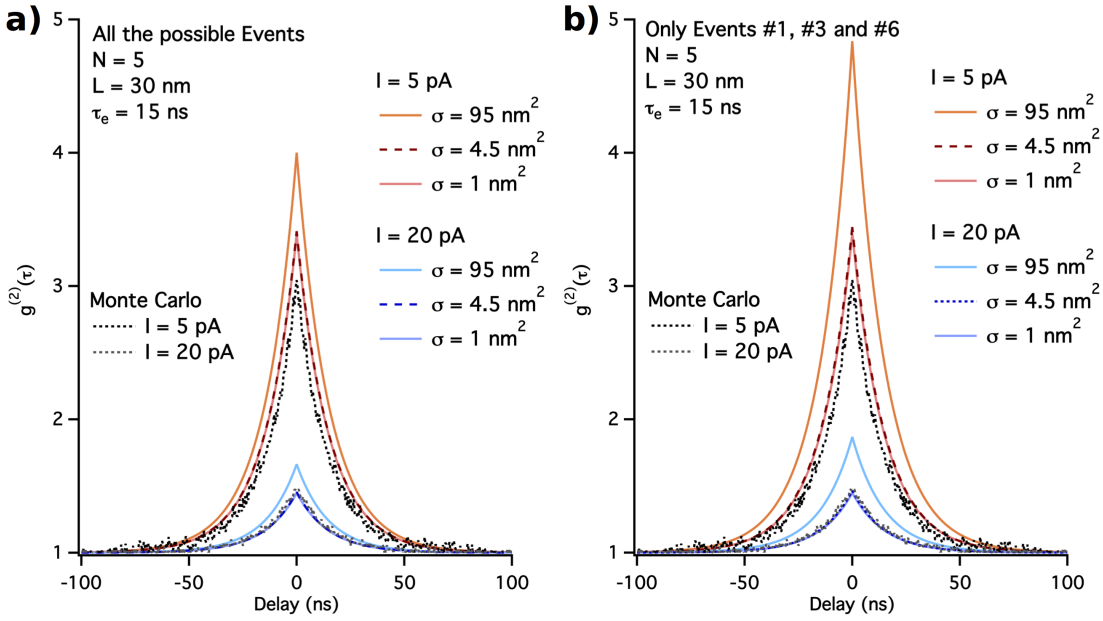

FIGURE 4.22: Comparison with Monte Carlo simulation. a) Comparison with Monte Carlo simulation (dashed line) for the analytical model where all the events of table 4.3 are taken into account. Three values of σ (and therefore C) are represent for the analytical model σ = 95 nm^2 (C = 0.06), σ = 4.5 nm^2 (C = 0.03) and σ = 1 nm^2 (C = 0.01). b) Same as a) but the simplified analytical model where only events #1,#3 and #6 are taken into account.

of the electron interaction is reduced compared to Monte Carlo simulations. It has the same effect as reducing the current and therefore it increases the $g^{(2)}(0)$ values.

This seems to prove that a small value of C increases the accuracy of the $g^{(2)}(0)$ values. In any case, the order of magnitude is respected and this model allowed even in a qualitative way to apprehend the tendency of the bunching effect for a few number of centers N. In the last section, we will adapt this model to understand qualitatively how background subtraction for $g^{(2)}(\tau)$ is affected by the bunching effect.

4.3.3 Consequences on Background Subtraction

In chapter 3, we applied background subtraction on the HBT-CL experiment. However, there is no reason why the background emission would not be affected by the bunching effect that, could come for example, from $H3$ defects (see chapter 3 section 3.21). We therefore adapted the analytical model to the case where two kinds of emitters can be excited by the electron beam: SPEs (we consider N SPEs) and a super-Poissonian emitter. We will refer to them respectively as S (for signal) and B (for background). For the sake of simplicity only events where two photons are emitted have been taken into account, which means events #1, #3 and #6 of table 4.1. But this time we have to

consider for each event the possibility that the two photons are coming from S, or one from S and one from B or two from B.

If we consider that the quantum efficiency of S and B is 100 % and knowing the signal to background ratio r we can deduce the probability of interaction P_{int}^{B} of the eh pairs with the background emitter:

$$\begin{aligned} r &= \frac{P_{int}^{S}}{P_{int}^{B} + P_{int}^{S}} \\ P_{int}^{B} &= \frac{1-r}{r} P_{int}^{S} \end{aligned} \tag{4.12}$$

We also need to take into account the two different lifetimes τ_S and τ_B. In figure 4.23, I have represented the influence of the bunching effect as a function of the SBR for a system constituted by one SPE with a lifetime of τ_S = 26 ns and a background emitter with τ_B = 18 ns. This is similar to the situation of an NV^0 with a $H3$ as background emitter (lifetime of $H3$ has been taken from [186]). We can see that at low current (I = 5 pA) the dip at zero delay is blurred for $SBR < 0.7$. At high current I = 20 pA the dip is blurred for $SBR < 0.5$. Moreover, in the case of I = 20 pA, if we apply the Poissonian background subtraction, we retrieve for SBR = 0.7 a $g^{(2)}(0)$ = 0.5. This clearly shows that the rule $g^{(2)}(0) = 1 - 1/N$ cannot be applied in $HBT - CL$ if a background is present. But due to the bunching effect we know that we have, after background subtraction, $g^{(2)}(0) \geq 1 - 1/N$. Moreover if we apply classical background subtraction as explained in chapter 3, the number of centers N_t retrieved later by applying the formula $g^{(2)}(0) = 1 - 1/N$ is greater or equal to the number of centers actually in the particle N_r. Indeed, in figure 4.23-b, after background subtraction for a SBR = 0.7 (0.7-SBR) we have $g^{(2)}(0)$ = 0.5 instead of $g^{(2)}(0)$ = 0. Because the model cannot be considered quantitative, a fit to the experimental data shown in chapter 3 will have no sense, but it shows clearly the impact of the bunching effect on background subtraction and highlights the need to work at high excitation current for HBT-CL measurement.

In the case of h-BN, the lifetime of the emitter was measured to be τ_S = 2.5 ns and the broad band emission is known to have a lifetime of $\tau_B \approx 20$ ns [170] (see figure 3.14 chapter 3). The effect strongly influences the $g^{(2)}(0)$ values as shown in figure 4.24. In our experiment, as $g^{(2)}(0) < 0.5$, we know that the number of centers is N = 1, we thus could try to compare experiment and theory. During the experiment, current was close to 200 pA, the value found for a $g^{(2)}(0)$ at current I = 200 pA and SBR = 0.83 is much higher ($g_{\text{sim}}^{(2)}(0)$ = 0.83) than the one obtained during the experiment of chapter 3 ($g_{\text{CL}}^{(2)}(0)$ = 0.58). This difference could be explained by the differences in thickness. In the experiment the thickness was of the order of 150 nm, whereas in the simulation, to

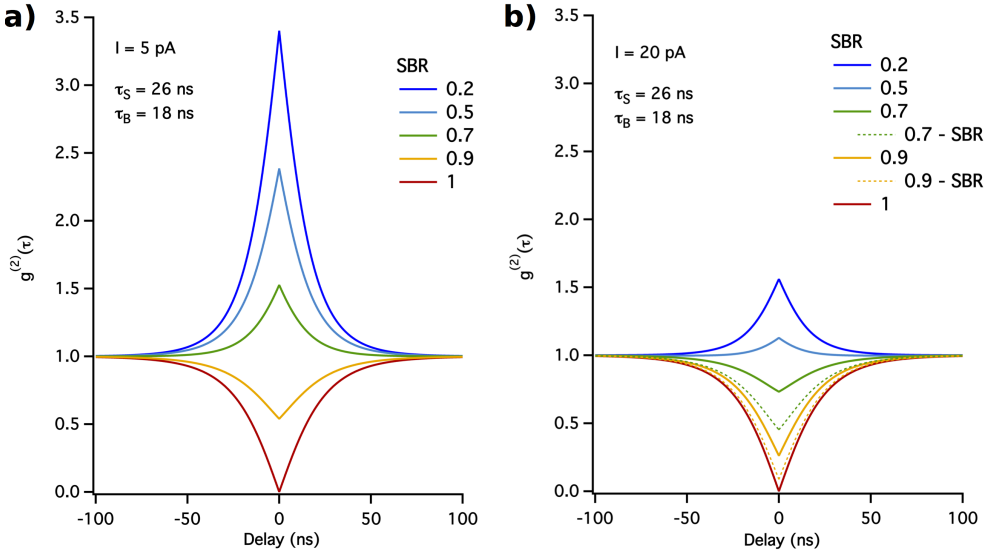

FIGURE 4.23: $g^{(2)}_{\mathrm{CL}}(\tau)$ for one single emitter $N = 1$ with a lifetime of $\tau_S = 26$ ns and a background emitter with a lifetime of $\tau_B = 18$ ns for a) $I = 5$ pA and b) $I = 20$ pA. In b) the $g^{(2)}_{\mathrm{CL}}(\tau)$ after a Poissonian background subtraction is represented for $SBR = 0.7$ and $SBR = 0.9$ (dashed line), one can see that we don't retrieve the $g^{(2)}_{\mathrm{CL}}(0)$ expected after subtraction.

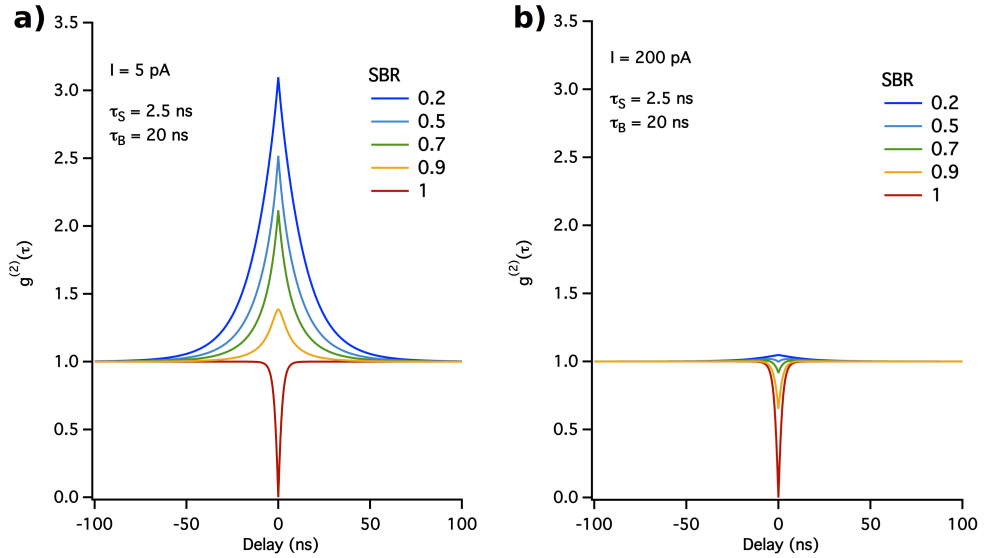

FIGURE 4.24: $g^{(2)}_{\mathrm{CL}}(\tau)$ for one single emitter $N = 1$ with a lifetime of $\tau_S = 2.5$ ns and a background emitter with a lifetime of $\tau_B = 20$ ns for a) $I = 5$ pA and b) $I = 20$ pA.

stay in the regime of weak interaction we have a thickness of 30 nm and the bunching effect, as shown in figure 4.11, is known to decrease when the thickness increases.

In conclusion, we have shown that $g^{(2)}_{\mathrm{CL}}(\tau)$ of defect centers, in two examples of wide band-gap semiconductors, exhibits a bunching behavior depending on the excitation current and the lifetime of the emitter. This phenomenon has been shown to arise from

the synchronization of multiple excitations via primary excitation decay into multiple e-h pairs and should be observable in any luminescent system by CL. Moreover, the autocorrelation shape with a single peak and a large $g^{(2)}_{\mathrm{CL}}(0) \gg 2$ might be recovered with an optical excitation, if emitters are excited with intense short laser pulses **which are randomly separated in time**. In the case where we can model the emitter's lifetime with a simple exponential, we are able to easily and quantitatively measure the lifetime with a spatial resolution only limited by e-h pair diffusion lengths [23] and with a high signal-to-noise ratio, we will develop this application in detail in the next chapter. Finally, the high observed $g^{(2)}_{\mathrm{CL}}(0)$ value is independent from the emission wavelength (tunable by material choice), meaning such photon sources could be of interest in two-photon excitation fluorescence [39], where the amplitude of the effect depends linearly on $g^{(2)}(\tau)$.

Chapter 5

Lifetime Measurement in Cathodoluminescence

Time is an illusion.
Bunchtime doubly so.

D. Adam / M. Kociak

5.1 Lifetime Measurement at the Nanometer Scale

Charge carrier lifetime is a key parameter for understanding the physics of electronic or optical excitations. For the excited state, it can unveil details of environmental influence, specifically the role of non-radiative transitions. From a practical point of view, lifetimes can largely determine the performances of devices, such as Light Emitting Devices (LEDs) or photovoltaic cells. These usually rely on nanometer scale structures for which small details, such as the presence of single point defects, have to be known with atomic precision. Despite the success of super resolution optical microscopies, they fail as general purpose tools for lifetime measurement at the nanometer scale. Taking advantage of the nanometer probe size formed in a Transmission Electron Microscope and the bunching behavior studied in chapter 4, we introduce a technique able to study lifetimes at the nanometer scale by measuring the second order correlation function,$\big(g^{(2)}(\tau)\big)$, of light emitted from nanostructures excited by fast electrons, without the need for a pulsed electron source. In this chapter, we prove the possibility to measure lifetimes of Gallium Nitride quantum wells (QWs) separated by less than 15 nm, together with their emission energy and atomic structure. Experiments on well separated individual

quantum structures shows an excellent agreement with combined time-resolved micro-photoluminescence. We also demonstrate the possibility to measure the lifetimes of emitters of different kinds (defects, QWs, bulk) within a distance of a tenth of nanometers even for spectrally overlapping emissions. This technique is readily applicable to large ensembles of single photon sources and various emitters such as QWs, quantum dots, point defects and extended defects, such as stacking faults (SF).

5.1.1 Measurement with CL of Multiple AlN/GaN Quantum Wells

We showed in chapter 4 that the $g^{(2)}(\tau)$ function of an ensemble of identical single photon emitters allows for the retrieval of the emitters lifetime with nanometer spatial resolution. By using a nanometer wide electron probe we can access lifetimes at the nanometer scale. The experiment presented here is basically the same as in the last chapter: the $g^{(2)}(\tau)$ is recorded during an integration time T, which depends on the required signal to noise ratio, an issue to be discussed in section 5.1.3. In this chapter, we will correlate these measurements with all the information available on an STEM: high resolution HADF image, EELS measurement and CL spectrum. In our case the CL system has been installed on an STEM without aberration corrector, which means that HADF images are not atomically resolved, but sufficient to localize object of interest with a 1 nanometer precision. Atomically-resolved images associated with the data have been acquired later on an Ultra-STEM Nion operated at 100 or 200 keV. In the future, this kind of study will be done on the same microscope without the need of sample transfer between microscopes, allowing full characterization without changes in the sample environment.

We illustrate such ensemble of readily correlated measurements in figure 5.1 on a sample, the properties of which are unaccessible by optical techniques due to spatial resolution constraints. This sample is composed of a set of eight GaN quantum wells (QWs, a few angströms thick) separated by 15 nm AlN barriers in a nanowire. A color-coded compression of the spectrum image (SPIM) of a NW is shown in Figure 5.1-b, where each energy layer has been encoded with a different color. Despite their proximity, the emission of each QW (in the 3.8 eV to 4.7 eV range) is clearly distinguishable. As the position of the QWs can be identified from the HADF image (Figure 5.1-a), we can deduce the exact emission energy of each QW. The emission energy distribution along the NWs is not uniform among different NWs due to QW thickness variation and strain effects. Each QW lifetime can be obtained from their respective $g^{(2)}(\tau)$ (Figure 5.1-c), and varies from 2.3 to 0.5 ns. From the two data sets, we can correlate the lifetime to the emission energy and deduce that lifetimes are longer for lower emission energy. This is expected as lower emission energy corresponds to lower confinement strength, and

therefore lower electron hole overlap and increased lifetimes. This behavior have been aready extensively studied [43, 187, 188].

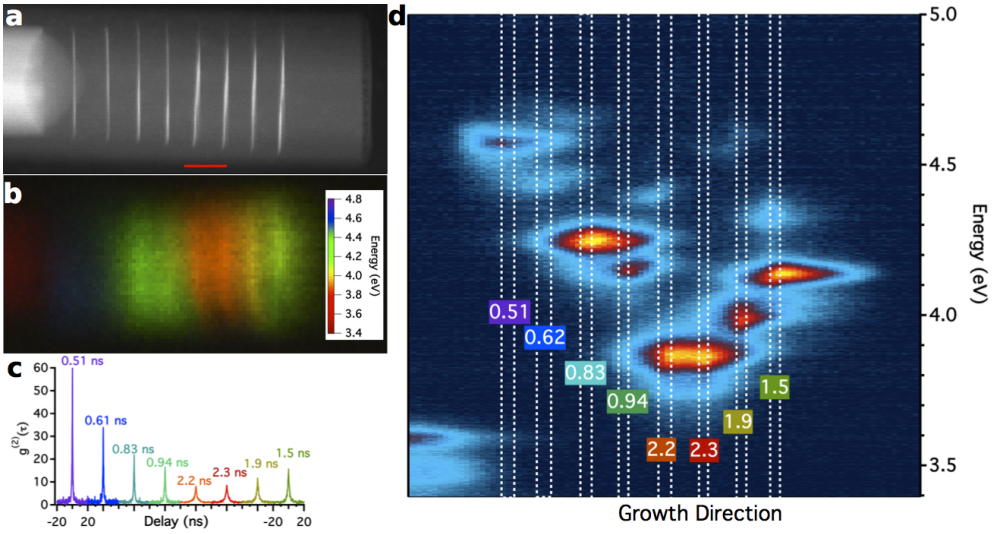

FIGURE 5.1: Nanometer scale lifetime measurement. a) the HAADF image of an AlN nanowire containing 8 GaN QWs. The scale bar is 20 nm b) Compression of a spectral image acquired on the same NW. c) Series of $g^2(\tau)$ measured at each QW position. These have been shifted on the abscissa for clarity. The deduced lifetime is printed close to each bunching peak. d) Emission intensity versus energy and of the position along the growth direction. The lifetime measured for each quantum well (dashed white rectangle) have been displayed on the graph for clarity.

These results show how spectral and lifetime information can be retrieved from individual quantum-confined objects in close proximity. These experiments can be performed in a short period of time (less than one hour per NW) including CL spectrum imaging, HADF imaging and lifetime measurements for all QWs. For example, in a one day experiment we have measured 80 QWs in 10 different NWs. Such large throughput is ideal for the acquisition of statistically relevant informations, considering the known variations between different nano-objects within the same sample. Out of the fifteen similar nanowires studied, only the nanowire presented in figure 5.1, called hereafter NW0, has a straightforward dependence between energy and lifetime. Three other examples are shown in figure 5.2-a,b and c called respectively NW 1, 2 and 3. In these examples the general tendency is respected, the QWs of NW2 have shorter lifetimes and higher emission energies than those of NW1. In figure 5.2-d, the lifetime as a function of the energy of emission of the different quantum wells is shown. Among the 120 quantum wells measured (15×8) only the 38 ones where a main single emission energy can be assigned to a quantum well have been used. One can see the large distribution of lifetimes for a given energy, even if the tendency of shorter lifetime for higher energy is still visible. On the other quantum wells, due to secondary emissions localized on fraction of the quantum well, most probably assign to defect during the growth, any designation of an emission energy is uncertain.

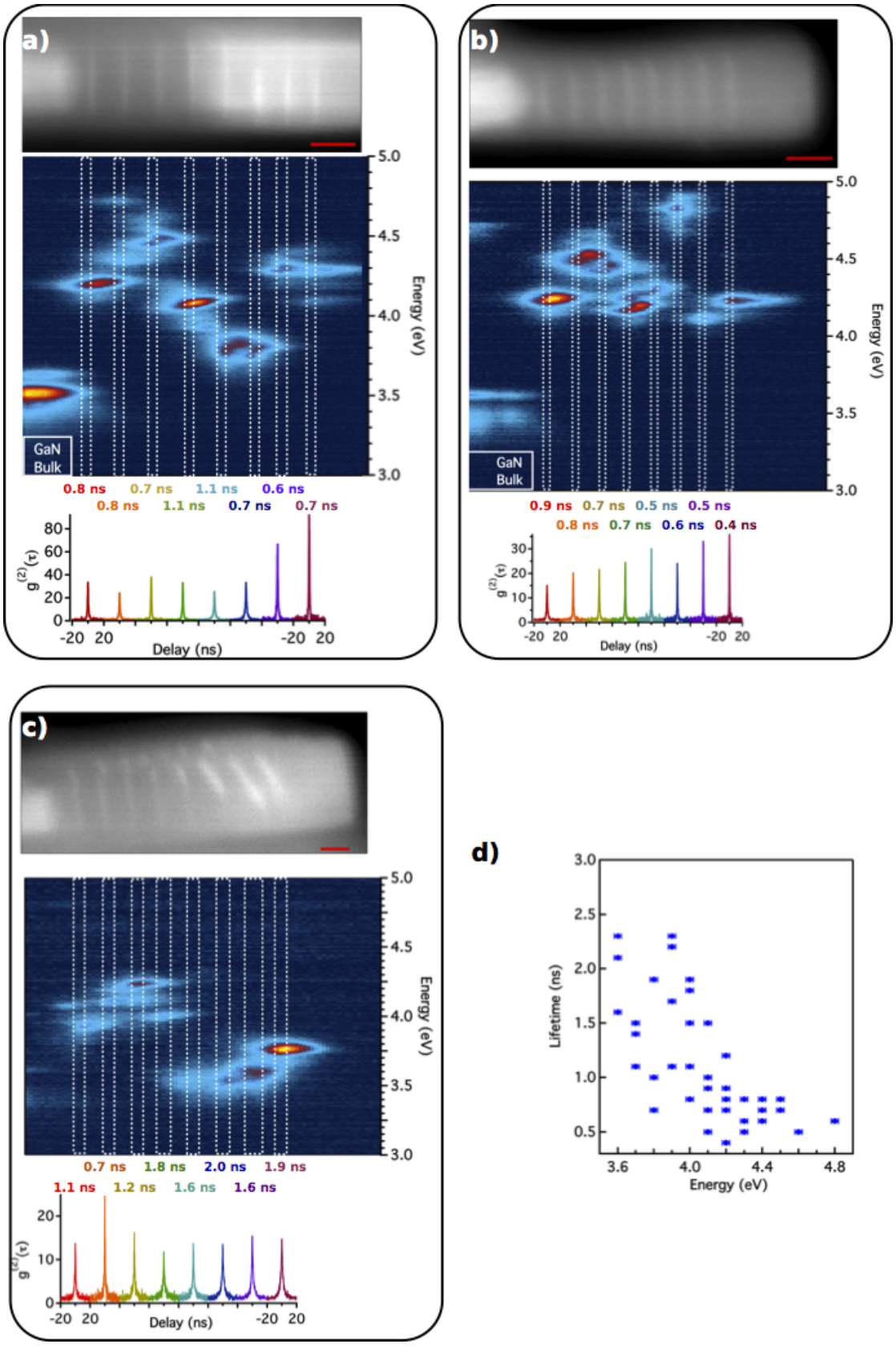

FIGURE 5.2: a),b),c) HADF image (top), projection of a SPIM (see chapter 2) along the growth direction (middle) and the correlation function $g^{(2)}(\tau)$ taken on each QW (bottom). a: NW1; b: NW2; c: NW3. The dashed rectangles represent the QW location. Scale bar in the HADF is 20 nm. d) Lifetime as a function of the emission energy for the quantum wells taken from the fifteen nanowires studied. Only quantum wells with a clear single emission energy are reported.

This large distribution of lifetimes at a given energy can be understood by looking at the distribution inside the same nanowire. Indeed, for NW1 the quantum well with the lowest emission energy (E ≈ 3.8 eV)(third from the right) has a shorter lifetime (0.7 ns) than the fourth and fifth (1.1 ns) having a similar or higher emission energy (respectively 3.8 eV and 4 eV). This could be due to structural reasons that, in principle, a more advanced experiment coupling high resolution HADF and EELS measurements could unveil. Indeed, we need to remember that only the overall lifetime is measured, and not only the radiative one, for which the relation between energy and lifetime holds. In the present set-up, however, no spectral filtering has been done yet and it is more likely that the lifetime measured with a beam position located on each quantum well is the lifetime of the emission of the quantum well convoluted with those of the two quantum wells close to it. For example in the case of NW1, the third and the forth quantum wells counting from the left have approximately the same emission energy. But the second quantum well has a energy higher than the fifth. This means that, considering the convolution effect, the lifetime measured on the third is actually smaller than the lifetime of the fourth. In section 5.1.2 we are going to discuss the effect of two emissions with different lifetimes on lifetime measurements thanks to Monte Carlo simulations.

In order to show the benefit of spectral filtering to increase the measurement accuracy, we did some preliminary tests by using filters to separate two spatially overlapped emissions. For that purpose, we have used a GaN/AlN nanowire where the GaN confined structure emit at two different energies. The results are presented in figure 5.3. Some EELS measurements have been performed by L. Tizei on the Ultra-Stem Nion microsope on the same sample but not the same nanowire (figure 5.3-a) and b)). In this analysis we can see that the GaN structure has a complex pyramidal form allowing different recombination centers inside the GaN confined structure (figure 5.3-c)).

As shown in figure 5.3-d, we have used two paths on the HBT experiment (Ch1 and Ch2) one with a band pass filter (F) set at 3.6-4.1 eV and a second one where the first lens (L_3) plays the role of high-pass wavelength filter (< 3.5 eV). The third lens (L_3) is common to the two paths and is an uncoated UV lens that works for UV and visible light. This spectral selection allowed a clear distinction of the two emissions and their lifetimes could be retrieved separately. The lifetime for the top of the inclusion was 1 ns while it was equal to 8 and 9 ns for the two emissions coming from the base (figure 5.3-d)-e)). The smaller lifetime of the emission from the top is most probably due to a higher confinement and also a leak of the carriers to the second center of recombination at the bottom of the pyramid.

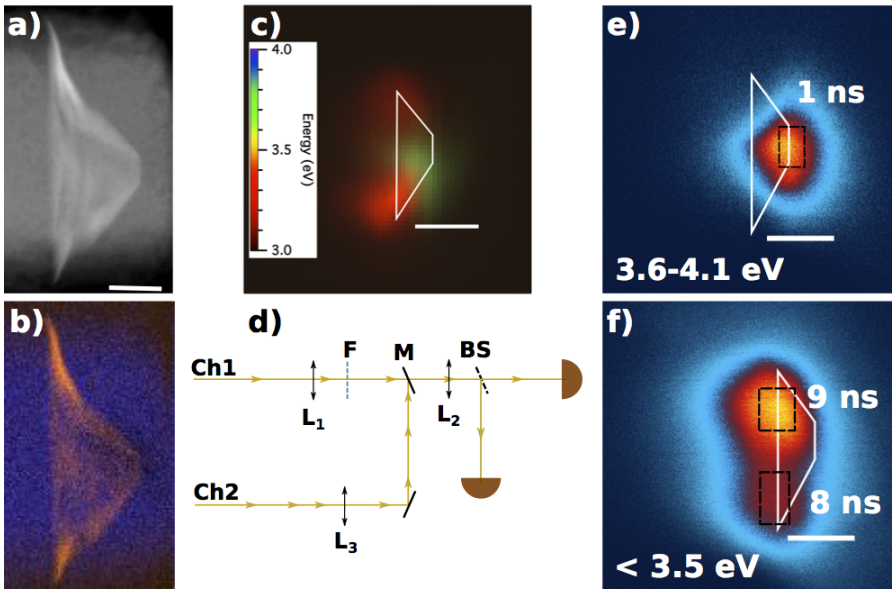

FIGURE 5.3: Lifetime measurements with spectral filtering on a nanowire AlN/GaN. a) HADF image taken in an atomic resolved microscope (Ultra-STEM) at the same time as the EELS measurement presented in b). The scale bar is 20 nm. The gallium is colored in orange and the aluminum in blue. The pyramidal shape is clear on the EELS elements map. c) Compression of a spectral image acquired on the same nanowire as e) and f). There are clearly three emissions visible, the two at the base of the GaN pyramid respectively at each corner around 3.2 eV and the one at the top of the pyramid around 3.8 eV. The scale bar is 50 nm. The HBT-STEM experiment was modified to perform spectral filtering as shown in d) the mirror (M) is removable to allow the signal to go on the direct path (ch1) where the lenses L_1 and L_2 are UV compatible and the filter (F) is a band pass filter set at $3.6 - 4.1$ eV. The second path (ch2) used a visible lense L_3 that is not UV compatible and therefore acts as a high-pass wavelenght filter < 3.5 eV.

Spectral filtering has thus a clear beneficial effect on lifetime measurement. In any case, the best solution would be to install a spectrometer into the HBT experiment to spectrally filter the emission in addition to the spatial selection, increasing the spatial resolution of the experiment. The main problem of using a spectrometer is losses due to the grating. Also a software that allows the acquisition of spectra with the HBT detectors to select easily emission energy would be needed.

5.1.2 Monte Carlo Simulation with Two Lifetimes

In complex structures like GaN/AlN nanowires or nano-diamonds, it is often the case that despite the nanometer size of the beam, we excite more than one emission center, mostly because of the diffusion length of carriers in the material. In such a case, the $g^{(2)}(\tau)$ contains a mixture of signals coming from different emitters. To know if we can accurately retrieve two emission lifetimes, we have performed Monte Carlo simulations considering the excitation of two emitters. Here we made the assumption that the decay

is exponential, however in some heterostructures as, for example, InGaN/GaN nanowire [189] or thick GaN/AlGaN quantum wells under high excitation power [190], the carrier recombination dynamic is not exponential. In this case, a more complex modeling of the decay have to be replace into the Monte Carlo model. It has not been done for now, and our study will be restricted to exponential decay. Knowing from chapter 4 that the probability of interaction P_{int} of the electron-hole (eh) pairs with the emitter has no influence on the result, we take $P_{int} = 1$. However, as the eh pairs can excite either the first emitter E_1 or the second emitter E_2, we have defined the emission ratio r_e as the probability that eh pairs interact with E_1 instead of E_2. The principle of the Monte Carlo simulations is the same as in chapter 4, but this time for each incoming electron the number n_{eh} of created eh pairs is distributed between E_1 and E_2 by generating n_{eh} random numbers $r_{and}[0,1]$. If the j^{th} random number is such that $r^j_{and} < r_e$, the j^{th} eh pair interacts with E_1; otherwise it interacts with E_2. Depending on which emitter the eh pair interacts with, it will decay with the radiative probability P^1_{rad} or P^2_{rad} associated with the lifetime τ_1 or τ_2, respectively.

Results of simulations show that by fitting the $g^{(2)}(\tau)$ function with the sum of two exponentials (equation 5.1) we can retrieve the two lifetimes τ_1 and τ_2, independently.

$$g^{(2)}(\tau) \quad = \quad 1 + g_1 * exp\left(-\frac{\tau}{\tau_1}\right) + g_2 * exp\left(-\frac{\tau}{\tau_2}\right) \tag{5.1}$$

However the accuracy of the fit depends, of course, on the signal to noise ratio, which will be discussed in the next section, on the similarity of the two lifetimes and the emission intensity ratio between the two emitters. In figures 5.4 and 5.5, results are shown for τ_1 = 1 ns and τ_2 = 2 ns and τ_2 = 5 ns, respectively. The other parameters are set to I = 5 pA, P_{int} = 1 and L/λ_e = 1. For each case, 300 Monte Carlo simulations have been performed and further fitted. The different lifetime distributions retrieved for both emitters are shown as well as the typical $g^{(2)}(\tau)$ functions for $r_e = 0.3,\ 0.5$ and 0.7. The total number of incoming electrons is 50000, which corresponds to an integration time of about 200 s for 10^4 counts/s on the HBT detectors, as it will be explained in section 5.1.3.

Figures 5.4 and 5.5 show that the accuracy increases with the difference between the two lifetimes. Some simulations at higher currents have been performed showing that the accuracy decreases if the current increases, as it is expected since $g^{(2)}(0)$ decreases with I. However, even for I = 50 pA, the accuracy is still sufficient to retrieve the two lifetimes with an error of about 20 %.

With this new approach, we return to the nanowires presented in figure 5.2. A fit with equation 5.1 has been realized for each quantum well of the nanowires NW1 and NW2 of figure 5.2. For some of the quantum wells, the fit did not converge and the lifetime

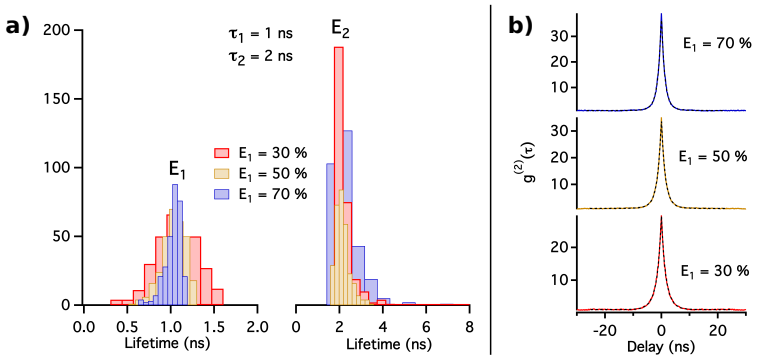

FIGURE 5.4: Monte Carlo simulations for τ_1 = 1 ns and τ_2 = 2 ns. a) Monte Carlo simulations for r_e = 0.3, 0.5 and 0.7, were iterated 300 times, we show the histogram distribution of lifetimes τ_1 and τ_2 retrieved after a fit with equation 5.1. The time resolution was set to 100 ps, I = 5 pA, P_{int} = 1 and L/λ_e = 1. b) Typical $g^{(2)}(\tau)$ functions for the three E_1/E_2 ratios presented in a) showing that measurements was done for a high signal to noise ratio.

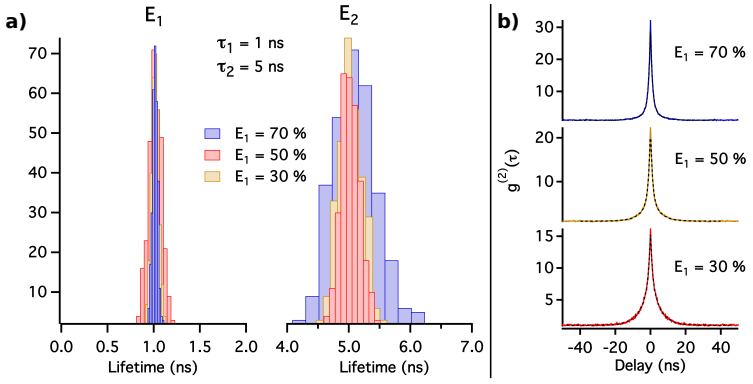

FIGURE 5.5: Monte Carlo simulations for τ_1 = 1 ns and τ_2 = 5 ns. a) Monte Carlo simulations for r_e = 0.3, 0.5 and 0.7, were iterated 300 times, we show the histogram distribution of lifetimes τ_1 and τ_2 retrieved after a fit with equation 5.1. The time resolution was set to 100 ps, I = 5 pA, P_{int} = 1 and L/λ_e = 1. b) Typical $g^{(2)}(\tau)$ function for the three E_1/E_2 ratios presented in a).showing that measurements was done for a high signal to noise ratio.

value of the simple fit was kept. Results are shown in figure 5.6. Where two lifetimes are retrieved, we can distinguish a shorter lifetime (between 0.4 and 1 ns) often associated with emission above 4.4 eV and a much longer second lifetime associated with emission below 4.4 eV. However, the uncertainty in the second lifetime value is high, often more than 1 ns. This uncertainty is due to the signal to noise ratio but also because the amplitude associated to the second lifetime (parameter g_2 of equation 5.1) is much smaller than the amplitude associated to the first lifetime. This is due to the fact that the amplitude increases when the lifetime decreases. It is very likely that in fact the second lifetime is an average lifetime of two secondary contributions (coming from the quantum well of the right and the quantum well on the left) however a fit with a sum of three exponentials does not converge in our case due to an increase in the number of free parameters.

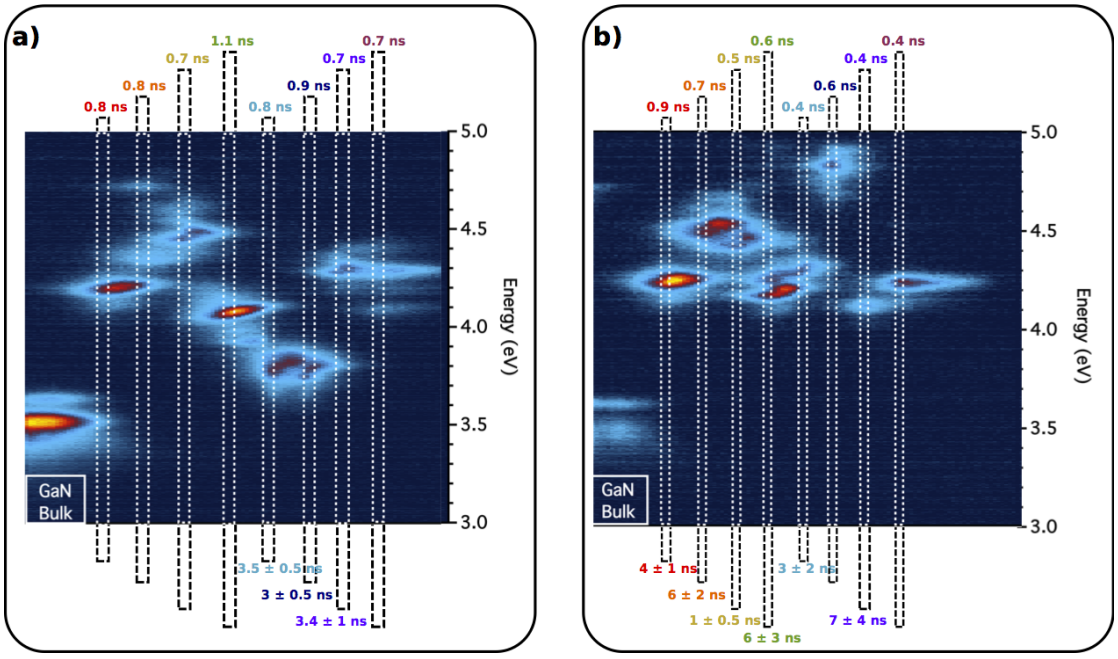

FIGURE 5.6: Nanowires of figure 5.5-a and 5.5-b, the $g^{(2)}(\tau)$ function of each quantum well has been fitted with a sum of two exponentials (equation 5.1). Map of the emission energy along the growth direction. Each quantum well is localized thanks to a dashed white rectangle. The lifetimes τ_1 and τ_2 retrieved after the fit are indicated respectively above and below each quantum well. If no values is indicated for τ_2, it means that the fit with two lifetimes didn't work and the value of τ_1 correspond to a fit with a simple exponential.

Proposal for time-resolved imaging experiment

The fit with a sum of exponential shows that we can retrieve different lifetimes from a $g^{(2)}_{\mathrm{CL}}(\tau)$ curve as in time resolved μ-PL. Of course the accuracy of the fit will decrease if the number of contributions increases. Moreover if more than one lifetime is found associated with multiple emission peaks in the spectrum, the association of each lifetime to the right emission center is a question of interpretation. However, in the case of cathodoluminescence, one can extrapolate the method of spectrum images (SPIM) to lifetime measurements. Indeed in the SPIM, we have an emission spectrum at each pixel. By fitting each spectrum with multiple Gaussian functions, we are able to identify each emission center. For example, in figure 2.6 of chapter 2 the maximum of intensity for each fitted emission peak allows one to localize more precisely than the diffusion length the emission center. In the case of lifetimes, if we have two emitters (E_1 and E_2) we will have $g^{(2)}(0) = g_1 + g_2$ (see equation 5.1). g_1 or g_2 will depend on the associated emitter lifetime (respectively τ_1 and τ_2) but also on r_e the emission ratio associated to E_1. Figure 5.7 shows the coefficient g_1 and g_2 for the Monte Carlo simulations of figure 5.5 (τ_1 = 1 ns and τ_2 = 5 ns) . One can see that the higher the percentage coming from the emitter, the higher the related coefficient.

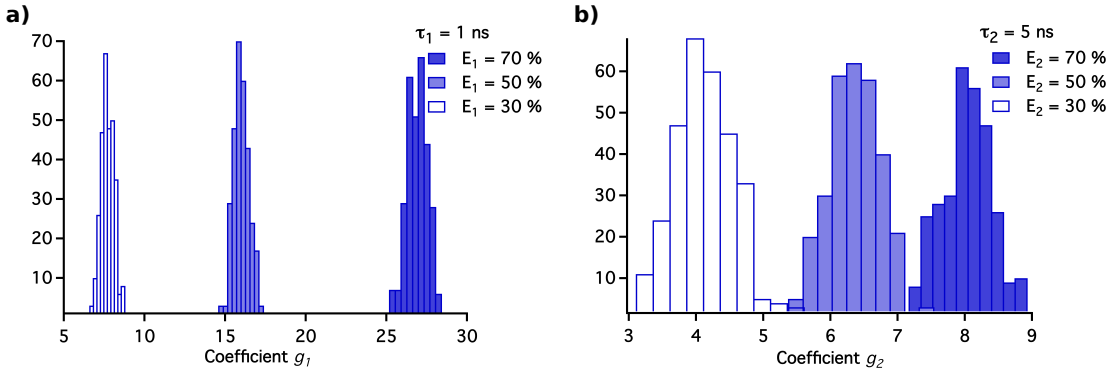

FIGURE 5.7: Monte Carlo simulations for τ_1 = 1 ns and τ_2 = 5 ns. a) Monte Carlo simulations for r_e = 0.3, 0.5 and 0.7, iterated 300 times. We show the histogram distribution of coefficients g_1 and g_2, respectively in figures a) and b), retrieved after a fit with equation 5.1 ($g^{(2)}(\tau) = 1 + g_1 * exp\left(-\frac{\tau}{\tau_1}\right) + g_2 * exp\left(-\frac{\tau}{\tau_2}\right)$). The time resolution was set to 100 ps, I = 5 pA, P_{int} = 1 and L/λ_e = 1

We can therefore imagine that if we acquire a $g^{(2)}(\tau)$ at each pixel and fit each curve with equation 5.1 we can retrieve for each lifetime the emission center location with a resolution greater than the diffusion length. A sketch representing this idea is proposed in figure 5.8. For the example of lifetime measurements in AlN/GaN nanowires, the acquisition time of a $g^{(2)}(\tau)$ is about 30 s. But this is the beginning and an improvement of the collection and detection system can reduce this time easily to 10 s. Moreover if multiple $g^{(2)}(\tau)$ are acquired the signal to noise ratio can be smaller, reducing also the time of acquisition. We can also use a drift corrector, already used in a lot of research teams for SPIM acquisition, that realign the sample after each measurement using an HADF image.

5.1.3 Discussion on the Accuracy

The accuracy of the fits depends, of course, on the signal to noise ratio (SNR) of the $g^{(2)}(\tau)$ functions. Moreover, the SNR depends also on the lifetime because it will change the value of $g^{(2)}(0)$. We can evaluate the integration time needed to obtain a certain precision on the lifetime value for different lifetimes and different counts rate on each detector thanks to Monte Carlo simulations. To evaluate the integration time we proceed as follows:

1. For a given number of electrons N_e^{MC}, we run N Monte Carlo simulations with the same parameters: lifetime T_f^{theo}, interaction probability P_{int}, L/λ_e and the current I.

2. Every $g^{(2)}(\tau)$ function resulting from simulations is fitted with an exponential. The resulting lifetime T_f of each curve is recorded.

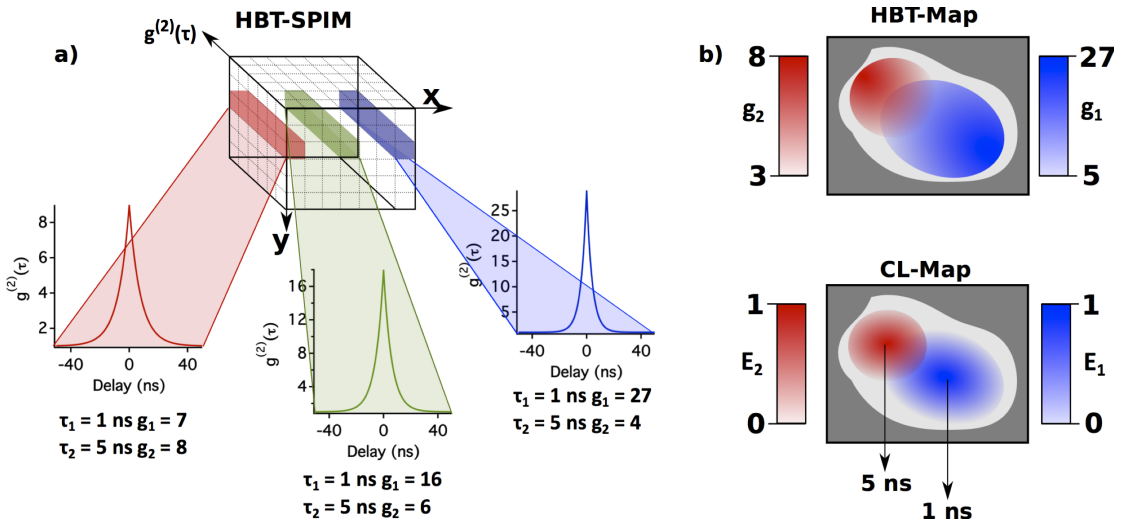

FIGURE 5.8: Sketch of the HBT-Spim. At each pixel of the scan we take the $g^{(2)}(\tau)$ function of the CL signal. We imagine a situation where the sample under study has two centers of emission, one with an emission energy E_1 and a lifetime of τ_1 = 1 ns and a second with an emission energy E_2 with a lifetime of τ_2 = 5 ns. We fit each $g^{(2)}(\tau)$ function with the expression $g^{(2)}(\tau) = 1 + g_1 exp(-|\tau|/\tau_1) + g_2 exp(-|\tau|/\tau_2)$. For each pixel we retrieve a value for g_1 and g_2 as the three examples shown in a). We can therefore plot the value of the two coefficients for each pixel as shown on the top figure of b). By correlating this map with the CL intensity map one can associate the center of emission with its lifetime.

3. We compare the average lifetime T_f^{avg} of the N simulations with the input parameter T_f^{theo}. If $T_f^{avg} = T_f^{theo} \pm x * T_f^{theo}$ and if the standard deviation is also smaller than x, the number of electrons N_e^{MC} is recorded as well as the total number of emitted photons N_p^{MC}. Otherwise the number of electrons is increased and the whole procedure is done again. Therefore, x defines the wanted accuracy.

This procedure is done for each desired lifetime. Therefore we know, eventually, the number of photons N_p needed to have the required SNR for each lifetime. We now want to convert N_p^{MC} to the integration time needed in our actual experiment. In the simulation, to decrease the calculation time we calculate the delay between each photon and its neighbors, contrary to the real HBT experiment where each delay is recorded only for different photons pairs. In the simulation we can define the ratio r between incoming electrons and emitted photons as N_e^{MC}/N_p^{MC}. The fit is done only for $\tau < 300$ ns, thus in the simulation one photon gives a number of events N_p^{ev} for the time windows T = 300 ns equal to the number of emitted photons during this time window. If we define N_e as the number of incoming electrons on a time window of 300 ns we can write that:

$$
\begin{aligned}
I &= \frac{N_e}{T} 1.6\ 10^{-7} \\
&= \frac{r\ N_p^{ev}}{300\ 10^{-9}} 1.6\ 10^{-7} \\
N_p^{ev} &= \frac{3I}{1.6\ r} \qquad (5.2)
\end{aligned}
$$

Thus, the true number of photons required to obtain the same signal to noise ratio as in the HBT experiment is $N_p^{exp} = 4 N_p^{ev} N_p^{MC}$ the factor of 4 coming from the fifty-fifty probability for the photons to go on the correct detector. In order to go from simulations to experiments, we evaluate the experimental ratio r_{exp} between incoming electrons and detected photons, by comparing the current I (pA) and the number of counts per second C on the HBT detectors:

$$
r_{exp} = \frac{10^7 I}{1.6\ C} \qquad (5.3)
$$

Equation 5.3 implies that the number of electrons N_e^{exp} needed experimentally to have the SNR of the simulation is:

$$
\begin{aligned}
N_e^{exp} &= r_{exp}\ N_p^{ev} \\
&= 4\ \frac{10^7\ I}{1.6\ C}\ \frac{3\ I}{1.6\ r} N_p^{MC} \qquad (5.4)
\end{aligned}
$$

From equation 5.4 we can deduce the experimental integration time needed T:

$$
\begin{aligned}
T &= \frac{N_e^{exp}}{I}\ 1.6\ 10^{-7} \\
T &= \frac{12\ I}{1.6\ C\ r}\ N_p^{MC} \qquad (5.5)
\end{aligned}
$$

Figure 5.9 shows for $C = 10^4$ c/s and $C = 10^5$ c/s the integration time T needed to get a 2 % precision as a function of the lifetime of the emitter. Comparing with experiments, the good order of magnitude seems to be retrieved. However the experiment tends to

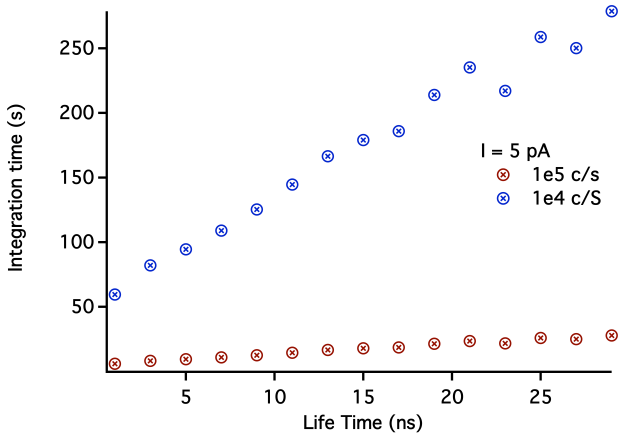

FIGURE 5.9: Integration time T as a function of the lifetime of the emitter for a precision x = 2 %, a current I = 5 pA and a ratio $r \approx 0.8$. We evaluated T for two different numbers of counts per second $C = 10^4$ c/s and $C = 10^5$ c/s with an accuracy x = 2 % of the lifetime.

show that the real integration time is two to four times larger. The integration times we found are close to the ones expected in time-resolved photoluminescence experiments for the same order of accuracy.

5.2 Comparison with Time-Resolved μ-Photoluminescence

In chapter 4 and in the first part of this one we have shown that we measure emitter lifetimes. However, for now, there is no clear evidence that emitter lifetimes measured in CL are in fact similar to the ones measured in PL. Indeed, the bunching effect shows clearly that there are some differences between CL and PL excitation mechanisms. Even if the lifetime retrieved for the diamond in chapter 4 tends to prove that the two lifetimes are similar, the large distribution of nano-diamond lifetimes (between 10 and 30 ns) renders difficult any accurate comparison. Therefore, we have performed, in collaboration with Bruno Gayral at INAC, a statistical comparison between time resolved micro-photoluminescence (TR-μPL) and HBT-CL measurements. We will first explain the principle of TR-μPL and then compare the techniques.

5.2.1 Principle of Time-Resolved μ-PL

Time-Resolved μ-PL measures the deexcitation time of the sample submitted to an excitation. The sample is excited with a pulsed laser beam. If the time between two laser pulses is much longer than the emitter lifetime then the emitter is in its ground state at each excitation pulse. The clock of a correlator, similar to the one used for HBT experiments, is triggered by the pulse of the laser beam and stopped by the associated

emitted photon. We therefore record the delay τ between the excitation and the emission. A sketch of the experiment is shown in figure 5.10. In our case, the experiment was performed in the laboratory INAC in Grenoble in collaboration with Bruno Gayral and Thomas Auzelle. Their experiment is optimized to work in the UV range. We used a titanium sapphire (Coherent Mira 900) pulsed laser emitting at 750 nm with a repetition rate of 82 MHz. The output average power is about 100 mW. The wavelength is then tripled with a non-linear crystal to obtain a wavelength of excitation at 250 nm, which lowers the power to about 10 mW. An attenuator is then added to choose the excitation power, in our case between (10 μW and 100 μW). All the optics used are UV compatible. However the technology in the UV range is less efficient and the objective lens used to focus the beam on the sample has a small numerical aperture (ON = 0.4) with a magnification of only 20. The chromatic aberration is not easily corrected. The poor quality of the objective and the use of a wavelength-tripled laser increases the size of the spot on the sample, the spatial resolution was therefore of the order of ≈ 2 μm. The sample is cooled at liquid helium temperature (T = 4 K) thanks to a Oxford cryostat. The emitted photons are transmitted to a spectrometer that can either send the signal to a CCD camera giving an emission spectrum or select a given wavelength to be sent to a PMT detector. The PMT is linked to the correlator that will start a clock, stopped with the laser pulse, when it detects a photon at a given wavelength. In this configuration the clock is start by the PMT because there is not always emission after, therefore it is worst recording only if an event is detected.

The pulse excites the sample at time t_0. The probability that the emitter will return to its ground state due to radiative or non-radiative recombination is linked to the lifetime of the emitter τ_e. The measurement of the delay between the laser pulse and the emitted photons gives the probability for the sample to emit a photon after a certain time τ. This probability is the radiative probability P_{rad}, that is taken exponential in our case event if some other law can be found for more complex system as discussed before [189, 190] :

$$P_{rad}(\tau) = \frac{1}{\tau_e} exp\left(-\frac{\tau}{\tau_e}\right) \tag{5.6}$$

By simply fitting the obtained curves with an exponential, we can retrieve the lifetime of the emitter. As in the HBT-CL experiment, we extract the total lifetime of the emitter (radiative and non-radiative). The radiative lifetime can be known by studying, for example, the lifetime dependence on temperature. But this quantity is difficult and long to obtain, and this has not been done on the present study. We studied nanowires of AlN/GaN with only one quantum well of GaN per nanowire. The emission wavelength of the quantum wells were typically between 3.1 eV and 3.9 eV. As it will be explained in

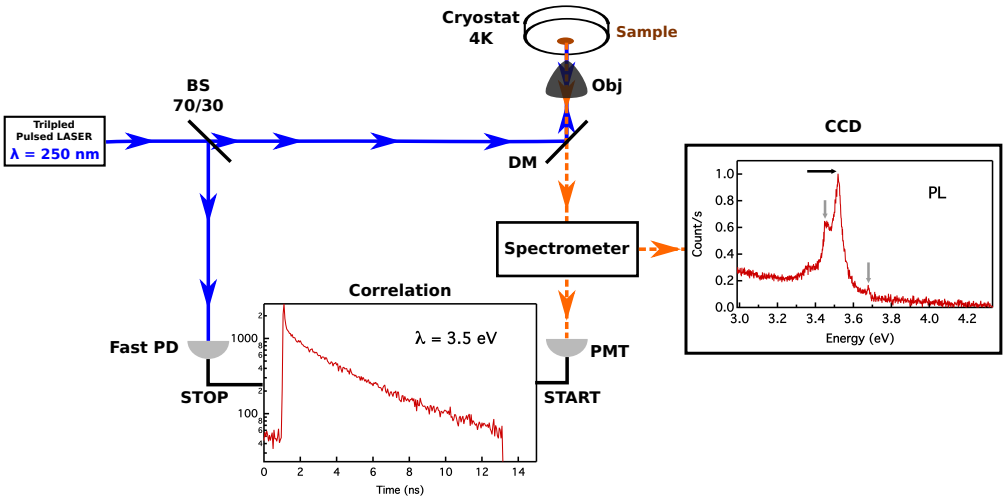

FIGURE 5.10: Sketch of TR-μPL experiment. The pulsed laser beam tripled to λ = 250 nm (blue continuous line) is sent on a beam splitter (BS). It transmits 70 % of the laser beam intensity to the sample and reflects 30 % to a fast photodetector (fast PD) that stops the clock of the correlator. The laser beam is focused on the sample thanks to an objective (Obj), that also collects the signal emitted by the sample (dashed orange line). A dichroic mirror (DM), reflect 100 % of the laser beam and transmit 100 % of the signal. It sends the signal to a spectrometer. The spectrometer can distribute the signal to a CCD camera to obtain an emission spectrum (graph on the right). The emission spectrum allows to note the wavelength of interest (for example the black arrow on the graph : 3.5 eV). The signal can then be sent to the PMT detector, the spectrometer grating and an entrance slit allow to select the wavelength of interest with a spectral resolution of about 1 nm. The PMT starts the clock stopped by the laser beam when it detects a photon. A delay is then recorded, the number of events recorded at a certain delay τ gives the graph at the bottom allowing to extract the lifetime τ_e of the emitter.

section 5.3.2, some defects on the AlN matrix can also be observed between 3.5 and 5.0 eV. Due to the restricted spatial resolution of the experiment, more than one nanowire was excited at the same time. Spectral selection before the PMT usually allows the selection of only one emission. However, in most of the thirty measurements, the fit was the sum of two lifetimes, a shorter lifetime between 60 and 600 ps and a longer lifetime between 0.7 and 5 ns. The first contribution is associated to a secondary emission, coming either from the overlap with the GaN bases of the nanowire or some defect in the AlN matrices (see section 5.3.2). Even if the intensity of this secondary signal is small, its short lifetime makes a visible contribution in the TR-μPL experiment. The second lifetime is associated with the luminescence coming from the GaN quantum well. Without any imaging at the nanometer scale it is difficult to be certain about the origin of each signal and their different contributions. However, from CL measurements we know that defects in AlN have a weaker intensity than the quantum wells. We would therefore expect that the clear emission peaks of the spectrum are related to quantum wells and not defects. We are thus confident to measure a signal coming from the GaN insertion and not from the AlN matrix in the energy range between 3.5 and 4 eV.

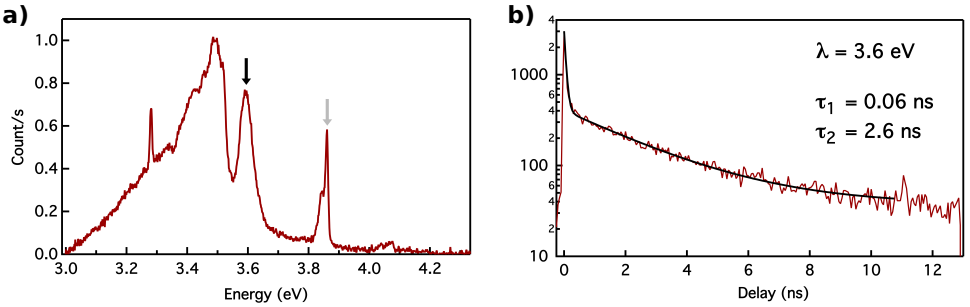

FIGURE 5.11: TR-μPL measurement. a) Emission spectrum obtained with the CCD camera. b) Correlation function of signal filtered around 3.6 eV (black arrow on a)), with a resolution of 50 ps and an integration time of 400 s. The curve was fitted with a sum of two exponentials and two lifetimes τ_1 = 0.06 ns and τ_2 = 2.6 ns was retrieved.

For the experiment, the sampling time of the histogram was 50 ps and the integration time was 400 s. A typical spectrum and lifetime measurement are shown in figure 5.11. On the emission spectrum displayed in figure 5.11-a we can clearly see multiple emission peaks at different energies, with a broad signal around 3.4 eV probably an overlap between a thick quantum well emission and the GaN bulk emission. We select successively two emission energies 3.6 eV and 3.85 eV. The lifetime measurement of the peak at 3.6 eV is shown in figure 5.11-b. The curve was fitted with a sum of two exponentials and we retrieve a short lifetime of τ_1 = 0.06 ns probably associated to the GaN bulk and a second lifetime at τ_2 = 2.6 ns associated to the emission of the GaN quantum well. The broad signal at 3.4 eV was always visible, thus identification of emission coming from thick GaN quantum wells was difficult, limiting the study to thinner quantum wells with emission energy above 3.4 eV.

5.2.2 Comparison between PL and CL

The same sample was studied in HBT-CL. Initially, the goal was to study the same nanowire in TR-μPL and in HBT-CL, as it would have been a more accurate way to compare the two techniques. We therefore deposited the nanowires on a TEM grid lithographied with an alignment pattern similar to the one presented in figure 2.15-a of chapter 2. However, even with the pattern, it was difficult to precisely locate the nanowires due to the poor spatial resolution of the PL imaging system. Moreover, if the intensity was too high (> 40μW) the thin membrane of Si_3N_4 didn't resist to the laser excitation most probably because the gold pattern heats up under laser excitation. Most of the measurements were therefore realized outside of the membrane on the thick part of the TEM grid, allowing us to increase the intensity of the laser beam ($\approx$ 150μW) and another part was done on a grid without pattern. Surprisingly, what really makes difficult to find in CL the nanowire studied in PL was that the number of nanowires emitting in CL was ten times higher than in PL. One explanation for this observation

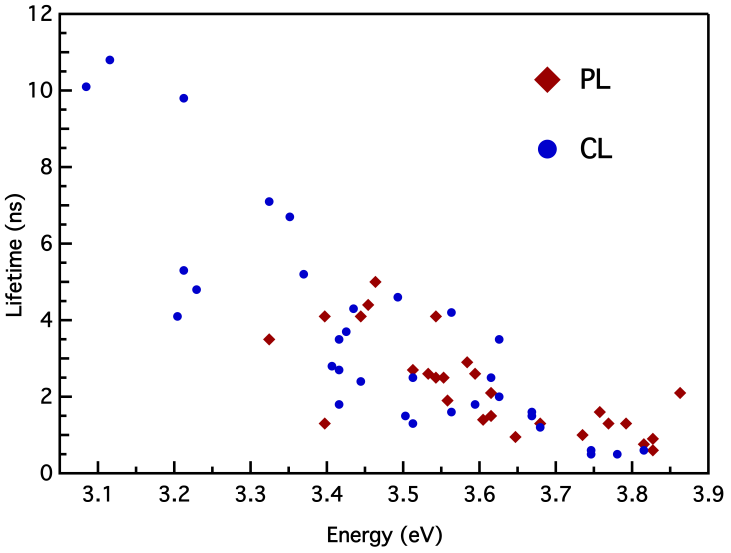

FIGURE 5.12: Lifetime versus emission energy. QWs lifetimes have been measured using TR-PL and HBT-CL in NWs containing single QWs. NW have been sufficiently dispersed so that only a few NW were hit at a time in the μ-PL experiment. Statistically, the expected trend of smaller lifetime for higher energy is observed in both sets of experiments.

could be that the cross section in CL is really high due also to the selectivity of the excitation point, increasing the chance to truly excite a quantum well. We therefore compare the lifetime measurements between the two experiments only statistically even if the data were acquired for the most part on the same grid and approximately at the same location. Of course, in the future, a comparison on the same nanowire would have to be done, with a pattern best suited to the spatial resolution of the PL experiment and with a higher dispersion of the nanowire into the grid. Figure 5.12 shows a statistical comparison of individual QW lifetime measurements in PL and CL. As explained before, time resolved μ-PL measurements for emission below 3.4 eV were difficult to perform due to the overlap with GaN bulk signal coming from the bottom of the NW. Figure 5.12 shows that the statistical distributions of lifetimes for PL and CL are similar. Again, as expected, the lifetime increases for decreasing emission energy [43]. The large amount of studies on this behavior [187, 190, 191] tends to show that the large distribution of energy at a given lifetime can be explained in part by the relatively high temperature of the set-up (150 K) and also because of the structure differences from one nanowire to another that could result into different strain conditions for the quantum wells.

Knowing that we can access lifetimes which are essentially identical to PL ones, we can now exploit the high spatial resolution of the technique to probe situations more complicated than the textbook example of section 5.1.1 of NWs containing individual QWs. In the following section, we are going to exploit this system to study lifetimes in NV^0, of which we acquire a large statistics in the past three years. The CL experiments

also highlight the profusion of defects in the AlN matrix of AlN/GaN nanowire and the defects at the interface GaN/AlN, CL coupled to HBT gives an incredible tool to study those defects. Finally some preliminary results on the influence of the electron beam in the Stark effect existing in thick GaN quantum wells and explained in chapter 1 will be measured.

5.3 Lifetime Measurement on Other Systems

5.3.1 Statistical Measurements in NV^0

The lifetime of NV centers has been extensively studied over the past decades [56, 156]. However it is difficult to perform systematical measurements connecting size and lifetime. Our set-up is optimized to fully characterize a large number of individual nano-diamonds thanks to the synchronization of the measurement with HADF image. We performed a study on nano-diamonds with a large number of NV^0 centers inside the particle. The measurements have been done on 100 nano-diamonds at liquid nitrogen temperature (150 K), distributed on different days of experiments and different substrates. The statistical distribution of the lifetime is shown in figure 5.13. Each fit of the $g^{(2)}(\tau)$ functions were obtained with an accuracy better than 10 %. The distribution found is broad, between 10 and 50 ns with most of the lifetimes between 20 and 30 ns. It is worth noticing that measurement of NDs with lifetimes between 30 and 50 ns was difficult to perform because the lifetime is too long to obtain a meaningful signal to noise ratio over a reasonable time (less than 400s), even at small current, because $g^{(2)}(0) \approx 1$. Thus, most probably the population of diamonds with an average lifetime between 30 and 40 ns is underestimated. No correlation between the substrate and the lifetime have been established although it is known that lifetime of NV center in nano-diamond depends of the environment [56, 192].

It is surprising that the distribution of the average lifetimes is so large for nano-diamonds of similar sizes. It is often said that the large variation of NV centers lifetime in nano diamond is due to the relationship between the surface of the particle and the NV center position [192]. However in our case there are about 900 centers homogeneously distributed into a particle of 100 nm size. Therefore the different key positions comparing to the surface are always present. Thus, for similar sizes we would have expected similar average lifetimes with a tendency to come closer to the bulk value ($\approx$ 11 ns) when the size of the particle increases. Thanks to our set-up, it is straightforward to link lifetime and size of the particle thanks to the HADF. Of course, the HADF is a two dimensional image, we therefore miss one of the three dimensions. Results of the lifetime as a function

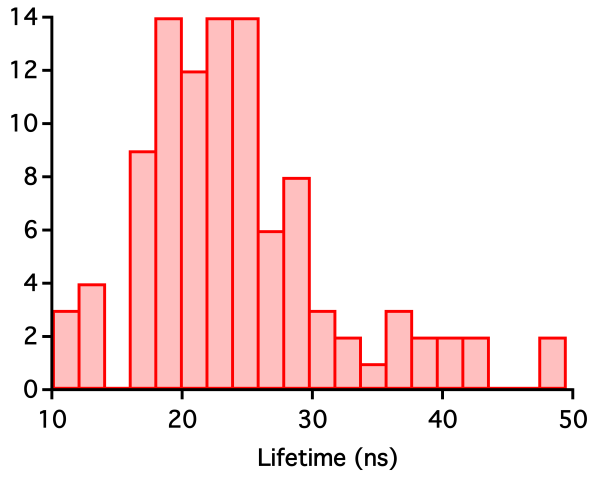

FIGURE 5.13: Distribution of the average lifetime measured on nano diamonds with about 900 centers per nanodiamond. 100 nanodiamonds have been measured with a fit accuracy better than 10 %.

of the size are depicted in figure 5.14 and show no correlation between the size of the particle (or its aspect ratio) and the lifetime. It is worth noticing that we observed some variation up to 5 ns on the same nano diamond after taking the sample out of the microscope and putting it back. The environment seems thus to have a higher impact on the lifetime of the nano-diamond and could explain the variations observed but too many parameters could be responsible to draw a conclusion at the moment.

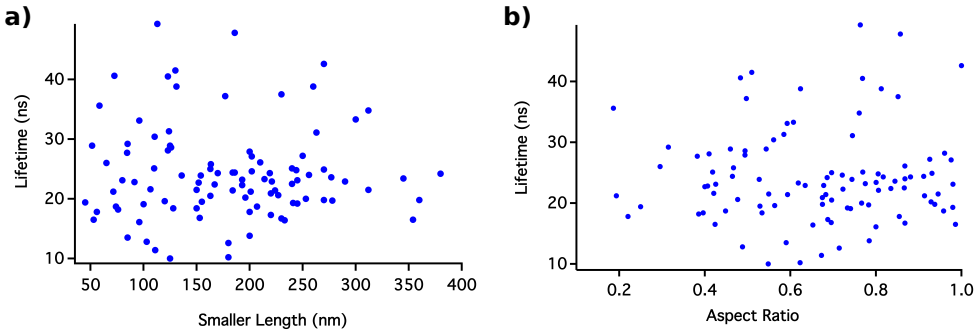

FIGURE 5.14: HBT-CL lifetime measurements as a function of the size of the nanodiamond. a) Lifetime function of the smallest of the two dimension measure and b) function of the aspect ratio of the particle. No correlation between lifetime and size of nano-diamond is seen.

5.3.2 Defects in AlN

As it was already mentioned in this thesis, cathodoluminescence is an appropriate tool to study emission in the UV range without loss of spatial resolution. And due to SPIM methods, one can limit the loss of spectral resolution even if the relatively high cooling temperature (150 K) of the set-up render difficult deep physical insight as one can have

in photoluminescence experiment [190, 191, 193] or in time resolved CL experiment at Helium temperature [194, 195]. Many of our experiments on different kinds of AlN/GaN nanowires show that the luminescence of the GaN quantum wells was often accompanied with localized emission(s) in the AlN matrices. We associated these localized emissions with defects in AlN. But "defects" is a generic term that hides the complexity of the problem. Thanks to the high resolution of the CL system, the synchronization with the HADF images and the lifetime measurement, we were able to better characterize these emissions. We conducted a systematical study on a sample of AlN/GaN nanowires with a high density of defects, but all the observed defects were also observed on the other studied samples. It is the same sample as the one of figure 5.3. Three main kinds of emission have been identified and studied.

The first kind of emission arises above 4 eV. We have investigated the parts of the nanowires emitting at this energy in CL and conventional TEM but not in HBT-CL due to the poor efficiency of PMTs in this region. In figure 5.15, a typical study of defects above 4 eV is shown. The emission is characterized by multiple sharp peaks at each excitation pixel (see figure 5.15-b), one pixel being 10 nm wide. The emission energies are always different, as well as the distance between different associated peaks. It seems that each emission peak is coming from a different location like different point defects. They appear usually in clusters as shown in figure 5.15-d. Moreover, in the conventional TEM contrast shown in figure 5.15-a, we can see no sign of these defects, corroborating the theory of point defects being too small to be revealed by EELS or electron microscopy images. In the literature, emission of AlN in this range is associated with acceptor-donor transitions between recombination of electrons bound to nitrogen vacancy with three positive charges (V_N^{3+}) and neutral magnesium acceptors [196, 197]. However, the signal observed in the literature is a broad band emission spectrum at 4.2 eV, quite different from the one we studied. The high resolution of the experiment could explain that in CL we excite each defect individually compared to PL where a broad band may appear. But the contamination of the MBE chamber is not important enough to explain as many Mg-doped point defects. Moreover, some AlN nanowires (without GaN quantum wells) were grown at the same period in the MBE chamber and this luminescence was not retrieved in PL (not studied in CL). Another explanation could be the incorporation of clusters of GaN into the AlN matrices during the growth of the GaN quantum well. The different sizes of each GaN clusters, and the strain acting differently on each ones [198], could explain the multiplicity of the emission energy. Of all nanowires studies, none has these kind of defects above the GaN quantum well which sustain the hypothesis of GaN clustering during the growth of the GaN inclusion. Indeed the AlN growth after the quantum well is GaN cluster free because no gallium has been incorporated after its growth. However no formal proof of the presence of gallium into

the AlN lattice could be found in EELS most probably because the clusters are made up of only few atoms. These kinds of defects have been seen also in $Al_xG_{1-x}N$ nanowires in cathodoluminescence [199, 200], a fact also explained as due to the inhomogeneity of GaN concentration along the nanowire.

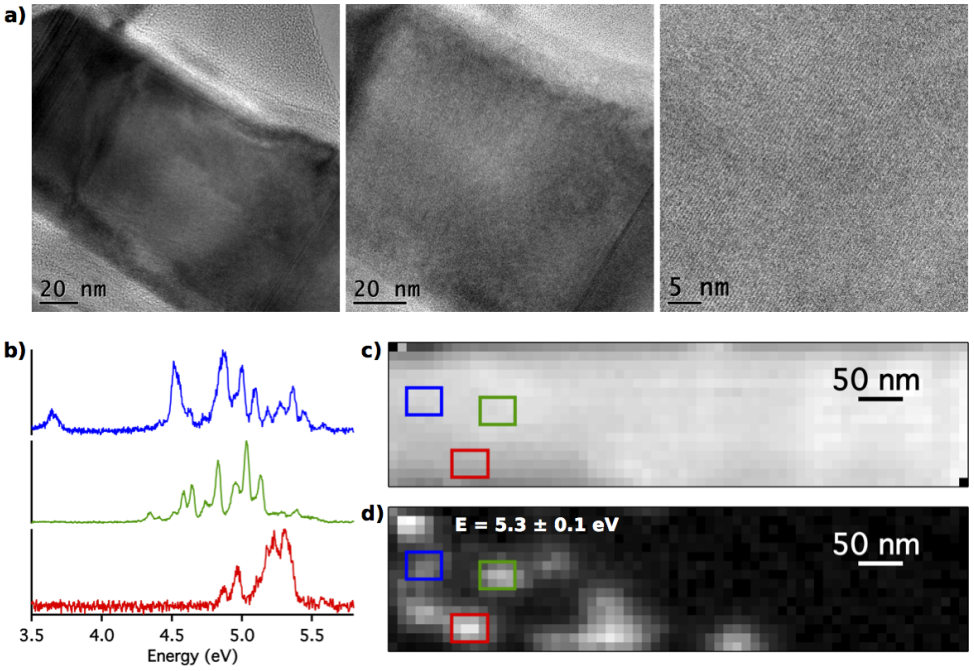

FIGURE 5.15: CL of defects in AlN matrices above 4 eV. a) High resolution TEM images where no sign of defect is visible. b) typical emission spectrum extracted from the SPIM, multiple sharp peaks are visible, the peak pattern and energies is different from the three different locations. The three locations are marked with the square of the corresponding color on the HADF image of the spim in c) and on the intensity map taken at 5.3 ± 0.1 eV. The emission spots are small, about 50 nm, however in each pixel (10 nm) multiple sharp emission peaks are recorded.

The second type of defects is associated with a localized emission between 3.5 and 4 eV. The characteristics of this emission seem slightly different when compared to the first type studied. The second emission is often constituted by two close (less than 100 meV) broader peaks and the emission spots are localized in a 50 nm area often isolated from other defects. An example taken on the same nanowire as in figure 5.15 is shown in figure 5.16. In the literature, a broad band emission around 3.6 eV is associated with complex of AlN vacancies and oxygen impurities [201–203]. Oxygen, as magnesium, is also a possible contaminant during the growth even if it seems unlikely to have such a large contamination. Moreover the lifetime expected for such donor-acceptor transition in the AlN band gap is of the order of 1 μs or longer ([201, 204]), which is not the case here. For the fifteen similar defects investigated the retrieved lifetime were between 0.7 and 2 ns. As for the other defects, it is more likely due to clusters of GaN in

the AlN matrices but with sizes similar to the one expected for a quantum dots of 6-7 monolayers [43] explaining the relative high energy of emission and the nanosecond lifetime. Conventional TEM shows maybe the presence of gallium but EDX at high resolution needs to be performed to validate this observation. However, if these GaN clusters act as quantum dots we could expect an anti-bunching behavior ($g^{(2)}(0) < 1$) for isolated GaN clusters, but a bunching behavior ($g^{(2)}(0) > 1$) was always found. The reason could be, as it has been discussed at the end of chapter 4, that anti-bunching behavior cannot be retrieved from quantum dot with HBT-CL experiments because of the bunching effect.

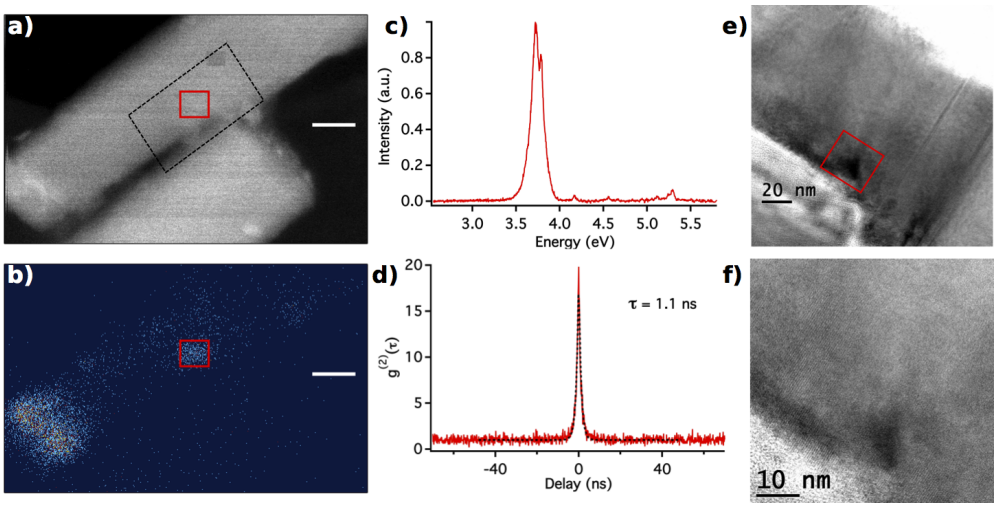

FIGURE 5.16: CL of defects in AlN matrices between 3.5 and 4 eV. a) HADF image of the AlN/GaN matrices and b) emission map recorded thanks to the PMT detector and synchronized with the HADF contrast of a). c) Emission spectrum taken on the red square in a) and the lifetime measurement taken with the HBT-CL experiment with a retrieved lifetime of τ = 1.1 ns. e) and f) conventional TEM images taken at the dashed black area of a). A contrast is visible at the location of the luminescence (red square).

As this kind of defects has a luminescence close to that of narrow quantum wells of GaN, the signal can be interpreted the wrong way in photoluminescence. For example in the case shown in figure 5.17 the luminescence of the quantum well is in fact at an energy similar to that of the GaN at the bottom of the nanowire (3.4 eV) and the luminescence at 4 eV is associated to a defect. Thanks to the spatial resolution we can separate the lifetime of the GaN at the base (τ_3 = 2 ns) and the lifetime of the insertion (τ_1 = 8 ns). As we can see in the HADF image (figure 5.17-d) the defect at 4 eV is localized close to the interface with the GaN base, the presence of the interface changes the environment of the defect, it can explain the high energy and the small lifetime (τ_2 = 0.5 ns) compared to the former example.

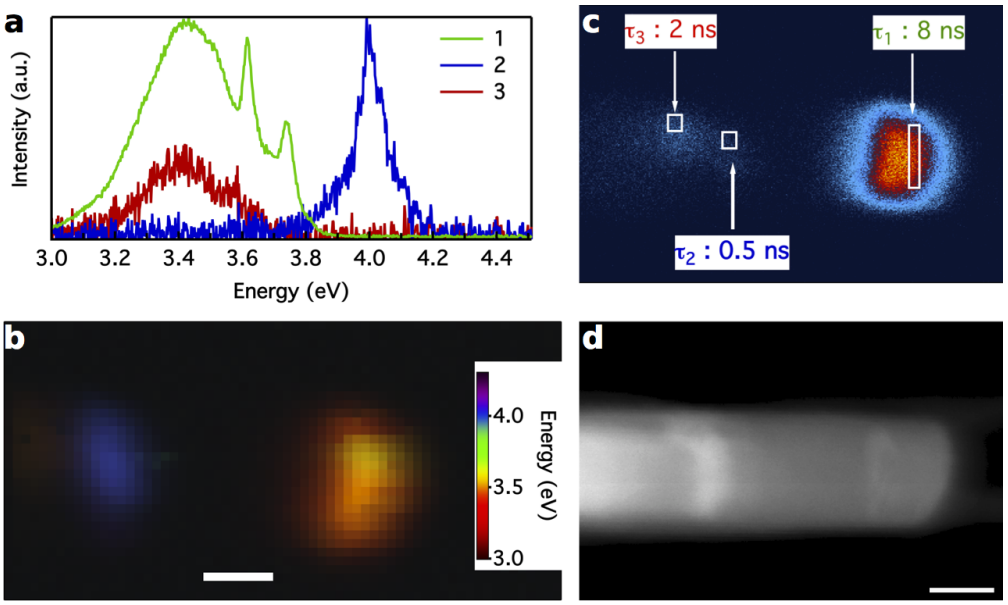

FIGURE 5.17: a) Emission spectra extracted from a spim at three different locations, on the insertion (1), in AlN close to the interface with the GaN base (2) and in the GaN base (3). b) Compression of a spectral image acquired on the nanowire. We can see the emission of the defect at 4 eV and the emission of the insertion around 3.4 eV. c) Filtered emission imaging taken with the PMT detectors and synchronized with the HADF image of d). The lifetime for each measurement is indicated, the white squares show the area of excitation and correspond to the location of the three emission spectra of a. The scale bar is 50 nm.

A third type of emission coming from AlN was found, it is a broad emission, less intense than the first two. Figure 5.18 shows the study in CL and HBT-CL of one of these defects. It appears that the emission pattern revealed in figure 5.18-b is associated with white lines on the HADF image (Figure 5.18-a). This HADF contrast is often the signature of stacking fault (SF). Luminescence from stacking faults has been extensively studied in GaN [205] with PL [206], CL [207, 208] and by Corfdir et al in time resolved CL [194]. In the wurzite III-V material, stacking fault is a local deviation from the hexagonal wurtzite (WZ) to the cubic zinc-blende (ZB) crystal structure [205]. So, it can be seen as a WZ/ZB/WZ quantum well [209, 210] leading to emission energy lower than the band gap exciton. As for a quantum well, the emission energy depends on the size of the SF, which means its crystallographic type, and the band structure will be influenced by the quantum confined Stark effect (QCSE) due the strong internal electric field (see chapter 1 and the following section). However, in our case, the energy found (3 eV) is very far from the band gap exciton ($\approx$ 6 eV) of the AlN. No experimental measurement could be found in the literature; however, theoretically, we expect a value close to the gap [211] as it is case in the GaN [205]. This energy has been observed several times on different nanowires.

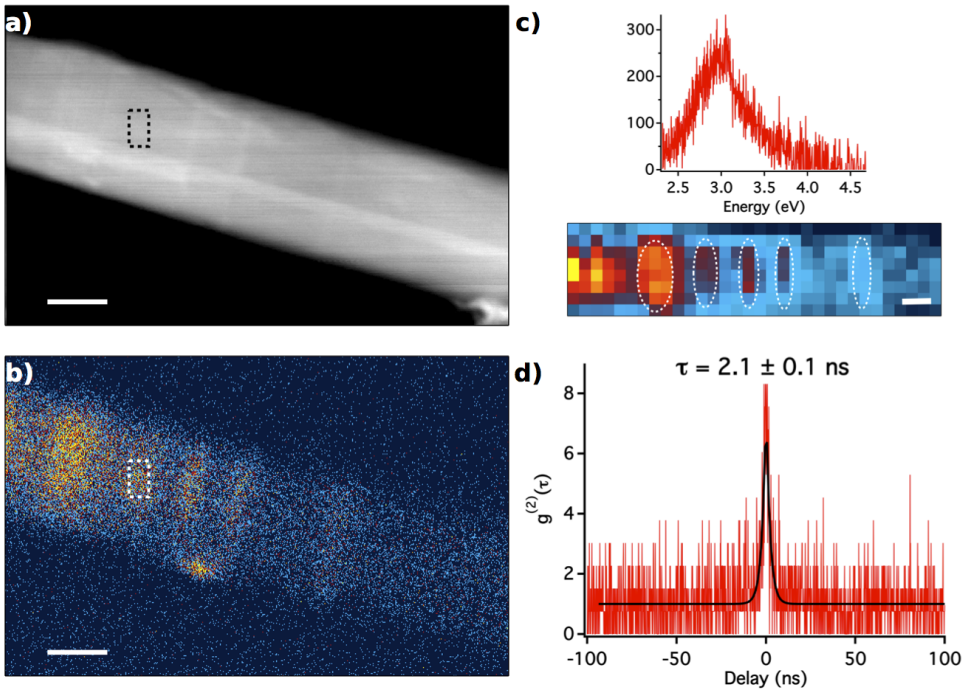

FIGURE 5.18: CL and HBT-CL measurement of stacking faults in AlN. a) HADF image synchronized with the filtered image of b) taken with PMT detector. c) Emission spectrum of the area noted by black dashed square in a) and the filtered images of the spim at E = 3±0.5 eV where we can see the same pattern of emission as in b). d) $g^{(2)}(\tau)$ taken on the same area taken with the HBT-CL experiment, we retrieve a lifetime of 2.1 ± 0.1 ns. The scale bars are 50 nm.

Despite the low energy of the luminescence, emission from the SF seems to be the right explanation. To confirm this hypothesis, conventional TEM images were acquired by L. Tizei on the same nanowire. Results are depicted in figure 5.19. In Figure 5.19, one can see that each emission line of figure 5.19-a) corresponds to a stacking fault in figure 5.19-b). One of the stacking fault (2) is magnified in figure 5.19-e) where we can see clearly the disorder in the crystallographic plane. This is to the best of our knowledge the first measurement of SF luminescence in AlN nanowire at the nanometer scale combined to lifetime measurement.

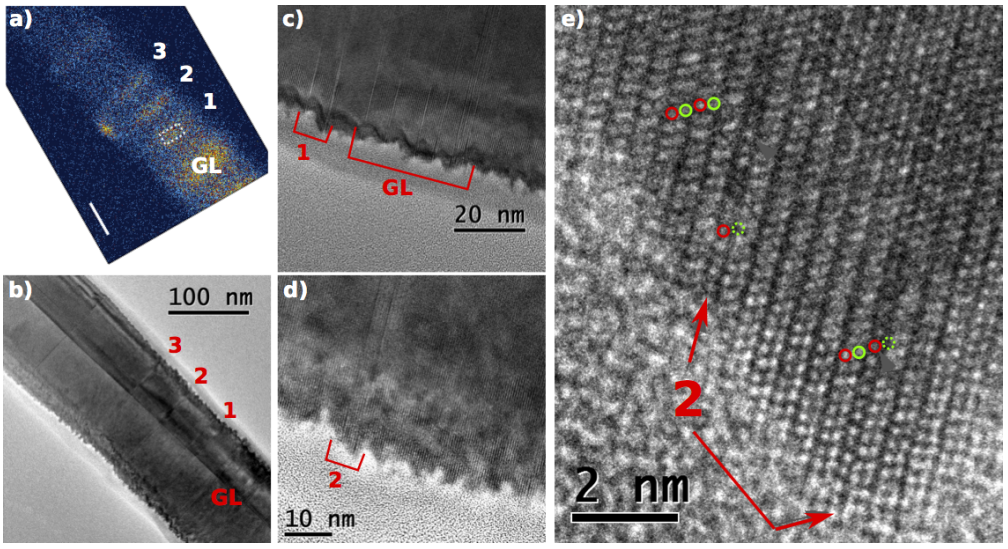

FIGURE 5.19: Conventional TEM contrast of the Stacking fault. a) Filtered images (320-400 nm) of the emission. b) Conventional TEM bright field image, one can see a group of stacking faults (GL) followed by three thinner lines marked as line 1, 2 and 3. c) and d) are magnification respectively of the region with the GL and line 1 and of the line 2. One can see that in fact line 1 and 2 are constituted of two lines. e) Atomically resolved images of line 2, the colored circle highlights the two stacking faults. One can see that each line is only a single inversion, therefore it is a type I_1 [205].

5.3.3 Quantum Confined Stark Effect

To conclude this overview of the different examples of lifetime measurements thanks to HBT-CL experiments, we used the HBT-CL experiment to measure the effect of the electron beam on the internal electric field which is very strong in AlN/GaN nanowires [1, 43, 127]. As explained in chapter 1 (section 1.3.1) the internal electric field induces a band distortion resulting in the so-called quantum confined stark effect (QCSE), that changes the transition energy and increases the lifetime. The electron beam effect will be to screen the QSCE (less distortion of the band) by increasing the beam current or by changing the distance between the electron beam and the quantum well. Indeed, in both cases, it will increase the number of carriers in the quantum well that will screen the internal fields [136, 190]. We used AlN/GaN nanowires with single GaN quantum well. As we wanted to measure the lifetime, we took nanowires where the QCSE was still small to keep a lifetime emission of the order of nanoseconds. Figure 5.20-a and b) shows CL emission along the nanowire. In figure 5.20-a, we can see that the emission energy, when the electron beam excites directly inside the quantum well is higher (E = 3.5 eV) than when it is excited from outside (E = 3.45 eV). We then studied, thanks to HBT-CL, the lifetime variation of the emission for different values of the beam current at a fixed position (about 10 nm from the quantum well). Only three points were recorded and a more systematical study has to be performed to validate these preliminary results.

However it seems, as expected, that the lifetime decreases when the current increases. The acquisition time for the $g^{(2)}(\tau)$ function was between 100 and 230 s and the time sampling of the histogram was 512 ps.

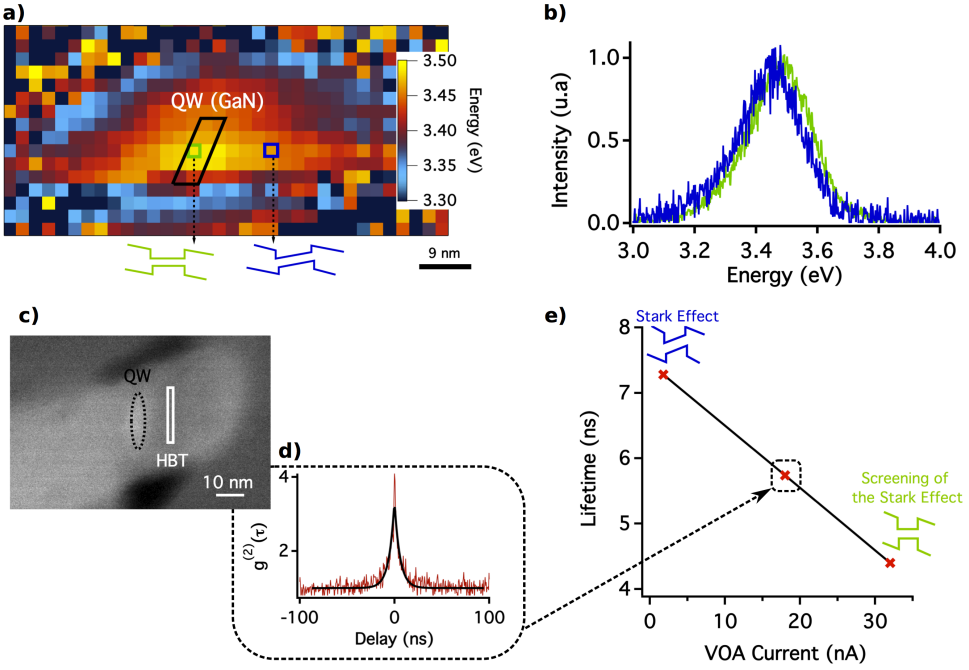

FIGURE 5.20: HBT-CL study of the Stark effect. a) Emission energy map for the different positions of the electron beam. Energies were found thanks to a fit to the emission spectrum at each pixel. b) Emission spectrum at two positions of the electron beam represented by square of the same color in a) (green inside the quantum well and blue outside). c) HADF of the nanowire, the white square shows the HBT-CL excitation area. d) $g^{(2)}(\tau)$ function acquired at $I \approx 18 \pm 2$ nA (on the objective aperture). The measurement of the current was done on the objective aperture (VOA) (see chapter 4). e) Lifetime measurement function of the current, the schematic and amplified effect of the current on the band distortion is drawn as a visual aid.

5.3.4 Comparison with other time resolved spectroscopies

In this chapter we demonstrate the possibility to use the bunching for time-resolved measurement at the nanometer scale. As stated throughout this chapter this is not the first technique to measure lifetime. The two main ones are **time-resolved μ-PL** and **time-resolved CL in a scanning electron microscope** (SEM), each having benefits and drawbacks.

Time-resolved μ-PL is a widely used technique which offers the benefits of a laser excitation that allows a softer interaction with matter. The excitation to a specific wavelength also permits a better selectivity of the excited emission. The studies are almost always done at Helium temperature (4K) which enable to observe fine physical phenomenon [187, 212] supported by a much better energy resolution [190, 193] than what we can

achieve for now in HBT-CL. However, the laser excitation makes it impossible to reach a spatial resolution better than hundreds of nanometer at best and even worst in the UV range. Moreover the absence of images of the excited area limited the correlation of the emission with the structure of the material. For all these reasons time-resolved μ-PL is, for now, a much better tool than HBT-CL to obtain insight into the physics of the sample but is limited as a tool to characterize material and therefore to improve synthesis.

On the other hand, time-resolved CL in a SEM [213] relies on a pulsed electron gun to excite the sample. Contrary to μ-PL due to the electron probe, one can obtain a resolution of 50 nm which is less than the HBT-CL experiment but much better than PL. It is important to note that the pulsed electron gun allows, in opposition to the HBT-CL experiment, to retrieve the carrier dynamics [214]. Some experiments have been done at 4K [194, 195] but it is still difficult to master. The synchronization of the spectroscopy study with a secondary electron image gives insight into the relation between the emission and the material morphology. However the use of a pulse electron gun limited the brightness of the electron gun, and its current. Therefore the time of integration for a single measure is relatively long compare to what is achievable thanks to HBT-CL measurement. The latter reaches a resolution of 1 nm and allows the correlation with atomic HADF images. For now only nitrogen temperature is available but there is room for improvements. In conclusion, it seems that the HBT-CL experiment is a very good tool to characterize material, combining cathodoluminescence, HADF images, HBT-CL and EELS measurement on the same experiment. But the possibility to see very fine physical phenomenon still have to be demonstrated, and there is no doubt that helium temperature and spectral filtering are two necessary steps.

In this chapter, we have seen the application of the bunching effect to lifetime measurements on several samples. Performing CL, HADF images and lifetime measurements on the same region allowed more accurate and reliable measurements. It is now easy to acquire statistical data where before it was difficult to obtain all this information for one specimen. Obviously it opens more questions than it answers, as for example the reason for the large distribution of lifetime in nano-diamonds which seems to be uncorrelated to the size of the particle, or the nature of emission of point defect in AlN. However, all these new questions show the pertinence to perform nano-optics at the nanometer scale.

Chapter 6

Quantum Non-Linearities in EELS

> It is at this point that normal language gives up, and goes and has a drink
>
> *Terry Pratchett*

6.1 Challenges in Quantum Plasmonic

6.1.1 A Quantization, what for?

Diffraction imposes a limit on the size of dielectric-based systems currently used for optical communications at visible and near-infrared frequencies. The use of plasmons to transport information is a way to break this limit and push light manipulation down to the nanometer scale. The ability of plasmons to carry classical information is well known, becoming the natural bridge between opto-electronics and nano-electronics [215]. Moreover, it has been recently demonstrated that plasmons can also carry and preserve quantum information embodied in the light used to generate them [45, 216]. Additionally, nanoparticles are able to sustain single plasmon modes that are themselves quantum entities. For example, detection of single plasmon modes has been demonstrated [45] as well as the wave-particle duality of these excitations [217]. Recently, plasmon entanglement [218] and squeezing [219] have been observed on specific plasmonic structures like gold strips. The quantum nature of plasmons is thus well established and the basic of the field of quantum plasmonics.

Quantum theoretic treatments of plasmons have been formulated in order to exploit them, for example optimizing the coupling with single photon emitters [48]. In this context, Archambault et al. quantized plasmons using a simple model of harmonic oscillators [220, 221]. They were able to explain the spontaneous emission rate of two-level systems interacting with surface plasmons and also evaluate the Einstein coefficients. Manjavacas et al [222] use the Zubarev Green function formalism [223] to introduce plasmon damping, showing that in the small damping regime an emitter placed between two plasmonic nanoparticles exhibits an optical Fano resonance.

It is well known that the smaller the structure is, the more dissipative the plasmon modes are [224]. Therefore the effect of damping cannot be overlooked for applications in quantum plasmonics. As it has been explained in chapter 1, electron energy-loss spectroscopy is an ideal tool to probe plasmons at the nanometer scale and therefore on dissipative structures. In collaboration with Javier Garcia de Abajo at ICFO we formulate a theoretical proposal to monitor the quantum behavior of plasmons in an STEM.

6.1.2 Electron Energy-Loss Spectroscopy as a Probe

Some of the above mentioned experiments show that a plasmon acts as a boson. It is well known that, the probability to add one boson to a system depends on the number n of bosons already present. If P_1 is the probability to create a plasmon when there is none in the system, the probability P_2 to create a plasmon if there are already n will be $P_2 = (n+1) * P_1$. Therefore, in EELS, the energy lost by the electron after interaction with the system will depend on the number of plasmons present in the system. For example, let us consider two electrons passing near a metallic particle in its ground state ($n = 0$) and assume that first electron creates one plasmon. If the plasmon is still present when the second electron arrives, the probability that the second electron creates a second plasmon is higher than when no plasmon remains.

We can imagine an experiment in which one records each electron detected in EELS, which means each electron that interacts with the nanoparticle and has created a plasmon. As the electron beam is Poissonian, if plasmons are classical then the times the electron-plasmon at which interactions takes place are stochastically distributed, and therefore, the autocorrelation function of the EELS signal will be $g^{(2)}(0) = 1$. If plasmons are bosons then, as $P_2 = (n+1)P_1$, the probability to create a plasmon will be higher at short delay between the arrivals of the two electrons, which means that $g^{(2)}(0) > 1$ (bunching). Short delay is linked here to the lifetime of the bosonic state τ_p : indeed the longer the plasmons are staying in the nanoparticle, the longer the delay can be between

the two noted electron arrivals. In contrast, if plasmons were fermions, an electron could not create a plasmon if there is already one in the system, so we should have $g^{(2)}(0) < 1$ (anti-bunching), with the correlation time also depending on τ_p. Figure 6.1 shows a Monte Carlo simulation of the arrival times for the three situations discussed above (classical, Bosonic and Fermionic) for different lifetimes τ_p. The horizontal axis is the time at which an electron that has created a plasmon has been detected, normalized to Δ_{eff}, which is the average interval between two incoming electrons interacting with the sample. For a given τ_p (vertical axis), the black dots represent the time of detection of an electron on the EELS detector. We can see for example for the Bosonic case that if τ_p increases, the correlation time is longer, thus increasing the time duration of the bunch producing almost a continuous line for $\tau_p > 7\Delta_{eff}$. These simulations are considering the decay in the simplest way given for P_2 :

- Classical : $P_2 = P_1$
- Bosonic : $P_2 = (n+1)\ P_1\ e^{-t/\tau_p}$
- Fermionic : $P_2 = \left(1 - n\ e^{-t/\tau_p}\right) P_1$.

This thought experiment can be a test to measure the quantum behavior of plasmons when we aim at dissipative systems. One of our goals is to determine the effect of dissipation on this type of experiment, the effect being more complex than the above description. We therefore need to find a way to theoretically describe the experiment taking into account dissipation. In order to do so, we use the formalism of the density matrix ρ of a system consisting of a nanoparticle with a boson mode with population number n and a beamed electron passing near the nanoparticle. The electron is described as a plane wave of wave vector k_0. At a given time t, the plasmon population is described by the diagonal terms of its density matrix, so we need to calculate the terms $\underset{k',n+1}{\rho_{k',n+1}}(t)$ and $\underset{k'',n-1}{\rho_{k'',n-1}}(t)$ assuming an initial state $\rho(0) = \underset{k_0,n}{\rho_{k_0,n}} = 1$. The next section describes in detail the steps of the calculation.

6.2 Theoretical Developpement

In this section we are going to describe the interaction of a fast electron with a nanoparticle that sustains Bosonic modes decaying with a rate $\Gamma_0 = \frac{1}{\tau_p}$. As this is a single electron interaction, we need to have a full quantum description of the system. The electron is

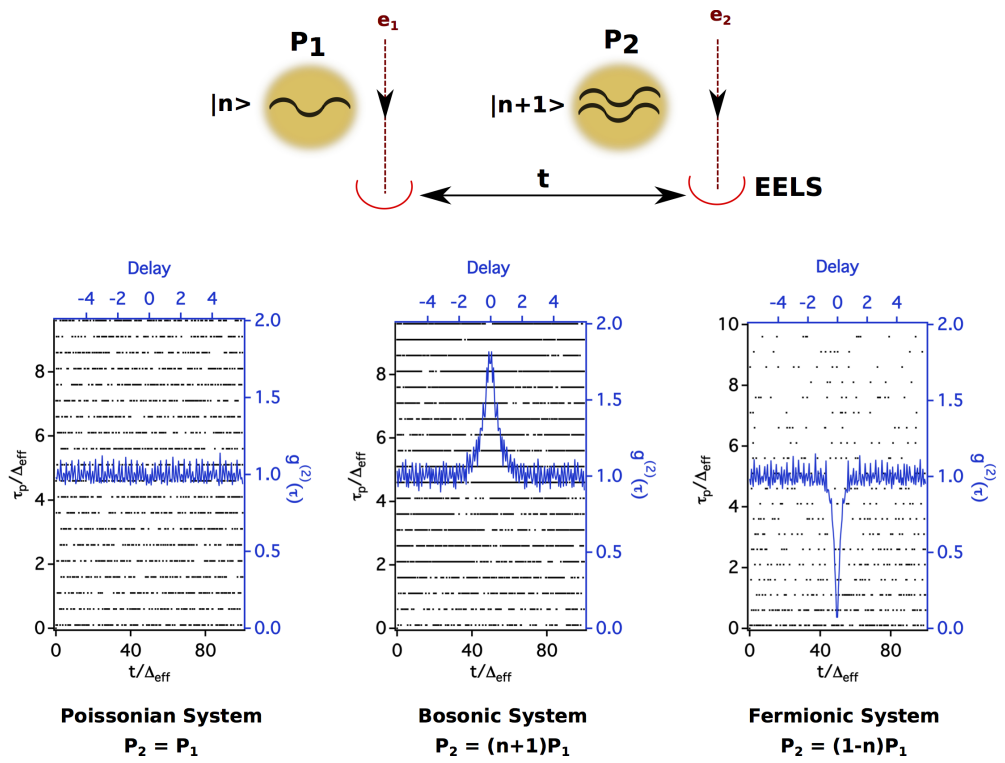

FIGURE 6.1: Simple Monte Carlo simulation of the quantum non-linearities in EELS experiment. Top : Sketch of the experiment. At $t = 0$ a first electron e_1 passing near a plasmon-supporting particle (yellow sphere) leaves the plasmon state as $|n\rangle$. At a subsequent time $t = t_2$ a second electron e_2 interacts with the particle, whose plasmon state goes from $|n\rangle$ to $|n+1\rangle$. Bottom : For each panel the black dots represent the detection times t of an electron in EELS as a function of the lifetime τ_p of the plasmon. t and τ_p are normalized to the average time interval Δ_{eff} between two electron interactions with the nanoparticle, taking into account the current I and P_1 the probability of interaction if there is no excited plasmon in the nanoparticle. Each plot correspond to a different situation in which plasmons are considered to be, from left to right, Poissonian, bosononic and fermionic.

therefore described as a plane wave of wave vector k and the nanoparticle as a quantum field filled with n Bosons. The Hamiltonian can be written as follow:

$$\begin{aligned} H &= H_0 + H_{el}, \\ H_0 &= \hbar\omega_0 \left(a^+ a\right) + \hbar\epsilon \; b^+ b, \\ H_{el-pl} &= \sum_{k_1,k_2} b^+_{k_1} b_{k_2} \; g_{k_1,k_2} \left(a^+ + a\right), \end{aligned}$$

where a and a^+ are the Boson annihilation and creation operators, while b_k and b^+_k are the electron annihilation and creation operators. Also, ω_0 and ϵ are the resonance frequencies of the boson and the electron, respectively, and $g_{k,k'}$ is the coupling constant between the electron and the nanoparticle. In the density matrix formalism, the master

equation can be written as follow:

$$\dot{\rho} \;=\; \frac{i}{\hbar}[\rho, H] + \frac{\Gamma_0}{2}\left[2a\rho a^+ - a^+ a\rho \;-\; \rho a^+ a\right],$$

where the boson damping is taken into account by adding a Lindblad term [225, 226] and Γ_0 is the damping rate such that $\Gamma_0 = \frac{1}{\tau_p}$. As the interaction time between the electron and the nanoparticle is very small, we can consider that first the electron interacts with the nanoparticle, and then the boson evolves. This means that we can deal sequentially with the two parts of the master equation for the density matrix,

$$\text{Interaction} \;:\; \dot{\rho} = \frac{i}{\hbar}[\rho, H] \tag{6.1}$$

$$\text{Damping} \;:\; \dot{\rho} = \frac{\Gamma_0}{2}\left[2a\rho a^+ - a^+ a\rho \;-\; \rho a^+ a\right] \tag{6.2}$$

Figure 6.2 describes the different steps of the calculation. At $t = 0$, a first electron interacts with the nanoparticle and is eventually detected and therefore, we know the number n of Bosons present at $t = 0$. Then, the Bosons decay to a state l with a certain probability. At $t = t_2$, a second electron interacts with the nanoparticle leaving it in the state $l+1$ or $l-1$ depending whether the electron loses energy or gains energy during the interaction. Eventually, the second electron is detected, and once again, we know the number of Bosons present at time t_2. We iterate this process, so our time t_2 becomes t_0 and we restart the first step. Therefore, from the initial state $\rho = \underset{k_0,n}{\rho_{k_0,n}} = |n, k_0\rangle\langle k_0, n|$, we need to calculate $\forall\ l \leq n\ \underset{l,k_0}{\rho_{l,k_0}}(t_2 - \delta t)$ the density matrix element after the decay, but at an infinitesimally small time before the interaction. Then, we need to calculate the evolution over time, giving $\forall\ l \leq n\ \underset{l+1,k'}{\rho_{l+1,k'}}(t_2)$ and $\underset{l-1,k''}{\rho_{l-1,k''}}(t_2)$.

These two steps, interaction and decay, form a sequence repeated for each electron interacting with the nanoparticle. We will first calculate the interaction part in section 6.2.1, that occurs at t_0 and t_2, then the decay part, in section 6.2.2, that takes place between t_0 and t_2.

6.2.1 Interaction of the Electron with the Nanoparticle

Interaction from $\underset{k_0,l}{\rho_{k_0,l}}(t_2)$ to $\underset{k',l+1}{\rho_{k',l+1}}(t_2)$ and $\underset{k'',l-1}{\rho_{k'',l-1}}(t_2)$

Let us define ϵ_k as the frequency of the electron and ω_0 the frequency of the Boson. The state consisting of the electron and the boson field is described by the ket $|n, k\rangle$, where n is the boson number and k is the electron wave vector (the electron being in a plane wave state along the beam direction). We can write the density matrix ρ in the

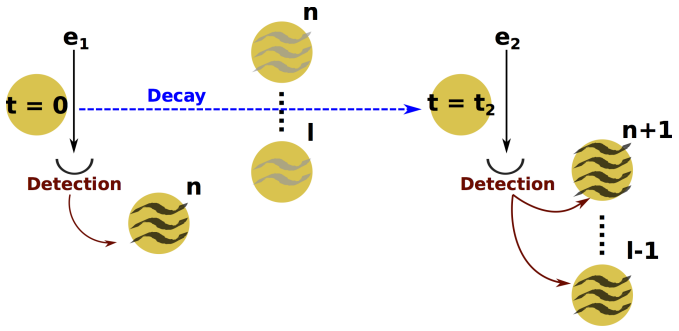

FIGURE 6.2: The electron e_1 interacts with the sample at t = 0. We detect it in EELS. Therefore we know the number n of plasmons in the system at t = 0 (black waves). Before the second electron arrives at t, the system can decay into a number l of plasmons less or equal to n (grey waves). Electron e_2 arrives at t_2 and creates or absorbs a plasmon from the system, which then evolves to state $l+1$ or $l-1$, respectively.

interaction picture:

$$\begin{aligned}\rho &= \sum_{\substack{k,n\\k',n'}} \rho_{\substack{k,n\\k',n'}} |k,n\rangle\langle n',k'| \\ &= \sum_{\substack{k,n\\k',n'}} \rho^I_{\substack{k,n\\k',n'}} e^{-i((n-n')\omega_0+(\epsilon_k-\epsilon_{k'}))t} |k,n\rangle\langle n',k'| \end{aligned} \tag{6.3}$$

with $\rho^I_{\substack{k,n\\k',n'}}$ being the density matrix element in the interaction picture. In this representation, equation 6.1 becomes:

$$\dot{\rho^I} = \frac{i}{\hbar}\left[\rho^I, H_{el-pl}\right], \tag{6.4}$$

and therefore,

$$\begin{aligned}&\sum_{\substack{k,n\\k',n'}} \dot{\rho}^I_{\substack{k,n\\k',n'}} e^{-i((n-n')\omega_0+(\epsilon_k-\epsilon_{k'}))t} |k,n\rangle\langle n',k'| \\ &= \frac{i}{\hbar} \sum_{\substack{k,n\\k',n'}} \rho^I_{\substack{k,n\\k',n'}} e^{-i((n-n')\omega_0+(\epsilon_k-\epsilon_{k'}))t} \sum_{k_1,k_2} |k,n\rangle\langle n',k'| b^+_{k_1} b_{k_2} g_{k_1,k_2} (a^+ + a) \\ &\qquad - b^+_{k_1} b_{k_2} g_{k_1,k_2} (a^+ + a) |k,n\rangle\langle n',k'| . \end{aligned} \tag{6.5}$$

We show in appendix B that equation 6.5 can be written as:

$$\begin{aligned}\dot{\rho}^{I}_{\substack{k,n\\k',n'}} = \frac{i}{\hbar}\sum_{k_2}\sum_{n_2,n_2'} & G^{1}_{\substack{n,n'\\n_2,n_2'}}\, g_{k_2,k'}\rho^{I}_{\substack{k,n_2\\k_2,n_2'}}\, e^{-i\left(\left(\epsilon_{k'}-\epsilon_{k_2}\right)-\omega_0\right)t} \\ & + G^{2}_{\substack{n,n'\\n_2,n_2'}}\, g_{k_2,k'}\rho^{I}_{\substack{k,n_2\\k_2,n_2'}}\, e^{-i\left(\left(\epsilon_{k'}-\epsilon_{k_2}\right)+\omega_0\right)t} \\ & - G^{3}_{\substack{n,n'\\n_2,n_2'}}\, g_{k,k_2}\rho^{I}_{\substack{k_2,n_2\\k',n_2'}}\, e^{-i\left(\left(\epsilon_{k_2}-\epsilon_{k}\right)+\omega_0\right)t} \\ & - G^{4}_{\substack{n,n'\\n_2,n_2'}}\, g_{k,k_2}\rho^{I}_{\substack{k_2,n_2\\k',n_2'}}\, e^{-i\left(\left(\epsilon_{k_2}-\epsilon_{k}\right)-\omega_0\right)t}\end{aligned} \tag{6.6}$$

with the matrices G^1, G^2, G^3, G^4 given by

$$\begin{aligned}G^{1}_{\substack{n,n'\\n_2,n_2'}} &= \delta_{n,n_2}\delta_{n'+1,n_2'}\sqrt{n'+1} \\ G^{2}_{\substack{n,n'\\n_2,n_2'}} &= \delta_{n,n_2}\delta_{n'-1,n_2'}\sqrt{n'} \\ G^{3}_{\substack{n,n'\\n_2,n_2'}} &= \delta_{n+1,n_2}\delta_{n',n_2'}\sqrt{n+1} \\ G^{1}_{\substack{n,n'\\n_2,n_2'}} &= \delta_{n-1,n_2}\delta_{n',n_2'}\sqrt{n}\end{aligned}$$

Equation 6.6 is easy to calculate numerically after integration over k_2 and over time t. To do so, we make the approximation that the coupling constant g depends only on k_0. This means that we consider that $k_0 \gg \frac{\omega_0}{v}$ (a generally valid approximation for low-loss EELS), and therefore, we consider that $g_{k,k_2} = g_{k_0}$ and $g_{k,k_2} = g^*_{k_2,k}$. We discuss how to obtain g in section 6.2.3.

Integration over Time of the Interaction Part (equation 6.6)

We can thus rewrite equation 6.6 as:

$$\begin{aligned}\dot{\rho}^{I}_{\substack{k,n\\k',n'}} = \frac{i}{\hbar}\sum_{k_2}\sum_{n_2,n_2'} & G^{1}_{\substack{n,n'\\n_2,n_2'}}\, g^*_{k_0}\rho^{I}_{\substack{k,n_2\\k_2,n_2'}}\, e^{-i\left(\left(\epsilon_{k'}-\epsilon_{k_2}\right)-\omega_0\right)t} \\ & + G^{2}_{\substack{n,n'\\n_2,n_2'}}\, g^*_{k_0}\rho^{I}_{\substack{k,n_2\\k_2,n_2'}}\, e^{-i\left(\left(\epsilon_{k'}-\epsilon_{k_2}\right)+\omega_0\right)t} \\ & - G^{3}_{\substack{n,n'\\n_2,n_2'}}\, g_{k_0}\rho^{I}_{\substack{k_2,n_2\\k',n_2'}}\, e^{-i\left(\left(\epsilon_{k_2}-\epsilon_{k}\right)+\omega_0\right)t} \\ & - G^{4}_{\substack{n,n'\\n_2,n_2'}}\, g_{k_0}\rho^{I}_{\substack{k_2,n_2\\k',n_2'}}\, e^{-i\left(\left(\epsilon_{k_2}-\epsilon_{k}\right)-\omega_0\right)t}\end{aligned} \tag{6.7}$$

We know that $\rho(t_2-\delta t) = \rho_{\substack{k_0,n\\k_0,n}}(t_2)\,|k_0,n\rangle\langle n,k_0|$ before the interaction takes place. Equation 6.7 shows that the electron can gain energy (G^1 and G^3) or lose energy (G^2 and G^4) when interacting with the Bosonic field. This corresponds to a loss or a gain of

a Boson for the nanoparticle, respectively. As explained above, we are interested in calculating the diagonal elements of the density matrix $\rho(t_2 + \delta t)$ after interaction with the nanoparticle (at t_2). Here, δt represents the interaction time that is considered to be negligibly small (less than one femtosecond) compared to the arrival time interval between two electrons (of the order of nanoseconds). In the formalism of the density matrix, we can calculate the diagonal terms by going to second-order perturbation. If the initial state is $|k_0, n\rangle\langle n, k_0|$:

$$\begin{aligned}
|k_0, n\rangle\langle n, k_0| &\to |k_0, n\rangle\langle n-1, k_1'| \to |k_1', n-1\rangle\langle n-1, k_1'| \quad (1)\\
&\to |k_0, n\rangle\langle n+1, k_1| \to |k_1, n+1\rangle\langle n+1, k_1| \quad (2)\\
&\to |k_1', n-1\rangle\langle n, k_0| \to |k_1', n-1\rangle\langle n-1, k_1'| \quad (3)\\
&\to |k_1, n+1\rangle\langle n, k_0| \to |k_1, n+1\rangle\langle n+1, k_1| \quad (4)
\end{aligned}$$

An arrow represents the application of the master equation. We will describe the calculation of $\rho_{\substack{k_1,n+1\\k_1,n+1}}$ (paths (2) and (4)) but the calculation of $\rho_{\substack{k_2,n-1\\k_2,n-1}}$ proceeds in a similar way so we do not show it as it can be easily deduced from the calculation of $\rho_{\substack{k_1,n+1\\k_1,n+1}}$

Calculation of $\rho_{\substack{k_1,n+1\\k_1,n+1}}$

We describe the calculation with the example of path (2). Therefore, the first process that we analyze with the master equation will give $\rho_{\substack{k_0,n\\k_0,n}} \to \rho_{\substack{k_0,n\\k_1,n+1}}$. In this case, the matrices G^1, G^2, G^3, G^4 become:

$$\begin{aligned}
G^1_{\substack{n,n+1\\n_2,n_2'}} &= \delta_{n,n_2}\delta_{n+2,n_2'}\sqrt{n+2} \quad & G^3_{\substack{n,n+1\\n_2,n_2'}} &= \delta_{n+2,n_2}\delta_{n+1,n_2'}\sqrt{n+2}\\
G^2_{\substack{n,n+1\\n_2,n_2'}} &= \delta_{n,n_2}\delta_{n,n_2'}\sqrt{n'} & G^4_{\substack{n,n+1\\n_2,n_2'}} &= \delta_{n-1,n_2}\delta_{n+1,n_2'}\sqrt{n}
\end{aligned}$$

As only state $\rho_{\substack{k_0,n\\k_0,n}} \neq 0$, only G^2 gives nonzero elements

$$\dot{\rho}^I_{\substack{k,n\\k',n'}} = \frac{i}{\hbar}\sum_{k_2}\sum_{n_2,n_2'} G^2_{\substack{n,n'\\n_2,n_2'}}\, g^*_{k_0}\rho^I_{\substack{k,n_2\\k_2,n_2'}}\, e^{-i\left((\epsilon_{k'}-\epsilon_{k_2})+\omega_0\right)t}$$

In order to perform the integration over k, we make the approximation that the plane wave is in fact a Gaussian packet, peaked around k. This means that the width of the Gaussian packet, $1/\Delta$, needs to be very small compared to ω_0/v, which is the case in the non-recoil approximation. Therefore, the density matrix element before interaction can be defined as (see Apendix C) $\rho_{\substack{k_0,n\\k_0,n}}(t_2 - \delta t) = C_{k_0}C^*_{k_0}\rho_{n,n}(t_2 - \delta t) =$

$\frac{\Delta}{\sqrt{2\pi^3}} e^{-2(k-k_0)^2\Delta^2} \rho_{n,n}(t_2 - \delta t)$, with $\rho_{n,n}(t_2 - \delta t)$ being the bosonic state of the nanoparticle before the interaction.

Integration over k

$$\begin{aligned}
\dot{\rho}_{\substack{k_0,n \\ k_1,n+1}} &= \frac{i}{\hbar}\frac{L}{2\pi}\int_{-\infty}^{\infty} dk\sqrt{n+1}\rho_{\substack{k_0,n \\ k,n}} g_{k_0}^* e^{-i((\epsilon_{k_1}-\epsilon_k)-\omega_0)t} \\
&= \frac{i}{\hbar}\frac{L}{2\pi}\frac{\Delta}{\sqrt{2\pi^3}} C_{k_0}\sqrt{n+1}\rho_{n,n} g_{k_0}^* \int_{-\infty}^{\infty} dk\ C_{k_0}^* e^{-i((\epsilon_{k_1}-\epsilon_k)-\omega_0)t} \\
&= \frac{i}{\hbar}\frac{L}{2\pi^2}\frac{g_{k_0}^*}{\sqrt{2}} C_{k_0}\sqrt{n+1}\rho_{n,n} e^{-ik_0 z_1} e^{-i((\epsilon_{k_1}-\epsilon_{k_0})-\omega_0)t} e^{-\left(\frac{z_1-vt}{2\Delta}\right)^2}
\end{aligned} \tag{6.8}$$

The complete derivation of equation 6.8 is presented in appendix B. z_1 is the z coordinate along the direction of the electron path where the interaction takes place. We now have to integrate over the time.

Integration over t

$$\begin{aligned}
\rho_{\substack{k_0,n \\ k_1,n+1}} &= \frac{i}{\hbar}\frac{L}{2\pi^2}\frac{g_{k_0}^*}{\sqrt{2}} C_{k_0}\sqrt{n+1}\rho_{n,n} e^{-ik_0 z_1}\int_{-\infty}^{\infty} dt\ e^{-i((\epsilon_{k_1}-\epsilon_{k_0})-\omega_0)t} e^{-\left(\frac{z_1-vt}{2\Delta}\right)^2} \\
&= \underbrace{\frac{i}{\hbar}\frac{L}{\pi^2}\frac{\Delta\sqrt{\pi}}{v}\frac{g_{k_0}^*}{\sqrt{2}}\sqrt{n+1} e^{-ik_0 z_1} e^{\left(\frac{a\Delta}{v}\right)^2} e^{-\left(\frac{z_1}{2\Delta}\right)^2}}_{F_1} C_{k_0}\rho_{n,n}
\end{aligned} \tag{6.9}$$

$$\text{With}: \ a = \left(\frac{z_1 v}{2\Delta^2} - i\left((\epsilon_{k_1} - \epsilon_{k_0}) + \omega_0\right)\right)$$

We do the same calculation for $\rho_{\substack{k_0,n \\ k_1,n+1}} \rightarrow \rho_{\substack{k_1,n+1 \\ k_1,n+1}}$, this time the only term contributing to the calculation is G^4:

$$\begin{aligned}
\dot{\rho}_{\substack{k_1,n+1 \\ k_1,n+1}} &= -\frac{i}{\hbar}F_1\frac{L}{2\pi}\frac{\Delta}{\sqrt{2\pi^3}}\sqrt{n+1} g_{k_0}\rho_{n,n}\int_{-\infty}^{\infty} dk\ C_k\ e^{-i(\epsilon_k-\epsilon_{k_1}-\omega_0)t} \\
&= -\frac{i}{\hbar}F_1\frac{L}{2\pi}\frac{\Delta}{\sqrt{2\pi^3}}\sqrt{n+1} g_{k_0}\rho_{n,n} e^{ik_0 z_1} e^{i(\epsilon_{k_1}-\epsilon_{k_0}+\omega_0)t} e^{-\left(\frac{z_1-vt}{2\Delta}\right)^2} \\
\rho_{\substack{k_1,n+1 \\ k_1,n+1}} &= -\frac{i}{\hbar}F_1\frac{L}{2\pi}\frac{\Delta}{\sqrt{2\pi^3}}\sqrt{n+1} g_{k_0}\rho_{n,n} e^{ik_0 z_1} e^{-\left(\frac{z_1}{2\Delta}\right)^2}\frac{2\Delta\sqrt{\pi}}{v} e^{\left(\frac{\Delta a^*}{v}\right)^2}
\end{aligned} \tag{6.10}$$

Thanks to equations 6.9 and 6.10, and without forgetting to take into account the two paths (2) and (4), we can write $\rho_{\substack{k_1,n+1 \\ k_1,n+1}}$ as

$$\boxed{\rho_{\substack{k_1,n+1 \\ k_1,n+1}}(t_2) = (n+1)\ \frac{|g_{k_0}|^2 L^2\Delta^2}{\hbar^2\pi^3 v^4} e^{-\frac{\left((\epsilon_{k_1}-\epsilon_{k_0})+\omega_0\right)^2\Delta^2}{v^2}}\rho_{n,n}(t_2)} \tag{6.11}$$

Proceeding in a similar way with $\rho_{\substack{k'_1,n-1\\k'_1,n-1}}$, we find

$$\boxed{\rho_{\substack{k'_1,n-1\\k'_1,n-1}}(t_2) = n\ \frac{|g_{k_0}|^2 L^2 \Delta^2}{\hbar^2 \pi^3 v^4} e^{\frac{\left(\left(\epsilon_{k'_1} - \epsilon_{k_0}\right) - \omega_0\right)^2 \Delta^2}{v^2}} \rho_{n,n}(t_2)} \tag{6.12}$$

One can see from equations 6.11 and 6.12 that $\rho_{\substack{k_1,n+1\\k_1,n+1}}(t_2)$ and $\rho_{\substack{k'_1,n-1\\k'_1,n-1}}(t_2)$ depend on $\rho_{n,n}(t_2)$. This term depends on the decay of the nanoparticle state during the interval $t_0 \to t_2$. Its calculation is the purpose of the next section.

6.2.2 Damping Process after Interaction

Between interactions with the electrons, the Bosons in the nanoparticle will decay. The rate depends on the lifetime of Bosons, which in turn vary with the structure and the type of Boson (photonic modes, plasmons...).

As shown at the beginning of this section, if we only consider dissipation, the master equation for the density matrix becomes

$$\begin{aligned}
\dot{\rho} &= \frac{\Gamma_0}{2}\left[2a\rho a^+ - a^+ a\rho\ -\ \rho a^+ a\right] \\
&= \frac{\Gamma_0}{2} \sum_{\substack{k,n\\k',n'}} \rho^I_{\substack{k,n\\k',n'}} \left[2\sqrt{n}\sqrt{n'}\,|k,n-1\rangle\langle n'-1,k'| - (n+n')\,|k,n\rangle\langle n',k'|\right] e^{-i((n-n')\omega_0 + (\epsilon_k - \epsilon_{k'}))t} \\
&= \frac{\Gamma_0}{2} \sum_{\substack{k,n\\k',n'}} \left[2\sqrt{n+1}\sqrt{n'+1}\rho^I_{\substack{k,n+1\\k',n'+1}} e^{-i((n+1-n'-1)\omega_0 + (\epsilon_k - \epsilon_{k'}))t}\right. \\
&\quad \left. - (n+n')\rho^I_{\substack{k,n\\k',n'}} e^{-i((n-n')\omega_0 + (\epsilon_k - \epsilon_{k'}))t}\right] |k,n\rangle\langle n',k'|
\end{aligned}$$

$$\dot{\rho}^I_{\substack{k,n\\k',n'}} = \frac{\Gamma_0}{2}\left(2\sqrt{n+1}\sqrt{n'+1}\rho^I_{\substack{k,n+1\\k',n'+1}} - \left(n+n'\right)\rho^I_{\substack{k,n\\k',n'}}\right) \tag{6.13}$$

We define the matrix M though

$$\begin{aligned}
\left(M\rho^I_{k,k'}\right)_{n,n'} &= 2\sqrt{n+1}\sqrt{n'+1}\rho^I_{\substack{k,n+1\\k',n'+1}} - \left(n+n'\right)\rho^I_{\substack{k,n\\k',n'}} \\
\dot{\rho}^I_{\substack{k,n\\k',n'}} &= \frac{\Gamma_0}{2}\left(M\rho^I_{k,k'}\right)_{n,n'}
\end{aligned} \tag{6.14}$$

We implement equation 6.14 numerically, by defining the base $\{n, n'\}$ with the numerical base J defined as $j_i = n * (N+1) + n'$, N being a maximum number of Bosons allowed in the nanoparticle. This allows us to calculate the eigenvalues $\{\lambda_\alpha\}$ and the eigenvector

$\{v_\alpha\}$ of M such as $Mv_\alpha = \lambda_\alpha v_\alpha$. In order to properly describe dissipation, we use the base defined by the eigenvectors of M as $\Upsilon = \{v_\alpha\}$. We then have

$$\rho_{\substack{k,n\\k',n'}} |k,n\rangle\langle k',n'| = \sum_\alpha {}^\alpha D_{n,n'}\ \rho_{\substack{k,n\\k',n'}}\ |k,v_\alpha\rangle\langle v_\alpha,k'|,$$

Where ${}^\alpha D_{n,n'}$ are elements of the change-of-basis matrix to go from base $\{n,n'\}$ to the base Υ and after projection on state $|k\rangle\langle k'|$. Equation 6.14 then becomes

$$\begin{aligned}\sum_\alpha {}^\alpha D_{n,n'}\ \dot\rho_{\substack{k,n\\k',n'}}\ |v_\alpha\rangle\langle v_\alpha| &= \frac{\Gamma_0}{2}\sum_\alpha {}^\alpha D_{n,n'}\ \ \rho_{\substack{k,n\\k',n'}}\ M|v_\alpha\rangle\langle v_\alpha| \\ &= \frac{\Gamma_0}{2}\sum_\alpha {}^\alpha D_{n,n'}\rho_{\substack{k,n\\k',n'}}\ \lambda_\alpha\ |v_\alpha\rangle\langle v_\alpha| \end{aligned} \tag{6.15}$$

The integration over time, if Bosons are created at t_0 gives:

$$\rho_{\substack{k,n\\k',n'}}(t)\ |v_\alpha\rangle\langle v_\alpha| = \rho_{\substack{k,n\\k',n'}}(t_0)\ e^{\lambda_\alpha\frac{\Gamma_0}{2}(t-t_0)}\ |v_\alpha\rangle\langle v_\alpha| \tag{6.16}$$

Therefore, if we define ${}^\alpha B_{n,n'}$, elements of the change-of-basis matrix to go from base Υ to $\{n,n'\}$ one can write $\rho_{k,k'}(t)$, the projection of the density matrix into the vectorial subspace $|k\rangle\langle k'|$:

$$\begin{aligned}\rho_{k,k'}(t) &= \sum_\alpha {}^\alpha D_{n,n'}\ \rho_{\substack{k,n\\k',n'}}(t)\ |k,v_\alpha\rangle\langle v_\alpha,k'| \\ &= \sum_\alpha {}^\alpha D_{n,n'}\ \rho_{\substack{k,n\\k',n'}}(t_0)\ e^{\lambda_\alpha\frac{\Gamma_0}{2}t}\ |k,v_\alpha\rangle\langle v_\alpha,k'| \\ &= \sum_{\substack{\alpha\\n_1,n_1'}} {}^\alpha D_{n,n'}\ {}^\alpha B_{n_1,n_1'}\ \rho_{\substack{k,n\\k',n'}}(t_0)\ e^{\lambda_\alpha\frac{\Gamma_0}{2}t}|k,n_1\rangle\langle n_1',k'| \end{aligned} \tag{6.17}$$

This means that the initial state $|k,n\rangle\langle n',k'|$ will decay into other states $|k,n_1\rangle\langle n_1',k'|$. In other words, the nanoparticle has a probability to lose Bosons due to damping. Due to the form of the matrix M, a diagonal element of the matrix M will decay only to other diagonal elements. This means that there is no coherence between the different states. The final state will be a superposition of Boson states with $n_1 < n$. We are therefore looking for a law such as, if we defined l the final state and n the initial state

$$\rho_{\substack{k,l}}(t) = \rho_{\substack{k,n\\k,n}}(t_0)\sum_j C_j(l,n)\ e^{-c(j)\Gamma_0(t-t_0)}$$

Numerically, we found the following empirical rule:

$$\boxed{\rho_{\substack{k,l}}(t) = {}^0\rho_{\substack{k,n\\k,n}}(t_0)\sum_{j=l}^n {}^jC_l\ {}^nC_j\ (-1)^{i-l}e^{-j\Gamma_0(t-t_0)}} \tag{6.18}$$

$$\text{with } {}^{a}C_b = {}^{a-1}C_{b-1} + {}^{a-1}C_b \text{ if } b \neq (0, a)$$
$${}^{a}C_a = {}^{a}C_0 = 1$$

One can notice that $c(j) = j$, which is probably due to the simple form of the matrix M. We will therefore have a damping that depends of the initial state n. One can see that the form of the decay is much more complicated than the one used in section 6.1.2.

Figure 6.3 shows the probability to find the system at t in the state $|n_f\rangle\langle n_f|$ if the system was $|n_i\rangle\langle n_i|$ at $t = 0$. One can see that the decay of the plasmon induces a superposition of states for $t > 0$. We take for the coupling constant $\tau_p = 1/\Gamma_0 = 400$ fs, which is relatively long for a plasmon [94]. This issue will be discussed in section 6.3.

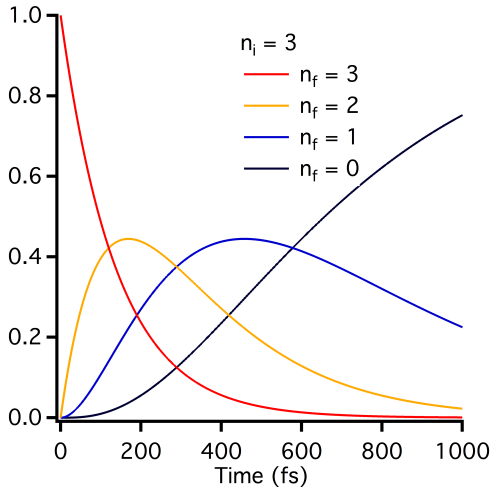

FIGURE 6.3: At t=0 electron e_1 interacts with the sample and leaves the system in the state $|n_i><n_i|$. It represents $\frac{\rho_{nf,nf}(t)}{\rho_{ni,ni}(0)}$, for $n_f \leq n_i$

We now have a full description of the system during the two different steps, the interaction (equation 6.11 and equation 6.12) and the damping (equation 6.18). Before applying this development to the experiment described in section 6.1.2, where the quantum nature of plasmons is directly measured thanks to electron energy loss spectroscopy, we will use a second formalism to describe the interaction in order to apprehend better the coupling constant g introduced in section 6.2.1.

6.2.3 The coupling constant g_{k_0}

In order to have an expression for the coupling constant, we used the formalism of Glauber and Lewenstein developed in [227, 228] and adapted to the problem of electron

microscopy by Garcia de Abajo et al in [229].

In this formalism the interaction Hamiltonian is:

$$H_{el-pl} = -\frac{ie\hbar}{mc}\hat{A}.\nabla$$
$$\hat{A} = c\sum_j \sqrt{\frac{2\pi\hbar}{\omega_j}}\left(\mathbf{f}_j^*(\mathbf{r})a_j^+ + \mathbf{f}_j(\mathbf{r})a_j\right)$$
$$\text{with } \nabla\wedge\nabla\wedge\mathbf{f}_j(\mathbf{r}) - \frac{\omega_j^2}{c^2}\epsilon(r,\omega)\mathbf{f}_j(\mathbf{r}) = 0.$$

Here, a^+ and a are the creation and annihilation operators of the Bosonic state, $\omega_j = ck$, and $\hat{A}$ is the extension of the potential vector in terms of photon creation and annihilation operators defined in equation 7.8 of [228], where $\mathbf{f}_j(\mathbf{r})$ are solutions of the Heelmoltz equation. The wave function of the system before interaction is constituted by a Gaussian packet for the electrons (wave vector k_0, speed v), moving into the z direction, and a number n_i of Bosons in the nanoparticle.

$$|\psi_i(z,t)\rangle = \aleph e^{ik_0 z}e^{-i\epsilon_{k_0}t}e^{-(z-vt)^2/\Delta^2}e^{-in_i\omega_0 t}|n_i\rangle \tag{6.19}$$

Δ is the extension of the Gaussian packet. In first approximation, one can consider that $\Delta \gg v/\omega_0$. This means that the Gaussian packet along z will keep its form during the interaction and that the interaction can be considered instantaneous compared to the lifetime of the Boson. Indeed the interaction time will be of the order of 0.1 femtosecond compared to the lifetime that is of the order of femtoseconds or more. $\aleph$ is the normalization constant (see Appendice C):

$$\aleph = \sqrt{\frac{\Delta}{\sqrt{2\pi^3}}}$$

We can consider the variation only in the z direction, thus we can write H_{int} as:

$$H_{el-pl}(z) = -\frac{ie\hbar}{m}\sum_j \sqrt{\frac{2\pi\hbar}{\omega_j}}\left(\mathbf{f}_{j_z}^*(\mathbf{z})a^+\frac{\partial}{\partial z} + \mathbf{f}_{j_z}(\mathbf{z})a\frac{\partial}{\partial z}\right)$$

We define the Green function for the motion along z as:

$$G\left(z-z',t-t'\right) = -\frac{1}{2\pi\hbar}\sum_n \int dk\; e^{i\left(k-\frac{n\omega_0}{v}\right)(z-z')}e^{-i\epsilon_k(t-t')}|n\rangle\langle n|$$

The wave function of the system after interaction will be:

$$|\psi_f(z,t)\rangle = |\psi_0\rangle + \int dz' \int dt'\; G(z-z',t-t')H_{int}(z')|\psi_i(z',t')\rangle \tag{6.20}$$

We make the assumption that the electron after interaction with the nanoparticle can still be modeled by a Gaussian packet. We show in Appendix B that equation 6.20 becomes:

$$\begin{aligned}|\psi_f(z,t)\rangle = &-\frac{e}{m}\frac{\aleph}{v}k_0 e^{\frac{-(z-vt)^2}{\Delta^2}} \\ &\mathrm{A}^*\sqrt{n+1}\; e^{i\left(k_0-\frac{\omega_0}{v}\right)z}e^{-i(\epsilon_{k_0}-\omega_0)t}e^{-i(n+1)\omega_0 t}\,|n+1\rangle \\ &+\mathrm{A}\sqrt{n}\; e^{i\left(k_0+\frac{\omega_0}{v}\right)z}e^{-i(\epsilon_{k_0}+\omega_0)t}e^{-i(n-1)\omega_0 t}\,|n-1\rangle\end{aligned} \tag{6.21}$$

As expected, we retrieve the form of the wave function described in equation 6.19:

$$\begin{aligned}|\psi_f(z,t)\rangle = &-\frac{e}{m}\frac{\aleph}{v}k_0 e^{\frac{-(z-vt)^2}{\Delta^2}} \\ &\mathrm{A}^*\sqrt{n+1}\; e^{ik_1 z}e^{-i\epsilon_{k_1}t}e^{-i(n+1)\omega_0 t}\,|n+1\rangle + \mathrm{A}\sqrt{n}\; e^{ik_1' z}e^{-i\epsilon_{k_1'}t}e^{-i(n-1)\omega_0 t}\,|n-1\rangle\end{aligned}$$

$$\begin{aligned}\text{With}: \; k_1 &= k_0 - \omega_0/v \\ \epsilon_{k_1} &= \epsilon_{k_0} - \omega_0 \\ k_1' &= k_0 + \omega_0/v \\ \epsilon_{k_1'} &= \epsilon_{k_0} + \omega_0\end{aligned}$$

$$\text{With}: \; A = \sum_j \sqrt{\frac{2\pi\hbar}{\omega_j}} \int dz' \mathbf{f}_{j_z}(\mathbf{z'}) e^{-i\left(\frac{\omega_0}{v}\right)z'}$$

From equation 6.21, we can deduce the equivalent of the coupling constant in this formalism:

$$|g|^2 = \left(\frac{k_0}{m}\frac{e}{v}\right)^2 |\mathrm{A}|^2 \tag{6.22}$$

Equation 6.22 seems to justify the approximation made in section 6.2.1 where we consider that g depends only on k_0. This is because one can consider that $k_1 \approx k_0$. We will now apply the theory developed in this section, and summarized by equation 6.11, 6.12 and 6.18, to the experiment described in section 6.1.2.

6.3 Discussion and Possible Systems

6.3.1 Theory Applied to the Hypothetic Experiment

The nanoparticle interacts successively with two electrons that will be detected using EELS. Figure 6.2 schematically represents the designed experiment. An electron interacts with the sample at t=0, we detect it using EELS. Therefore we know the number

n of plasmons in the system at t= 0. Before that, a second electron arrives at t_2, the system will decay and the number l of plasmons will be less or equal to n. The second electron arrives at t_2 and creates or annihilates a plasmon leaving respectively the system in the state $l+1$ or $l-1$.

Thanks to equations 6.11, 6.12 and 6.18 we can write the density matrix for the different steps, the system being constituted by the number n of plasmons in the nanoparticle and of the plane wave of the second electron defined by its wave vector k ($|k,n\rangle\langle n,k|$):

At t=0: After the interaction with the first electron

$$\rho(0) = |n,k_0\rangle\langle k_0,n| \tag{6.23}$$

At t_1 < t_2: Decay of the initial state

$$\rho(t_1) = \sum_{l=0}^{l=n} \rho_{\substack{k_0,l\\k_0,l}}(t_1)\,|k_0,l\rangle\langle l,k_0| \tag{6.24}$$

$$\rho_{\substack{k_0,l\\k_0,l}}(t_1) = \rho_{\substack{k_0,n\\k_0,n}}(0)\sum_{i=l}^{n} {}^iC_l\ {}^nC_i\ (-1)^{i-l}e^{-i\Gamma_0 t_1}$$

At t_2: Interaction with the second electron

$$\rho^n(t_2) = \rho_{\substack{k_1,1\\k_1,1}}(t_2)\,|k_1,1\rangle + \sum_{l=1}^{l=n}\rho_{\substack{k_1,l+1\\k_1,l+1}}(t_2)\,|k_1,l+1\rangle\langle l+1,k_1| + \rho_{\substack{k_1',l-1\\k_1',l-1}}(t_2)\,|k_1',l-1\rangle\langle l-1,k_1'|$$

$$\rho_{\substack{k_1,l+1\\k_1,l+1}}(t_2) = (l+1)\frac{|g_{k_1}|^2L^2\Delta^2}{\hbar^2\pi^3v^4}e^{\frac{\left(\epsilon_{k_1}-\epsilon_{k_0}+\omega_0\right)^2\Delta^2}{v^2}}\rho_{\substack{k_0,n\\k_0,n}}(0)\sum_{i=l}^{n} {}^iC_l\ {}^nC_i\ (-1)^{i-l}e^{-i\Gamma_0 t_2} \tag{6.25}$$

$$\rho_{\substack{k_1',l-1\\k_1',l-1}}(t_2) = l\ \frac{|g_{k_1}|^2L^2\Delta^2}{\hbar^2\pi^3v^4}e^{\frac{\left(\epsilon_{k_1}-\epsilon_{k_0}-\omega_0\right)\Delta^2}{v^2}}\rho_{\substack{k_0,n\\k_0,n}}(0)\sum_{i=l}^{n} {}^iC_l\ {}^nC_i\ (-1)^{i-l}e^{-i\Gamma_0 t_2} \tag{6.26}$$

With $\rho^i(t_2)$ the density matrix element after interaction with the electron, if there were i plasmons before interaction. Taking into account that $\rho_{\substack{k_0,n\\k_0,n}}(0) = 1$ and that we are at resonance either with $(\epsilon_{k_1} = \epsilon_{k_0} - \omega_0)$ or with $\left(\epsilon_{k_1'} = \epsilon_{k_0} + \omega_0\right)$ equation 6.25 becomes:

$$\rho_{\substack{k_1,l+1\\k_1,l+1}}(t_2) = (l+1)\ \frac{|g_{k_1}|^2L^2\Delta^2}{\hbar^2\pi^3v^4}\sum_{i=l}^{n} {}^iC_l\ {}^nC_i\ (-1)^{i-l}e^{-i\Gamma_0 t_2} \tag{6.27}$$

$$\rho_{\substack{k_1',l-1\\k_1',l-1}}(t_2) = l\ \frac{|g_{k_1}|^2L^2\Delta^2}{\hbar^2\pi^3v^4}\sum_{i=l}^{n} {}^iC_l\ {}^nC_i\ (-1)^{i-l}e^{-i\Gamma_0 t_2} \tag{6.28}$$

If plasmons are Bosons, we see that the probability to create a plasmon with an electron increases if the number of plasmons already present in the system increases. We therefore compare $\rho^0(t_2)$ with $\rho^n(t_2)$. In the case of $\rho^n(t_2)$ we are in the situation of equation 6.27 where the first electron has created a plasmon at $t = 0$ leaving the system in the

state $|k_0, n\rangle \langle n, k_0|$. We therefore have:

$$\frac{\rho^n(t_2)}{\rho^0(t_2)} = \sum_{i=0}^{n} {}^iC_l \ {}^nC_i \ (-1)^{i-l} e^{-i\Gamma_0 t_2} |k_1, 1\rangle + \sum_{l=1}^{l=n} \sum_{i=l}^{n} {}^iC_l \ {}^nC_i \ (-1)^{i-l} e^{-i\Gamma_0 t_2} \left((l+1) |k_1, l+1\rangle \langle l+1, k_1| + l \ |k_1', l-1\rangle \langle l-1, k_1'| \right) \tag{6.29}$$

We retrieve, as expected, the Bosonic behavior. One can see from equation 6.29 that the probability to create a plasmon will increase if the number l of plasmons already in the nanoparticle increases. However the probability that the electron gains a plasmon also increases with the number of plasmons in the system, and the decay of the state will also depend on l.

6.3.2 Discussion on Real Systems

We implemented the situation described in the last section thanks to a Monte Carlo based model. The incoming electron beam is Poissonian (see section 4.2.1 of chapter 4). For each electron we proceed as follow:

1. The system is in the state n ($n = 0$ at the beginning). The time of arrival t_e of the electron is determined with the same routine as the one used in chapter 4.

2. We define t_0 as the last time where an electron has interacted with the sample (either by losing energy or gaining energy)

3. **Damping before interaction:** We generate a first random number r_1 between 0 and 1 and we find P_l^S such as $r_1 \in \left[P_{l-1}^S, P_l^S\right]$ with $P_l^S = \sum_{i=0}^{l} P_i(t_e)$. $P_i(t_e)$ is calculated thanks to equation 6.18. The system is therefore at the time t_e in the state l. This means that we project the system into a state l. This is an approximation to simplify the simulation, that can be justified by the absence of non diagonal terms in the density matrix after damping of the state $|k, n\rangle \langle n, k|$.

4. **Interaction with the system:** We generate a second random number r_2, if $r_2 < (l+1) * P_1 * P_l(t_e)$ then the electron has lost a quantum of energy, we record t_e and n becomes $l+1$. If $(l+1) * P_1 * P_l(t_e) < r_2 < (2*l+1) * P_1 * P_l(t_e)$ then the electron has gained a quantum of energy, we record t_e and n becomes $l-1$. Finally if, $(2*l+1) * P_1 * P_l(t_e) < r_2$ the electron has not interacted with the system. Here, due to the detection, the field state after interaction is considered known.

5. We start the loop once again for the next electron

Figure 6.4 represents the times t_e at which the electron interacted with the system ($t_e = t_2$). We trace t_2 for different lifetimes τ_p with a Poissonian electron beam with a current fixed at $I = 200$ pA. This means in average an electron every 0.8 ns. The probability of interaction is deduced from equation 6.29. The probability of interaction if there is no plasmon in the system is set at $P_1 = 0.04$.

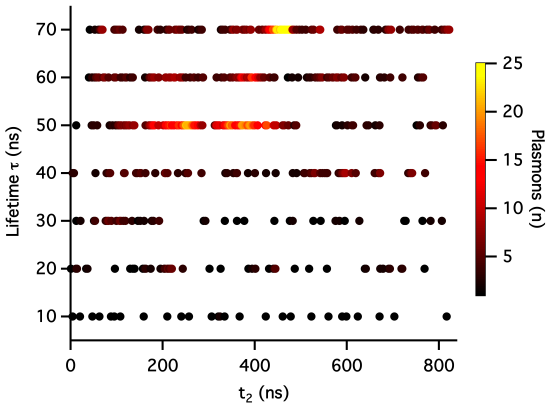

FIGURE 6.4: For a given plasmon lifetime τ_p, we represent the times t_2 where electrons have interacted with the sample and created a plasmon (loss of energy), using equation 6.29. Each line is the interaction time for a different lifetimes $\Gamma_0 = 1/\tau_p$ with the probability to create a plasmon $P_1 = 0.04$. The current of the electron beam is I = 200 pA. The number of plasmons present in the system is color coded, the scale is depicted at the right of the figure (maximum number of plasmons n = 35).

The main difference with the simulation of figure 6.1 is the damping factor that depends on the state. In order to obtain some Bosonic correlations, the time between two electrons must be smaller than the lifetime of the plasmon mode. However the beam is Poissonian, so even at 200 pA there is a chance that two electrons arrive close from one another. The same correlation will therefore be present even for a small lifetime as it will be discussed later. Figure 6.4 shows that for $\tau_p > 40$ ns (more than a hundred times too high compared to the lifetime of plasmons) a high number of plasmons in the system is directly correlated to a shorter time between two successive interactions, meaning that the probability of interaction is higher. However, the best way to see the correlation is by measuring the autocorrelation function of the EELS signal $g^{(2)}(\tau)$. It is worth noticing that the correlation at zero delay $g^{(2)}(0)$ doesn't depend on the lifetime of the surface plasmon. Indeed if $t_2 = t_0$ the damping has no influence (see equation 6.18). Contrary to the full width at half maximum of the bunching peak that will depend on the damping. This means that the limitation will be the time resolution of the EELS detector, which is a technical limitation on which one can expect improvements in the future. Figure 6.5 shows the $g^{(2)}(\tau)$ function for different lifetimes τ_p and three different currents $I = 200$ pA, $I = 700$ pA and $I = 2$ nA. Of course, by increasing the current we increase the chance to have two electrons close from one another and therefore we improve the signal

to noise ratio, leading to the possibility, for $P_1 = 0.04$, to observe the bunching behavior of plasmons at $\tau_p = 1$ ps. The simulation was done for 4 10^6 incoming electrons which corresponds to $I = 2$ nA to $T \approx 0.3$ ms. However, as explained in chapter 5 section 5.1.3, to link this simulated time to the real time we need to have the experimental ratio r_{exp} between the current and the real number of electrons detected by the EELS detectors.

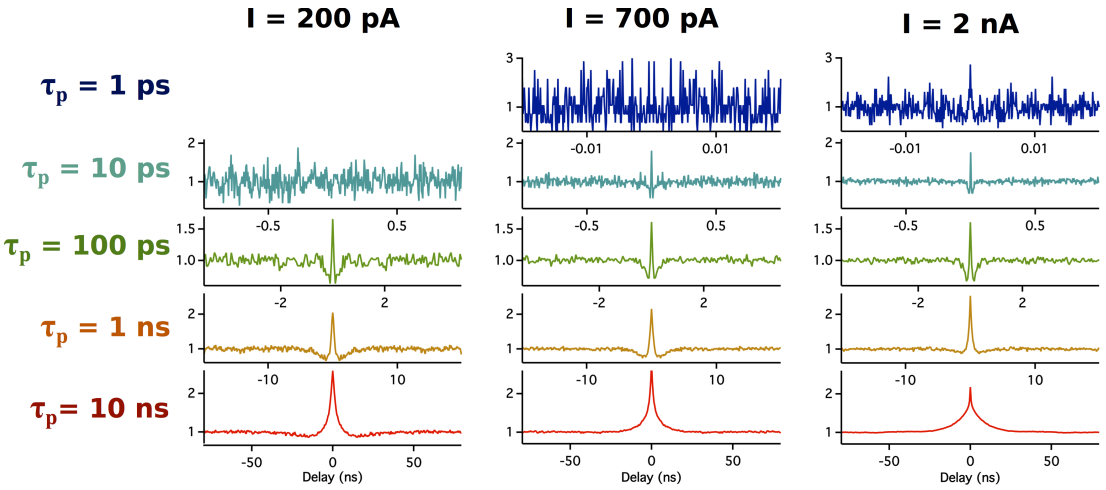

FIGURE 6.5: Autocorrelation function $g^{(2)}(\tau)$ of the EELS signal. For I = 200 pA (left column), I = 700 pA (middle) and I = 2 nA (right column). For each current, the $g^{(2)}(\tau)$ is plotted for different plasmon lifetimes τ_p from $\tau_p = 10$ ns (bottom) to $\tau_p = 1$ ps (top). On can see that increasing the current increases the signal to noise ratio allowing us to probe more dissipative plasmonic structures. In all this case $P_1 = 0.04$.

In any case, it appears that, by increasing the current, one can decrease the smallest lifetime detectable, of course putting aside the time resolution of the detectors. Moreover, by increasing P_1, we also increase the probability of interaction and therefore the signal to noise ratio. For example in figure 6.6, we calculate the $g^{(2)}(\tau)$ function of the EELS signal for $\tau_p = 10$ ps and $I = 200$ pA for a number of electrons which is half the number of electrons of figure 6.5 but with $P_1 = 0.4$.

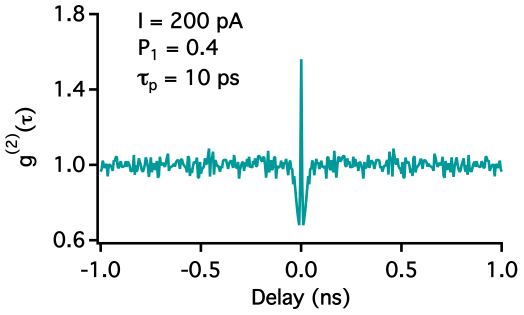

FIGURE 6.6: $g^{(2)}(\tau)$ of the EELS signal with $P_1 = 0.4$ which means ten times larger than for figure 6.5. The lifetime of the plasmon mode is set to $\tau_p = 10$ ps and the current at $I = 200$ pA. It correspond to the situation depicted on the top of the left column of figure 6.5. Due to the increase of P_1 the bunching behavior is clearly visible.

This means that, with this method, there is no limitation apart from technical ones to perform this measurement on damped system. In figure 6.5, another interesting result has to be noted: the presence of anti-bunching at small delay superimposed to the bunching peak. This can be explained by the probability of the electron to gain energy rather than lose some. This probability also depends on the number of plasmons in the system and therefore at small delay $t_2 - t_0$ the probability for the electron to gain energy is higher. The spectroscopy of energy gain by the electron is called electron energy gain spectroscopy (EEGS) [230]. In figure 6.7, we plot the correlation function $g^{(1)}(t_g - t_l)$ between electrons having lost energy and electrons having gained energy. One can see a huge correlation at zero delay between the two. It is important to notice the asymmetry of the peak with correlation only for $t_g > t_l$ which is logical if the number of plasmons in the system is around 1. In this case, the loss of one plasmon means almost directly the return to the fundamental level (τ_p = 10 ns in figure 6.4). Correlation at negative delay is visible for I = 2 nA and τ_p = 10 ns. This is due to the presence of a lot of plasmons in the system (up to 10) that allows the system to stay in the excited state for more than one cycle (τ_p = 70 ns in figure 6.4). This correlation is also a clear signature of the quantum behavior of plasmons. If the signal to noise ratio was much better, this measurement could be another way to probe the quantum nature of plasmon. However the number of electrons detected in EEGS in our simulation is ten times less than in EELS, which could render the experiment difficult.

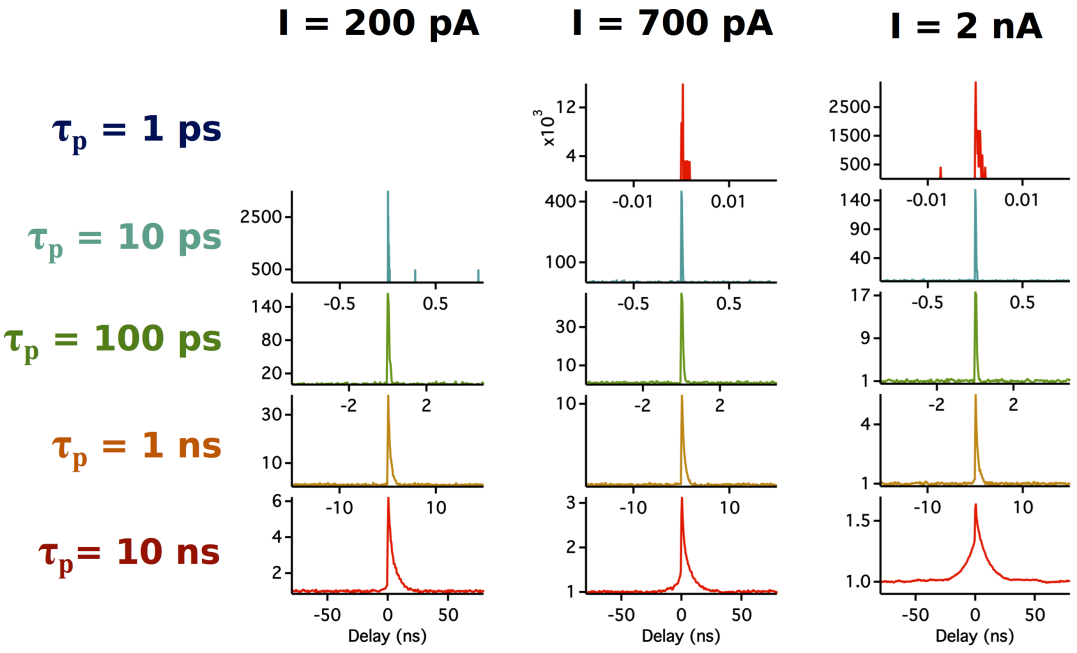

FIGURE 6.7: Correlation between EELS and EEGS signal. For an electron beam current I = 200 pA (left column), I = 700 pA (middle) and I = 2 nA (right column). And for plasmon lifetime τ_p from bottom to top respectively from 10 ns to 1 ps. The correlation for $t_g \approx t_l$ and $t_g > t_l$.

We have seen here that it can be possible with a high current (I = 2 nA) to study systems with 1 ps lifetime, which is far from the femtosecond lifetime of dissipative plasmonic system. However, for now, detectors are not good enough to allow sub-picosecond resolution. Therefore, for the first experiment, it will be best to start with optical systems rather than plasmonic ones. For example, photonic cavities have nowadays really high quality factor Q that can lead to lifetime of the excited state of the order of nanoseconds or more [231]. To continue, surface plasmon-polariton as the ones present in plasmonic cavities [232], can have lifetimes up to 5 ps and could be studied. But this experiment has potential to probe much more dissipative systems, the only intrinsic limitation comes from the width of the zero-loss peak that can hide plasmon modes of energy smaller than 1 eV. The use of a monochromated electron microscope will be, in this case, required.

To conclude, it is important not to forget that EELS gives the time of creation of plasmons but also the number of plasmons present in the system at a given time. It allows to fix the system into a Fock state. Therefore one can imagine quantum plasmonic interferences experiment with EELS spectroscopy.

Conclusion and Perspectives

Conclusion

In this thesis, we used fast electrons to probe matter thanks to a scanning transmission electron microscope. Especially, we used cathodoluminescence (CL) spectroscopy to study light emission properties of entities like NV centers in diamond or III-N semiconductor heterostructure such as GaN/AlN quantum wells. The CL set-up was coupled to an intensity interferometry experiment (HBT-CL set-up) to measure the intensity autocorelation function of the CL signal $g^{(2)}_{\mathrm{CL}}(\tau)$.

Continuing the work started by L. Tizei and M. Kociak, we were able to confirm the possibility of using electrons to characterize single photon emitters (SPE), allowing to perform quantum optics at the nanometer scale. Indeed the anti-bunching behavior of NV centers in diamond was retrieved. Moreover, the high spatial resolution of the set-up and its ability to easily probe UV light allowed us to observe a new SPE in Boron Nitride (BN) that was never characterized as single photon emitter. The use of the HADF image, the emission spectrum and the HBT-CL experiment allow obtainning a background subtraction method of the $g^{(2)}_{\mathrm{CL}}(\tau)$ retrieving for the SPE in BN a dip at zero delay of $g^{(2)}_{\mathrm{CL}}(0) = 0.2$.

However, we showed that, beyond the obvious gain in spatial resolution, the specificities of electronic excitation influence the statistics of emission. Indeed, at low excitation current ($I < 200$ pA), materials with more than one SPE or having super-Poissonnian emitters emit photons in bunches. This is characterized by a huge peak at zero delay in the autocorrelation function $g^{(2)}_{\mathrm{CL}}(0) \gg 1$ (bunching) which depends on the current and on the emitters lifetime. We proved, thanks to two theoretical models, that this phenomenon is due to the features of the excitations relaxation mechanisms. The first model based on Monte Carlo simulations, reproduced the experimental results emphasizing the role of bulk plasmons into the excitation of matter by fast electrons. While the analytical model reveals in the case of SPE the transition from bunching to anti-bunching when the current increases, allowing to evaluate the correct experimental conditions to

study SPE. Moreover, the influence of the bunching effect on the background signal was studied, showing that the bunching effect can amplify at low currents the effect of background. Therefore, a Poissonian subtraction method, as the one used in chapter 3, underestimates part of the background in the final function.

The two theoretical models also showed that a simple exponential fit of the $g^{(2)}_{\mathrm{CL}}(\tau)$ function allowed to retrieve the lifetime of the emitter. We can therefore use this specificity of the bunching effect to measure the lifetime of the excited state of different kinds of emitters at the nanometer scale. With this new method, which is added to HADF images and CL emission spectrum, we have access to a full characterization of every optically active nano-system likely to be studied in an STEM. A statistical comparison of the lifetime measured by time resolved photoluminescence and by HBT-CL, shows that the quantities measured are similar. This means that we can compare the results obtained with the two kinds of experiment, but also that despite the fact that electrons change the statistics of emission, they don't disturb the system more than a photon would, as it was explained in the beginning of this thesis. In chapter 5 we used this techniques to study GaN/AlN nanostructures and to retrieve the expected correlation between lifetime and emission energy. But beyond this already well known result, the high spatial resolution of the CL system allows us to fully characterize defects in the AlN matrices of small GaN nano-clusters and stacking faults.

This thesis proves the feasibility of doing quantum optics and nano-optics with fast electrons. Moreover electron energy loss spectroscopy (EELS) or CL are already widely used to study surface plasmons. Thus, it seems that the next logical step is to perform quantum plasmonics with fast electrons. We showed in chapter 6 how one can use EELS to directly measure the quantum nature of plasmons, taking into account damping. We showed that with this technique, time resolution of the detection system is the main limitation. This means that there is no reason in the future for not being able to measure the quantum nature of plasmons beyond surface plasmon-polariton. This last chapter opens perspectives about quantum plasmonic in an STEM. We can now think of experiments that will bring nano-optics and nano-plasmonic together.

Perspectives

The coupling between plasmons and single photon emitters is a hot issue of quantum optics and quantum plasmonics [44, 45]. This is a topic where the high spatial resolution of CL for emitters [46] and the relevance of EELS spectroscopy for surface plasmons make these two techniques complementary tools to study at sub-wavelength resolution the plasmons/quantum emitter coupling. Moreover it is very well known that coupling

between emitters and plasmons reduces the lifetime of the emitter [47, 48]. One can imagine to use the bunching effect to study the coupling between plasmons and emitters at the nanometer scale thanks to lifetime measurements. In order to introduce this field, some preliminary simulations and experiments have been done. We performed simulations with the Matlab MNPBEM toolbox designed for EELS and CL simulation [49, 50]. The theory and first results of simulation are shown in appendix D. In this section we will focus on the first experiments.

We conducted two kinds of experiments with nano-diamonds containing a high density of NV^0 centers. As explained in chapter 4, the lifetime measured will be the average lifetime of the NV^0 excited by the electron. The first experiment was to measure the lifetime of the same diamond before and after gold deposition (details of the experiment can be found in appendix D). The result is shown in figure 6.8. We measured for each diamond the difference in lifetime $\Delta\tau = \tau_0 - \tau_g$ between the first measurement without gold τ_0 and the second with gold τ_g. One can see in figure 6.8-d) that $\Delta\tau$ is on average higher for the nanodiamond with gold. However results are still preliminary because of the bad signal to noise ratio of the $g^{(2)}(\tau)$ curves leading to large error bars and a poor statistics. Here the large distribution of lifetime in nano diamonds is a major drawback. To improve this experiment, the use of an emitter with shorter lifetime for an increase of the signal to noise ratio (see chapter 5) and a more significant statistics is required.

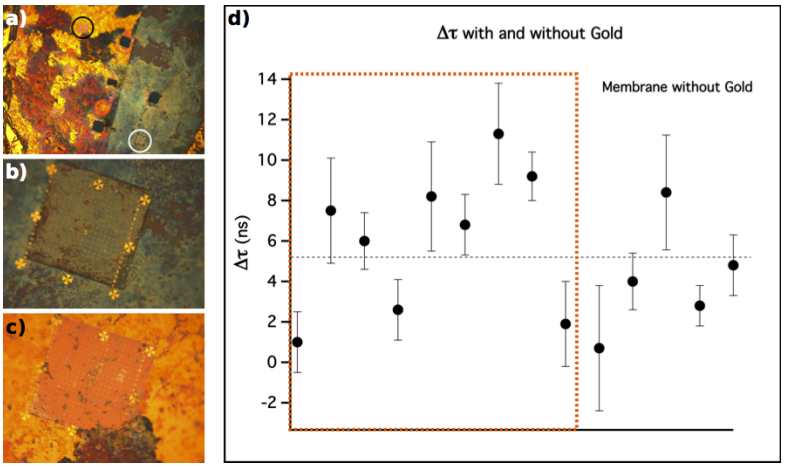

FIGURE 6.8: Lifetime measurement on nanodiamonds before gold deposition τ_0 and after gold deposition τ_g. Optical images of the TEM grid after gold deposition is depicted in a),b),c). a) TEM grid with half of the grid recovered by gold. b) membrane without gold, corresponding to the membrane with the white circle in a). c) image of a membrane covered by gold, corresponding to the membrane with the black circle in a). d) $\Delta\tau = \tau_0 - \tau_g$ for each diamond. The diamonds covered by gold are the ones depicted in the orange dashed rectangle.

The second experiment consisted in performing lifetime measurements on the same diamond before and after the deposition of a nano-triangle close to it. This experiment required a lot of steps and was therefore only successful for two diamonds (details of

the lithographic process are given in appendix D). The best one is shown in figure 6.9. It seems that we observed a change in the lifetime. However, no emission from the nano-triangle is visible (see figure 6.9-b) which seems unlikely if there is coupling. The change can be due to the different lithographic steps that induced variation in the nano-diamond environment. Once again, to have more accurate results, a brighter emitter with a smaller lifetime needs to be found.

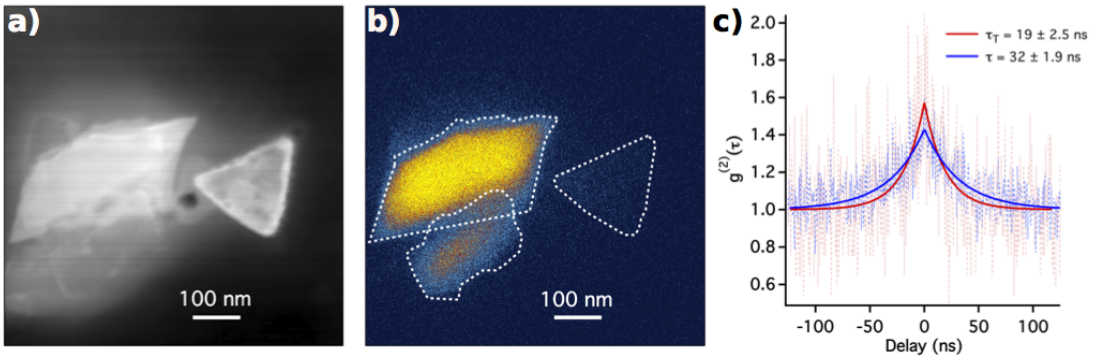

FIGURE 6.9: Gold nano triangle drawn close to a nano diamond with a high density of centers. a) HADF image and b) filtered emission map. c) $g^{(2)}_{\mathrm{CL}}(\tau)$ function of the nano diamond before (τ = 32 ± 1.9 ns) and after (τ_t = 19 ± 2.5 ns) gold nanotriangle deposition. We have that $\tau \gg \tau_t$.

These simulations and experiments are the first step toward quantum plasmonic and emitter-plasmons coupling in an STEM. They open the way to a wide range of experiments exploiting the high resolution of fast electrons and the complementarity of the informations supplied by the HADF image, the CL emission spectrum and the HBT-CL experiment. The easy set-up of this technique allows us to use it for the simple characterization of any optically active material or for more complex structures like plasmon-emitter systems.

⋆ ⋆ ⋆

Appendix A

Analytical Model of the Bunching Effect: Development for Events #4 and #8

A.1 Event #4 : Calculation of $P^{(4)}(\tau)$

In chapter 4, the analytical model was described in its simplest form i.e. only with the most significant events. Only the chain of events where two photons were emitted have been considered (see table 4.3). Our goal here is to calculate $P^4(\tau)$ the probability that event #4 happens. The chain of events associated to #4 is the following :

- Electron e_1 interacts at $t = 0$ and creates a plasmon p_1
- p_1 decays into two e-h pairs and each one of them excites an NV center
- Electron e_2 interacts at $t = \Delta t$ and creates a plasmon p_2
- p_2 decays into two e-h pairs but only one of the two excites an NV center
- The three NV centers return to their fundamental level by emitting a photon at times t_1, t_2 and t_3

Therefore, three photons are emitted after this event. The probability $P^{(4)}(\tau)$ results from the combination of

i The probability of creating one plasmon per electron $P_{\text{el}}^{(4)} = (P_{\text{el}}(1))^2$ (equation 4.1)

ii The probability of interaction of the plasmons with the centers $P_I^{(4)}$

iii The radiative probability $P_{rad}^{(4)}$ of emitting three photons at t_1, t_2 and t_3.

Probability of interaction $P_I^{(4)}$

As in section 4.3.1 of chapter 4, we want to calculate the probability $P_{\mathrm{I}}^{(4)}$ that the e-h pairs created consecutively by the two electrons, interact with centers. As in section 4.3.1, we consider the extended expression of the probability P_{int} defined in equation 4.3 taking into account the number N_{ex} of centers already in the excited state:

$$P_{\mathrm{int}}(N_{\mathrm{ex}}) = \left(1 - e^{-l_{\mathrm{d}}\sigma\frac{N-N_{\mathrm{ex}}}{V_{\mathrm{ND}}}}\right) \approx \left(l_{\mathrm{d}}\sigma\frac{N-N_{\mathrm{ex}}}{V_{\mathrm{ND}}}\right) = C(N-N_{\mathrm{ex}}) \tag{A.1}$$

As $P_{\mathrm{int}}(N_{\mathrm{ex}})$ depends on N_{ex}, $P_I^{(4)}$, it will be different depending if the electron e_2 arrives before or after the two centers excited by e_1 retrieved their fundamental levels. Therefore we retrieve the equation presented in table 4.3:

$$\text{(a) If } \Delta t < t_1\text{:}\quad P_I^{(4a)} = P_{\mathrm{int}}(0)P_{\mathrm{int}}(1) \times P_{\mathrm{int}}(2)(1 - P_{\mathrm{int}}(3)) \tag{A.2}$$

$$\text{(b) If } t_1 < \Delta t < t_2\text{:}\quad P_I^{(4b)} = P_{\mathrm{int}}(0)P_{\mathrm{int}}(1) \times P_{\mathrm{int}}(1)(1 - P_{\mathrm{int}}(2)) \tag{A.3}$$

$$\text{(c) If } t_2 < \Delta t\text{:}\quad P_I^{(4c)} = P_{\mathrm{int}}(0)P_{\mathrm{int}}(1) \times P_{\mathrm{int}}(0)(1 - P_{\mathrm{int}}(1)) \tag{A.4}$$

Radiative Probability $P_{rad}^{(4)}$

Three photons are emitted in this chain of events. The two due to the interaction with e_1 are referred to as P_{e_1} and the one due to the interaction with e_2 is referred to as P_{e_2}.

$$P_{rad}^{(4)} = \frac{1}{\tau^3}e^{\left(-\frac{(t_1+t_2+t_3-\Delta t)}{\tau_e}\right)} \tag{A.5}$$

$P^{(4)}(\tau)$: Sum over all the possible detection configurations

As in the case of event #3 developed in the main text, $P^{(4)}(\tau)$ is a sum of the different time line configurations and detections. Except that this time, as there are three photons emitted by the sample and that only two are detected, depending on which photons are detected the probability $P^{(4)}(\tau)$ will not be the same. If we defined the time line of emission as (t_1, t_2, t_3), three configurations are possible (P_{e_1}, P_{e_1}, P_{e_2}), (P_{e_1}, P_{e_2}, P_{e_1}) and (P_{e_2}, P_{e_1}, P_{e_1}). And for each emission configuration i, three detection configurations

j have to be considered : $t_2 = t_1 + \tau$, $t_3 = t_1 + \tau$, $t_3 = t_2 + \tau$. We calculate the different $P^{(4)}_{i,j}(\tau)$ in the same way as in table 4.4 of section 4.3.1 for events #3 and #6.

1/ $(P_{e_1}, P_{e_1}, P_{e_2})$: $\Delta t < t_3$

i- $t_2 = t_1 + \tau$: Correlated

$$P^{(4)}_{1,i} = \frac{1}{8} P^{(4)}_{el} P^{(4a)}_{I} \int_0^{+\infty} dt_1 \int_{t_1+\tau}^{+\infty} dt_3 \int_0^{t_1} P^{(4)}_{rad}\, d\Delta t$$

ii- $t_3 = t_1 + \tau$: Uncorrelated

$$P^{(4)}_{1,ii} = \frac{1}{8} P^{(4)}_{el} \int_0^{+\infty} dt_1 \int_{t_1}^{t_1+\tau} dt_2 \left(P^{(4a)}_{I} \int_0^{t_1} P^{(4)}_{rad}\, d\Delta t + P^{(4b)}_{I} \int_{t_1}^{t_2} P^{(4)}_{rad}\, d\Delta t + P^{(4c)}_{I} \int_{t_2}^{t_1+\tau} P^{(4)}_{rad}\, d\Delta t \right)$$

iii- $t_3 = t_2 + \tau$: Uncorrelated

$$P^{(4)}_{1,iii} = \frac{1}{8} P^{(4)}_{el} \int_0^{+\infty} dt_2 \int_0^{t_2} dt_1 \left(P^{(4a)}_{I} \int_0^{t_1} P^{(4)}_{rad}\, d\Delta t + P^{(4b)}_{I} \int_{t_1}^{t_2} P^{(4)}_{rad}\, d\Delta t + P^{(4c)}_{I} \int_{t_2}^{t_2+\tau} P^{(4)}_{rad}\, d\Delta t \right)$$

2/ $(P_{e_1}, P_{e_2}, P_{e_1})$: $\Delta t < t_2$

i- $t_2 = t_1 + \tau$: Uncorrelated

$$P^{(4)}_{2,i} = \frac{1}{8} P^{(4)}_{el} \int_0^{+\infty} dt_1 \int_{t_2+\tau}^{+\infty} dt_3 \left(P^{(4a)}_{I} \int_0^{t_1} P^{(4)}_{rad}\, d\Delta t + P^{(4b)}_{I} \int_{t_1}^{t_1+\tau} P^{(4)}_{rad}\, d\Delta t \right)$$

ii- $t_3 = t_1 + \tau$: Correlated

$$P^{(4)}_{2,ii} = \frac{1}{8} P^{(4)}_{el} \int_0^{+\infty} dt_1 \int_{t_1}^{t_1+\tau} dt_2 \left(P^{(4a)}_{I} \int_0^{t_1} P^{(4)}_{rad}\, d\Delta t \right)$$

iii- $t_3 = t_2 + \tau$: Uncorrelated

$$P^{(4)}_{2,iii} = \frac{1}{8} P^{(4)}_{el} \int_0^{+\infty} dt_2 \int_0^{t_2} dt_1 \left(P^{(4a)}_{I} \int_0^{t_1} P^{(4)}_{rad}\, d\Delta t + P^{(4b)}_{I} \int_{t_1}^{t_2} P^{(4)}_{rad}\, d\Delta \right)$$

3/ $(P_{e_2}, P_{e_1}, P_{e_1})$: $\Delta t < t_1$

i- $t_2 = t_1 + \tau$: Uncorrelated

$$P^{(4)}_{3,i} = \frac{1}{8} P^{(4)}_{el} P^{(4a)}_{I} \int_0^{+\infty} dt_1 \int_{t_1+\tau}^{+\infty} dt_3 \int_0^{t_1} P^{(4)}_{rad}\, d\Delta t$$

ii- $t_3 = t_1 + \tau$: Uncorrelated

$$P^{(4)}_{3,ii} = \frac{1}{8} P^{(4)}_{el} P^{(4a)}_{I} \int_0^{+\infty} dt_1 \int_{t_1}^{t_1+\tau} dt_2 \int_0^{t_1} P^{(4)}_{rad}\, d\Delta t$$

iii- $t_3 = t_2 + \tau$: Correlated

$$P^{(4)}_{3,iii} = \frac{1}{8} P^{(4)}_{el} P^{(4a)}_{I} \int_0^{+\infty} dt_2 \int_0^{t_2} dt_1 \int_0^{t_1} P^{(4)}_{rad}\, d\Delta t$$

Three of these configurations are correlated events (photons originate from the same electron), $P^{(4)}_{2,iii}$, $P^{(4)}_{1,i}$, $P^{(4)}_{3,iii}$. Therefore, only the integration of Δt until t_1 is considered. Apart from these three events, all the others have to be weighted by the factor $\frac{I}{I_0}$ as explained in section 4.3.1 of chapter 4.

A.2 Calculation of $P^{(8)}(\tau)$ and Normalization of $g^{(2)}$

Event #8, corresponds to the emission of 4 photons, two due to e_1 and two due to e_2. The principle of the calculation is exactly the same as for event #4. Therefore we follow the same pattern :

$$\begin{aligned}
P^{(8)}_{el} &= P^{(4)}_{el} \\
P^{(8a)}_{I} &= P_{\text{int}}(0)P_{\text{int}}(1) \times P_{\text{int}}(2)P_{\text{int}}(3) \\
P^{(8b)}_{I} &= P_{\text{int}}(0)P_{\text{int}}(1) \times P_{\text{int}}(1)P_{\text{int}}(2) \\
P^{(8c)}_{I} &= P_{\text{int}}(0)P_{\text{int}}(1) \times P_{\text{int}}(0)P_{\text{int}}(1) \\
P^{(8)}_{rad} &= \frac{1}{\tau^4} e^{\left(-\frac{(t_1+t_2+t_3+t_4-\Delta t)}{\tau_e}\right)}
\end{aligned}$$

We defined the time line of emission as (t_1, t_2, t_3, t_4). Six configurations appear, and for each emission configuration i, five detection configurations j are possible. We calculate the different $P^{(8)}_{i,j}(\tau)$ in the same way as $P^{(4)}_{i,j}(\tau)$:

1/ $(P_{e_1}, P_{e_1}, P_{e_2}, P_{e_2})$: $\Delta t < t_3$

i- $t_2 = t_1 + \tau$: Correlated

$$P^{(8)}_{1,i} = \frac{1}{16} P^{(8)}_{el} P^{(8a)}_{I} \int_0^{+\infty} dt_1 \int_{t_1+\tau}^{+\infty} dt_3 \int_{t_3}^{+\infty} dt_4 \int_0^{t_1} P^{(8)}_{rad}\, d\Delta t$$

ii- $t_3 = t_1 + \tau$: Uncorrelated

$$P^{(8)}_{1,ii} = \frac{1}{16} P^{(8)}_{el} \int_0^{+\infty} dt_1 \int_{t_1}^{t_1+\tau} dt_2 \int_{t_1+\tau}^{+\infty} dt_4 \left(P^{(8a)}_{I} \int_0^{t_1} P^{(8)}_{rad}\, d\Delta t + P^{(8b)}_{I} \int_{t_1}^{t_2} P^{(8)}_{rad}\, d\Delta t + P^{(8c)}_{I} \int_{t_2}^{t_1+\tau} P^{(8)}_{rad}\, d\Delta t \right)$$

iii- $t_4 = t_1 + \tau$: Uncorrelated

$$P^{(8)}_{1,iii} = \frac{1}{16} P^{(8)}_{el} \int_0^{+\infty} dt_1 \int_{t_1}^{t_1+\tau} dt_2 \int_{t_2}^{t_1+\tau} dt_3 \left(P^{(8a)}_{I} \int_0^{t_1} P^{(8)}_{rad}\, d\Delta t + P^{(8b)}_{I} \int_{t_1}^{t_2} P^{(8)}_{rad}\, d\Delta t + P^{(8c)}_{I} \int_{t_2}^{t_3} P^{(8)}_{rad}\, d\Delta t \right)$$

iv- $t_3 = t_2 + \tau$: Uncorrelated

$$P^{(8)}_{1,iv} = \frac{1}{16} P^{(8)}_{el} \int_0^{+\infty} dt_2 \int_0^{t_2} dt_1 \int_{t_2+\tau}^{+\infty} dt_4 \left(P^{(8a)}_{I} \int_0^{t_1} P^{(8)}_{rad}\, d\Delta t + P^{(8b)}_{I} \int_{t_1}^{t_2} P^{(8)}_{rad}\, d\Delta t + P^{(8c)}_{I} \int_{t_2}^{t_2+\tau} P^{(8)}_{rad}\, d\Delta t \right)$$

v- $t_4 = t_2 + \tau$: Uncorrelated

$$P^{(8)}_{1,v} = \frac{1}{16} P^{(8)}_{el} \int_0^{+\infty} dt_2 \int_0^{t_2} dt_1 \int_{t_2}^{t_2+\tau} dt_3 \left(P^{(8a)}_{I} \int_0^{t_1} P^{(8)}_{rad}\, d\Delta t + P^{(8b)}_{I} \int_{t_1}^{t_2} P^{(8)}_{rad}\, d\Delta t + P^{(8c)}_{I} \int_{t_2}^{t_3} P^{(8)}_{rad}\, d\Delta t \right)$$

vi- $t_4 = t_3 + \tau$: Correlated but divergent. We take $P^{(8)}_{1,vi} \approx P^{(8)}_{1,i}$

2/ $(P_{e_1}, P_{e_2}, P_{e_1}, P_{e_2})$: $\Delta t < t_2$

i- $t_2 = t_1 + \tau$: Uncorrelated

$$P_{2,i}^{(8)} = \frac{1}{16} P_{el}^{(8)} \int_0^{+\infty} dt_1 \int_{t_1+\tau}^{+\infty} dt_3 \int_{t_3}^{+\infty} dt_4 \left(P_I^{(8a)} \int_0^{t_1} P_{rad}^{(8)}\, d\Delta t + P_I^{(8b)} \int_{t_1}^{t_1+\tau} P_{rad}^{(8)}\, d\Delta t \right)$$

ii- $t_3 = t_1 + \tau$: Correlated

$$P_{2,ii}^{(8)} = \frac{1}{16} P_{el}^{(8)} \int_0^{+\infty} dt_1 \int_{t_1}^{t_1+\tau} dt_2 \int_{t_1+\tau}^{+\infty} dt_4 \left(P_I^{(8a)} \int_0^{t_1} P_{rad}^{(8)}\, d\Delta t \right)$$

iii- $t_4 = t_1 + \tau$: Uncorrelated

$$P_{2,iii}^{(8)} = \frac{1}{16} P_{el}^{(8)} \int_0^{+\infty} dt_1 \int_{t_1}^{t_1+\tau} dt_2 \int_{t_2}^{t_1+\tau} dt_3 \left(P_I^{(8a)} \int_0^{t_1} P_{rad}^{(8)}\, d\Delta t + P_I^{(8b)} \int_{t_1}^{t_2} P_{rad}^{(8)}\, d\Delta t \right)$$

iv- $t_3 = t_2 + \tau$: Uncorrelated

$$P_{2,iv}^{(8)} = \frac{1}{16} P_{el}^{(8)} \int_0^{+\infty} dt_2 \int_0^{t_2} dt_1 \int_{t_2+\tau}^{+\infty} dt_4 \left(P_I^{(8a)} \int_0^{t_1} P_{rad}^{(8)}\, d\Delta t + P_I^{(8b)} \int_{t_1}^{t_2} P_{rad}^{(8)}\, d\Delta t \right)$$

v- $t_4 = t_2 + \tau$: Correlated

$$P_{2,v}^{(8)} = \frac{1}{16} P_{el}^{(8)} \int_0^{+\infty} dt_2 \int_0^{t_2} dt_1 \int_{t_2}^{t_2+\tau} dt_3 \left(P_I^{(8a)} \int_0^{t_1} P_{rad}^{(8)}\, d\Delta t + P_I^{(8b)} \int_{t_1}^{t_2} P_{rad}^{(8)}\, d\Delta t \right)$$

vi- $t_4 = t_3 + \tau$: Uncorrelated

$$P_{2,vi}^{(8)} = \frac{1}{16} P_{el}^{(8)} \int_0^{+\infty} dt_3 \int_0^{t_3} dt_2 \int_0^{t_2} dt_1 \left(P_I^{(8a)} \int_0^{t_1} P_{rad}^{(8)}\, d\Delta t + P_I^{(8b)} \int_{t_1}^{t_2} P_{rad}^{(8)}\, d\Delta t \right)$$

3/ $(P_{e_1}, P_{e_2}, P_{e_2}, P_{e_1})$: $\Delta t < t_2$

i- $t_2 = t_1 + \tau$: Uncorrelated

$$P_{3,i}^{(8)} = P_{2,i}^{(8)}$$

ii- $t_3 = t_1 + \tau$: Uncorrelated

$$P_{3,ii}^{(8)} = \frac{1}{16} P_{el}^{(8)} \int_0^{+\infty} dt_1 \int_{t_1}^{t_1+\tau} dt_2 \int_{t_1+\tau}^{+\infty} dt_4 \left(P_I^{(8a)} \int_0^{t_1} P_{rad}^{(8)}\, d\Delta t + P_I^{(8b)} \int_{t_1}^{t_2} P_{rad}^{(8)}\, d\Delta t \right)$$

iii- $t_4 = t_1 + \tau$: Correlated

$$P^{(8)}_{3,iii} = \frac{1}{16} P^{(8)}_{el} \int_0^{+\infty} dt_1 \int_{t_1}^{t_1+\tau} dt_2 \int_{t_2}^{t_1+\tau} dt_3 \left(P^{(8a)}_I \int_0^{t_1} P^{(8)}_{rad}\, d\Delta t \right)$$

iv- $t_3 = t_2 + \tau$: Correlated

$$P^{(8)}_{3,iv} = P^{(8)}_{2,iv}$$

v- $t_4 = t_2 + \tau$: Uncorrelated

$$P^{(8)}_{3,v} = P^{(8)}_{2,v}$$

vi- $t_4 = t_3 + \tau$: Uncorrelated

$$P^{(8)}_{3,vi} = P^{(8)}_{2,vi}$$

4/ $(P_{e_2}, P_{e_1}, P_{e_1}, P_{e_2})$: $\Delta t < t_1$

i- $t_2 = t_1 + \tau$: Uncorrelated

$$P^{(8)}_{4,i} = \frac{1}{16} P^{(8)}_{el} \int_0^{+\infty} dt_1 \int_{t_1+\tau}^{+\infty} dt_3 \int_{t_3}^{+\infty} dt_4 \left(P^{(8a)}_I \int_0^{t_1} P^{(8)}_{rad}\, d\Delta t \right)$$

ii- $t_3 = t_1 + \tau$: Uncorrelated

$$P^{(8)}_{4,ii} = \frac{1}{16} P^{(8)}_{el} \int_0^{+\infty} dt_1 \int_{t_1}^{t_1+\tau} dt_2 \int_{t_1+\tau}^{+\infty} dt_4 \left(P^{(8a)}_I \int_0^{t_1} P^{(8)}_{rad}\, d\Delta t \right)$$

iii- $t_4 = t_1 + \tau$: Correlated

$$P^{(8)}_{4,iii} = \frac{1}{16} P^{(8)}_{el} \int_0^{+\infty} dt_1 \int_{t_1}^{t_1+\tau} dt_2 \int_{t_2}^{t_1+\tau} dt_3 \left(P^{(8a)}_I \int_0^{t_1} P^{(8)}_{rad}\, d\Delta t \right)$$

iv- $t_3 = t_2 + \tau$: Correlated

$$P^{(8)}_{4,iv} = \frac{1}{16} P^{(8)}_{el} \int_0^{+\infty} dt_2 \int_0^{t_2} dt_1 \int_{t_2+\tau}^{+\infty} dt_4 \left(P^{(8a)}_I \int_0^{t_1} P^{(8)}_{rad}\, d\Delta t \right)$$

v- $t_4 = t_2 + \tau$: Uncorrelated

$$P^{(8)}_{4,v} = \frac{1}{16} P^{(8)}_{el} \int_0^{+\infty} dt_2 \int_0^{t_2} dt_1 \int_{t_2}^{t_2+\tau} dt_3 \left(P^{(8a)}_I \int_0^{t_1} P^{(8)}_{rad}\, d\Delta t \right)$$

vi- $t_4 = t_3 + \tau$: Uncorrelated

$$P_{4,vi}^{(8)} = \frac{1}{16} P_{el}^{(8)} \int_0^{+\infty} dt_3 \int_0^{t_3} dt_2 \int_0^{t_2} dt_1 \left(P_I^{(8a)} \int_0^{t_1} P_{rad}^{(8)} \, d\Delta t \right)$$

5/ $(P_{e_2}, P_{e_1}, P_{e_2}, P_{e_1})$: $\Delta t < t_1$

i- $t_2 = t_1 + \tau$: Uncorrelated

$$P_{5,i}^{(8)} = P_{4,i}^{(8)}$$

ii- $t_3 = t_1 + \tau$: Correlated

$$P_{5,ii}^{(8)} = P_{4,ii}^{(8)}$$

iii- $t_4 = t_1 + \tau$: Uncorrelated

$$P_{5,iii}^{(8)} = P_{4,iii}^{(8)}$$

iv- $t_3 = t_2 + \tau$: Uncorrelated

$$P_{5,iv}^{(8)} = P_{4,iv}^{(8)}$$

v- $t_4 = t_2 + \tau$: Correlated

$$P_{5,v}^{(8)} = P_{4,v}^{(8)}$$

vi- $t_4 = t_3 + \tau$: Uncorrelated

$$P_{5,vi}^{(8)} = P_{4,vi}^{(8)}$$

6/ $(P_{e_2}, P_{e_2}, P_{e_1}, P_{e_1})$: $\Delta t < t_1$

i- $t_2 = t_1 + \tau$: Correlated

$$P_{6,i}^{(8)} = P_{4,i}^{(8)}$$

ii- $t_3 = t_1 + \tau$: Uncorrelated

$$P_{6,ii}^{(8)} = P_{4,ii}^{(8)}$$

iii- $t_4 = t_1 + \tau$: Uncorrelated

$$P_{6,iii}^{(8)} = P_{4,iii}^{(8)}$$

iv- $t_3 = t_2 + \tau$: Uncorrelated

$$P_{6,iv}^{(8)} = P_{4,iv}^{(8)}$$

v- $t_4 = t_2 + \tau$: Uncorrelated

$$P_{6,v}^{(8)} = P_{4,v}^{(8)}$$

vi- $t_4 = t_3 + \tau$: Correlated

$$P_{6,vi}^{(8)} = P_{4,vi}^{(8)}$$

Even if this exhaustive list seems redundant, in fact equal contributions are not associated either to correlated or uncorrelated terms. For example, $P^{(8)}_{6,i}$ is associated to a correlated emission while $P^{(8)}_{4,i}$ is associated to an uncorrelated emission. Therefore, of the two, only $P^{(8)}_{4,i}$ will be weighted by I/I_0. However, the redundancy of the terms simplified the calculation as well as the numerical implementation.

Normalization of the $g^{(2)}(\tau)$

We now have all the probabilities associated to relevant events #1, #3, #4, #6 and #8. The complete sum becomes :

$$P(\tau) = 2\left(P^{(1)}(\tau) + P^{(6)}(\tau) + P^{4}_{\mathrm{C}}(\tau)\right) + P^{(8)}_{\mathrm{C}}(\tau) + \frac{I}{I_0}\left(P^{(3)}(\tau) + 2 * P^{(4)}_{\mathrm{NC}}(\tau) + P^{(8)}_{\mathrm{NC}}(\tau)\right)$$

With $P^{4,8}_{\mathrm{C}}(\tau)$ and $P^{4,8}_{\mathrm{NC}}(\tau)$ respectively the sum of the correlated and uncorrelated terms of the events #4 and #8. P^{norm} the normalization of $P(\tau)$ needs to take into account the fact that the electron can interact twice with the material.

$$\begin{aligned} P^{\mathrm{norm}} &= \frac{I}{I_0}\left(P^{\mathrm{norm}}_1 + P^{\mathrm{norm}}_2\right)^2 \\ \text{With} \quad P^{\mathrm{norm}}_1 &= \frac{1}{2}P_{\mathrm{el}}(1)P_{\mathrm{int}}(0)(1 - P_{\mathrm{int}}(1)) \\ P^{\mathrm{norm}}_2 &= \frac{1}{4}P_{\mathrm{el}}(1)P_{\mathrm{int}}(0)P_{\mathrm{int}}(1) \end{aligned}$$

$$g^{(2)}(\tau) = \frac{P(\tau)}{P^{\mathrm{norm}}}$$

Appendix B

Development of chapter 6

B.1 Development of equation 6.5

$$\sum_{\substack{k,n\\k',n'}} \dot{\rho}^{I}_{\substack{k,n\\k',n'}} e^{-i((n-n')\omega_0+(\epsilon_k-\epsilon_{k'}))t} \left|k,n\right\rangle \left\langle n',k'\right|$$

$$= \frac{i}{\hbar} \sum_{\substack{k,n\\k',n'}} \rho^{I}_{\substack{k,n\\k',n'}} e^{-i((n-n')\omega_0+(\epsilon_k-\epsilon_{k'}))t} \sum_{k_1,k_2} \left|k,n\right\rangle \left\langle n',k'\right| b^{+}_{k_1} b_{k_2} g_{k_1,k_2} \left(a^{+}+a\right)$$
$$- b^{+}_{k_1} b_{k_2} g_{k_1,k_2} \left(a^{+}+a\right) \left|k,n\right\rangle \left\langle n',k'\right| \tag{B.1}$$

$$= \frac{i}{\hbar} \sum_{\substack{k,n\\k',n'}} \rho^{I}_{\substack{k,n\\k',n'}} e^{-i((n-n')\omega_0+(\epsilon_k-\epsilon_{k'}))t} \sum_{k_2} g_{k',k_2} \left|k,n\right\rangle \left\langle n',k_2\right| \left(a^{+}+a\right)$$
$$- g_{k_2,k} \left(a^{+}+a\right) \left|k_2,n\right\rangle \left\langle n',k'\right|$$

$$= \frac{i}{\hbar} \sum_{\substack{k,n\\k',n'}} \rho^{I}_{\substack{k,n\\k',n'}} \sum_{k_2} g_{k',k_2} e^{-i((n-n')\omega_0+(\epsilon_k-\epsilon_{k'}))t} \left|k,n\right\rangle \left\langle n'-1,k_2\right| \sqrt{n'}$$
$$+ g_{k',k_2} e^{-i((n-n')\omega_0+(\epsilon_k-\epsilon_{k'}))t} \left|k,n\right\rangle \left\langle n'+1,k_2\right| \sqrt{n'+1}$$
$$- g_{k_2,k} e^{-i((n-n')\omega_0+(\epsilon_k-\epsilon_{k'}))t} \left|k_2,n-1\right\rangle \left\langle n',k'\right| \sqrt{n}$$
$$- g_{k_2,k} e^{-i((n-n')\omega_0+(\epsilon_k-\epsilon_{k'}))t} \left|k_2,n+1\right\rangle \left\langle n',k'\right| \sqrt{n+1} \tag{B.2}$$

In each sum of equation B.2 we do a variable transformation in order to obtain for each part $|k,n\rangle\langle n',k'|$.

$$
\begin{aligned}
= \frac{i}{\hbar} \sum_{\substack{k,n \\ k',n'}} \sum_{k_2} & g_{k_2,k'} \rho^{I}_{\substack{k,n \\ k_2,n'+1}} e^{-i\left((n-n'-1)\omega_0+\left(\epsilon_k-\epsilon_{k_2}\right)\right)t} |k,n\rangle\langle n',k'| \sqrt{n'+1} \\
& + g_{k_2,k'} \rho^{I}_{\substack{k,n \\ k_2,n'-1}} e^{-i\left((n-n'+1)\omega_0+\left(\epsilon_k-\epsilon_{k_2}\right)\right)t} |k,n\rangle\langle n',k'| \sqrt{n'} \\
& - g_{k,k_2} \rho^{I}_{\substack{k_2,n+1 \\ k',n'}} e^{-i\left((n+1-n')\omega_0+\left(\epsilon_{k_2}-\epsilon_{k'}\right)\right)t} |k,n\rangle\langle n',k'| \sqrt{n+1} \\
& - g_{k,k_2} \rho^{I}_{\substack{k_2,n-1 \\ k',n'}} e^{-i\left((n-1-n')\omega_0+\left(\epsilon_{k_2}-\epsilon_{k'}\right)\right)t} |k,n\rangle\langle n',k'| \sqrt{n}
\end{aligned} \tag{B.3}
$$

Therefore $\dot{\rho}^{I}_{\substack{k,n \\ k',n'}}$ is equal to :

$$
\begin{aligned}
\dot{\rho}^{I}_{\substack{k,n \\ k',n'}} = \frac{i}{\hbar} \sum_{k_2} & g_{k_2,k'} \rho^{I}_{\substack{k,n \\ k_2,n'+1}} e^{-i\left(\left(\epsilon_{k'}-\epsilon_{k_2}\right)-\omega_0\right)t} \sqrt{n'+1} \\
& + g_{k_2,k'} \rho^{I}_{\substack{k,n \\ k_2,n'-1}} e^{-i\left(\left(\epsilon_{k'}-\epsilon_{k_2}\right)+\omega_0\right)t} \sqrt{n'} \\
& - g_{k,k_2} \rho^{I}_{\substack{k_2,n+1 \\ k',n'}} e^{-i\left(\left(\epsilon_{k_2}-\epsilon_{k}\right)+\omega_0\right)t} \sqrt{n+1} \\
& - g_{k,k_2} \rho^{I}_{\substack{k_2,n-1 \\ k',n'}} e^{-i\left(\left(\epsilon_{k_2}-\epsilon_{k}\right)-\omega_0\right)t} \sqrt{n}
\end{aligned} \tag{B.4}
$$

We defined the matrices $G^1,\ G^2,\ G^3,\ G^4$ such as :

$$
\begin{aligned}
G^{1}_{\substack{n,n' \\ n_2,n'_2}} &= \delta_{n,n_2}\delta_{n'+1,n'_2}\sqrt{n'+1} \\
G^{2}_{\substack{n,n' \\ n_2,n'_2}} &= \delta_{n,n_2}\delta_{n'-1,n'_2}\sqrt{n'} \\
G^{3}_{\substack{n,n' \\ n_2,n'_2}} &= \delta_{n+1,n_2}\delta_{n',n'_2}\sqrt{n+1} \\
G^{1}_{\substack{n,n' \\ n_2,n'_2}} &= \delta_{n-1,n_2}\delta_{n',n'_2}\sqrt{n}
\end{aligned}
$$

Therefore equation B.4 becomes :

$$
\begin{aligned}
\dot{\rho}^{I}_{\substack{k,n \\ k',n'}} = \frac{i}{\hbar} \sum_{k_2} \sum_{n_2,n'_2} & G^{1}_{\substack{n,n' \\ n_2,n'_2}}\, g_{k_2,k'} \rho^{I}_{\substack{k,n_2 \\ k_2,n'_2}} e^{-i\left(\left(\epsilon_{k'}-\epsilon_{k_2}\right)-\omega_0\right)t} \\
& + G^{2}_{\substack{n,n' \\ n_2,n'_2}}\, g_{k_2,k'} \rho^{I}_{\substack{k,n_2 \\ k_2,n'_2}} e^{-i\left(\left(\epsilon_{k'}-\epsilon_{k_2}\right)+\omega_0\right)t} \\
& - G^{3}_{\substack{n,n' \\ n_2,n'_2}}\, g_{k,k_2} \rho^{I}_{\substack{k_2,n_2 \\ k',n'_2}} e^{-i\left(\left(\epsilon_{k_2}-\epsilon_{k}\right)+\omega_0\right)t} \\
& - G^{4}_{\substack{n,n' \\ n_2,n'_2}}\, g_{k,k_2} \rho^{I}_{\substack{k_2,n_2 \\ k',n'_2}} e^{-i\left(\left(\epsilon_{k_2}-\epsilon_{k}\right)-\omega_0\right)t}
\end{aligned} \tag{B.5}
$$

B.2 Development of equation 6.20

The total wave function of the system is :

$$|\psi_f(z,t)\rangle = |\psi_0\rangle + \int dz' \int dt'\ G(z-z',t-t')H_{int}(z')\,|\psi_i(z',t')\rangle$$

$$\begin{aligned}|\psi_f(z,t)\rangle = \frac{ie}{m}\frac{\aleph}{2\pi}\sum_{n'}\sum_j \sqrt{\frac{2\pi\hbar}{\omega_j}}\int dz' \int dt' \int dk\ e^{i\left(k-\frac{n'\omega_0}{v}\right)(z-z')}e^{-i\epsilon_k(t-t')}\,|n'\rangle\langle n'| \\ (\mathbf{f}^*_{j_z}(\mathbf{z'})\sqrt{n+1}\left(ik_0-\frac{2}{\Delta^2}\left(z'-vt'\right)\right)e^{ik_0z'}e^{-\frac{(z'-vt')^2}{\Delta^2}}e^{-i(\epsilon_{k_0}+n\omega_0)t'}\,|n+1\rangle \\ +\mathbf{f}_{j_z}(\mathbf{z'})\sqrt{n}\left(ik_0-\frac{2}{\Delta^2}\left(z'-vt'\right)\right)e^{ik_0z'}e^{-\frac{(z'-vt')^2}{\Delta^2}}e^{-i(\epsilon_{k_0}+n\omega_0)t'}\,|n-1\rangle)\end{aligned}$$

We can consider that $k_0 >> \frac{2}{\Delta^2}(z'-vt')$, it means that the gaussian packet will not change its shape during the interaction.

$$\begin{aligned}|\psi_f(z,t)\rangle = -\frac{e}{m}\frac{\aleph}{2\pi}k_0\sum_j\sqrt{\frac{2\pi\hbar}{\omega_j}}\int dz' \int dk\ e^{-i\epsilon_k t}\underbrace{\int dt'\ e^{-i(\epsilon_{k_0}+n\omega_0-\epsilon_k)t'}e^{-\frac{(z'-vt')^2}{\Delta^2}}}_{I} \\ (\mathbf{f}^*_{j_z}(\mathbf{z'})\sqrt{n+1}\ e^{i\left(k-\frac{n+1\omega_0}{v}\right)(z-z')}e^{ik_0z'}\,|n+1\rangle \\ +\mathbf{f}_{j_z}(\mathbf{z'})\sqrt{n}\ e^{i\left(k-\frac{n-1\omega_0}{v}\right)(z-z')}e^{ik_0z'}\,|n-1\rangle)\end{aligned}$$

We used the Gauss Integral to calculate Part I of the previous equation :

$$\begin{aligned}&= \int dt' e^{-i(\epsilon_{k_0}+n\omega_0-\epsilon_k)t'}e^{-\frac{z'^2}{\Delta^2}}e^{\frac{2z'vt'}{\Delta^2}}e^{-\frac{v^2t'^2}{\Delta^2}} \\ &= e^{-\frac{z'^2}{\Delta^2}}\int dt' e^{\underbrace{\frac{2z'v}{\Delta^2}-i(\epsilon_{k_0}+n\omega_0-\epsilon_k)}_{a}t'}e^{-\frac{v^2t'^2}{\Delta^2}} \\ &= e^{-\frac{z'^2}{\Delta^2}}\underbrace{\int dt' e^{\left(t'-\frac{a\Delta^2}{2v^2}\right)^2\frac{v^2}{\Delta^2}}e^{\frac{a^2\Delta^2}{4v^2}}}_{\frac{\sqrt{\pi}\Delta}{v}} \\ &= \frac{\sqrt{\pi}\Delta}{v}e^{-\frac{z'^2}{\Delta^2}}e^{\left(\frac{2z'v}{\Delta^2}-i(\epsilon_{k_0}+n\omega_0-\epsilon_k)\right)^2\frac{\Delta^2}{4v^2}} \\ &= \frac{\sqrt{\pi}\Delta}{v}e^{-i(\epsilon_{k_0}+n\omega_0-\epsilon_k)\frac{z'}{v}}e^{-(\epsilon_{k_0}+n\omega_0-\epsilon_k)^2\frac{\Delta^2}{4v^2}}\end{aligned}$$

So the $|\psi_f(z,t)\rangle$ becomes :

$$|\psi_f(z,t)\rangle = -\frac{e}{m}\frac{\aleph}{2\pi}k_0\frac{\sqrt{\pi}\Delta}{v}\sum_j\sqrt{\frac{2\pi\hbar}{\omega_j}}\int dz'\int dk\ e^{-i\epsilon_k t}e^{-i(\epsilon_{k_0}+n\omega_0-\epsilon_k)\frac{z'}{v}}e^{-(\epsilon_{k_0}+n\omega_0-\epsilon_k)^2\frac{\Delta^2}{4v^2}}$$
$$(\mathbf{f}^*_{j_z}(\mathbf{z'})\sqrt{n+1}\ e^{i\left(k-\frac{n+1\omega_0}{v}\right)(z-z')}e^{ik_0z'}\,|n+1\rangle$$
$$+\mathbf{f}_{j_z}(\mathbf{z'})\sqrt{n}\ e^{i\left(k-\frac{n-1\omega_0}{v}\right)(z-z')}e^{ik_0z'}\,|n-1\rangle)$$

We defined $K = k - k_0 - \frac{n\omega_0}{v}$ and $\epsilon_k - \epsilon_{k_0} - n\omega_0 \approx Kv$

$$|\psi_f(z,t)\rangle = -\frac{e}{m}\frac{\aleph}{2\pi}k_0\frac{\sqrt{\pi}\Delta}{v}\sum_j\sqrt{\frac{2\pi\hbar}{\omega_j}}\int dz'\int dK\ e^{-iKvt}e^{-i(\epsilon_{k_0}+n\omega_0)t}e^{iKz'}e^{-K^2\frac{\Delta^2}{4}}$$
$$(\mathbf{f}^*_{j_z}(\mathbf{z'})\sqrt{n+1}\ e^{i\left(K+k_0+\frac{n\omega_0}{v}-\frac{n+1\omega_0}{v}\right)(z-z')}e^{ik_0z'}\,|n+1\rangle$$
$$+\mathbf{f}_{j_z}(\mathbf{z'})\sqrt{n}\ e^{i\left(K+k_0+\frac{n\omega_0}{v}-\frac{n-1\omega_0}{v}\right)(z-z')}e^{ik_0z'}\,|n-1\rangle)$$

$$|\psi_f(z,t)\rangle = -\frac{e}{m}\frac{\aleph}{2\pi}k_0\frac{\sqrt{\pi}\Delta}{v}e^{-i(\epsilon_{k_0}+n\omega_0)t}\sum_j\sqrt{\frac{2\pi\hbar}{\omega_j}}\int dz'\underbrace{\int dK\ e^{-iKvt}e^{-K^2\frac{\Delta^2}{4}}e^{iKz}}_{II}$$
$$(\mathbf{f}^*_{j_z}(\mathbf{z'})\sqrt{n+1}\ e^{i\left(k_0-\frac{\omega_0}{v}\right)(z-z')}e^{ik_0z'}\,|n+1\rangle$$
$$+\mathbf{f}_{j_z}(\mathbf{z'})\sqrt{n}\ e^{i\left(k_0+\frac{\omega_0}{v}\right)(z-z')}e^{ik_0z'}\,|n-1\rangle)$$

Part II of previous equation is equal to :

$$= \int dK\ e^{iK(z-vt)}e^{-K^2\frac{\Delta^2}{4}}$$
$$= \underbrace{\int dK\ e^{-\left(K-i\frac{2(z-vt)}{\Delta^2}\right)^2\frac{\Delta^2}{4}}}_{\frac{2\sqrt{\pi}}{\Delta}}e^{-\frac{(z-vt)^2}{\Delta^2}}$$
$$= \frac{2\sqrt{\pi}}{\Delta}e^{-\frac{(z-vt)^2}{\Delta^2}}$$

$$|\psi_f(z,t)\rangle = -\frac{e}{m}\frac{\aleph}{2\pi}k_0\frac{\sqrt{\pi}\Delta}{v}e^{-i(\epsilon_{k_0}+n\omega_0)t}\frac{2\sqrt{\pi}}{\Delta}e^{-\frac{(z-vt)^2}{\Delta^2}}\sum_j\sqrt{\frac{2\pi\hbar}{\omega_j}}$$
$$e^{i\left(k_0-\frac{\omega_0}{v}\right)z}\sqrt{n+1}\int dz'(\mathbf{f}^*_{j_z}(\mathbf{z'})e^{+i\left(\frac{\omega_0}{v}\right)z'}\,|n+1\rangle$$
$$+e^{i\left(k_0+\frac{\omega_0}{v}\right)z}\sqrt{n}\int dz'\mathbf{f}_{j_z}(\mathbf{z'})e^{-i\left(\frac{\omega_0}{v}\right)z'}\,|n-1\rangle)$$

$$|\psi_f(z,t)\rangle = -\frac{e}{m}\frac{\aleph}{2\pi}k_0\frac{\sqrt{\pi}\Delta}{v}e^{-i(\epsilon_{k_0}+n\omega_0)t}\frac{2\sqrt{\pi}}{\Delta}e^{\frac{-(z-vt)^2}{\Delta^2}}$$
$$e^{i\left(k_0-\frac{\omega_0}{v}\right)z}\sqrt{n+1}\underbrace{\sum_j\sqrt{\frac{2\pi\hbar}{\omega_j}}\int dz'\mathbf{f}^*_{j_z}(\mathbf{z'})e^{+i\left(\frac{\omega_0}{v}\right)z'}}_{\mathrm{A}^*}|n+1\rangle$$
$$+e^{i\left(k_0+\frac{\omega_0}{v}\right)z}\sqrt{n}\underbrace{\sum_j\sqrt{\frac{2\pi\hbar}{\omega_j}}\int dz'\mathbf{f}_{j_z}(\mathbf{z'})e^{-i\left(\frac{\omega_0}{v}\right)z'}}_{\mathrm{A}}|n-1\rangle$$

$$|\psi_f(z,t)\rangle = -\frac{e}{m}\frac{\aleph}{v}k_0e^{\frac{-(z-vt)^2}{\Delta^2}}$$
$$\mathrm{A}^*\sqrt{n+1}\;e^{\underbrace{i\left(k_0-\frac{\omega_0}{v}\right)}_{k_1}z}\;e^{\underbrace{-i\left(\epsilon_{k_0}-\omega_0\right)}_{\epsilon_{k_1}}t}\;e^{-i(n+1)\omega_0t}|n+1\rangle \tag{B.6}$$
$$+\mathrm{A}\sqrt{n}\;e^{\underbrace{i\left(k_0+\frac{\omega_0}{v}\right)}_{k_1'}z}\;e^{\underbrace{-i\left(\epsilon_{k_0}+\omega_0\right)}_{\epsilon_{k_1'}}t}\;e^{-i(n-1)\omega_0t}|n-1\rangle$$

B.3 Integration over k and t of the interaction part

Integration over k

$$\dot{\rho}_{\substack{k_0,n\\k_1,n+1}} = \frac{i}{\hbar}\frac{L}{2\pi}\int_{-\infty}^{\infty}dk\sqrt{n+1}\rho_{\substack{k_0,n\\k,n}}g^*_{k_1}e^{-i\left(\left(\epsilon_{k_1}-\epsilon_k\right)-\omega_0\right)t}$$
$$= \frac{i}{\hbar}\frac{L}{2\pi}\frac{\Delta}{\sqrt{2\pi^3}}C_{k_0}\sqrt{n+1}\rho_{n,n}g^*_{k_1}\underbrace{\int_{-\infty}^{\infty}dk\;C^*_{k_0}e^{-i\left(\left(\epsilon_{k_1}-\epsilon_k\right)-\omega_0\right)t}}_{VII} \tag{B.7}$$

Part VII of equation B.7 is equal to :

$$= \int_{-\infty}^{\infty}dk\;e^{-(k-k_0)^2\Delta^2}e^{-ikz_1}e^{-i\left(\left(\epsilon_{k_1}-\epsilon_k\right)-\omega_0\right)t}$$
$$\rightarrow k-k_0 = K \text{ and } \epsilon_k-\epsilon_{k_0}\approx Kv$$
$$= \int_{-\infty}^{\infty}dK\;e^{-(K\Delta)^2}e^{-iKz_1}e^{-ik_0z_1}e^{-i\left(\left(\epsilon_{k_1}-Kv-\epsilon_{k_0}\right)-\omega_0\right)t}$$
$$= e^{-ik_0z_1}e^{-i\left(\left(\epsilon_{k_1}-\epsilon_{k_0}\right)-\omega_0\right)t}\int_{-\infty}^{\infty}dK\;e^{-i(z_1-vt)K}e^{-(K\Delta)^2}$$
$$= e^{-ik_0z_1}e^{-i\left(\left(\epsilon_{k_1}-\epsilon_{k_0}\right)-\omega_0\right)t}\underbrace{\int_{-\infty}^{\infty}dK\;e^{-\left(K+i\frac{(z_1-vt)}{2\Delta}\right)^2\Delta^2}}_{\frac{\sqrt{\pi}}{\Delta}}e^{-\left(\frac{z_1-vt}{2\Delta}\right)^2}$$

Therefore equation B.7 becomes

$$\dot{\rho}_{\substack{k_0,n\\k_1,n+1}} = \frac{i}{\hbar}\frac{L}{2\pi^2}\frac{g^*_{k_1}}{\sqrt{2}}C_{k_0}\sqrt{n+1}\rho_{n,n}e^{-ik_0z_1}e^{-i\left((\epsilon_{k_1}-\epsilon_{k_0})-\omega_0\right)t}e^{-\left(\frac{z_1-vt}{2\Delta}\right)^2} \tag{B.8}$$

Integration over t

$$\rho_{\substack{k_0,n\\k_1,n+1}} = \frac{i}{\hbar}\frac{L}{2\pi^2}\frac{g^*_{k_1}}{\sqrt{2}}C_{k_0}\sqrt{n+1}\rho_{n,n}e^{-ik_0z_1}\underbrace{\int_{-\infty}^{\infty}dt\ e^{-i\left((\epsilon_{k_1}-\epsilon_{k_0})-\omega_0\right)t}e^{-\left(\frac{z_1-vt}{2\Delta}\right)^2}}_{VIII} \tag{B.9}$$

Part VIII of equation B.9 is equal to :

$$\begin{aligned}
&= \int_{-\infty}^{\infty}dt\ e^{-i\left((\epsilon_{k_1}-\epsilon_{k_0})-\omega_0\right)t}e^{-\left(\frac{z_1}{2\Delta}\right)^2}e^{-\left(\frac{vt}{2\Delta}\right)^2}e^{\left(\frac{z_1vt}{2\Delta^2}\right)}\\
&= e^{-\left(\frac{z_1}{2\Delta}\right)^2}\int_{-\infty}^{\infty}dt\ \underbrace{e^{\left(\frac{z_1v}{2\Delta^2}-i\left((\epsilon_{k-1}-\epsilon_{k_0})+\omega_0\right)\right)t}}_{a}e^{-\left(\frac{vt}{2\Delta}\right)^2}\\
&= e^{-\left(\frac{z_1}{2\Delta}\right)^2}\underbrace{\int_{-\infty}^{\infty}dt\ e^{-\left(t-\frac{a\Delta^2}{v^2}\right)^2\frac{v^2}{(2\Delta)^2}}}_{\frac{2\Delta\sqrt{\pi}}{v}}e^{\left(\frac{a\Delta}{v}\right)^2}
\end{aligned} \tag{B.10}$$

Therefore :

$$\rho_{\substack{k_0,n\\k_1,n+1}} = \underbrace{\frac{i}{\hbar}\frac{L}{\pi^2}\frac{\Delta\sqrt{\pi}}{v}\frac{g^*_{k_1}}{\sqrt{2}}\sqrt{n+1}e^{-ik_0z_1}e^{\left(\frac{a\Delta}{v}\right)^2}e^{-\left(\frac{z_1}{2\Delta}\right)^2}}_{F_1}C_{k_0}\rho_{n,n} \tag{B.11}$$

Appendix C

Normalization of the electron wave function

C.1 Wave function of the incoming electron

Before interaction the component of the density matrix describing the incoming electron and the plasmonic particle are independent, one can write the part describing the incoming electron as a gaussian packets :

$$\begin{aligned}\rho_{k_0,k_0} =& C_{k_0} C_{k_0}^* \\ =& \left|\phi_{k_0}(z,t)\right\rangle \left\langle\phi_{k_0}(z,t)\right|\end{aligned} \tag{C.1}$$

The wave function of the electron $\phi_{k_0}(z,t)$ is thus equal to :

$$\begin{aligned}\phi_{k_0}(z,t) =& \int dk C_{k_0} e^{i(kz-\epsilon_k t)} \\ C_{k_0} =& \aleph e^{-(k-k_0)^2\Delta^2}\end{aligned} \tag{C.2}$$

We defined $K = k - k_0$ which means in the non recoils approximation $Kv \approx \epsilon_k - \epsilon_{k_0}$:

$$\begin{aligned}\phi_{k_0}(z,t) =& \aleph e^{ik_0 z} e^{-i\epsilon_{k_0} t} \int dK e^{-(K\Delta)^2} e^{i(Kz-Kvt)} \\ =& \aleph e^{ik_0 z} e^{-i\epsilon_{k_0} t} e^{-\frac{(z-vt)^2}{4\Delta^2}} \underbrace{\int dK e^{-\left(K-i\frac{(z-vt)^2}{2\Delta^2}\right)^2\Delta^2}}_{=\sqrt{\pi}/\Delta} \\ =& \aleph \frac{\sqrt{\pi}}{\Delta} e^{ik_0 z} e^{-i\epsilon_{k_0} t} e^{-\frac{(z-vt)^2}{4\Delta^2}}\end{aligned} \tag{C.3}$$

Equation C.4 need to verify the normalization rule :

$$\begin{aligned}\int |\phi_{k_0}(z,t)|^2\, dz &= 1 \\ &= \frac{\pi}{\Delta^2}\aleph^2 \underbrace{\int dz e^{-\frac{(z-vt)^2}{4\Delta^2}}}_{=\sqrt{2\pi}\Delta} \\ &= \frac{\pi\sqrt{2\pi}\aleph^2}{\Delta} \;=\; 1 \end{aligned} \tag{C.4}$$

Therefore we defined the coefficient of normalisation $\aleph$ as :

$$\aleph = \sqrt{\frac{\Delta}{\sqrt{2\pi^3}}} \tag{C.5}$$

Appendix D

First steps towards coupling of a plasmonic nanoparticle and an emitter

The coupling between plasmons and single photon emitters is a hot issue of quantum optics in quantum plasmonics [44, 45]. This is a topic where the high spatial resolution of CL for emitters [46] and the relevance of EELS spectroscopy for surface plasmons make these two techniques complementary tools to study at sub-wavelength resolution the plasmons/quantum emitter coupling. Moreover it is very well known that coupling between emitters and plasmons reduces the lifetime of the emitter [47, 48]. One can imagine using the bunching effect to study the coupling between plasmons and emitters at the nanometer scale thanks to lifetime measurements. In order to introduce this field, some preliminary simulations and experiments have been done. We performed simulations with the Matlab MNPBEM toolbox designed for EELS and CL simulation [49, 50]. The theory behind coupling simulation with BEM was explained to me by Javier Garcia de Abajo. We then tried to implement it in MNPBEM. The BEM theory is described in the following section. Then the result of the first simulations will be shown along with the first experiments.

D.1 BEM simulation theory

We define the system as the metallic particle (yellow shape in figure D.1) and all the dipoles around it. For each dipole we defined a polarisability α_j and a position $\mathbf{r}_j$. The dipole orientation is defined for each dipole.

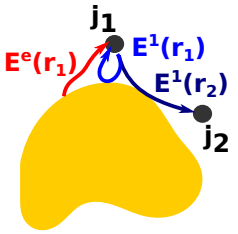

FIGURE D.1: Geometry of the problem. A nanoplasmonic structure is close to two emitters j_1 and j_2 respectively at position r_1 and r_2. For j_1 we represents $E^e(r_1)$ the field created by the metallic particle with the electron at the dipole position, $E^1(r_1)$ the field created by dipole j_1 and acting back on position r_1 and $E^1(r_2)$ the field created by dipole j_1 and acting on position r_2.

The first step is to calculate independently with BEM calculations (MNPBEM toolbox) the different field involved in the coupling:

1. The field created by the metallic particle with the electron, at each dipole position $\mathbf{E}^e(\mathbf{r}_j)$ and at infinity (the far-field) $\mathbf{f}^e(\mathbf{r})$.
2. The field created by each dipole (j), at each dipole position (j') $\mathbf{E}^j(\mathbf{r}_{j'})$ and at infinity (the far-field) $\mathbf{f}^j(\mathbf{r})$

Then we have to calculate the polarity $\mathbf{P}_j$ of each dipole j. We write a self consistent equation for each dipole:

$$\mathbf{P}_j = \alpha_j * [\mathbf{E}^e(\mathbf{r}_j) + \sum_{j \neq j'} \mathbf{E}^j(\mathbf{r}_{j'}) * \mathbf{P}_{j'} + \mathbf{E}^j(\mathbf{r}_j) * \mathbf{P}_j] \tag{D.1}$$

We define the matrix :

$$G_{jj'} = \mathbf{E}^{j'}(\mathbf{r}_j) \tag{D.2}$$

$$\Rightarrow \mathbf{P}_j = \alpha_j * [\mathbf{E}^e - j + \sum_{j'} G_{jj'} * \mathbf{P}_{j'}] \tag{D.3}$$

Which gives in a matrix formalism :

$$\mathbf{P} = \frac{1}{\frac{1}{\alpha} - G} * \mathbf{E}^e \tag{D.4}$$

The total far-field will be :

$$\mathbf{f}(\mathbf{r}) = \mathbf{f}^e(\mathbf{r}) + \sum_j \mathbf{f}^j(\mathbf{r}) * \mathbf{P}_j \tag{D.5}$$

In the case of a **weak coupling** between the dipole and the metallic particle, we can reduce the calculation of the polarity to

$$\mathbf{P} \approx \alpha * \mathbf{E}^e \tag{D.6}$$

In each case we calculate the far-field with the full equation for **P** (equation D.4) and the weak coupling limit (eq D.6). If the two calculations are equal, we are in the weak coupling regime.

D.2 Simulations and Experiments

For the simulations, we take a silver nano-triangle with an edge size of 150 nm size and an height of 50 nm on a15 nm tick Si_3N_4 substrate. The cathodoluminescence spectrum of such a nanoparticle by MNPBEM is shown on figure D.2.

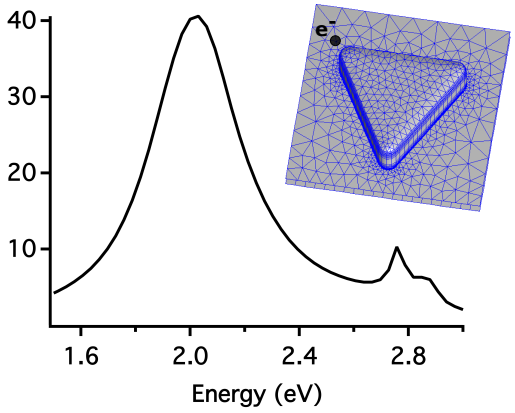

FIGURE D.2: BEM simulation of the cathodoluminescence spectrum of a silver nanotriangle of 150 nm side and 50 nm thick. On the insert a sketch of the simulated structure, where the black dot represents the impact point of the electron. The substrate is an Si_3N_4 membrane of 15 nm thick.

We set the energy of the emitter at 2.03 eV with a full width at half maximum of 20 meV. The emitter is therefore at resonance with the dipolar mode of the nanotriangle. Results of the obtained cathodoluminescence spectrum depending of the distance between the particle and the emitter is shown on figure D.3. One can see that the coupling amplifies the emitter emission, even if, in the strong coupling regime, there is quenching of the emission for $L < 20$ nm.

We conducted two kinds of experiments with nano-diamonds containing a high density of NV^0 centers. As explained in chapter 4, the lifetime measured will be the average lifetime of the NV^0 excited by the electron. The first experiment consisted to measure the lifetime of the same diamond before and after gold deposition. We use Si_3N_4 membrane

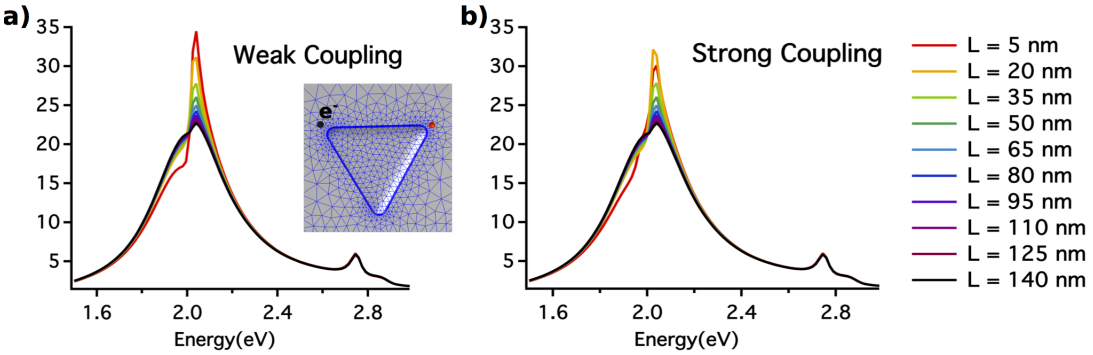

FIGURE D.3: a) weak coupling regime and b) strong coupling regime. The distance between the triangle corner and the emitter is changed (legend on the right). Insert of figure a) the simulated structure with the emitter in red and the silver nanotriangle. The emitter is put on the figure at 10 nm from the triangle corner.

where we draw the alignment lithographic pattern described in chapter 2 and visible in figure D.4-b. Then we dropped the nano-diamond on the TEM grid, and measured the lifetime of about 20 nano-diamonds. Each diamond was spotted thanks to the alignment pattern. After that we evaporated a film of 20 nm of gold on half of the grid as shown on figure D.4-a. The lifetime of the same nano diamonds was measured once again. As it has been explained in chapter 4, the lifetime of a single nano-diamond can change drastically from one experiment to another. This is the reason why half of the grid was kept without gold, in order to have witness diamonds to measure the possible variation of the lifetime without gold. The result is shown in figure D.4-c. We measured for each diamond the difference in lifetime $\Delta\tau = \tau_0 - \tau_g$ between the first measurement τ_0 and the second τ_g. One can see on figure D.4-c that $\Delta\tau$ is on average higher for the nano diamond with gold. However results are still preliminary because of the bad signal over noise ratio of the $g^{(2)}(\tau)$ curves leading to large error bars and a poor statistics. Here the large distribution of the lifetime in nano diamond is a major drawback. To improve this experiment, the use of an emitter with shorter lifetime for an increase of the signal over noise ratio (see chapter 5) and a more significant statistic is required.

The second experiment consisted in performing lifetime measurements on the same diamond before and after the deposition of a nano-triangle close to it. This experiment required a lot of steps and was therefore only successful for two diamonds. The best one is shown in figure D.5. First an alignment pattern was drawn and after a ionization of surface by a plasma cleaner during 3 minutes, diamonds were deposited on it. The plasma cleaning of the surface allowed theoretically a better adherence of the nano diamond to the surface, avoiding the diamonds to move during the second turn of lithographic process. Lifetimes of several nano diamonds are then measured and each nano-diamond was spotted in regards to the alignment pattern. The spotting have to be done carefully to ensure the drawing of the plasmonics structure at the right spot.

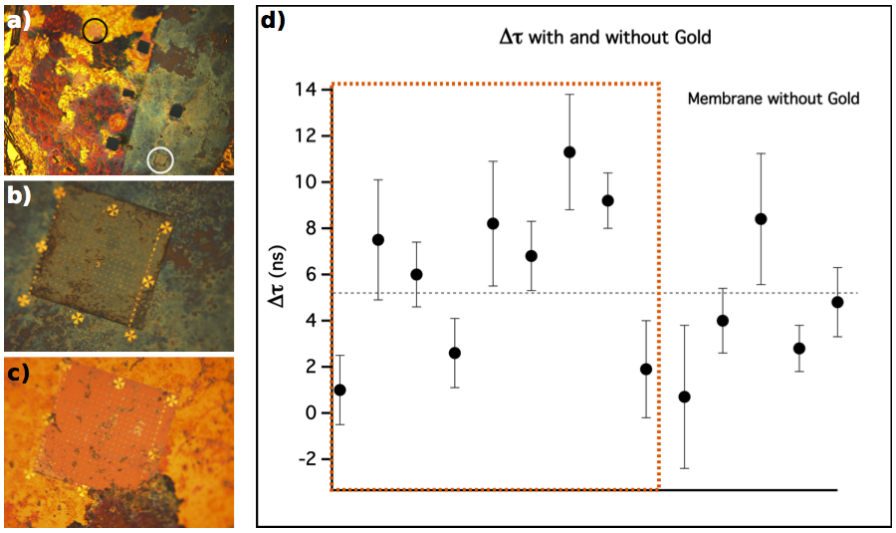

FIGURE D.4: Lifetime measurement on nano diamond before gold deposition τ_0 and after gold deposition τ_g. Optical images of the TEM grid after gold deposition is depicted in a),b),c). a) TEM grid with half of the grid recover by gold. b) membrane without gold, corresponding to the membrane with the white circle in a). c) image of a membrane recover in gold, corresponding to the membrane with the black circle in a). d) $\Delta\tau = \tau_0 - \tau_g$ for each diamond. The diamond recover in gold are the one depicted in the orange dashed square.

For each nano-diamond a plasmonic structure is drawn close to it, using the realignment process explained in chapter 2. Of course, during this step, the probability to break a window is high and it is therefore important to measure nano diamonds on every membrane. Then lifetimes were measured on diamonds which had survived. In our case, between breaking windows, misfit of the plasmonic location and disappearance of nano diamond, only two nano-diamonds were close to their plasmonic structure at the end. This validates, however, the feasibility of the technic. Results for the best one is shown on figure D.5. It seems that we observed a change in the lifetime. However no emission from the nano-triangle is visible (see figure D.5-b) which seems unlikely if there is coupling. The change can be due to the different lithographic steps that induced variation in the nano-diamond environment. Once again, to have more accurate results, a brighter emitter with a smaller lifetime needs to be found.

These simulations and experiments are the first step toward quantum plasmonic and emitter-plasmons coupling in an STEM. It opens the way to a wide range of experiments exploiting the high resolution of fast electrons and the complementarity of the information supply by the HADF image, the CL emission spectrum and the HBT-CL experiment. The easy set-up of this technic allows to use it for simple characterization of any optically active material or for more complex structure like plasmons-emitter system.

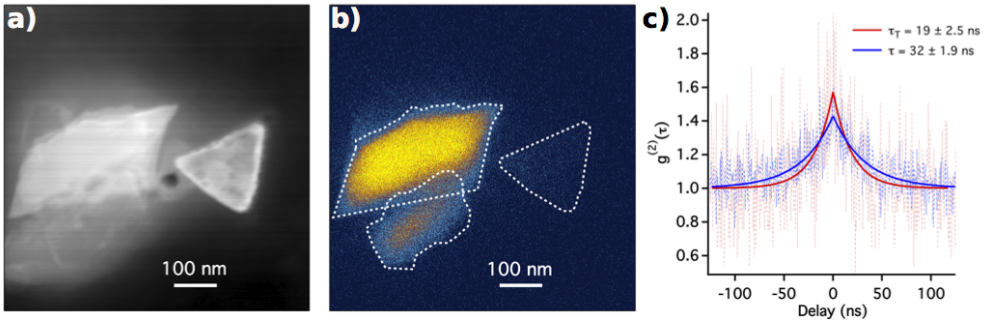

FIGURE D.5: Gold nano triangle drawn close to a nano diamond with a high density of center. a) HADF image and b) filtered emission map. c) $g^{(2)}_{\mathrm{CL}}(\tau)$ function of the nano diamond before (τ = 32 ± 1.9 ns) and after (τ_t = 19 ± 2.5 ns) gold nanotriangle deposition. We have that $\tau \gg \tau_t$.

Bibliography

[1] Luiz Fernando Zagonel, Stefano Mazzucco, Marcel Tencé, Katia March, Romain Bernard, Benoît Laslier, Gwénolé Jacopin, Maria Tchernycheva, Lorenzo Rigutti, Francois H Julien, Rudeesun Songmuang, and Mathieu Kociak. Nanometer scale spectral imaging of quantum emitters in nanowires and its correlation to their atomically resolved structure. Nano letters, 11(2):568–73, feb 2011.

[2] L. H. G. Tizei and M. Kociak. Spatially Resolved Quantum Nano-Optics of Single Photons Using an Electron Microscope. Physical Review Letters, 110(15):153604, April 2013. ISSN 0031-9007. doi: 10.1103/PhysRevLett.110.153604. URL `http://link.aps.org/doi/10.1103/PhysRevLett.110.153604`.

[3] Mark Fox. Optical Properties of Solids. Oxford University Press, 2001.

[4] Lukas Novotny and Bert Hecht. Principles of Nano-Optics. Cambridge University Press, 2012.

[5] B.R. Hanbury and R.Q. Twiss. Correlation between photons in two coherent beams of light. Nature (London), 178(1046), 1956.

[6] P Michler, a Kiraz, C Becher, W V Schoenfeld, P M Petroff, L Zhang, E Hu, and a Imamoglu. A quantum dot single-photon turnstile device. Science (New York, N.Y.), 290(5500):2282–5, December 2000. ISSN 0036-8075. doi: 10.1126/science.290.5500.2282. URL `http://www.ncbi.nlm.nih.gov/pubmed/11125136`.

[7] Charles Santori, Matthew Pelton, Glenn Solomon, Yseulte Dale, and Yoshihisa Yamamoto. Triggered Single Photons from a Quantum Dot. Physical Review Letters, 86(8):1502–1505, February 2001. ISSN 0031-9007. doi: 10.1103/PhysRevLett.86.1502. URL `http://link.aps.org/doi/10.1103/PhysRevLett.86.1502`.

[8] C.K. Hong, Z.Y. Ou, and L. Mandel. Measurement of subpicosecond time intervals between two photons by interference. Phys. Rev. Lett., 59(2044), 1987.

[9] Charles Santori, David Fattal, Jelena Vuckovic, Glenn S. Solomon, and Yoshihisa Yamamoto. Indistinguishable photons from a single-photon device. Nature, 419: 594–597, 2002.

[10] Benoit Mahler, Piernicola Spinicelli, Stephanie Buil, Xavier Quelin, Jean-Pierre Hermier, and Benoit Dubertret. Towards non-blinking colloidal quantum dots. Nat Mater, 7(8):659–664, 08 2008. URL http://dx.doi.org/10.1038/nmat2222.

[11] A. P. Alivisatos. Semiconductor cluster, nanocrystals, and quantum dots. Science, 271(5251):933–937, 1996.

[12] L. Rayleigh. Investigation in optics, with special reference to the spectroscope. Phil. Mag., 8(261-274, 403-411 and 477-486), 1879.

[13] Stefan W. Hell and Jan Wichmann. Breaking the diffraction resolution limit by stimulated emission : stimulated-emission-depletion fluorescence microscopy. Optics letters, 11:780, 1994.

[14] Stefan W. Hell. Far-field optical nanoscopy. Science, 316:1153–1158, 2007.

[15] Dominik Wildanger, Jeronimo R. Maze, and Stefan W. Hell. Diffraction unlimited all-optical recording of electron spin resonances. Phys. Rev. Lett., 107:017601, Jul 2011. doi: 10.1103/PhysRevLett.107.017601. URL http://link.aps.org/doi/10.1103/PhysRevLett.107.017601.

[16] Ludwig; Reimer. Scaning Electron Microscopy, volume 45 of Optical Sciences. Springer, 1998.

[17] L. Reimer and H. Kohl. Transmission Electron Microscope. Springer, 2008.

[18] B.G. Yacobi and D.B. Holt. Cathodoluminescence Microscopy of Inorganic Solids. Springer, 1990.

[19] David Pines. Collective Energy Losses in Solids. Reviews of Modern Physics, 28 (3), 1956.

[20] R.F. Egerton. Electron Energy-Loss Spectroscopy in the Electron Microscope. Springer, 1996.

[21] A. Rothwarf. Plasmon theory of electron-hole pair production: efficiency of cathode ray phosphors. Journal of Applied Physics, 44(2):752, 1973. ISSN 00218979. doi: 10.1063/1.1662257. URL http://link.aip.org/link/?JAP/44/752/1&Agg=doi.

[22] Zackaria Mahfoud, Arjen T. Dijksman, Clémentine Javaux, Pierre Bassoul, Anne-Laure Baudrion, Jérôme Plain, Benoît Dubertret, and Mathieu Kociak. Cathodoluminescence in a scanning transmission electron microscope: A nanometer-scale counterpart of photoluminescence for the study of ii–vi quantum dots. J. Phys. Chem. Lett., 4:4090 – 4094, 11/2013 2013. ISSN 1948-7185. doi: 10.1021/jz402233x.

[23] L F Zagonel, L Rigutti, G Jacopin, R Songmuang, and M Kociak. Visualizing highly localized luminescence in gan/aln heterostructures in nanowires. Nanotechnology, 23(45):455205, 2012.

[24] R Brouri, A Beveratos, J P Poizat, and P Grangier. Photon antibunching in the fluorescence of individual color centers in diamond. Optics letters, 25(17):1294–6, sep 2000.

[25] A. Beveratos, R. Brouri, J. Poizat, and P. Grangier. Bunching and anti bunching from single nv color centers in diamond. QCM C 3 Proceedings, 2001.

[26] Luc Museur, Eduard Feldbach, and Andrei Kanaev. Defect-related photoluminescence of hexagonal boron nitride. Phys. Rev. B, 78(155204), 2008.

[27] S. Meuret, L. H. G. Tizei, T. Cazimajou, R. Bourrellier, H. C. Chang, F. Treussart, and M. Kociak. Photon bunching in cathodoluminescence. Phys. Rev. Lett., 114: 197401, May 2015. doi: 10.1103/PhysRevLett.114.197401. URL `http://link.aps.org/doi/10.1103/PhysRevLett.114.197401`.

[28] Claude A Klein. Radiation ionization energies in semiconductors : Speculations about the role of plamons. Journal of the Physics Society of Japan Supp, 21, 1966.

[29] F. J. Garcia de Abajo. Optical excitations in electron microscopy. Review of Modern Physics, 82, 2009. URL `http://arxiv.org/pdf/0903.1669.pdf`.

[30] J. Nelayah, M. Kociak, O. Stephan, F. Javier Garcia de Abajo, M. Tencé, L. Henrard, D. Taverna, I. Pastoriza-Santos, L. M. Liz-Marzan, and C. Colliex. Mapping surface plasmons on a single metallic nanoparticle. Nature Physics, 3:348–353, 2007.

[31] M. Bosman, V. J. Keast, M. Wanabe, A. I. Maaroof, and M. B. Cortie. Mapping surface plasmons at the nanometer scale with an electron beam. Nanotechnology, 18(165505), 2007.

[32] N. Yamamoto, S. Ohtani, and F. Javier Garcia de Abajo. Gap and mie plasmons in individual silver nanospheres near a silver surface. Nano letters, 11:91–95, 2010.

[33] E. J. R. Vesseur, R. de Waele, M. Kuttge, and A. Polman. Direct observation of plasmoninc modes in au nanowires using high-resolution cathodoluminescence spectroscopy. Nano letters, 7(9):2843–2846, 2007.

[34] Olivia Nicoletti, Francisco de la Pena, Rowan K. Leary, Daniel J. Holland, Caterina Ducati, and Paul A. Midgley. Three-dimensional imaging of localized surface plasmon resonances of metal nanoparticles. Nature, 502(7469):80–84, 10 2013. URL `http://dx.doi.org/10.1038/nature12469`.

[35] Shu Fen Tan, Lin Wu, Ping Bai, Michel Bosman, and Christian A. Nijhuis. Quantum plasmon resonances controlled by molecular tunnel junctions. Science, 343: 1496–1499, 2014.

[36] Mark Fox. Quantum Optics: An Introduction. Oxford Master Series in Physics, 2006.

[37] N. Mizuochi, T. Makino, H. Kato, D. Takeuchi, M. Ogura, H. Okushi, M. Nothaft, P. Neumann, A. Gali, F. Jelezko, J. Wrachtrup, and S. Yamasaki. Electrically driven single-photon source at room temperature in diamond. Nat Photon, 6(5): 299–303, 05 2012. URL http://dx.doi.org/10.1038/nphoton.2012.75.

[38] R.Bourrellier, S.Meuret, L.Tizei, A. Zobelli, and M. Kociak. Single photon emitter in the uv range. submitted, 2015.

[39] Andreas Jechow, Michael Seefeldt, Henning Kurzke, Axel Heuer, and Ralf Menzel. Enhanced two-photon excited fluorescence from imaging agents using true thermal light. Nat Photon, 7(12):973–976, 12 2013. URL http://dx.doi.org/10.1038/nphoton.2013.271.

[40] M.Asif Khan, A. Bhattarai, J. N. Kuznia, and D. T. Olson. High electron mobility transistor based on a gan-al x ga1-x n heterojunction. Applied Physics Letters, 63:1214, 1993.

[41] Piprek, editor. Nitride Semiconductor Devices. WILEY-VCH Verlag, 2007.

[42] Shuji Nakamura, Takashi Mukai, and Masayuki Senoh. Cendela-class high-brightness ingan/algan double-heterostructure blue-light-emitting diodes. Applied Physics Letters, 64:1687–1689, 1994.

[43] P. Lefebvre and B. Gayral. Optical properties of gan/aln quantum dots. C.R. Physique, 9:816–829, 2008.

[44] D. E. Chang, A. S. Sørensen, P. R. Hemmer, and M. D. Lukin. Quantum optics with surface plasmons. Phys. Rev. Lett., 97:053002, Aug 2006. doi: 10.1103/PhysRevLett.97.053002. URL http://link.aps.org/doi/10.1103/PhysRevLett.97.053002.

[45] A. V. Akimov, A. Mukherjee, C. L. Yu, D. E. Chang, A. S. Zibrov, P. R. Hemmer, H. Park, and M. D. Lukin. Generation of single optical plasmons in metallic nanowires coupled to quantum dots. Nature, 450(7168):402–406, 11 2007. URL http://dx.doi.org/10.1038/nature06230.

[46] Gilles Nogues, Quentin Merotto, Guillaume Bachelier, Eun Hye Lee, and Jin Dong Song. Fabrication and tuning of plasmonic optical nanoantennas around droplet epitaxy quantum dots by cathodoluminescence. Applied Physics Letters, 102(23):231112, 2013. doi: http://dx.doi.org/10.1063/1.4809831. URL http://scitation.aip.org/content/aip/journal/apl/102/23/10.1063/1.4809831.

[47] Stefan Schietinger, Michael Barth, Thomas Aichele, and Olivier Benson. Plasmon-enhenced single photon emission from a nanoassembled metal-diamond hybrid structure at room temperature. Nano letters, 9(4):1694–1698, 2009.

[48] R. Marty, A. Arbouet, V. Paillard, C. Girard, and G. Colas des Francs. Photon antibunching in the optical near field. Phys. Rev. B, 82:081403, Aug 2010. doi: 10.1103/PhysRevB.82.081403. URL http://link.aps.org/doi/10.1103/PhysRevB.82.081403.

[49] U. Hohenester and A. Trügler. Mnpbem - a matlab toolbox for the simulation of plasmonic nanoparticles. Computer Physics Communication, 183:370–381, 2012.

[50] U. Hohenester. Simulation electron energy loss spectroscopy with the mnpbem toolbox. Computer Physics Communication, 185:1177–1187, 2014.

[51] L. Reimer. Scanning Electron Microscopy. Springer, 1998.

[52] G. A. Wolff, R. A. Hebert, and J. D. Broder. Electroluminescence of gap. Phys. Rev., 100:1144–1145, Nov 1955. doi: 10.1103/PhysRev.100.1144. URL http://link.aps.org/doi/10.1103/PhysRev.100.1144.

[53] A. Muller, E. B. Flagg, P. Bianucci, X. Y. Wang, D. G. Deppe, W. Ma, J. Zhang, G. J. Salamo, M. Xiao, and C. K. Shih. Resonance fluorescence from a coherently driven semiconductor quantum dot in a cavity. Phys. Rev. Lett., 99:187402, Nov 2007. doi: 10.1103/PhysRevLett.99.187402. URL http://link.aps.org/doi/10.1103/PhysRevLett.99.187402.

[54] Kenji Watanabe, Takashi Taniguchi, and Hisao Kanda. Direct-bandgap properties and evidence for ultraviolet lasing of hexagonal boron nitride single crystal. Nat Mater, 3(6):404–409, 06 2004. URL http://dx.doi.org/10.1038/nmat1134.

[55] Yoichi Kubota, Kenji Watanabe, Osamu Tsuda, and Takashi Taniguchi. Deep ultraviolet light-emitting hexagonal boron nitride synthesized at atmospheric pressure. Science, 317(5840):932–934, 2007. doi: 10.1126/science.1144216. URL http://www.sciencemag.org/content/317/5840/932.abstract.

[56] Abbas Mohtashami and A Femius Koenderink. Suitability of nanodiamond nitrogen–vacancy centers for spontaneous emission control experiments. New Journal of Physics, 15(043017), 2013.

[57] John Lambe and Clifford Klick. Model for luminesence and photoconductivity in the sulfides. Physical Review, 98(4):909–914, 1955.

[58] H. A. Klasens. Transfer of energy between centers in zinc sulphide phosphors. Nature, 158:306–307, 1946.

[59] F. Williams. Donor-acceptor pairs in semiconductors. Phys. Stat. Sol., 25:493–512, 1968.

[60] Jack Myers. Photosynthesis. eugene rabinowitch and govindjee. Science, 169 (3948):848–849, 1970. doi: 10.1126/science.169.3948.848. URL `http://www.sciencemag.org/content/169/3948/848.short`.

[61] Licensed under CC BY-SA 3.0 via Wikimedia Commons. "franck condon diagram" by samoza, 2015. URL `http://commons.wikimedia.org/wiki/File:Franck_Condon_Diagram.svg#/media/File:Franck_Condon_Diagram.svg`.

[62] N. Bohr. Discussion with einstein on epistemological problems in atomic physics. In Paul Arthur Shilpp, editor, Albert-Einstein, philosopher-scientist. Harper, 1949.

[63] E. Schrodinger. Are there quantum jumps ? part ii. British Journal for the Philosophy of Science, 3(11):233, 1952.

[64] J. S. Bell. On the einstein podolsky rosen paradox. Physics, 1(3):195–200, 1964.

[65] Claude Cohen-Tannoudji, Bernard Diu, and Frack Laloë. Mécanique Quantique I. Collection Enseignement des Sciences. Hermann, 2007.

[66] M. Brune, F. Schmidt-Kaler, A. Maali, J. Dreyer, E. Hagley, J. M. Raimond, and S. Haroche. Quantum rabi oscillation : A direct test of field quantization in a cavity. Physical Review Letters, 76(11):1800, 1996.

[67] Serge Haroche. Controlling photons in a box and exploring the quantum to classical boundary. In The Nobel Prize Fundation, editor, Nobel Lecture. The Nobel Prize Fundation, 2012.

[68] D. M. Meekhof, C. Monroe, B. E. King, W. M. Itano, and D. J. Wineland. Generation of nonclassical motional states of a trapped atom. Phys. Rev. Lett., 76(11): 1796, 1996.

[69] Alain Aspect, Philippe Grangier, and Gérard Roger. Experimental tests of realistic local theories via bell's theorem. Physical Review Letters, 47(7), 1981.

[70] Alain Aspect, Philippe Grangier, and Gérard Roger. Experimental realization of einstein-podolsky-rosen-bohm gedankenexperiment : A violation of bell's inequalities. Phys. Rev. Lett., 49(2), 1982.

[71] Alain Aspect and Jean Dalibard abd Gérard Roger. Experimental test of bell's inequalities using time-varying analyzers. Phys. Rev. Lett., 49(1804), 1982.

[72] A. Einstein, B. Podolsky, and N. Rosen. Can quantum-mechanical description of phyical reality be consider complete ? Physical Review, 47:777–780, 1935.

[73] R. P. Feynman. Simulating physics with computers. International Journal of Theoretical Physics, 21:467–488, 1982.

[74] Quantum Theory, the Chruch-Turing principle and universal quantum computer, volume 400, 1996. The Royal Society A.

[75] C.H. Bennett and G. Brassard. Quantum cryptography : Public key distributionand coin tossing. In Bangladore : IEE International Conference on Computers, Systems and Signal Processing, page 175, 1984.

[76] Pieter Kok, W. J. Munro, Kae Nemoto, T. C. Ralph, Jonathan P. Dowling, and G. J. Milburn. Linear optical quantum computing with photonic qubits. Rev. Mod. Phys., 79:135–174, Jan 2007. doi: 10.1103/RevModPhys.79.135. URL http://link.aps.org/doi/10.1103/RevModPhys.79.135.

[77] H. J. Kimble, M. Dagenais, and L. Mandel. Photon antibunching in resonance fluorescence. Phys. Rev. Lett., 39:691–695, Sep 1977. doi: 10.1103/PhysRevLett.39.691. URL http://link.aps.org/doi/10.1103/PhysRevLett.39.691.

[78] C Kurtsiefer, S Mayer, P Zarda, and H Weinfurter. Stable solid-state source of single photons. Physical review letters, 85(2):290–3, July 2000. ISSN 1079-7114. URL http://www.ncbi.nlm.nih.gov/pubmed/10991265.

[79] Beveratos, A., Kühn, S., Brouri, R., Gacoin, T., Poizat, J.-P., and Grangier, P. Room temperature stable single-photon source. Eur. Phys. J. D, 18(2):191–196, 2002. doi: 10.1140/epjd/e20020023. URL http://dx.doi.org/10.1140/epjd/e20020023.

[80] Edo Waks, Kyo Inoue, Charles Santori, Divid Fattal, Jelena Vuckovic, Glenn S. Solomon, and Yoshihisa Yamamoto. Secure communication : Quantum cryptography with a photon turnstile. Nature, 420:762, 2002.

[81] Alexios Beveratos, Rosa Brouri, Thierry Gacoin, André Villing, Jean-Philippe Poizat, and Philippe Grangier. Single photon quantum cryptography. Phys. Rev. Lett., 89:187901, Oct 2002. doi: 10.1103/PhysRevLett.89.187901. URL http://link.aps.org/doi/10.1103/PhysRevLett.89.187901.

[82] H. Heinzelmann and D.W. Pohl. Scanning near-field optical microscopy. Applied Physics A, 59:89–101, 1994.

[83] Eric Betzig and Jay K. Trautman. Near-field optics: Microscopy, spectroscopy, and surface modification beyond the diffraction limit. Science, 257(5067):189–195, 1992. doi: 10.1126/science.257.5067.189. URL http://www.sciencemag.org/content/257/5067/189.abstract.

[84] Lukas Novotny and Stephan J. Stranick. Near-field optical microscopy and spectroscopy wth pointed probes. Annu. Rev. Phys. Chem., 57(303-31), 2006.

[85] Zee Hwan Kim, Bing Liu, and Stephen R. Leone. Nanometer-scale optical imaging of epitaxially grown gan and inn islands using apertureless near-field microscopy†. The Journal of Physical Chemistry B, 109(17):8503–8508, 2005. doi: 10.1021/jp047425i. URL http://dx.doi.org/10.1021/jp047425i. PMID: 16851999.

[86] H. F. Hamann, A. Gallagher, and D. J. Nesbitt. Enhanced sensitivity near-field scanning optical microscopy at high spatial resolution. Applied Physics Letters, 73(1469), 1998.

[87] Fritz Keilmann. Scattering-type near-field optical microscopy. Journal of Electron Microscopy, 53(2):187–192, 2004. doi: 10.1093/jmicro/53.2.187. URL http://jmicro.oxfordjournals.org/content/53/2/187.abstract.

[88] S. W. Hell and M. Kroug. Ground-state-depletion fluorscence microscopy : a concept for breaking the diffraction resolution limit. Appl. Phys B, 60(495-497), 1995.

[89] Eva Rittweger, Kyu Young Han, Scott E. Irvine, Christian Eggeling, and Stefan W. Hell. Sted microscopy reveals crystal colour centres with nanometric resolution. Nat Photon, 3(3):144–147, 03 2009. URL http://dx.doi.org/10.1038/nphoton.2009.2.

[90] Dominik Wildanger, Brian R. Patton, Heiko Schill, Luca Marseglia, J. P. Hadden, Sebastian Knauer, Andreas Schönle, John G. Rarity, Jeremy L. O'Brien, Stefan W. Hell, and Jason M. Smith. Solid immersion facilitates fluorescence microscopy with nanometer resolution and sub-ångström emitter localization. Advanced Materials, 24(44):OP309–OP313, 2012. ISSN 1521-4095. doi: 10.1002/adma.201203033. URL http://dx.doi.org/10.1002/adma.201203033.

[91] Marta Fernandez-Suarez and Alice Y. Ting. Fluorescent probes for super-resolution imaging in living cells. Nat Rev Mol Cell Biol, 9(12):929–943, 12 2008. URL http://dx.doi.org/10.1038/nrm2531.

[92] Aurélien Cuche, Aurélien Drezet, Yannick Sonnefraud, Orestis Faklaris, François Treussart, Jean-François Roch, and Serge Huant. Near-field optical microscopy

with a nanodiamond-based single-photon tip. Opt. Express, 17(22):19969–19980, Oct 2009. doi: 10.1364/OE.17.019969. URL http://www.opticsexpress.org/abstract.cfm?URI=oe-17-22-19969.

[93] R.F. Egerton, P. Li, and M. Malac. Radiation damage in the tem and sem. Micron, 35:399–409, 2004.

[94] S. J. Pennycook and P. D. Nellist. Scanning transmission electron microscopy : imaging and analysis. Springer, 2011.

[95] Mathieu Kociak and Odile Stéphan. Mapping plasmons at the nanometer scale in an electron microscope. Chem Soc Rev, 43:386–3883, 2014.

[96] H. Raether. Excitation of plasmons and Interband Transitions by electrons. Springer, 1980.

[97] Roger H. French, Harald Mullejans, and David J. Jones. Optical properties of aluminium oxide : Determined from vacuum ultraviolet and electron energy-loss spectroscopies. Journal of the American Ceramic Society, 81(10):2549–57, 1998.

[98] Hiroshi Watanabe. Experimental evidence for the collective nature of the characteristic energy loss of electrons in solids - studies on the dispersion relation of plasma frequency-. Journal of the Physical Society of Japan, 11(2):112–119, 1956. doi: 10.1143/JPSJ.11.112. URL http://dx.doi.org/10.1143/JPSJ.11.112.

[99] P. E. Batson. Surface plasmon coupling in cluster of small spheres. Physical Review Letters, 49(13):936–940, 1982.

[100] D. Ugarte, C. Colliex, and P. Trebbia. Surface-plasmon and interface-plasmon modes on small semiconducting spheres. Phys Rev B, 45:4332–4343, 1992.

[101] A. Gloter, A. Douiri, M. Tencé, and C. Colliex. Improving energy resolution of eels spectra : an alternative to the monochromator solution. Ultramicroscopy, 96: 385–400, 2003.

[102] D. Rossouw, M. Couillard ans J. Vickery, E. Kumacheva, and G. A. Botton. Multipolar plasmonic resonances in silver nanowire antennas imaged with subnanometer electron probe. Nano letters, 11:1499–1504, 2011.

[103] F. J. Garcia de Abajo and M. Kociak. Probing the photonic local density of states with electron energy loss spectroscopy. Physical Review Letters, 100(106804), 2008.

[104] Arthur Losquin. Surface Plasmon modes revealed by fast electron based spectroscopies : from simple model to complex systems. PhD thesis, Université Paris Sud, 2013.

[105] F. J. Garcia de Abajo and J. Aizpurua. Numerical simulation of electro energy loss near inhomogeneous dielectrics. Phys Rev B, 56(24):15873–15884, 1997.

[106] Guillaume Boudarham and Mathieu Kociak. Modal decomposition of the local electromagnetic density of states and spatially resolved electron energy loss probability in terms of geometric modes. Physical Review B, 85(245447), 2012.

[107] Guillaume Boudarham. Nanooptique avec des électrons rapides ; métamateriaux, formulation modale de la EMLDOS pour des systémes plasmoniques. PhD thesis, Université Pierre et Marie Curie, 2011.

[108] A. Losquin, L.F. Zagonel, V. Myroshnychenko, B. Rodriguez-Gonzalez, M. Tencé, L. Scarabelli, J. Förstner, L. M. Liz-Marzan, F. J. Garcia de Abajo, O. Stephan, and M Kociak. Unveiling nanometer scale extinction and scattering phenomena through combined electron energy loss spectrosopy and cathodoluminescence measurement. Nano-Letters, 15:1229–1237, 2015.

[109] Naohiko Kawaski, Sophie Meuret, and Mathieu Kociak. Eels and cl measurement on systematic lithographic nanotriangle. in preparation.

[110] Uwe Jahn, Jelena Ristic, and Enrique Calleja. Cathodoluminescence spectroscopy and imaging of gan/(al,ga)n nanocolumns containing quantum disks. Applied Physics Letters, 90:161117, 2007.

[111] William Shockley. Problems related to p-n junctions in silicon. Solid-State Electronics, 2(1):35–67, 1961.

[112] Claude A Klein. Bandgap dependence and related features of radiation ionization energies in semiconductors. Journal of Applied Physics, 39(4):2029–2038, 1968.

[113] Piotr A. Rodnyi. Choice of compounds with fast core-valence transitions. MRS Proceedings, 348, 1994.

[114] W. Van Roosbroeck. Theory of the yield and fano factor of electron-hole pairs generated in semiconductors by high-energy particles. Physical Review, 139(5A): A1702 – A1716, 1965.

[115] D.J. Robbins. On predicting the maximum efficiency of phosphor systems excited by ionizing radiation. J. Electrochem. Soc., 127(12):2694–2702, 1980.

[116] R H Bartrama and A Lempickib. Efficiency of electron-hole pair production in scintillators. Journal of Luminescence, 68:225–240, 1996.

[117] Richard A. Ferrell. Predicted radiation of plasma oscillations in metal films. Physical Review, 111(5), 1958.

[118] Luke Campbell, Fei Gao, Ram Devanathan, and William J. Weber. Model of plasmon decay for electron cascade simulation. Nuclear Instruments and Methods in Physics Research A, 579:454–457, 2007.

[119] C.T. Foxon. Three decades of molecular beam epitaxy. Journal of Crystal Growth, 251(1–4):1 – 8, 2003. ISSN 0022-0248. doi: http://dx.doi.org/10.1016/S0022-0248(02)02396-5. URL http://www.sciencedirect.com/science/article/pii/S0022024802023965. Proceedings of the Twelfth International Conference on Molecular Beam Epitaxy.

[120] B. Daudin, F. Widmann, G. Feuillet, Y. Samson, M. Arlery, and J. L. Rouvière. Stranski-krastanov growth mode during the molecular beam epitaxy of highly strained gan. Phys. Rev. B, 56:R7069–R7072, Sep 1997. doi: 10.1103/PhysRevB.56.R7069. URL http://link.aps.org/doi/10.1103/PhysRevB.56.R7069.

[121] M. J. Ludowise. Metalorganic chemical vapor deposition of iii-v semiconductors. Journal of Applied Physics, 58(8):R31–R55, 1985. doi: http://dx.doi.org/10.1063/1.336296. URL http://scitation.aip.org/content/aip/journal/jap/58/8/10.1063/1.336296.

[122] L. H. G. Tizei, S. Meuret, K. March, K. Hestroffer, T. Auzelle, B. Daudin, and M. Kociak. A polarity-driven nanometric luminescence asymetry in aln/gan heterostructures. Applied Physics Letters, 105(143106), 2014.

[123] N. Yamamoto, S. Bhunia, and Y. Watanabe. Polarized cathodoluminescence study of inp nanowires by transmission electron microscopy. Applied Physics Letters, 88 (153106), 2006.

[124] L. H. G. Tizei and M. Kociak. Spectrally and spatially resolved cathodoluminescence of nanodiamonds: local variations of the NV(0) emission properties. Nanotechnology, 23(17):175702, May 2012. ISSN 1361-6528. doi: 10.1088/0957-4484/23/17/175702. URL http://www.ncbi.nlm.nih.gov/pubmed/22481219.

[125] Karine Hestroffer. Croissance et caracterisation de nanofils de GaN et d'hétérostructure filaires de GaN/AlN. Material science, Université de Grenoble, https://tel.archives-ouvertes.fr/tel-00863433v2, 2012.

[126] Fabio Bernardini, Vincenzo Fiorentini, and David Vanderbilt. Spontaneous polarization and piezoelectric constants of iii-v nitrides. Phys. Rev. B, 56:R10024–R10027, Oct 1997. doi: 10.1103/PhysRevB.56.R10024. URL http://link.aps.org/doi/10.1103/PhysRevB.56.R10024.

[127] D. Camacho Mojica and Yann-Michel Niquet. Stark effect in gan/aln nanowire heterostructures: Influence of strain relaxation and surface states. Phys. Rev. B, 81:195313, May 2010. doi: 10.1103/PhysRevB.81.195313. URL http://link.aps.org/doi/10.1103/PhysRevB.81.195313.

[128] J. Glazer, R. Ramesh, M. R. Hilton, and M. Sarika. Comparison of convergent-beam electron diffraction methods for determination of foil thickness. Phil. Mag., 52(L59), 1985.

[129] B. Damilano, N. Granjean, F. Semond, J. Massies, and M. Leroux. From visible to white light emission by gan quantum dots on si(111) substrate. Applied Physics Letters, 75:962, 1999.

[130] F. Widmann, J. Simon, B. Daudin, G. Feuillet, J. L. Rouvière, N. T. Pelekanos, and G. Fishman. Blue-light emission from gan self-assembled quantum dots due to giant piezoelectric effect. Phys. Rev. B, 58:R15989–R15992, Dec 1998. doi: 10.1103/PhysRevB.58.R15989. URL http://link.aps.org/doi/10.1103/PhysRevB.58.R15989.

[131] Wei Guo, Meng Zhan, Pallb Bhattcharya, and Junseok Heo. Auger recombination in iii-nitride nanowires and its effect on nanowire light-emitting diode characteristics. Nano letters, 11:1434–1438, 2011.

[132] Fabio Bernardini, Vincenzo Fiorentini, and David Vanderbilt. Spontaneous polarization and piezoelectric constants of iii-v nitrides. Phys. Rev. B, 56:R10024–R10027, Oct 1997. doi: 10.1103/PhysRevB.56.R10024. URL http://link.aps.org/doi/10.1103/PhysRevB.56.R10024.

[133] M. Leroux, N. Grandjean, M. Laügt, J. Massies, B. Gil, P. Lefebvre, and P. Bigenwald. Quantum confined stark effect due to built-in internal polarization fields in (al,ga)n/gan quantum wells. Phys. Rev. B, 58:R13371–R13374, Nov 1998. doi: 10.1103/PhysRevB.58.R13371. URL http://link.aps.org/doi/10.1103/PhysRevB.58.R13371.

[134] D. A. B. Miller, D. S. Chemla, T. C. Damen, A. C. Gossard, W. Wiegmann, T. H. Wood, and C. A. Burrus. Band-edge electroabsorption in quantum well structures: The quantum-confined stark effect. Phys. Rev. Lett., 53:2173–2176, Nov 1984. doi: 10.1103/PhysRevLett.53.2173. URL http://link.aps.org/doi/10.1103/PhysRevLett.53.2173.

[135] S. A. Empedocles and M. G. Bawendi. Quantum-confined stark effect in single cdse nanocrystallite quantum dots. Science, 278(5346):2114–2117, 1997.

[136] L.F. Zagonel, L.H. G. Tizei, G.Z. Vitiello, G. Jacopin, L. Rigutti, M. Tchernycheva, F.H. Julien, R. Songmuang, F. de la Peña, T. Ostasevicius, C. Ducati, P. A. Midgley, and M. Kociak. Nanometer scale manoitoring of the quantum confined stark effect and elission efficency droop in multiple gan/aln quantum disks in nanowires. in preparation, 2015.

[137] E.A. Muljarov and R. Zimmermann. Dephasing in quantum dots : quadratic coupling to acoustic phonons. Physical Review Letters, 93(237401), 2004.

[138] A. Berthelot, G. Cassabois, C. Voisin, C. Delalande, R. Feirreira, Ph. Rossignol, J. Skiba-Szymanska, R. Kolodka, A. I. Tartakovskii, M. Hopkinson, and M.S. Skolnick. Voltage-controlled motional narrowing in a semiconductor quantum dot. New Journal of Physics, 11(093032), 2009.

[139] C. Javaux, B. Mahler, B. Dubertret, A. Shabaev, A. V. Rodina, Al. L. Efros, D. R. Yakovlev, F. Liu, M. Bayer, G. Camps, L. Biadala, S. Buil, X. Quelin, and J-P. Hermier. Thermal activation of non-radiative auger recombination in charged colloidal nanocrystals. Nat Nano, 8(3):206–212, 03 2013. URL `http://dx.doi.org/10.1038/nnano.2012.260`.

[140] Botao Ji, Emerson Giovanelli, Benjamin Habert, Piernicola Spinicelli, Michel Nasilowski, Xiangzhen Xu, Nicolas Lequeux, Jean-Paul Hugonin, Francois Marquier, Jean-Jacques Greffet, and Benoit Dubertret. Non-blinking quantum dot with a plasmonic nanoshell resonator. Nat Nano, 10(2):170–175, 02 2015. URL `http://dx.doi.org/10.1038/nnano.2014.298`.

[141] A.M. Zaitsev. Optical Properties of Diamonds. Springer, 2001.

[142] L. Childress, M. V. Gurudev Dutt, J. M. Taylor, A. S. Zibrov, F. Jelezko, J. Wrachtrup, P. R. Hemmer, and M. D. Lukin. Coherent dynamics of coupled electron and nuclear spin qubits in diamond. Science, 314(5797):281–285, 2006. doi: 10.1126/science.1131871. URL `http://www.sciencemag.org/content/314/5797/281.abstract`.

[143] G. D. Fuchs, V. V. Dobrovitski, R. Hanson, A. Batra, C. D. Weis, T. Schenkel, and D. D. Awschalom. Excited-state spectroscopy using single spin manipulation in diamond. Phys. Rev. Lett., 101:117601, Sep 2008. doi: 10.1103/PhysRevLett.101.117601. URL `http://link.aps.org/doi/10.1103/PhysRevLett.101.117601`.

[144] H. Watanabe, T. Kitamura, S. Nakashima, and S. Shikata. Cathodoluminescence characterization of a nitrogen-doped homoepitaxial diamond thin film. Journal of Applied Physics, 105(9):093529, 2009. doi: http://dx.doi.org/10.1063/1.3117214.

URL http://scitation.aip.org/content/aip/journal/jap/105/9/10.1063/1.3117214.

[145] L. H. Robins, L. P. Cook, E. N. Farabaugh, and A. Feldman. Cathodoluminescence of defects in diamond films and particles grown by hot-filament chemical-vapor deposition. Phys. Rev. B, 39:13367–13377, Jun 1989. doi: 10.1103/PhysRevB.39.13367. URL http://link.aps.org/doi/10.1103/PhysRevB.39.13367.

[146] N. Yamamoto, J. C. H. Spence, and D. Fathy. Cathodoluminescence and polarization studies from individual dislocations in diamond. Philosophical Magazine Part B, 49(6):609–629, 1984. doi: 10.1080/13642818408227648. URL http://dx.doi.org/10.1080/13642818408227648.

[147] June 2013. URL http://phys.org/news/2013-06-spintronics-approach-enables-quantum-
html.

[148] Paul R. Edwards, David Sleith, Alastair W. Wark, and Robert W. Martin. Mapping localized surface plasmons within silver nanocubes using cathodoluminescence hyperspectral imaging. The Journal of Physical Chemistry C, 115(29):14031–14035, 2011. doi: 10.1021/jp202083p. URL http://dx.doi.org/10.1021/jp202083p. PMID: 23710265.

[149] Toon Coenen, Felipe Bernal Arango, A. Femius Koenderink, and Albert Polman. Directional emission from a single plasmonic scatterer. Nat Commun, 5, 02 2014. URL http://dx.doi.org/10.1038/ncomms4250.

[150] Ondrej L. Krivanek, Matthew F. Chisholm, Valeria Nicolosi, Timothy J. Pennycook, George J. Corbin, Niklas Dellby, Matthew F. Murfitt Christopher S. Own, Zoltan S. Szilagyi, Mark P. Oxley, Sokrates T. Pantelides, and Stephen J. Pennycook. Atom-by-atom structural and chemical analysis by annular dark-field electron microscopy. Nature, 464(25):571–574, 2010.

[151] I Rech, A. Ingargiola, R. Spinelli, S. Marangoni, I. Labanca, M. Ghioni, and S. Cova. A new model for optical crosstalk in single-photon avalanche diodes arrays. In 5th International Conference on New Developments in Photodetection, 2008.

[152] Ivan Rech, Antonino Ingargiola, Roberto Spinelli, Ivan Labanca, Stefano Marangoni, Massimo Ghioni, and Sergio Cova. Optical crosstalk in single photon avalanche diode arrays: a new complete model. Opt. Express, 16(12):8381–8394, Jun 2008. doi: 10.1364/OE.16.008381. URL http://www.opticsexpress.org/abstract.cfm?URI=oe-16-12-8381.

[153] R. Loudon. The Quantum theory of light. Oxford University Press, 1983.

[154] A. Beveratos, R. Brouri, J. Poizat, and P. Grangier. Bunching and anti bunching from single nv color centers in diamond. arXiv, arXiv:quant-ph/0010044, 2000.

[155] A Beveratos. Réalisation expérimental d'une source de photons uniques par fluorescence de centres colorés dans le diamant. Application à la cryptographie quantique. PhD thesis, Université Paris XI, 2002.

[156] Jelle Storteboom, Philip Dolan, Stefania Castelletto, Xiangping Li, and Min Gu. Lifetime investigation of single nitrogen vacancy centres in nanodiamonds. Opt. Express, 23(9):11327–11333, May 2015. doi: 10.1364/OE.23.011327. URL http://www.opticsexpress.org/abstract.cfm?URI=oe-23-9-11327.

[157] Adam Gali. Theory of the neutral nitrogen-vacancy center in diamond and its application to the realization of a qubit. Phys. Rev. B, 79:235210, Jun 2009. doi: 10.1103/PhysRevB.79.235210. URL http://link.aps.org/doi/10.1103/PhysRevB.79.235210.

[158] Dingwei Zheng. Study and manipulation of photoluminescent NV color center in diamond. Theses, École normale supérieure de Cachan - ENS Cachan, October 2010. URL https://tel.archives-ouvertes.fr/tel-00595302.

[159] Luiz Henrique Galvão Tizei, Sophie Meuret, Sounderya Nagarajan, François Treussart, Chia-Yi Fang, Huan-Cheng Chang, and Mathieu Kociak. Spatially and spectrally resolved cathodoluminescence with fast electrons: A tool for background subtraction in luminescence intensity second-order correlation measurements applied to subwavelength inhomogeneous diamond nanocrystals. Physica Status Solidi (a), 210(10):2060–2065, October 2013. ISSN 18626300. doi: 10.1002/pssa.201300044. URL http://doi.wiley.com/10.1002/pssa.201300044.

[160] Yoshitaka Taniyasu, Makoto Kasu, and Toshiki Makimoto. An aluminium nitride light-emitting diode with a wavelength of 210[thinsp]nanometres. Nature, 441 (7091):325–328, 05 2006. URL http://dx.doi.org/10.1038/nature04760.

[161] Asif Khan, Krishnan Balakrishnan, and Tom Katona. Ultraviolet light-emitting diodes based on group three nitrides. Nat Photon, 2(2):77–84, 02 2008. URL http://dx.doi.org/10.1038/nphoton.2007.293.

[162] B. Arnaud, S. Lebègue, P. Rabiller, and M. Alouani. Huge excitonic effects in layered hexagonal boron nitride. Phys. Rev. Lett., 96:026402, Jan 2006. doi: 10.1103/PhysRevLett.96.026402. URL http://link.aps.org/doi/10.1103/PhysRevLett.96.026402.

[163] Andrea Marini. *Ab Initio* finite-temperature excitons. Phys. Rev. Lett., 101: 106405, Sep 2008. doi: 10.1103/PhysRevLett.101.106405. URL `http://link.aps.org/doi/10.1103/PhysRevLett.101.106405`.

[164] Romain Bourrellier, Michele Amato, Luiz Henrique Galvão Tizei, Christine Giorgetti, Alexandre Gloter, Malcolm I. Heggie, Katia March, Odile Stéphan, Lucia Reining, Mathieu Kociak, and Alberto Zobelli. Nanometric resolved luminescence in h-bn flakes: Excitons and stacking order. ACS Photonics, 1(9):857–862, 2014. doi: 10.1021/ph500141j. URL `http://dx.doi.org/10.1021/ph500141j`.

[165] Nasim Alem, Rolf Erni, Christian Kisielowski, Marta D. Rossell, Will Gannett, and A. Zettl. Atomically thin hexagonal boron nitride probed by ultrahigh- resolution transmission electron microscopy. Phys Rev B, 80(15):155425, 2009.

[166] Ashley L. Gibb, Nasim Alem, Jian-Hao Chen, Kristopher J. Erickson, Jim Ciston, Abhay Gautam, Martin Linck, and Alex Zettl. Atomic resolution imaging of grain boundary defects in monolayer chemical vapor deposition- grown hexagonal boron nitride. J. Am. Chem. Soc., 135(18):6758–6761, 2013.

[167] Jamie H. Warner, Mark H. Rümmeli, Alicja Bachmatiuk, and Bernd Büchner. Atomic resolution imaging and topography of boron nitride sheets produced by chemical exfoliation. ACS Nano, 4(3):1299–1304, 2010.

[168] Nasim Alem, Quentin M. Ramasse, Che R. Seabourne, Oleg V. Yazyev, Kris Erickson, Michael C. Sarahan, Christian Kisielowski, Andrew J. Scott, Steven G. Louie, and A. Zettl. Subangstrom edge relaxations probed by electron microscopy in hexagonal boron nitride. Phys. Rev. Lett., 109(20):205502, 2012.

[169] Kazuhiko Hara, Xin Liu, Manabu Yamauchi, Yasumasa Kawanishi, Hiroko Kominami, and Yoichiro Nakanishi. Effects of annealing on 320 nm cathodo- luminescence from hexagonal boron nitride powders. Phys Status Solidi C, 8:2509–2511, 2011.

[170] Luc Museur, Demetrios Anglos, Jean-Pierre Petitet, Jean-Pierre Michel, and Andrei V. Kanaev. Photoluminescence of hexagonal boron nitride : Effect of surface oxidation under uv-laser irradiation. Journal of Luminescence, 127(595-600), 2007.

[171] Romain Bourrellier. Luminescence at Defects in h-BN : Excitons at Stacking Faults and Single Photon Emitters. PhD thesis, Université Paris Sud, 2014.

[172] Long-Jyun Su, Chia-Yi Fang, Yu-Tang Chang, Kuan-Ming Chen, Yueh-Chung Yu, Jui-Hung Hsu, and Huan-Cheng Chang. Creation of high density ensembles of nitrogen-vacancy centers in nitrogen-rich type ib nanodiamonds. Nanotechnology,

24(31):315702, 2013. URL http://stacks.iop.org/0957-4484/24/i=31/a=315702.

[173] J. Botsoa, T. Sauvage, M.-P. Adam, P. Desgardin, E. Leoni, B. Courtois, F. Treussart, and M.-F. Barthe. Optimal conditions for nV^- center formation in type-1b diamond studied using photoluminescence and positron annihilation spectroscopies. Phys. Rev. B, 84:125209, Sep 2011. doi: 10.1103/PhysRevB.84.125209. URL http://link.aps.org/doi/10.1103/PhysRevB.84.125209.

[174] B. L. Morgan and L. Mandel. Measurement of photon bunching in a thermal light beam. Physical review letters, 16(22):1012–1015, 1966.

[175] Martin Blazek, Sebastien Hartmann, Andreas Molitor, and Wolfgang Elsaesser. Unifying intensity noise and second-order coherence properties of amplified spontaneous emission sources. Optics letters, 36(17):3455–7, 2011.

[176] D. W. Snoke. When should we say we have observed Bose condensation of excitons? Physica Status Solidi (B), 238(3):389–396, August 2003. ISSN 03701972. doi: 10.1002/pssb.200303151. URL http://doi.wiley.com/10.1002/pssb.200303151.

[177] Martin Winger, Thomas Volz, Guillaume Tarel, Stefano Portolan, Antonio Badolato, Kevin J. Hennessy, Evelyn L. Hu, Alexios Beveratos, Jonathan Finley, Vincenzo Savona, and Ata ç Imamoğlu. Explanation of photon correlations in the far-off-resonance optical emission from a quantum-dot˘cavity system. Phys. Rev. Lett., 103:207403, Nov 2009. doi: 10.1103/PhysRevLett.103.207403. URL http://link.aps.org/doi/10.1103/PhysRevLett.103.207403.

[178] Young-Shin Park, Yagnaseni Ghosh, Yongfen Chen, Andrei Piryatinski, Ping Xu, Nathan H. Mack, Hsing-Lin Wang, Victor I. Klimov, Jennifer. A. Hollingsworth, and Han Htoon. Super-poissonian statistics of photon emission from single cdse-cds core-shell nanocrystals coupled to metal nanostructures. Phys. Rev. Lett., 110:117401, Mar 2013. doi: 10.1103/PhysRevLett.110.117401. URL http://link.aps.org/doi/10.1103/PhysRevLett.110.117401.

[179] A Auffèves, D Gerace, S Portolan, A Drezet, and M França Santos. Few emitters in a cavity: from cooperative emission to individualization. New Journal of Physics, 13(9):093020, 2011. URL http://stacks.iop.org/1367-2630/13/i=9/a=093020.

[180] S. C. Kitson, P. Jonsson, J. G. Rarity, and P. R. Tapster. Intensity fluctuation spectroscopy of small numbers of dye molecules in a microcavity. Phys. Rev. A, 58:620–627, Jul 1998. doi: 10.1103/PhysRevA.58.620. URL http://link.aps.org/doi/10.1103/PhysRevA.58.620.

[181] A. Lebreton, I. Abram, R. Braive, I. Sagnes, I. Robert-Philip, and A. Beveratos. Unequivocal differentiation of coherent and chaotic light through interferometric photon correlation measurements. Phys. Rev. Lett., 110:163603, Apr 2013. doi: 10.1103/PhysRevLett.110.163603. URL http://link.aps.org/doi/10.1103/PhysRevLett.110.163603.

[182] Y.-S. Choi, M.T. Rakher, K.Hennessy, S.Strauf, and A.Badolato. Evolution of the onset of coherence in a family of photonic crystal nanolasers. Applied Physics Letters, 91(031108), 2007.

[183] John M Blatt, K.W. Böer, and Werner Brandt. Bose-Einstein Condensation of Excitons. Physical Review, 126(5):1691–1692, 1962.

[184] M Assmann, F Veit, M Bayer, M van der Poel, and J M Hvam. Higher-order photon bunching in a semiconductor microcavity. Science (New York, N.Y.), 325 (5938):297–300, July 2009. ISSN 1095-9203. doi: 10.1126/science.1174488. URL http://www.ncbi.nlm.nih.gov/pubmed/19608912.

[185] Robert Chapman and Taras Plakhotnik. Quantitative luminescence microscopy on nitrogen-vacancy centres in diamond: Saturation effects under pulsed excitation. Chemical Physics Letters, 507(1–3):190 – 194, 2011. ISSN 0009-2614. doi: http://dx.doi.org/10.1016/j.cplett.2011.03.057. URL http://www.sciencedirect.com/science/article/pii/S0009261411003265.

[186] Jui-Hung Hsu, Wei-De Su, Kai-Lin Yang, Yan-Kai Tzeng, and Huan-Cheng Chang. Nonblinking green emission from single h3 color centers in nanodiamonds. Applied Physics Letters, 98(19):193116, 2011. doi: http://dx.doi.org/10.1063/1.3591156. URL http://scitation.aip.org/content/aip/journal/apl/98/19/10.1063/1.3591156.

[187] T. Bretagnon, S. Kalliakos, P. Lefebvre, P. Valvin, B. Gil, N. Grandjean, A. Dussaigne, B. Damilano, and J. Massies. Time dependence of the photoluminescence of gan/aln quantum dots under high photoexcitation. Phys. Rev. B, 68:205301, Nov 2003. doi: 10.1103/PhysRevB.68.205301. URL http://link.aps.org/doi/10.1103/PhysRevB.68.205301.

[188] T. Bretagnon, P. Lefebvre, P. Valvin, R. Bardoux, T. Guillet, T. Taliercio, B. Gil, N. Grandjean, F. Semond, B. Damilano, A. Dussaigne, and J. Massies. Radiative lifetime of a single electron-hole pair in gan/aln quantum dots. Phys. Rev. B, 73: 113304, Mar 2006. doi: 10.1103/PhysRevB.73.113304. URL http://link.aps.org/doi/10.1103/PhysRevB.73.113304.

[189] A. Morel, P. Lefebvre, S. Kalliakos, T. Taliercio, T. Bretagnon, and B. Gil. Donor-acceptor-like behavior of electron-hole pair recombinations in low-dimensional (ga,in)n/gan systems. Phys. Rev. B, 68:045331, Jul 2003. doi: 10.1103/PhysRevB.68.045331. URL http://link.aps.org/doi/10.1103/PhysRevB.68.045331.

[190] P. Lefebvre, S. Kalliakos, T. Bretagnon, P. Valvin, T. Taliercio, B. Gil, N. Grandjean, and J. Massies. Observation and modeling of the time-dependent descreening of internal electric field in a wurtzite gan/$al_{0.15}ga_{0.85}N$ quantum well after high photoexcitation. Phys. Rev. B, 69:035307, Jan 2004. doi: 10.1103/PhysRevB.69.035307. URL http://link.aps.org/doi/10.1103/PhysRevB.69.035307.

[191] S. Kalliakos, T. Bretagnon, P. Lefebvre, T. Taliercio, B. Gil, N. Granjean, B. Damilano, A. Dussaigne, and J. Massies. Photoluminescence energy and linewidth in gan/aln stacking of quantum dot planes. Journal of Applied Physics, 96(1):180, 2004.

[192] G Liaugaudas, G Davies, K Suhling, R U A Khan, and D J F Evans. Luminescence lifetimes of neutral nitrogen-vacancy centres in synthetic diamond containing nitrogen. Journal of Physics: Condensed Matter, 24(43):435503, 2012. URL http://stacks.iop.org/0953-8984/24/i=43/a=435503.

[193] R. Bardoux, T. Guillet, P. Lefebvre, T. Taliercio, T. Bretagnon, S. Rousset, B. Gil, and F. Semond. Photoluminescence of single gan/aln hexagonal quantum dots on si(111): Spectral diffusion effects. Phys. Rev. B, 74:195319, Nov 2006. doi: 10.1103/PhysRevB.74.195319. URL http://link.aps.org/doi/10.1103/PhysRevB.74.195319.

[194] P. Corfdir, J. Ristić, P. Lefebvre, T. Zhu, D. Martin, A. Dussaigne, J. D. Ganière, N. Grandjean, and B. Deveaud-Plédran. Low-temperature time-resolved cathodoluminescence study of exciton dynamics involving basal stacking faults in a-plane gan. Applied Physics Letters, 94(20):201115, 2009. doi: http://dx.doi.org/10.1063/1.3142396. URL http://scitation.aip.org/content/aip/journal/apl/94/20/10.1063/1.3142396.

[195] P. Corfdir, P. Lefebvre, L. Balet, S. Sonderegger, A. Dussaigne, T. Zhu, D. Martin, J.-D. Ganière, N. Grandjean, and B. Deveaud-Plédran. Exciton recombination dynamics in a-plane (al,ga)n/gan quantum wells probed by picosecond photo and cathodoluminescence. Journal of Applied Physics, 107(4):043524, 2010. doi: http://dx.doi.org/10.1063/1.3305336. URL http://scitation.aip.org/content/aip/journal/jap/107/4/10.1063/1.3305336.

[196] M. L. Nakarmi, N. Nepal, J. Y. Lin, and H. X. Jiang. Photoluminescence studies of impurity transitions in mg-doped algan alloys. Applied Physics Letters,

94(9):091903, 2009. doi: http://dx.doi.org/10.1063/1.3094754. URL http://scitation.aip.org/content/aip/journal/apl/94/9/10.1063/1.3094754.

[197] K. B. Nam, M. L. Nakarmi, J. Li, J. Y. Lin, and H. X. Jiang. Mg acceptor level in aln probed by deep ultraviolet photoluminescence. Applied Physics Letters, 83(5):878–880, 2003. doi: http://dx.doi.org/10.1063/1.1594833. URL http://scitation.aip.org/content/aip/journal/apl/83/5/10.1063/1.1594833.

[198] A Pierret, C Bougerol, S Murcia-Mascaros, A Cros, H Renevier, B Gayral, and B Daudin. Growth, structural and optical properties of algan nanowires in the whole composition range. Nanotechnology, 24(11):115704, 2013. URL http://stacks.iop.org/0957-4484/24/i=11/a=115704.

[199] A Pierret, C Bougerol, B Gayral, M Kociak, and B Daudin. Probing alloy composition gradient and nanometer-scale carrier localization in single algan nanowires by nanocathodoluminescence. Nanotechnology, 24(30):305703, 2013. URL http://stacks.iop.org/0957-4484/24/i=30/a=305703.

[200] A. Pierret, C. Bougerol, M. den Hertog, B. Gayral, M. Kociak, H. Renevier, and B. Daudin. Structural and optical properties of alx ga1–xn nanowires. physica status solidi (RRL) – Rapid Research Letters, 7(10):868–873, 2013. ISSN 1862-6270. doi: 10.1002/pssr.201308009. URL http://dx.doi.org/10.1002/pssr.201308009.

[201] Robert A. Youngman and Jonathan H. Harris. Luminescence studies of oxygen-related defects in aluminum nitride. Journal of the American Ceramic Society, 73 (11):3238–3246, 1990. ISSN 1551-2916. doi: 10.1111/j.1151-2916.1990.tb06444.x. URL http://dx.doi.org/10.1111/j.1151-2916.1990.tb06444.x.

[202] Qimin Yan, Anderson Janotti, Matthias Scheffler, and Chris G. Van de Walle. Origins of optical absorption and emission lines in aln. Applied Physics Letters, 105(11):111104, 2014. doi: http://dx.doi.org/10.1063/1.4895786. URL http://scitation.aip.org/content/aip/journal/apl/105/11/10.1063/1.4895786.

[203] T. Koyama, M. Sugawara, T. Hoshi, A. Uedono, J. F. Kaeding, R. Sharma, S. Nakamura, and S. F. Chichibu. Relation between al vacancies and deep emission bands in aln epitaxial films grown by nh3-source molecular beam epitaxy. Applied Physics Letters, 90(24):241914, 2007. doi: http://dx.doi.org/10.1063/1.2748315. URL http://scitation.aip.org/content/aip/journal/apl/90/24/10.1063/1.2748315.

[204] Leah Bergman and Jeanne L. McHale, editors. Handbook of luminescent Semiconductor Materials. CRC Press, 2011.

[205] Jonas Lahnemann, Uwe Jahn, Oliver Brandt, Timur Flissikowski, Pinar Dogan, and Holger T Grahn. Luminescence associated with stacking faults in gan. Journal of Physics D: Applied Physics, 47(42):423001, 2014. URL http://stacks.iop.org/0022-3727/47/i=42/a=423001.

[206] G. Jacopin, L. Rigutti, L. Largeau, F. Fortuna, F. Furtmayr, F. H. Julien, M. Eickhoff, and M. Tchernycheva. Optical properties of wurtzite/zinc-blende heterostructures in gan nanowires. Journal of Applied Physics, 110(6):064313, 2011. doi: http://dx.doi.org/10.1063/1.3638698. URL http://scitation.aip.org/content/aip/journal/jap/110/6/10.1063/1.3638698.

[207] R. Liu, A. Bell, F. A. Ponce, C. Q. Chen, J. W. Yang, and M. A. Khan. Luminescence from stacking faults in gallium nitride. Applied Physics Letters, 86(2):021908, 2005. doi: http://dx.doi.org/10.1063/1.1852085. URL http://scitation.aip.org/content/aip/journal/apl/86/2/10.1063/1.1852085.

[208] Gilles Nogues, Thomas Auzelle, Martien Den Hertog, Bruno Gayral, and Bruno Daudin. Cathodoluminescence of stacking fault bound excitons for local probing of the exciton diffusion length in single gan nanowires. Applied Physics Letters, 104(10):102102, 2014. doi: http://dx.doi.org/10.1063/1.4868131. URL http://scitation.aip.org/content/aip/journal/apl/104/10/10.1063/1.4868131.

[209] W. Rieger, R. Dimitrov, D. Brunner, E. Rohrer, O. Ambacher, and M. Stutzmann. Defect-related optical transitions in gan. Phys. Rev. B, 54:17596–17602, Dec 1996. doi: 10.1103/PhysRevB.54.17596. URL http://link.aps.org/doi/10.1103/PhysRevB.54.17596.

[210] Y. T. Rebane, Y. G. Shreter, and M. Albrecht. Stacking faults as quantum wells for excitons in wurtzite gan. physica status solidi (a), 164(1):141–144, 1997. ISSN 1521-396X. doi: 10.1002/1521-396X(199711)164:1⟨141::AID-PSSA141⟩3.0.CO;2-G. URL http://dx.doi.org/10.1002/1521-396X(199711)164:1<141::AID-PSSA141>3.0.CO;2-G.

[211] C. Stampfl and Chris G. Van de Walle. Energetics and electronic structure of stacking faults in aln, gan, and inn. Phys. Rev. B, 57:R15052–R15055, Jun 1998. doi: 10.1103/PhysRevB.57.R15052. URL http://link.aps.org/doi/10.1103/PhysRevB.57.R15052.

[212] P. Corfdir, P. Lefebvre, J. Levrat, A. Dussaigne, J.-D. Ganière, D Martin, J. Ristić, T. Zhu, N. Grandjean, and B. Deveaud-Plédran. Exciton localization on basal stacking faults in a-plane epitaxial lateral overgrown gan grown by hydride vapor phase epitaxy. Journal of Applied Physics, 105(4):043102, 2009. doi: http://

dx.doi.org/10.1063/1.3075596. URL http://scitation.aip.org/content/aip/journal/jap/105/4/10.1063/1.3075596.

[213] M. Merano, S. Sonderegger, A. Crottini, S. Collin, P. Renucci, E. Pelucchi, A. Malko, M. H. Baier, E. Kapon, B. Deveaud, and J. D. Ganiere. Probing carrier dynamics in nanostructures by picosecond cathodoluminescence. Nature, 438(7067):479–482, 11 2005. URL http://dx.doi.org/10.1038/nature04298.

[214] Xuewen Fu, Gwenole Jacopin, Mehran Shahmohammadi, Ren Liu, Malik Benameur, Jean-Daniel Ganière, Ji Feng, Wanlin Guo, Zhi-Min Liao, Benoit Deveaud, and Dapeng Yu. Exciton drift in semiconductors under uniform strain gradients: Application to bent zno microwires. ACS Nano, 8(4):3412–3420, 2014. doi: 10.1021/nn4062353. URL http://dx.doi.org/10.1021/nn4062353. PMID: 24654837.

[215] Ekmel Ozbay. Plasmonics: Merging photonics and electronics at nanoscale dimensions. Science, 311(5758):189–193, 2006. doi: 10.1126/science.1114849. URL http://www.sciencemag.org/content/311/5758/189.abstract.

[216] Go Fujii, Toshiya Segawa, Shigehiko Mori, Naoto Namekata, Daiji Fukuda, and Shuichiro Inoue. Preservation of photon indistinguishability after transmission through surface-plasmon-polariton waveguide. Opt. Lett., 37(9):1535–1537, May 2012. doi: 10.1364/OL.37.001535. URL http://ol.osa.org/abstract.cfm?URI=ol-37-9-1535.

[217] Roman Kolesov, Bernhard Grotz, Gopalakrishnan Balasubramanian, Rainer J. Stohr, Aurelien A. L. Nicolet, Philip R. Hemmer, Fedor Jelezko, and Jorg Wrachtrup. Wave-particle duality of single surface plasmon polaritons. Nat Phys, 5(7):470–474, 07 2009. URL http://dx.doi.org/10.1038/nphys1278.

[218] Sylvain Fasel, Matthäus Halder, Nicolas Gisin, and Hugo Zbinden. Quantum superposition and entanglement of mesoscopic plasmons. New Journal of Physics, 8(1):13, 2006. URL http://stacks.iop.org/1367-2630/8/i=1/a=013.

[219] Alexander Huck, Shailesh Kumar, Abdul Shakoor, and Ulrik L. Andersen. Controlled coupling of a single nitrogen-vacancy center to a silver nanowire. Phys. Rev. Lett., 106:096801, Feb 2011. doi: 10.1103/PhysRevLett.106.096801. URL http://link.aps.org/doi/10.1103/PhysRevLett.106.096801.

[220] A. Archambault, T. V. Teperik, F. Marquier, and J. J. Greffet. Surface plasmon fourier optics. Phys. Rev. B, 79:195414, May 2009. doi: 10.1103/PhysRevB.79.195414. URL http://link.aps.org/doi/10.1103/PhysRevB.79.195414.

[221] Alexandre Archambault, Fran çois Marquier, Jean-Jacques Greffet, and Christophe Arnold. Quantum theory of spontaneous and stimulated emission of surface plasmons. Phys. Rev. B, 82:035411, Jul 2010. doi: 10.1103/PhysRevB.82.035411. URL http://link.aps.org/doi/10.1103/PhysRevB.82.035411.

[222] A. Manjavacas, F. J. García de Abajo, and P. Nordlander. Quantum plexcitonics: Strongly interacting plasmons and excitons. Nano Letters, 11(6):2318–2323, 2011. doi: 10.1021/nl200579f. URL http://dx.doi.org/10.1021/nl200579f. PMID: 21534592.

[223] D.N. Zubarev. Soviet. Phys. Usp., 3:320, 1960.

[224] Stephan Link, , and Mostafa A. El-Sayed*. Size and temperature dependence of the plasmon absorption of colloidal gold nanoparticles. The Journal of Physical Chemistry B, 103(21):4212–4217, 1999. doi: 10.1021/jp984796o. URL http://dx.doi.org/10.1021/jp984796o.

[225] P. Meystre and M. Sargent. Elements of Quantum Optics. Springer, 1990.

[226] Alejandro Manjavacas, Peter Nordlander, and F. Javier García de Abajo. Plasmon blockade in nanostructured graphene. ACS Nano, 6(2):1724–1731, 2012. doi: 10.1021/nn204701w. URL http://dx.doi.org/10.1021/nn204701w. PMID: 22224435.

[227] Roy J. Glauber. Coherent and incoherent states of the radiation field. Physical Review, 131(6), 1963.

[228] Roy J. Glauber and M. Lewenstein. Quantum optics of dielectric media. Physical Review A, 43(1), 1991.

[229] F. J. Garcia de Abajo, Ana Asenjo-Garcia, and Mathieu Kociak. Multiphoton absorption and emission by interaction of swift electrons with evanescent light fields. Nano Letters, 10:1859–1863, 2010.

[230] F J García de Abajo and M Kociak. Electron energy-gain spectroscopy. New Journal of Physics, 10(7):073035, 2008. URL http://stacks.iop.org/1367-2630/10/i=7/a=073035.

[231] Yoshihiro Akahane, Takashi Asano, Bong-Shik Song, and Susumu Noda. High-q photonic nanocavity in a two-dimensional photonic crystal. Nature, 425(6961):944–947, 10 2003. URL http://dx.doi.org/10.1038/nature02063.

[232] Bumki Min, Eric Ostby, Volker Sorger, Erick Ulin-Avila, Lan Yang, Xiang Zhang, and Kerry Vahala. High-q surface-plasmon-polariton whispering-gallery microcavity. Nature, 457(7228):455–458, 01 2009. URL http://dx.doi.org/10.1038/nature07627.

ÉCOLE DOCTORALE
Physique en Île-de-France (EDPIF)

Titre : L'expérience de Hanbury Brown and Twiss dans un microscope électronique à transmission à balayage : la physique et les applications

Mots clés : Microscopie électronique, cathodoluminescence, optique quantique, émetteur de photon unique, spectroscopie, nano-optique.

Résumé : Etre capable de réaliser des expériences d'optique quantique à l'échelle du nanomètre est un des grands défit actuel de la recherche. En particulier pour la caractérisation des émetteurs de photon unique, c'est à dire des émetteurs qui n'émettent qu'un photon à la fois. Dans cette thèse nous montrerons comment la cathodoluminescence (CL) dans un microscope électronique à transmission à balayage (STEM) a permis de caractériser un nouvel émetteur de photon unique (SPE), d'utiliser le signal produit par l'expérience de CL-STEM pour l'expérience HBT. Cependant, en étudiant l'excitation de multiple SPE en CL, on a découvert un nouveau phénomène d'émission, caractérisé par un grand effet de regroupement (bunching) dans la fonction $g^{(2)}(\tau)$ ($g^{(2^\circ}(0)>35$), en complète contradiction avec les mesures de Photoluminescence (PL) ($g^{(2^\circ}(\tau) \sim 1$). Dans mon manuscrit de thèse, cet effet surprenant a été expérimentalement étudié, théoriquement expliqué et appliqué à la mesure de temps de vie à l'échelle du nanomètre. Et parce que l'optique quantique est souvent liée à la plasmonique quantique, je présenterai pour conclure une proposition théorique en collaboration avec Javier Garcia de Abajo pour étudier la plasmonique quantique dans un microscope électronique à transmission.

Title : Intensity Interferometry Experiments in a Scanning Transmission Electron Microscope : Physics and Applications

Keywords : Electronic microscope, cathodoluminescencen quantum optics, single photon emitter, spectroscopy, nano-optics.

Résumé : Quantum optics performed at the nanometer scale is an important challenge, especially for the characterization of single photon emitter (SPE). SPE are emitter that emit only one photon at a time. In this thesis we will see how cathodoluminescence (CL) in a STEM (scanning transmission electron microscope) allowed to characterize a new point defect in h-BN (boron nitride), showing the relevance of the Hanbury Brown and Twiss (HBT) experiments in a CL-STEM for discovering and characterizing new SPE. However, by studying the excitation of multiple SPE in CL, we discovered a new emission phenomenon, characterized by a huge bunching effect of the $g^{(2)}(\tau)$ function ($g^{(2)}(0) > 35$), in complete contradiction to PL measurements and expectations ($g^{(2^\circ}(\tau) \sim 1$). In my thesis manuscript, this surprising effect will be experimentally investigated, theoretically explained and applied to lifetime measurement at the nanometer scale. Because quantum optics is often linked to quantum plasmonics, I will present, in conclusion, a theoretical proposal, in collaboration with J. Garcia de Abajo, about quantum plasmonics measurement in a STEM.

Université Paris-Saclay
Espace Technologique / Immeuble Discovery
Route de l'Orme aux Merisiers RD 128 / 91190 Saint-Aubin, France